

Magnetic Field-based Localization System

Vom Fachbereich Informatik der
Technischen Universität Kaiserslautern
zur Verleihung des akademischen Grades
Doktor der Ingenieurwissenschaften (Dr.-Ing.)
genehmigte Dissertation
von

Gerald Stephan Pirkl

Datum der wissenschaftlichen Aussprache: 25.11.2016

Dekan: Prof. Dr. Klaus Schneider

Berichterstatter: Prof. Dr. Karsten Berns

Berichterstatter: Prof. Dr. Paul Lukowicz

Berichterstatter: Prof. Dr. Kristoph Van Laerhoven

Kurzzusammenfassung

Diese Dissertation beschäftigt sich mit einem auf oszillierenden Magnetfeldern basierendem Lokalisierungssystem und der zugrunde liegenden Verarbeitungsstruktur. Das System besteht aus mehreren stationären Ankerpunkten (Sender), die oszillierende Magnetfelder erzeugen, und tragbaren Magnetfeldmesseinheiten (Empfänger), deren Positionen bestimmt werden sollen. Das System wird in verschiedenen Umgebungen und Anwendungsgebieten evaluiert. Desweiteren werden verschiedene Einsatzmöglichkeiten des Lokalisierungssystems in den Bereichen *Ubiquitous* und *Pervasive Computing* sowie *Ambient Assisted Living* diskutiert und bewertet. Zuletzt wird die Kombination von magnetfeldbasierten Abstandsinformationen und Positionsinformationen aus LIDAR Abstandsmessungen beschrieben und evaluiert.

Die Systemarchitektur besteht aus drei Schichten: einer physikalischen Schicht, einer Schicht, die für die Positions- und Abstandsbestimmung zwischen einem Magnetfeldtransmitter und einem Empfänger verantwortlich ist und einer Schicht, die Abstands- und Positionsinformationen zu verschiedenen Ankerpunkten betrachtet, um daraus die absolute Position der tragbaren Messeinheit zu bestimmen.

Jede der Schichten beleuchtet dabei verschiedene Aspekte, die bei der Verarbeitung der Magnetfeldinformationen beachtet werden müssen. Insbesondere die Eigenschaften der erzeugten Magnetfelder fließen in die Verarbeitungsalgorithmen ein. Die physikalische Schicht deckt dabei Magnetfelderzeugung, magnetfeldbasierte Informationsübertragung, Synchronisation von Magnetfeldtransmittern und Empfänger sowie die Abbildung des Verhaltens der Magnetfelder ab. Nachdem diese Information dann an einen zentralen Verarbeitungsrechner übertragen wurde, werden die hardware-spezifischen Signallevele auf das Niveau des theoretischen Magnetfeldmodells gehoben, und dann mittels des physikalischen Modells in Kandidatenpositionen und Abstandsinformationen umgewandelt. Bedingt durch Magnetfeldsymmetrien können die Messdaten auf nur acht Punkte (ein Punkt pro Koordinatensystemoktant) reduziert werden. Die ermittelten Positionen haben einen durchschnittlichen Fehler von 108 cm, der ermittelte Abstand einen durchschnittlichen Fehler von 40 cm.

Abschließend werden die Abstands- und Positionsdaten verschiedener Transmitter-ankerpunkte zusammengeführt. Hierbei spielen sowohl die zeitliche Synchronisation der Transmitter untereinander und die Reihenfolge der Auslösung der Transmitter als auch die abstands- und punkt-basierten Lokalisierungs- und Trackingalgorithmen eine Rolle.

Das Lokalisierungssystem wird in verschiedenen Anwendungen und Umgebungen evaluiert, die Position kann vom magnetfeldbasierten Lokalisierungssystem abhängig von der Umgebung mit einem durchschnittlichen Fehler von 60 cm - 70 cm ermittelt werden. Ein Vergleich mit einem funkbasierten Innenraumlokalisierungssystem zeigt die Robustheit des Magnetfeldes auch in

Bereichen mit Funk-Abschattungen wie zum Beispiel unter großen metallischen Gegenständen. Wir zeigen Algorithmen zur Bereichserkennung (Regions of Interest, ROIs), die sowohl auf den Magnetfeldrohdaten als auch auf den transformierten Positions- und Abstandsinformationen arbeiten. Eingesetzt in größeren Räumen, können Bereiche unterschieden werden, die mindestens 50cm voneinander entfernt liegen, kleine Spulenaufbauten (3 Spulen in $2m^3$) ermöglichen eine Auflösung von unter 20 cm.

Abschließend zeigen wir die Kombination eines tragbaren, auf 4 LIDAR Abstandssensoren basierenden Lokalisierungssystems mit dem magnetfeldbasierten Lokalisierungssystem. Das Magnetfeldlokalisierungssystem stellt dabei Abstandsinformationen zur Verfügung, um mehrdeutige Sensorinformationen des LIDAR Systems zu unterscheiden. Hier ist in einem Raum mit $8m \times 10m$ Fläche ein durchschnittlicher Positionsfehler von 8 cm zu erwarten.

Abstract

This dissertation describes an indoor localization system based on oscillating magnetic fields and the underlying processing architecture. The system consists of several fixed anchor points, generating the magnetic fields (transmitter), and wearable magnetic field measurement units, whose position should be determined (receiver). The system is evaluated in different environments and application areas. Additionally, various fields of application are discussed and assessed in ubiquitous and pervasive computing and Ambient Assisted Living. The fusion of magnetic field-based distance information and positions derived from LIDAR distance measurements is described and evaluated.

The system architecture consists of three layers, a physical layer, a layer for position and distance estimation between a magnetic field transmitter and a receiver, and a layer which uses several measurements to different transmitters to estimate the overall position of a wearable measurement unit.

Each layer covers different aspects which have to be taken care of when magnetic field information is processed. Especially the properties of the generated magnetic field information are considered in the processing algorithms.

The physical layer covers the magnetic field generation and magnetic Field-Based information transfer, synchronization of a transmitter and the receivers and the description of the locally measured magnetic fields on the receiver side. After a transfer of this information to a central processing unit, the hardware specific signal levels are transformed to the levels of the theoretical magnetic field models. The values are then used to estimate candidate positions and distances. Due to symmetrical effects of the magnetic fields, it is only possible to reduce the receiver position to 8 points around the transmitter (one position in each of the octants of the coordinate system). The determined positions have a mean error of 108 cm, the average error of the distance is 40 cm.

On top of this, the distance and position information against different transmitters are fused, this covers clock synchronization of transmitters, triggering and scheduling sequences and distance and position based localization and tracking algorithms. The magnetic-field-based indoor localization system has been evaluated in different applications and environments; the mean position error is 60 cm to 70 cm depending on the environment. A comparison against an RF-based indoor localization system shows the robustness of magnetic fields against RF shadows caused by big metal objects.

We additionally present algorithms for regions of interest detection, working on raw magnetic field information and transformed position and distance information. Setups in larger areas can

distinguish regions which are further than 50 cm apart, small scale coil setups (3 transmitters in $2m^3$) allow to resolve regions below 20 cm.

In the end, we describe a fusion algorithm for a wearable localization system based on 4 LIDAR distance measurement units and magnetic field-based distance estimation. The magnetic field indoor localization system provides distance proximity information which is used to resolve ambiguous position estimates of the LIDAR system. In a room ($8m \times 10m$), we achieve a mean error of 8 cm.

Contents

| | | |
|----------|--|-----------|
| 1 | Introduction | 11 |
| 2 | Available Localization Systems | 15 |
| 2.1 | Classification | 15 |
| 2.1.1 | Scene Analysis | 16 |
| 2.1.2 | Proximity | 17 |
| 2.1.3 | Triangulation | 19 |
| 2.2 | Indoor Localization Systems and their underlying Physical Phenomenon | 22 |
| 2.2.1 | Radio Frequency-based Systems | 22 |
| 2.2.2 | Sound-based Systems | 24 |
| 2.2.3 | Light-based Systems | 26 |
| 2.2.4 | IMU, Pedestrian Dead Reckogning | 30 |
| 2.2.5 | Smart Environments | 31 |
| 2.3 | Environmental Influences on the Signal | 32 |
| 2.3.1 | RF-based Approaches | 32 |
| 2.3.2 | Optical Approaches | 34 |
| 2.3.3 | Sound-based Approaches | 34 |
| 2.3.4 | IMU-based Systems | 34 |
| 2.4 | Conclusion | 36 |
| 3 | System Overview | 37 |
| 3.1 | Advantages of Magnetic Fields over other Physical Modalities | 37 |
| 3.2 | Magnetic Field-based Localization System | 39 |
| 3.3 | Available Magnetic Field-based Localization Systems | 42 |
| 3.3.1 | Medical Systems | 43 |
| 3.3.2 | Motion Tracking | 44 |
| 3.3.3 | Industrial Indoor Localization Systems and Tracking in Science | 45 |
| 3.4 | Conclusion | 46 |
| 4 | Physical Layer | 47 |
| 4.1 | Contribution | 48 |
| 4.2 | Physical Background | 49 |
| 4.2.1 | Law of Biot Savart | 49 |
| 4.2.2 | Law of Faraday | 50 |
| 4.3 | Magnetic Field Generation | 52 |
| 4.3.1 | Hardware for Field Generation | 52 |
| 4.3.2 | Behavior of different Transmitter Coil Architectures | 54 |

Contents

| | | |
|----------|--|------------|
| 4.4 | Hardware Calibration | 56 |
| 4.5 | Magnetic Field Gathering and Representation | 57 |
| 4.5.1 | Sampling and Amplification Control | 57 |
| 4.5.2 | Receiverside Magnetic Field Representation | 59 |
| 4.5.3 | Discussion | 63 |
| 4.6 | Amplification Control | 64 |
| 4.7 | Transmitter-Receiver Synchronization | 65 |
| 4.7.1 | RF Trigger Messages | 65 |
| 4.7.2 | Magnetic Field-based Synchronization | 67 |
| 4.7.3 | Data Transfer in a quasi-static Magnetic Field | 78 |
| 4.8 | Conclusion | 89 |
| 5 | Signal to Position / Distance Estimation | 91 |
| 5.1 | Contributions | 92 |
| 5.2 | Calibration | 93 |
| 5.3 | Calibration and Common Signal Level | 95 |
| 5.4 | Distance and Position Magnetic Field Model | 99 |
| 5.4.1 | Nearest Neighbor Lookup | 100 |
| 5.4.2 | Intersection of Equipotential Magnetic Field Shells | 100 |
| 5.4.3 | Cube-shaped 3D Division of Theoretical Magnetic Field Transmitter Space | 108 |
| 5.4.4 | Comparison | 108 |
| 5.5 | Conclusion | 113 |
| 6 | Multi Coil Position Estimation | 115 |
| 6.1 | Contribution | 115 |
| 6.2 | Synchronization of the components | 117 |
| 6.2.1 | Trigger Messages | 117 |
| 6.2.2 | Distributed Algorithm for Clock Synchronization | 119 |
| 6.2.3 | Conclusion | 125 |
| 6.3 | Transmitter Scheduling | 126 |
| 6.3.1 | Round Robin | 126 |
| 6.3.2 | Graph Coloring-based Scheduling | 127 |
| 6.4 | Multi Coil Localization Approaches | 130 |
| 6.4.1 | Data Set for Position Accuracy Evaluation | 130 |
| 6.4.2 | Candidate Points | 131 |
| 6.4.3 | Multilateration | 135 |
| 6.4.4 | Fusion of Point- and Distance-based Algorithms | 145 |
| 6.5 | Comparison against an RF-based Localization System | 147 |
| 6.5.1 | Evaluation | 148 |
| 6.6 | Detection of Regions of Interest | 149 |
| 6.6.1 | Large Scale Transmitter Setup in different Environments | 149 |
| 6.6.2 | Small Scale Transmitter Setup for Industrial Maintenance Tasks | 154 |
| 6.6.3 | Combination of Magnetic Field-based Localization and mBeacon-based ROIs | 158 |
| 6.7 | Conclusion | 159 |

| | | |
|----------|---|------------|
| 7 | Fusion of Magnetic Field Distance Estimations and LIDAR-based Position Estimations | 161 |
| 7.1 | Contribution | 162 |
| 7.2 | Related Work | 162 |
| 7.3 | LIDAR Helmet | 162 |
| 7.4 | LIDAR-based Localization | 163 |
| 7.5 | Influence of Distance, Heading and Map Errors on LIDAR Position Accuracy . . | 169 |
| 7.6 | Fusion of Magnetic Field Distance Information and LIDAR Positions | 171 |
| | 7.6.1 Experiment and Evaluation | 171 |
| 7.7 | LIDAR supported Estimation of Magnetic Field Transmitter Positions | 175 |
| 7.8 | Conclusion | 180 |
| 8 | Conclusion | 181 |

1 Introduction

Mobile devices provide voice-controlled information access (for example Apple Siri), which also takes the current position of the device into account. It is possible to retrieve information about restaurants nearby, get the route to the nearest gas station or to provide information about the next train reachable when walking. All these examples have one thing in common: the underlying source of information is location. To estimate the position, mobile phones rely on a global navigation satellite system (GNSS). The accuracy of these systems in outdoor applications is below $5m$; additionally fusion algorithms combine WIFI and inertial navigation information to the position information to improve the accuracy. A drawback of GNSSs is that the used RF signals do not permeate concrete structures in most cases and therefore are hardly suitable for indoor applications.

In contrast to outdoor environments, which typically provide direct line-of-sight between the system components, indoor environments are usually self-contained volumes. Scientists have researched this field for many years and have found specific approaches for indoor localization. Although many localization systems are available and a variety of applications relying on location and position information can be found, mobile phone producers have not integrated specialized indoor localization techniques due to their high costs and the high installation and maintenance efforts to be considered.

Taking the covered or the served area into account, different classes of indoor applications can be distinguished.

Large scale environments are typically found in industrial places. For example, the indoor localization system has to provide information about the current position of a particular product (storage system) or the positions of autonomous transport devices in a warehouse. They also provide information about the shortest path between the current location of a worker and the aimed machine.

Medium scale applications are for example found in shopping environments: location-based services are broadly used to adjust the presented information depending on the context of the person. Detecting RF anchor points, using Bluetooth LE or similar techniques, is used to detect proximity and show information about a product in a mobile app.

Small scale applications usually cover a very limited area (a room or even less). Particular tasks are considered in these environments, such as motion capturing, surveillance of persons (Ambient Assisted Living, AAL) or scientific tasks such as ground truth information for later data evaluation.

In addition to requirements of the broad field of applications, the researched and developed

1 Introduction

localization systems have to concern more complex environmental conditions compared to GNSS. Buildings typically consist of a variety of materials. Depending on the used localization system, the underlying physical source of information is influenced/ altered or even completely blocked by the components of the building. A possible way of reducing these effects is to combine dynamic signal influences, such as humans or autonomous vehicles with the environmental model. Therefore dynamic influences are the second object in the development of indoor localization systems, to reduce the effects of for instance humans living and working within the environment. Their dynamic influence is not only caused by their simple presence but persons also interact with the environment, furniture is opened, moved around, added or removed. Electrical devices can be turned on automatically or by the humans. All these impacts either have to be considered, modeled, or reduced when choosing and implementing a localization system. Still, although models for these effects exist, a robust physical measurement principle with no or little environmental dependencies is preferable.

There is a huge variety of localization techniques commercially available or currently under development. This dissertation presents an indoor localization system using artificial oscillating magnetic fields as an underlying measurement principle. Although being a well-known effect in physics, magnetic fields for position estimation have only been used in small scale and niche applications. The magnetic fields provide, compared to principles based on RF or IR, a higher robustness against influences and do not require line of sight. Magnetic fields permeate non-ferromagnetic materials, are not influenced by humans and are comparably easy to generate. This property allows modeling the field behavior accurately. Although impacts of ferromagnetic materials are locally visible, the overall magnetic field behavior is not changing.

In contrast to optical- or RF-based localization systems, magnetic field-based localization systems are more reliable in industrial environments without the effort of additional heavy filtering to reduce outliers. On the downside, magnetic fields have a high dynamic range due to its significant distance dependent nature. Particularly in great distances, noise dominates the signal. Hard- and software components (amplification, filtering and signal adaption) have to be developed and applied to deal with this effect.

In this dissertation, we present and evaluate a processing architecture which is being implemented to the well-known principles of oscillating magnetic fields to design and build a localization system in ubiquitous indoor environments. Similar to the ISO/OSI model in network communication, we aggregate approaches to different layers: on the hardware level, we evaluate signal gathering and signal representation methods which take the physical behavior of oscillating magnetic fields and the high dynamic range of the signal into account. Additionally, this layer includes different well-known synchronization and scheduling algorithms which are adapted and applied to the magnetic field localization system. On top of the hardware part, a hardware abstraction layer integrated into a centralized processing unit collects the sampled magnetic field information from different transmitter anchor points at the wearable receiver side and abstracts from the hardware dependent influences by applying polynomial calibration functions. The described approaches consider both, the calibration effort and the accuracy of the position estimation.

A specific transmitter coil architecture with three perpendicular transmitter axes provides sufficient information to restrict the position of a receiver to a point in each of the eight octants around the transmitter coordinate system. We describe a magnetic field model for distance and (rough) position estimation using information from a single transmitter coil. The mean distance error is 40 cm within the sphere (radius 4.5m)of coverage. Combining distance information to several transmitters allows estimating the position of a receiver with a mean error of 60cm in a $8 \times 10m$ big area. The system is evaluated in different scenarios, determining regions of interest in large-scale environments (the minimum space between parts has to be 50cm) and small scale industrial environments to support maintenance applications (the minimum distances between areas is below 20cm). Additionally, a fusion algorithm for a LIDAR supported helmet is described and evaluated. In this application, the magnetic field information is used to dissolve ambiguous locations derived from the LIDAR localization system. We achieve an accuracy of 8cm in an $8m \times 6m$ room. Additionally, we describe an algorithm for transmitter coil position estimation using the fusion algorithm.

Contribution

The following contributions have been achieved:

- Research, development, and evaluation of a **signal processing architecture** for a magnetic field-based localization system (physical layer, single coil position, and distance estimation layer, multi-coil position estimation layer)
 - **Physical Layer**
 - * Micro-controller-based **signal gathering, amplification control and magnetic field representation** to compensate the high dynamic range of the magnetic field and to reduce the effects of noise to maximize the range of the system (4.5m range)
 - * **Evaluation of different synchronization schemes** regarding robustness in different environments and sampling rates. (Cable-based, RF-based and magnetic field-based synchronization and information transfer).
 - **Single coil position and distance estimation layer**
 - * **Hardware Abstraction Layer** to compensate hardware related effects (hardware tolerances and production inaccuracies), evaluation of different calibration approaches to align the signal levels of various transmitter-receiver pairs with the theoretical signal level
 - * **Theoretical magnetic field model** for distance and position estimation
 - Evaluation of different **single coil position estimation** approaches resulting in 8 candidate positions around the transmitter. The methods rely on the three axes emitter coil setup (Magnetic field magnitude shells and cube shaped division of the volume around an emitter coil) (mean error below 117 cm in the covered area of 4.5m radius)
 - **Distance estimation** on top of the candidate position estimation (mean distance error below 40 cm)

- **Description of a fast model to estimate the position and distance** in $\mathcal{O}(\log(n))$ using $\mathcal{O}(n)$ space where n is the number of possible model elements.
- **Multi coil position estimation layer**
 - * Evaluation of different **Scheduling and synchronization** approaches between multiple transmitters.
 - * **Fusion of localization algorithms** relying on distance and candidate positions derived from the magnetic field model.
 - * **Evaluation of the magnetic field-based localization system** in different environments including tracking and filtering with a mean error of below $77cm$. Comparison against an RF-based localization systems (mean error $67cm \leftrightarrow 77cm$)
- **Evaluation in different application environments** including regions of interest in large scale environments (at least 50cm apart) and small scale industrial applications (at least 20cm apart)
- **Sensor fusion of LIDAR- and magnetic field-based localization**, including the LIDAR-based position estimation (mean position error below 8 cm in a 8 times 10m big area)

2 Available Localization Systems

Many applications are using or requiring position information. Therefore indoor localization has been a broad field of research over the last decades. A wide-reaching spectrum of localization techniques tries to estimate the location of persons in office environments, their living rooms or Ambient Assisted Living (AAL) applications, devices (as robots or products in manufacturing environments) and other elements of interest. Although location itself is only one possible source of context (as discussed in [SBG99]), position information limits the set of possible activities in activity recognition tasks. Reliability, robustness, and accuracy of such systems have been the primary goal of the regarded research, but an entirely satisfying solution still has not been found. This chapter will present an overview of possible localization systems as they can be consulted in the literature. We will discuss available localization techniques concerning localization accuracy and robustness. As the field of localization supported applications is broad, only selected work, influencing mainly ubiquitous and pervasive applications, will be included in this chapter. This chapter gives a general overview of indoor localization systems and approaches, magnetic field related scientific research is presented in section ?? after the general discussion and presentation of our localization system.

2.1 Classification

In literature different ways of organizing indoor localization systems are available. In most cases, the underlying physical modality like RF, infrared or ultrasound is used to categorize the systems, other texts use the developed and applied algorithms.

A combination of both, the algorithmic-based categories and examples of technical approaches for indoor localization are presented. Well known overviews of localization systems in ubiquitous environments have been given in [HB01] and [LDBL07]. In [Mau12] Mautz presents a list of user requirements and a detailed list of indoor localization systems. An overview of passive indoor localization systems not requiring any wearable devices is given in [KVPV14]. We present the categories as discussed by Hightower ([HB01]) or the authors of [FNI13]:

triangulation, proximity and scene analysis

Figure ?? shows the different categories more detailed.

Later we present and describe these categories and different physical approaches of indoor localization systems.

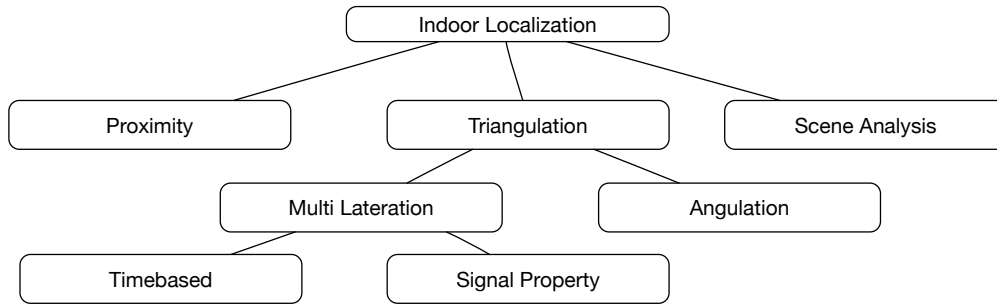


Figure 2.1: Overview of the different indoor localization categories, adapted from [FNI13]

2.1.1 Scene Analysis

Scene Analysis is a localization method which compares the sensor information of the current position against the data of pre-recorded positions. The sensor information is compared to the data set, and the most similar reference point is typically used. In most cases, a scene analysis-based positioning approach consists of two steps:

The first step maps/records position information and the corresponding sensor reading. In the second phase, the online phase, the position estimation takes place. The data recording step also involves the creation of a suitable lookup data structure for fast data comparison and position estimation. Therefore a feature extraction mechanism has to provide meaningful feature tuples to avoid misclassification. To achieve the aimed accuracy, the number of measurement points have to be carefully chosen. Changes in the environment can lead to different sensor readings and therefore misclassification / different position estimations.

Typical scene analysis-based approaches are RF fingerprinting-based localization systems as RADAR [BP00] or visual / camera-based systems as for example described in [LCCVG07].

Camera-based scene analysis systems have to match the images of a scene to the (3D) model of the environment. Microsoft research groups have worked on the 3D Model generation using mobile phone photographs of city parts [ASS⁺09]. This approach is called *structure from motion* and has additionally been examined in [COSH11], [FFGG⁺10] and [HTP10].

Many research groups work on the localization of pedestrians ([IZFB09], [RC04], [CBK⁺11], [ZK06]) using image information and scene analysis approaches. Also robot groups estimate the positions of their robots using *Simultaneous Localization and Mapping* (SLAM) approaches with support of image processing and scene analysis ([CN08], [ED06], [WIB11]).

A broad market in consumer electronics has been reached with the occurrence of cleaning robots using indoor localization algorithms and techniques. A vision-based localization system has been integrated into these systems: The Miele vacuum cleaning robot Scout RX1 utilizes a camera pointing towards the ceiling. The system matches previously recorded features of the ceiling against the current picture and therefore can limit positioning errors which occur from using the odometrical information derived from motor steps and environmental sensors.

WIFI fingerprinting-based approaches as the RADAR [BP00] system rely on a database of

measured RSSI (Received Signal Strength Indicator) values relative to multiple WIFI access points. In urban areas and office environments, usually, various numbers of access points can be found. The access points can be distinguished using unique MAC addresses. A mobile phone or a wearable device collects for a discrete set of coordinates the visible access points and the signal strength of received packets of the individual base stations. A database aggregates for each measurement point the corresponding access point ids and RSSI values. The localization step surveils the visible access points and the corresponding RSSI values, a mapping algorithm retrieves the best coordinate for the id and RSSI tuples. Changes in the environment after the mapping step influence the visibility and signal strength of the base stations and therefore reduce the accuracy of the localization systems. The human body also attenuates the signal when the receiver and the base station is shielded by the body. This influence is reduced by collecting RSSI values at different receiver orientations so that human bodies attenuate the signals. This approach has a high calibration/data collection overhead. To compensate RSS fluctuations, propagation models and statistical models have been researched in [CLZ⁺13], [ZZXL14] (Definition of lookup metrics to detect and deal with fluctuations), a review of probabilistic localization methods is given in [MMWKH14]. The accuracy of WIFI fingerprinting-based approaches is typically only on room level granularity. A combination of different sensing modalities allows increasing accuracy.

The authors of [BK12] use a more adequate and accurate RF propagation model and deal with falsified or missing RSSI measurements. In a competition¹ the system achieved a mean localization error of 1.6m.

2.1.2 Proximity

In a *proximity-based* indoor localization approach, the system provides information when a user to be localized is close to an anchor point whose position is known. In most cases, the term "close" is linked to the coverage of a single device.

Typical examples are RFID-based systems ([JLP06] or [BSM07]) or infrared-based systems. Near field communication (NFC) has also been proposed for proximity-based localization as described in [HHZN12] and in [BJRGN11]. When the reader detects an id in the used physical phenomenon, a lookup mechanism retrieves the related 3D position or semantic information (for example, the person is close to a kitchen appliance). Current state mobile phone devices are equipped with NFC readers, so it is possible to detect NFC tags in the environment and limit the mobile phone position to the known position of the NFC tag. Notice that there is a need to identify these reference points correctly. RFID-based systems, therefore, use unique identifiers, infrared-based systems encode these unique identifiers in their pulses. We discuss these techniques in later sections of this chapter.

In cell phone environments, a tuple of visible cell towers allows limiting the position of the cell phone to the intersection of the transmission ranges around the cell towers. In most cases, the system assumes that the coverage is circular. In the context of sensor networks this approach is

¹ISPN 2014, M. Klepal, Wifi-based Localization system

2 Available Localization Systems

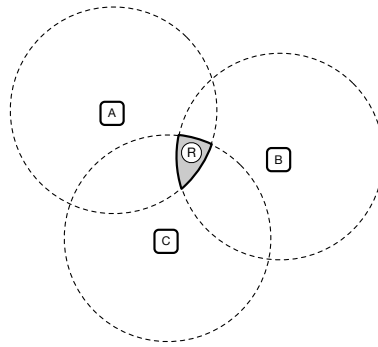


Figure 2.2: Using the transmission range of several base stations allows to limit the position of a receiver to the intersection of the transmission areas.

also called *connectivity*. By using a bounding box intersection algorithm, the position of sensor nodes can be deduced from this information.

The iBeacon approach specified by Apple Inc. provides a Bluetooth low energy (BLE)-based localization service for cell phones. The modules consist of a chip emitting their unique id using the BLE standard. Applications include shop navigation, location-based services ("Alert the user if the phone is close to a specific position") or when several beacons are combined, indoor localization based on BLE beacons. An advantage compared to other systems is that iBeacons allow distinguishing between several proximities ("close", "medium distance", "far").

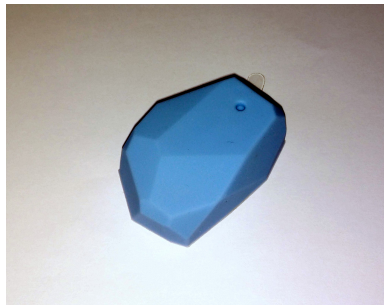


Figure 2.3: Estimote iBeacon. The beacon allows a proximity-based localization approach which also supports multilevel proximities like ("close", "medium distance", "far").

As in RF-based localization systems, the proximity-based approach has weaknesses. Environmental effects like signal attenuation or signal scattering deforms the circular transmission range, which leads to positions where anchor points are either visible (although not visible with regard to the model) or they are not visible (although they should). A more detailed discussion of these RF problems is given in the latter. One must also keep in mind that installation and maintenance of this localization approach can be complex. Changes in the anchor point positions also need to be updated in the anchor point database. Additionally, RF-based systems require power supplies, either based on batteries or cables.

2.1.3 Triangulation

This approach uses distance (Lateration) or angle (Angulation) estimations between fixed base stations (anchors) and the position to estimate. These algorithms derive the necessary information from time-based approaches or extract it from the signal behavior by applying models to the sensor data. Mathematical algorithms then process the distance or angle information and return the position in 2D or 3D space. Typically these algorithms include least square minimization for hyperboloids or spheres.

Multilateration

A *multilateration* approach uses distance estimations between the position of the mobile receiver and multiple anchor points. Each distance reduces the number of possible positions to a sphere around the corresponding anchor point with the radius of the estimated distance. Distances can be estimated with different techniques such as light, sound, magnetic fields or time difference of arrival techniques as in UWB Systems ('Ubisense') or ultrasound-based systems.

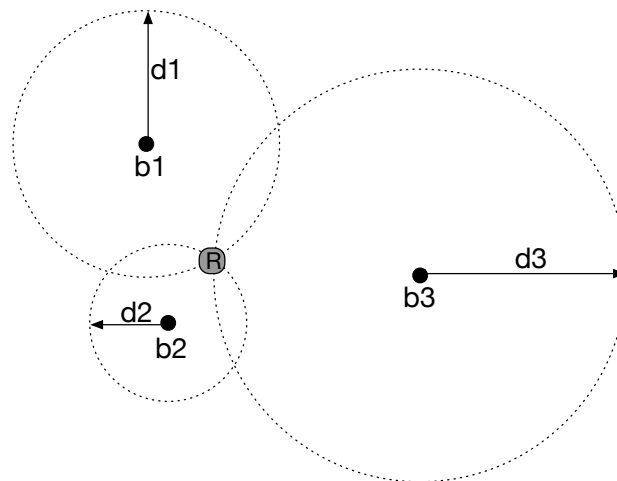


Figure 2.4: Multilateration approach. The base stations b_i act as anchor points against which the distances d_i are estimated. Using spherical intersections, it is possible to determine the position of the receiver R .

The estimation of a 3D coordinate with four distances against four signal reception base stations is complex as the distance from a base station describes the possible point of residence in a nonlinear manner. Therefore in literature, least square optimizations (for example nonlinear least square estimators Gauss-Newton or Levenberg Marquardt) or closed form position estimation algorithms are used to solve this problem. The minimization approach also works with error prone distance estimations which typically result in an "intersection" volume instead of a single point.

We described this approach in [PL13]. Let \mathbf{b}_i be the position of the anchor point i . The basic idea is to find a coordinate $\mathbf{p} = (x, y, z)$ in 3D space minimizing the difference Δ_i between the

2 Available Localization Systems

distances $d_i^t = \|\mathbf{b}_i - \mathbf{p}\|$ and the estimated distances d_i^e :

$$\Delta_i = |d_i^t - d_i^e| \quad (2.1)$$

With this approach it is also possible to favor lower distance estimations, typically involving lower errors, by drawing the point closer to the corresponding and more accurate base stations. Notice that for an n -dimensional position estimation, at least $n + 1$ measurements to different anchors are required.

Multilateration algorithms are present in literature: In addition to the field of ubiquitous computing, position estimation also plays a great role in aviation as described in [MLG08]. The authors formulate a closed form description of multilateration-based on hyperbolic intersections. Comparable approaches for this can be found in [UR04].

As presented in [LDBL07] possible lateration techniques are for example based on *time of arrival*, *time of flight* (US), *time difference of arrival*, *received signal phase*, *received signal strength* (conversion to distances) and *round trip time of arrival*. All these techniques allow determining the distance between the anchor points and the point of interest. The time difference of arrival approaches (also part of multilateration algorithms) are based on the intersection of hyperboloids defined by the time differences between the base stations.

Time-based Approaches

Time of arrival or time of flight -based approaches use the **absolute** time difference between transmission and reception of the signal on the receiver side. Using the time difference and the known propagation speed of the physical signal allows estimating the distance between the two components. This approach either requires a strict clock synchronization, a trigger signal with a much higher propagation speed than the used measurement signal or a compensation of the clock phase differences.

Ultrasound-based systems use this approach and are discussed later. Examples of *time of arrival*-based approaches are WIFI-based *time of flight* ranging and IMU fusion ([SBA14]), ultrasound-based localization ([MSDIT13], [Pri05] or [TNNL02]) or *time of flight* cameras as presented in [Li], [BMB⁺13] and [HLCH12]. These cameras provide, in addition to the recorded 2D scene, distance information between obstacles and the camera. A special form of *time of arrival* is *round trip time of arrival* which uses the time measurements for forward and backward signal transfer. This approach is described in [PAY07] and [GH05].

Time difference of arrival approaches correlate the signals of several anchor points to estimate the differences in the arrival of the signal. In ultrasound / sound-based localization systems the time differences describe hyperboloids of possible positions around the anchor points. Intersecting these geometrical entities results in the position. Examples of *time difference of arrival*-based localization systems use a microphone array to estimate the position of sounds ([PSP13], [GG03] or in robotics [VMRL03]).

Phase of arrival and phase difference of arrival [PS11] use the phase or phase shift between two receiver nodes to estimate their spatial relationship. It is also possible to estimate the angle of arrival. A clear differentiation whether these approaches are multilateration- or angulation-based is therefore often not possible.

Most commonly this technique is found in wave-based technologies. Deriving distance information from *phase of arrival* is presented in [PS10], [SPM⁺13] and in [NMR⁺10]. *Phase difference of arrival*-based RFID position estimation is presented in [PS11] and [QHZ⁺].

Signal Property-based Approaches

The wave nature of RF signals introduces a reduction of the amplitude with rising distance. This phenomenon is used to estimate distances between the receiver and transmitter unit. We use this approach in our work. Artificial magnetic fields have a similar behavior. The field strength drops with $\frac{1}{d^2}$, where d is the distance in m. There are also articles ([XTL⁺14]) which use an energy measure derived from artificial light sources to accurately measure the distances and angles between a photodiode and a led.

RF-based distance estimations have been performed in [AFD07], [XLL⁺10] and in [BMPC08], due to signal reflections and signal attenuation the RSSI-based distance estimation is of poor quality. A discussion of these problems can be found in subsection 2.3.1.

Angulation

According to [LDBL07], *angulation* approaches rely on the estimation of angles instead of distances for finding the position. Possible techniques for this are RF, ultrasound, light or UWB. RF requires directional antennas to estimate the angle of arrival. Multiple antennas and therefore the differences in the arrival times of the signals also allow estimating the angle of arrival.

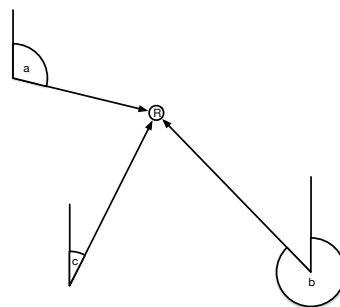


Figure 2.5: In angulation approaches, the used technique has to determine the angles of multiple base stations against the corresponding position. The angles are then used to determine the position.

Typical techniques for finding angles are the usage of phases and phase differences as already mentioned in the lateration section. *Angle of arrival* or *phase difference of arrival* information is

2 Available Localization Systems

used to estimate the *angle of arrival* in [QHZ⁺] and [ACD⁺11]. Models for spatial and angular behavior in indoor environments for UWB-based systems of the in [SJJ⁺00].

A basic model for the angulation positioning is described in [Xio98]:

Let D_i be the distances from the mobile position (x_m, y_m) to the transmitter $t_i = (X_i, Y_i)$ and θ_i the corresponding estimated angle:

$$A = \sum_{i=1}^N \frac{\sin^2 \theta_i}{D_i^2 \sigma_i^2} \sum_{i=1}^N \frac{\cos^2 \theta_i}{D_i^2 \sigma_i^2} - \left(\sum_{i=1}^N \frac{\sin \theta_i \cos \theta_i}{D_i^2 \sigma_i^2} \right)^2$$

$$x_m = \sum_{i=1}^N \frac{\cos^2 \theta_i}{D_i^2 \sigma_i^2} \left(\sum_{i=1}^N \frac{\sin^2 \theta_i X_i}{D_i^2 \sigma_i^2} - \sum_{i=1}^N \frac{\sin \theta_i \cos \theta_i Y_i}{D_i^2 \sigma_i^2} \right) + \sum_{i=1}^N \frac{\sin \theta_i \cos \theta_i}{D_i^2 \sigma_i^2} \left(\sum_{i=1}^N \frac{\cos^2 \theta_i Y_i}{D_i^2 \sigma_i^2} - \sum_{i=1}^N \frac{\sin \theta_i \cos \theta_i X_i}{D_i^2 \sigma_i^2} \right) A$$

$$y_m = \sum_{i=1}^N \frac{\sin^2 \theta_i}{D_i^2 \sigma_i^2} \left(\sum_{i=1}^N \frac{\cos^2 \theta_i Y_i}{D_i^2 \sigma_i^2} - \sum_{i=1}^N \frac{\sin \theta_i \cos \theta_i X_i}{D_i^2 \sigma_i^2} \right) + \sum_{i=1}^N \frac{\sin \theta_i \cos \theta_i}{D_i^2 \sigma_i^2} \left(\sum_{i=1}^N \frac{\sin^2 \theta_i X_i}{D_i^2 \sigma_i^2} - \sum_{i=1}^N \frac{\sin \theta_i \cos \theta_i Y_i}{D_i^2 \sigma_i^2} \right) A$$

2.2 Indoor Localization Systems and their underlying Physical Phenomenon

2.2.1 Radio Frequency-based Systems

Many research groups have conducted research on radio frequency (RF)-based localization systems. RF is a well-known technique with a broad spectrum of applications. Additionally, RF supports high data throughput. Integrated circuits for standard frequencies allow reducing the size of the hardware. Mobile phones have several radio modules for body area and great distance communication, therefore, RF has been a broad field of research.

The authors of [LDBL07], [SCGL05] and [GLN09] give an overview for RF-based indoor localization systems. Applications of these indoor localization systems cover sensor networks (for example [HHB⁺03], [PAK⁺05], [HE04]), location-based services ([BP00], [HWB00], [BJ09]) and applications in ambient assisted living (AAL) as presented by Stelios et al. in [SNE⁺08].

RF localization systems rely on different physical phenomena: Amongst others, measurements of the amplitude of the received RF signal, an angle of arrival (using a set of antennas), time difference of arrival (multiple receiver stations) or RF phase shift estimation. The different approaches have been described on page 19 and page 21. Additionally WIFI-based fingerprinting is a scene-based approach and has been researched excessively (e.g. [BP00], [BK12], [RS01], [CLZ⁺13], [ZZXL14], [MMWKH14]). In most cases WIFI-based localization is used as anchor information for inertial measurement units, this requires strong fusion algorithms as we showed in [PMF⁺12].

Ultra Wide Band-based Systems

A particular form of radio-based localization is ultra wide band (UWB)-based localization. According to [SKCB02], a radio signal should be called ultra wide band "when the 3dB bandwidth of a radio signal becomes 25% or more of the signal's center frequency". The WiMedia Alliance specifies the UWB Spectrum between 3100MHz and 10600MHz. The output level has a maximum of $-41.3\text{dBm}/\text{MHz}$.

Compared to other RF communications, the output level is very low, as visible in figure 2.6. UWB-based localization systems use both time difference of arrival and angle of arrival (system as in [TDM11]). The high frequencies allow estimating the distances very accurately. Compared to e.g. radar, material penetration is better as stated in [SWH⁺00]. Due to the high bandwidth of the pulse, information such as transmitter IDs, are encoded in the pulse. Additionally, this can be used as a synchronization mechanism.

Correlating the input signals of the receiver antennas at different positions in 3D space results in time difference of arrival estimations. Multiple receiver antennas at the base stations allow angulation approaches. Therefore both (hyperbolic) angulation algorithms and lateration algorithms are used to determine the position of the pulse emitter.

The sampling rate of UWB systems is comparably high, and the accuracy is lower than 30 cm in laboratory environments. Metal objects strongly influence the measurement accuracy due to common RF problems like signal reflection or scattering.

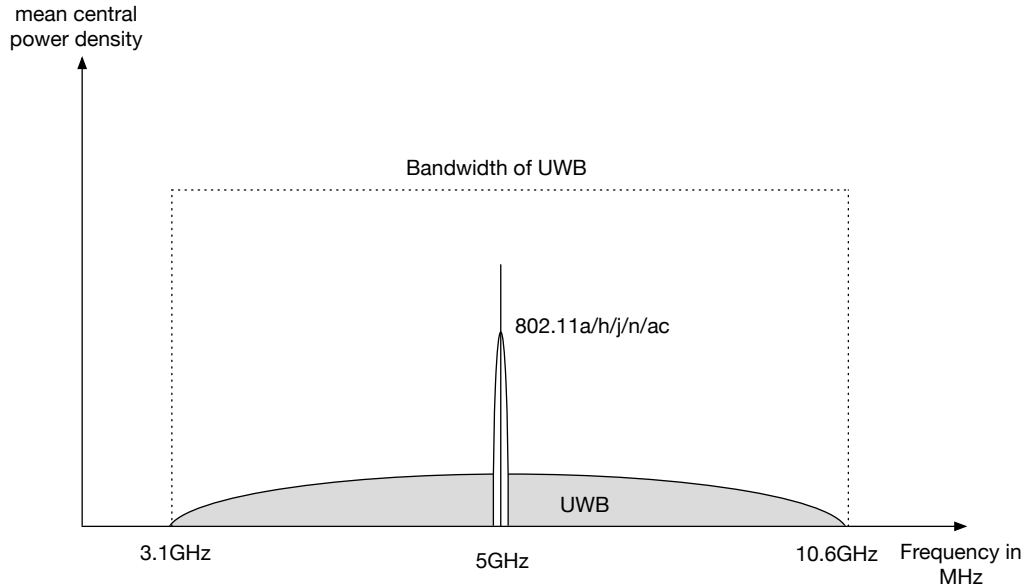


Figure 2.6: Spectrum and signal energy of WIFI 802.11a/h/j/n/ac 5GHz RF systems and ultra wide band pulse.

A good UWB overview can be found in [SGG08]. UWB related research has to deal with multi path environments (for example [TSH05]) resulting in echoes, signal attenuations or fading, and has to compete with other narrow band data communications such as 204.11a which uses parts

of the UWB spectrum. To limit the power output of the transceivers, the antenna design is complex. Solutions for these problems and examples for UWB localization systems are described in [IHQ04], [ZSHZ12], [KZM⁺08] or [YRL10]. Applications of UWB localization systems can be tracking of persons in hospitals ([HGRL08], [WMP⁺12]) or robotics([GBG⁺09], [SHSM10])

2.2.2 Sound-based Systems

Ultra Sound

Ultrasound-based localization systems typically consist of two components: an ultrasound transducer which emits an ultrasound pulse at frequencies above 20 kHz and a receiving unit (basically a microphone) sensing for the ultrasound pulses. They require the installation of transducer/receiver units at the room elements. A wearable device measures the distances to several ultrasound emitters and multilaterates its positions.

In literature two approaches are presented: *time of flight* and *time difference of arrival*. In the first the distance between the emitter and the receiver can be calculated using the propagation speed of sound in air, in the latter, multiple transducers are used to correlate angle and time information derived from the signal to apply hyperbolic localization approaches. Notice that the speed of ultrasound waves depends on the air pressure and temperature, therefore the receiver units are typically equipped with at least a temperature sensor to compensate the temperature's influence.

Ultrasound-based systems rely on a strict time synchronization and are prone to noise and sound reflections caused by walls or furniture. A direct line-of-sight is preferable since multi-path effects reduce the accuracy of the system. As described in [BK88] ultrasound signals can also be used to detect obstacles, and in the automotive industry, these systems support parking procedures. They are also used in robotics to either estimate obstacles (reflected ultrasound pulses are used) or estimate the distance between two robots (one emitting the pulse, the other one measuring the distance).

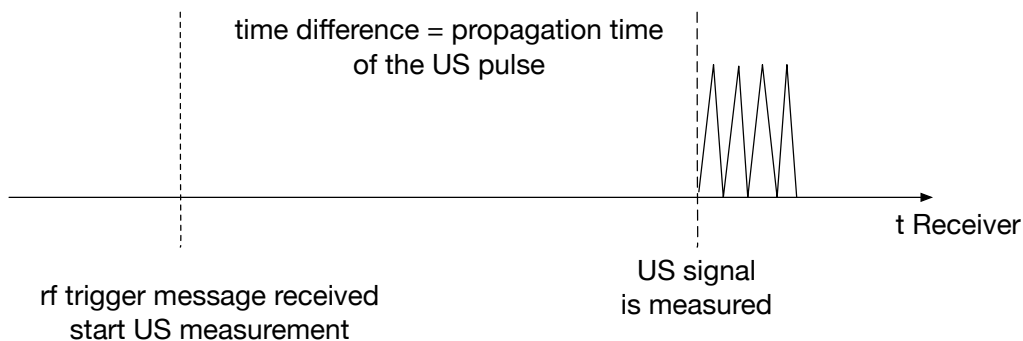


Figure 2.7: The receiver measures the time until the ultrasound pulse is received. To trigger a measurement, an RF packet can be used.

Well known systems in literature are the Cricket System [Pri05] or The Bat [WJH97]. In robotics,

2.2 Indoor Localization Systems and their underlying Physical Phenomenon

ultrasound signals are used in [LR12], [SSHH04] and [RBML08]. Ultra sound has influenced the ubiquitous computing community [HW02], [TNNL02]. Gesture recognition during a bicycle maintenance task has been supported with ultrasound beacons in [SOJ⁺06]. The authors fuse the information of inertial measurement units and the ultrasound beacons to estimate the body postures during the repair task.

Human Audible Sound

In robotics and other areas, researchers have surveilled localization using mapping hearable audio information. Differences in the times of arrival of some transmitter and determining the position of a sound source using hyperbolic localization algorithms (multilateration-based algorithms). The authors of [VMRL03] use this approach to determine the origin of a sound using eight microphones within a sphere with an accuracy of 3 degrees. The authors of [AZ01] combine two camera systems and an array of 3 microphones to estimate the position of a sound source with an average error of 15 cm. Multi-path effects caused by reflections, sound attenuation or sound superposition have to be solved. Also, strict time synchronization between the microphones needs to be established. The microphone-based localization algorithm relies on time difference of arrival. The time difference of arrival estimations lead, as previously described, to a positioning algorithm based on hyperboloids.

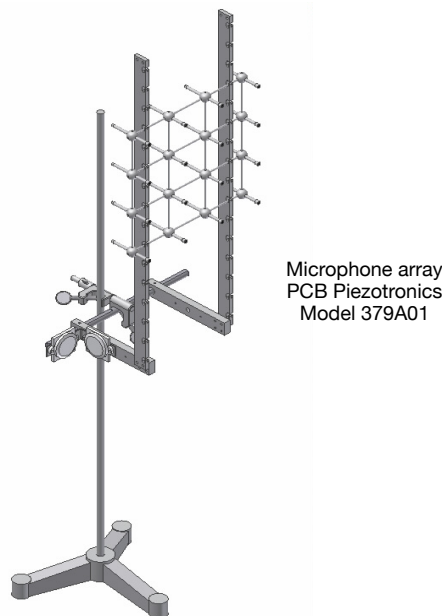


Figure 2.8: Microphone array used to estimate the position of the sound source. The relative position of the microphones have to be known.

Liu et al. describe different physical mobile phone-based localization using audio signals to perform a time-of-arrival-based position estimation. They equip the environment with speakers and encode information about the anchor position in a 15kHz to 20kHz signal. The encoded

2 Available Localization Systems

information is recorded by the mobile phone microphones and distance information against the anchor points is extracted using signal processing algorithms. The authors have to rely on the mobile phone hardware limiting the accuracy of the localization system. The evaluation in an office environment and a classroom shows an accuracy below 10 cm. Still, environmental noise, echoes, the limited signal range and signal attenuation caused by human bodies or elements of the environment have not been used to update the map.

2.2.3 Light-based Systems

Light-based systems rely on the availability of light and its behavior. These systems either try to estimate the positions using active light elements (the elements actively emit light as for example LEDs or light bulbs) or passive systems work with reflected light (markers or directly from the object). Different algorithms for position estimation have been researched and presented; the algorithms cover the search for known geometric formations (which can either be passive illuminated or actively emit light), a search of corresponding points in pictures of two or more cameras or algorithm describing the environment model. An overview of optical localization systems is given in [MT11].

Light propagation and Information encoding

As the availability of controllable LED light systems rises, researchers (for example [LHP⁺14], [KN04]) implemented methods to use visible light to support indoor localization. One or multiple LED light sources modulate information (anchor information) and wearable devices like tablets or mobile phones with ambient light sensors or cameras demodulate this information to locate themselves with an accuracy below 1 meter. The simplest form of localization is proximity ("close to lamp"). Light propagation models allow determining the distance towards the light sources accurately. The authors present algorithms and models to derive angle and distance information towards the light sources and estimate the position using multi-lateration / angulation.

A direct line-of-sight is necessary. Sunlight or artificial light sources strongly influence the localization quality. Also, reflections result in a reduction of localization accuracy.

LIDAR, 3D Laser Scanner

Light Detection and Ranging (LIDAR) is a typical scene analysis-based localization approach. A laser diode is constantly emitting laser pulses, which are reflected by obstacles. The reflected light is used to estimate the phase shift dependent distance. A mapping algorithm estimates the position of the scanner using a pre-recorded/generated model of the environment. It is also possible to apply a SLAM algorithm to the distance and angle estimations to create the environmental map. Deeper insights of LIDAR systems can be found in [MS11], evaluations of systems are described in [Boe]. The authors of [SNH03] describe in their work how to use the LIDAR information for robot positioning. LIDAR systems allow to localize users accurately,

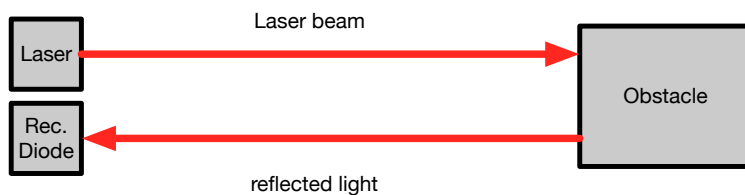


Figure 2.9: Schematic of LIDAR. A laser diode emits a beam, which is reflected by obstacles, the phase shift of the signal (therefore the time difference between emission and reception of the laser pulse) is used to estimate the distance between the LIDAR scanner and the obstacle.

although the systems require direct line-of-sight and an accurate model of the environment. Additionally, the localization algorithms have to evaluate if the sensor measures against obstacles part of the model or whether the system measures against dynamic obstacles which are not part of the model.

Camera-based Localization

Camera-based localization requires either two or more cameras or a single camera and a sensor which additionally provides depth information. In [IKH⁺11] the authors explain a 3D reconstruction algorithm using depth information derived from a Microsoft Kinect. As explained in [Zha12], the depth information stems from an infrared grid projected in the environment. Obstacles and humans cause distortions which are used to calculate the distance to the Kinect sensor. Multi-camera approaches derive the silhouettes of humans from their images and different positions to estimate the motion of persons as described in [CKBH00]. The authors of [ACRC09] developed a combination of mobile phone and webcams which distinguish between several individuals in the picture and to estimate the current 3D coordinates of these persons using the camera pictures.

Using landmark information derived from mobile phone cameras implement a camera-based localization. The authors of [MWBS09] implemented this system and evaluated this in several large scale setups. Ravi et al. compared cell phone images against images of locations to estimate the position of mobile phones in [RSF⁺06]. To determine the position, this requires a larger picture database of known locations. The authors of [HKH⁺10] used Kinect depth information to generate an indoor model of the environment.

Using the known positions of LEDs in the environment for position estimation has been researched in [VB12]. The authors attached different LEDs to the ceiling of the room and recorded the scene with a single camera. Due to the known relative positions of the LEDs, the position of the camera could be estimated.

Infrared

Indoor localization and tracking systems relying on infrared light use either active or passive tags to identify the position while at least two cameras cover an area. In the passive approach, the cameras are also equipped with infrared light emitters. The markers reflect the infrared light. Active tags emit infrared pulses; a synchronization approach allows to map the registered light point in the picture with the position of the tag. In both methods, the tags occur as white spots in the infrared picture of the scene. A combination of two or more camera pictures allows to retrieve the position of the marker. The authors of [KL08] describe the challenges of infrared-based localization systems.

2.2 Indoor Localization Systems and their underlying Physical Phenomenon

Several commercial tracking systems appeared using the passive or active approach. Amongst others there are infrared-based localization systems from AR Tracking² or OptiTrack³. A special motion tracking system for sports environment has been developed by Lukotronic⁴.

Infrared beacons for position estimation as landmarks have been used in [YGA⁺14] and [HTU09].

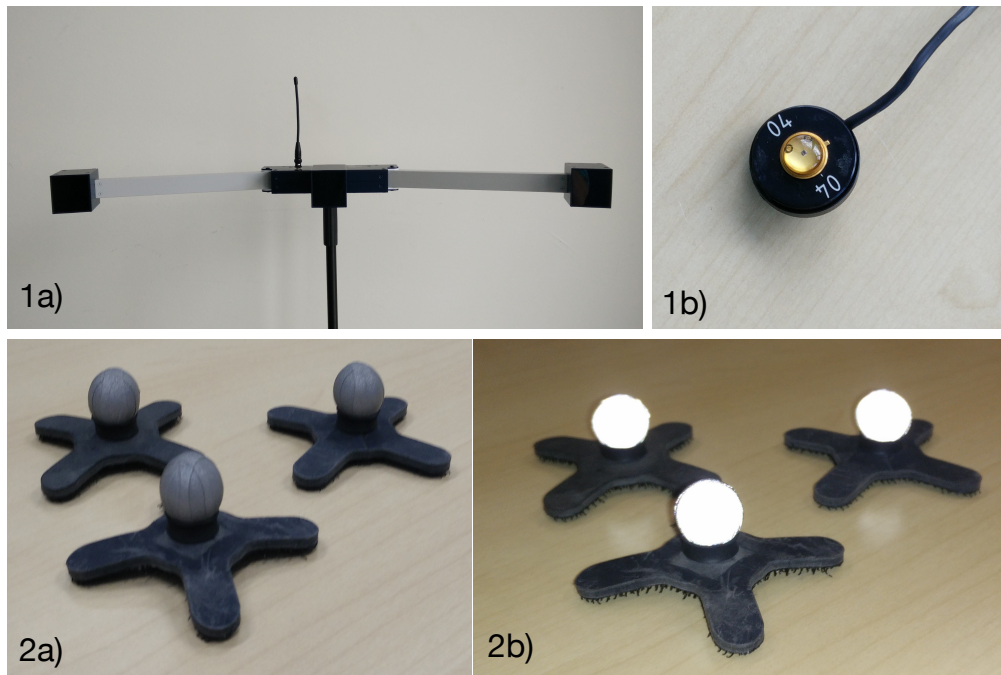


Figure 2.10: The active infrared marker system Lukotronic (1a) is used for on-body tracking. The three cameras record the scene from different angles, the active infrared tags (1b) periodically pulse, the infrared light dots of the tags are used to estimate the position of the tag relatively to the camera system. 2a and 2b show passive infrared tags.

Typical camera-based problems occur in these approaches. Field of application is motion tracking applications. Due to the high accuracy, even facial expressions can be recorded and used for animations. Also, analysis of the movement sequences as in sports applications are performed.

IR-based Room Ids

A proximity-based system providing room level accuracy is described by [WHFaG92]. The authors of the so-called *Active Badge* system equipped workers in an office building with infrared diodes. IR tags periodically transmit a unique id which is encoded in the infrared pulses. Readers in all rooms of the building detect the presence of the tag and Additionally, location

²<http://www.ar-tracking.com>

³<http://www.optitrack.com/>

⁴<http://www.steinbichler.de/produkte/3d-bewegungsanalyse>

of the person in the location database. To reduce shadowing effects, the readers have been attached to the ceiling to reduce t

In robotics, different approaches are used: The authors of [LS07] attached infrared reflective ids at ceilings. The robots record the ceiling with a camera during movement and can then estimate their position whenever a reflective tag is found in the images. The encoded id is then linked to a location. This approach is also commercially available⁵.

A landmark-based approach has been presented in [OKL14], the authors equipped the environment with infrared reflective tags, lighted and filmed by a camera. The tag information is decoded, and the position of the person carrying the camera is retrieved.

Problems

Light-based systems typically have problems with regard to obstacles and changing light conditions. Camera-based systems generate a large data stream which requires strong, complex and efficient algorithms for information processing. Due to this, mobile applications cannot perform the processing because of their low resources. Sunlight negatively influences the performance of the system, as it covers the infrared pulses. They also require direct line-of-sight, and in the case of active tags on the (infrared) emitter side a power source. The synchronization of multiple tags is also a difficult problem: Either a round-robin-based approach has to be applied in which each active emitter is triggered alone, or tracking algorithms have to be applied to link the positions of (passive tags) over multiple frames.

2.2.4 IMU, Pedestrian Dead Reckoning

Localization systems based on inertial methods for pedestrians have been surveyed in [Har13]. These systems use acceleration and bearing information derived from an inertial measurement unit (IMU). This unit is equipped with acceleration, gyroscope, and earth magnetic field sensors, allowing to detect steps and estimate the free acceleration. The IMUs fuse orientation information derived from the acceleration, gyroscope and compass sensors to compensate errors caused by environmental influences like metal objects or lifetime magnetic fields. The fusion algorithm has been described in [MHV11].

To estimate the traveled distance between two measurement points, free acceleration and bearing information derived from the unit is double integrated.

Let $\mathbf{p}_i = (x, y, z)$ be the current position, \mathbf{p}_{i-1} is the previous position estimation. $\mathbf{A} = (a_x, a_y, a_z)$ is the estimated free acceleration (this is the measured acceleration without the superposition of the gravitation vector), dt is the time difference between measurement i and $i - 1$. $d_i = \iint a_i dt$ is the distance in axis i ($i \in x, y, z$) since the last measurement

$$\mathbf{p}_i = \mathbf{p}_{i-1} + (d_x, d_y, d_z) \tag{2.2}$$

⁵Hagisonic StarGazer Robot Localization System

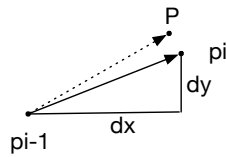


Figure 2.11: The current position p_i is derived from the previous position and the position difference calculated using the acceleration measurement. Measurement errors result in inaccurate estimations (P is the exact position, p_i the error prone position.)

A drawback of this approach is that the free acceleration estimation is error prone and therefore introduces big position errors with increasing time. Two error sources are immanent: the separation of gravitation vector and linear acceleration and the estimated bearing information relying on these inaccurate measurements. Therefore it is necessary to stabilize and improve the position:

Using additional information sources derived from proximity or lateration-based systems results in sensor fusion algorithms and therefore increased positioning accuracies. Depending on the aimed accuracy, proximity, landmark-based or multilateration-based techniques are fused. The authors of [MVFB10] state that these algorithms achieve accuracies below $1.5m$. These fusion algorithms also included RF-based propagation models as presented in [Sey05], additional work can be found in [GO02], [CCG], [MJF⁺08], [AV04], and [TSFC].

2.2.5 Smart Environments

Instead of equipping the humans with wearable devices, it is possible to integrate the sensors in the environment. This can either be active (localization systems requiring the user to wear tracking devices) or passive systems. Passive systems can either be camera-based systems surveilling the environment, infrared thermal sensors (as we presented in [PHW⁺14]) or smart floors ([SL07], [VMV09] or [SL08]) providing binary or weight information whenever a person steps on the floor. Also, the sound of the steps can be used for identification and localization as presented in [DCR10]. By integrating RFID tags in the floor, the position estimation of robots in smart environments can be achieved as shown in [SYS12]. Integrated RFID readers constantly search for RFID tags and retrieve the corresponding tag location from a database.

An overview of smart environments and its localization possibilities is given for example in [MLH05], [KVPV14] or in [DCFPF11].

2.3 Environmental influences of underlying measurement principle of indoor localization systems

As already mentioned, indoor environments strongly influence signals which makes it hard to model the signal behavior of the systems. Due to edges and corners, the diversity of materials, electronic appliances and humans themselves, the underlying physical technics are influenced, and the quality of localization suffers. Additionally, the environment itself is altered, persons interact with the environment, furniture is added, moved or removed. All these factors make a model-based approach which tries to reduce the effects mentioned above, very time-consuming or even impossible. Complex algorithms try to reduce the influences on the signal or remove outliers caused by environments by statistical/probabilistic weights([TFBD01] in robotics). In the following sections, we describe the problems which occur when different physical phenomena are used for indoor localization.

2.3.1 RF-based Approaches

RF-based approaches have several problems in indoor environments: The RF waves typically do not have a line-of-sight propagation path between the transmitter and the receiver. Instead, the waves interact with building elements, walls, corners, and furniture. Three main effects occur and lead to problems in RF-based position estimation: reflection, diffraction and scattering([Rap01]).

According to [Rap01, p.113] *reflection occurs when a propagating electromagnetic wave impinges upon an object which has vast dimensions when compared to the wavelength of the propagating wave. [...] Diffraction occurs when the radio path between the transmitter and receiver is obstructed by a surface that has sharp irregularities(edges). The secondary waves resulting from the obstructing surface are present throughout the space and even behind the obstacle, giving rise to a bending of waves around the obstacle even when a the line-of-sight path does not exist between transmitter and receiver. [...] Scattering occurs when the medium through which the wave travels consists of objects with dimensions that are small compared to the wavelength, and where the number of obstacles per unit volume is large.*

In addition to these three problems, a so-called **multi path effect** is noticeable at the receiver side: Multi-path effects arise when multiple versions of the same wave (reflected and diffracted for example from a wall) arrive at different times at the receiver antenna. This effect causes fluctuations in the signal strength (amplitude) and the phase. The behavior of the RF wave is influenced by **longer period environmental effects** as presented above but also include effects caused by dynamic elements as persons wandering in the transmission area, changes of the environment, other electro magnetic sources which are superposing the initial RF wave.

Figure 2.12 depicts the result of an RF simulation of the RF signal propagation in an indoor environment. RF signals are attenuated by the different building materials, refraction and reflections cause multipath effects and signal receptions at points which do not have direct line-of-sight to the access points.

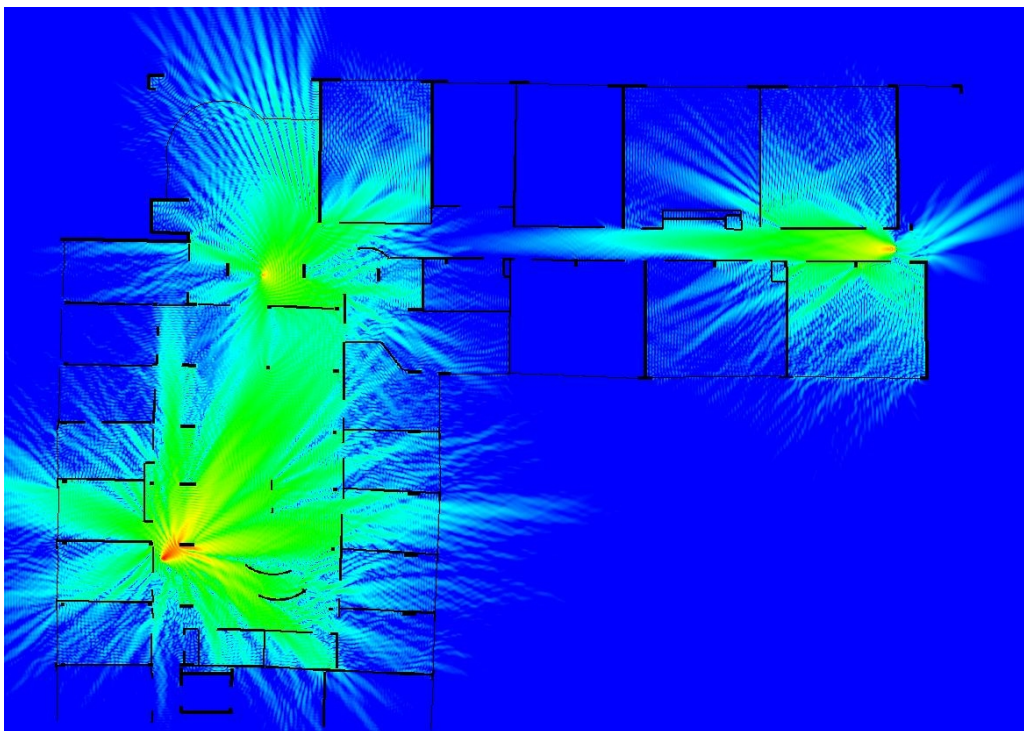


Figure 2.12: Signal strength of WIFI transmissions from three access points in an office environment. Signal refraction, multipath effects, and reflections lead to problems in the localization process. Permission granted from [LUV⁺11]

Several RF-based position estimation algorithms try to use the signal attenuation to calculate the rough distance between the transmitter and the receiver. The simplest way to describe the attenuation is an RSSI distance estimation. Taken from [MVFB10]:

$$P_r = P_t \left(\frac{\lambda}{4\pi d} \right)^n G_t G_r \quad (2.3)$$

P_t is the transmitter power, P_r is the measured signal strength on the receiver side, λ the wavelength, G_t and G_r gains of the transmitter and receiver antennas, d is the distance between transmitter and receiver and n is the path loss coefficient.

To model the *longer period effects*, the impact of materials on the signal attenuation has been surveilled in [SRF⁺92]. The authors present tables of attenuation factors (n). Notice that various materials can be found in indoor environments and therefore the signal propagation and attenuation is hard to model. More complex propagation models have been evaluated and described in the literature but are not part of this work.

Solutions for the complex description of indoor environments are based on statistics ([SRJJ97] and [Has93]). The authors of the RADAR WIFI fingerprinting([BP00]) approach do not model the RF signal behavior by hand but record the signal propagation at multiple points. Dynamic effects arising from humans are neglected.

As modern buildings are typically built in such a way that there are metal or concrete parts

which are hardly altered during the Additionally, of a building and drywall components which allow flexible, cheap and fast changes in the floor plan, RF propagation models have to be maintained from time to time.

2.3.2 Optical Approaches

Image or video-based approaches rely on video equipment installed in the area of interest. The algorithms either require continuous recordings or use movement information (infrared sensor or vision-based) to trigger processing to detect persons and their movement path. In addition to privacy concerns, the camera-based approaches require a high installation effort, high data rates, and energy consumption for recording and light require cable bound links. As the cameras produce a huge information stream, processing of the gathered information requires massive computing power. Since the image-based systems require line-of-sight, persons or objects in the field of view can obscure activities or movements of other individuals. Another issue is the problem of changing light conditions resulting in more complex algorithms or hardware equipment as infrared filters and infrared spotlights to brighten the field of view. Also, the identification of multiple users in passive localization systems are problematic, therefore tracking algorithms need to be researched which can track persons who cross each others path.

2.3.3 Sound-based Approaches

As previously described, sound-based approaches rely on the time differences between several microphones. The time difference between multiple microphones is then calculated in distance differences using the propagation speed c_{sonic} of (ultra) sonic waves in the air with air temperature θ :

$$c_{sonic} = (331.6 + 0.6 * \frac{\theta}{\text{°C}}) \frac{m}{s} \quad (2.4)$$

Sound-based systems rely in contrast to RF-based systems, on the environmental temperature. A more complex measuring setup including a thermometer needs to be applied. Additionally, ultrasound waves suffer from similar influences as RF signals like signal reflections, shattering or shadowing. Sound attenuation caused by fabrics has to be taken into account. Also, echoes of the signal are typically present.

A superposition of environmental noises, especially in the measurement sound frequency spectrum, is more easily to achieve, for example by home appliances or even keys.

2.3.4 IMU-based Systems

As PDR-based approaches rely on the combination of multiple sensor modalities as acceleration, compass and RF localization, the set of problems is bigger:

Earth Magnetic Field-based Heading

The estimation of the person's heading depends on the earth magnetic field sensor/compass sensor. As human-built objects typically consist of steel or concrete, the earth magnetic field is highly non-conform in buildings (in contrast to outdoor magnetic field measurements). Electromagnetic fields also negatively influence the heading estimation based on magnetic field readings. To remove these influences, IMU producers provide sensor fusion algorithms using acceleration and gyroscope information to filter the heading information.

Magnetic Field Fingerprints

As in other fingerprinting-based approaches, earth magnetic field-based fingerprinting relies on the local changes of the field. These magnetic field anomalies in buildings are used for self-localization as in [HK09]. They use a particle filter to support the localization. Authors of [CDS⁺11] state that they achieve an accuracy of 45 cm if outliers of the measurements are removed. [WSE⁺12] provide a self-learning algorithm which automatically records the Wifi and earth magnetic field information in the environment. Changes in the environment such as placements of metal objects or interaction of humans with the environments (opening/closing fridge doors) result in (local) changes of the maps which therefore need maintenance operations to reset the map.

Acceleration-based Inertial Tracking

Acceleration information is often used for step detection, where simple approaches assume a fixed step length. Other approaches estimate the step length by double integration of the acceleration information. As all measurements are a sum of error readings (due to the complex separation of gravitation and linear acceleration based on the fusion algorithms) and physical sensor readings, the double integration of the measurements lead to errors in the step length. Without continuous correction of the position, commutative errors in step and position estimation arise. Depending on the walked distance the accuracy can be below 2 m (see e.g. [PWH12]) for longer paths. The separation of linear acceleration and gravitation strongly depends on the used filter algorithm.

2.4 Conclusion

In this chapter, we presented a variety of different localization approaches. The algorithms cover proximity, triangulation and scene analysis. The systems often rely on radio frequency pulses, sound, optical or inertial measurement units.

Problems in indoor environments arise due to the complexity and inhomogeneity of the different materials which are found in apartments, office or industrial environments. Static influences, causing signal diffraction or attenuation, are modeled or compensated using fingerprinting approaches or signal attenuation lookup tables. Dynamic situations often require a combination of several sensor systems. If the dynamic effects are neglected, this results in higher positioning errors. Also, electromagnetic sources, either unintentionally or used on purpose, lead to different signal behavior. Direct line-of-sight is always a preferable option to improve the signal quality and therefore the position estimation accuracy, but this unobstructed signal path is not always achievable. A large number of approaches and techniques have been proposed in literature trying to reduce these influences on the signals. On the side of the underlying physical phenomenon, systems based on waves such as RF or ultrasound has been researched. Sensor fusion algorithms try to limit the influence of dynamic and static effects in the indoor environment by statistically judging the signal input information. Although the accuracy of most systems lies within room level or below, the installation effort including setup and calibration varies. Most of the problems mentioned in this chapter arise as the used physical phenomenon is not able to permeate obstacles found in the environment which results in **unpredictable or inaccurate signal behavior**.

To overcome problems caused by shielding or attenuation, a physical phenomenon should be used which is hardly influenced by humans and the materials being found in indoor environments. We, therefore, present a localization system based on magnetic fields which solve most of the issues mentioned above. Magnetic fields permeate nonferromagnetic objects and are hardly influenced by persons. The field emitters can be used in a non-intrusive way, do not need line-of-sight and can therefore even be stored in cupboards.

3 System Overview

Our indoor localization system is based on magneto-inductance: stationary magnetic field emitters sequentially generate oscillating magnetic fields, and wearable receivers measure the corresponding induced voltage at their current position. In the following sections, we describe the system architecture and its components. As there are also other researchers and companies work on magnetic field-based localization systems, a clear differentiation from these systems is given.

3.1 Advantages of Magnetic Fields over other Physical Modalities

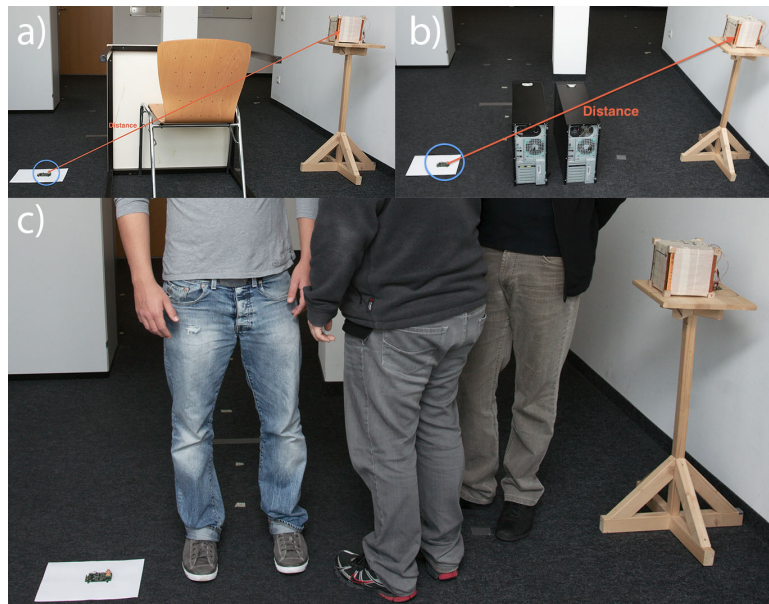


Figure 3.1: Evaluation of different materials' influence on the magnetic field.

The quantity of different available indoor localization methods presented in the related work chapter in addition to the problems illustrated in the previous chapter shows that an indoor environment is very challenging for localization systems. Signal attenuation, shadowing, scattering and diffraction lead to differences between the measured signal and the theoretical model and therefore to positioning errors. Reasons for this are the variety of different materials and shapes, humans who enter and leave the environment or interact with furniture and other indoor

3 System Overview

elements. This interaction with the environment results in measurable changes, for example in the RF signal strength (RSSI value) of mobile phones. Researchers used this principle to perform activity recognition (Sigg et al. in [SBT14]). Another issue of the affected signal is that the range of the systems is restricted as the materials reduce the propagation range.

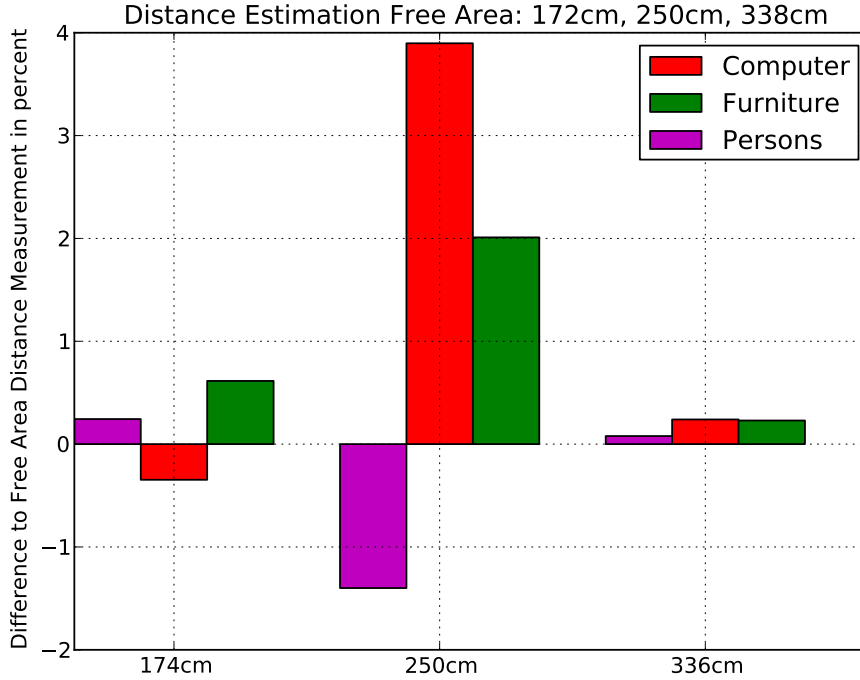


Figure 3.2: Estimated influence of different objects and persons on the estimated distance.

We argue that magnetic fields allow overcoming most of these negative influences on position estimation. Initial experiments with magnetic fields showed that the presence of human bodies in the magnetic field between a transmitter and a receiver coil hardly change the measured signals. To prove this, we place persons, furniture, and computers with metal cases between the magnetic field transmitter coil and a receiver coil. The effects on the estimated distance between the transmitter and the emitter vary in the magnitude of several percents (1 to 4 percent) depending on the distance and the relative position of the obstacle in the magnetic field.

A significant advantage of magnetic fields is that they permeate walls, which allows to reduce the number of necessary anchor points as multiple rooms can be covered by a single transmitter coil. Compared to ultrasound emitters or camera-based systems which require direct line-of-sight, this reduces the installation effort.

Thus, we investigate and present the magnetic field-based localization system and evaluate different applications.

3.2 Magnetic Field-based Localization System

Our localization system based on oscillating magnetic fields consists of two main components: magnetic field emitters, and wearable magnetic field sensing units.

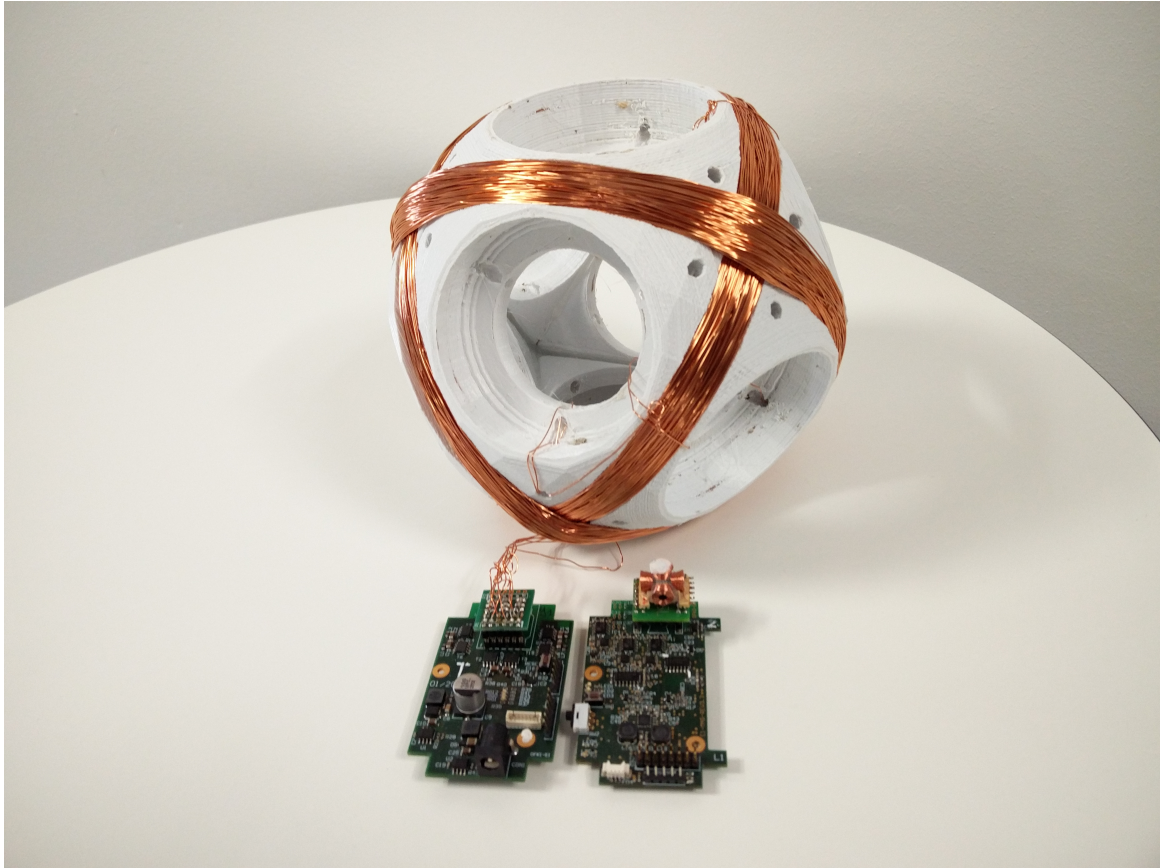
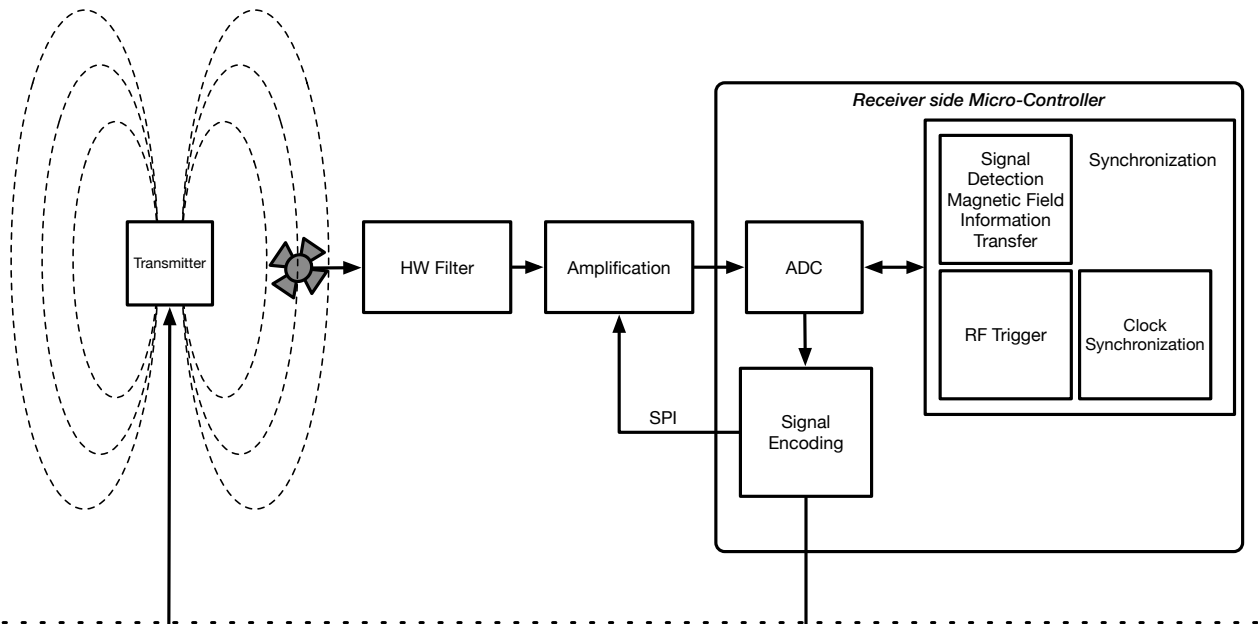


Figure 3.3: Transmitter coil with attached driver circuit and wearable receiver with 3d receiver coil.

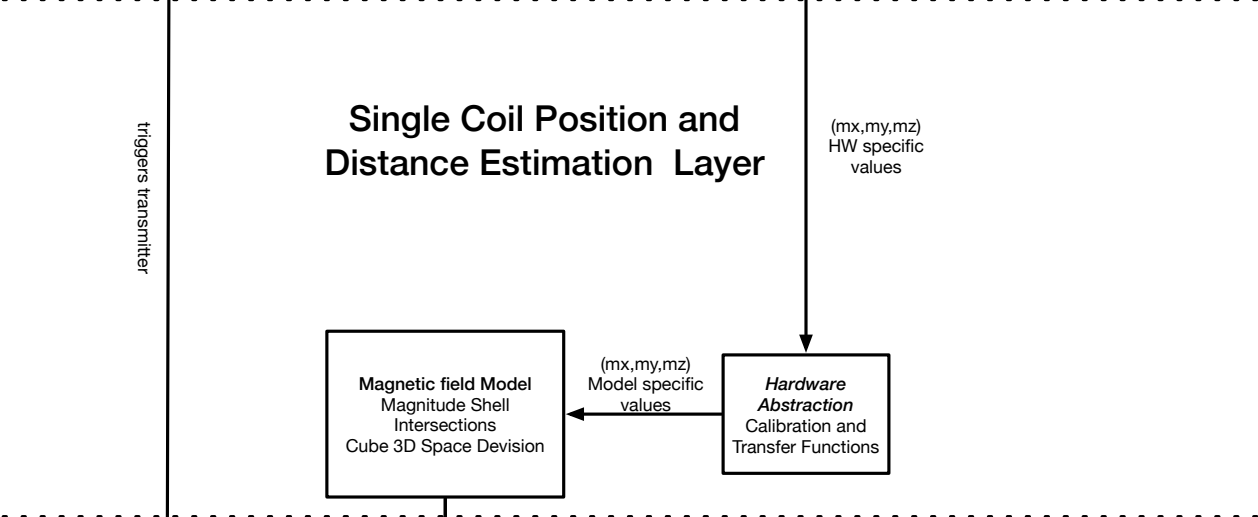
For position estimation, several processing layers (overview presented in figure 3.4) have to be addressed to retrieve this information from the magnetic field. We, therefore, define and introduce the processing architecture. This architecture consists of three layers:

- a **physical layer**, responsible for synchronization and raw signal gathering which also takes the physical behavior of magnetic fields into account,
- a **single coil position and distance estimation layer**, which covers the transformation of the measured signal to a position and distance estimation relative to the corresponding transmitter and which abstracts from hardware related parameters, and
- a layer which performs **multi coil position estimation** using the position and distance information from several transmitters.

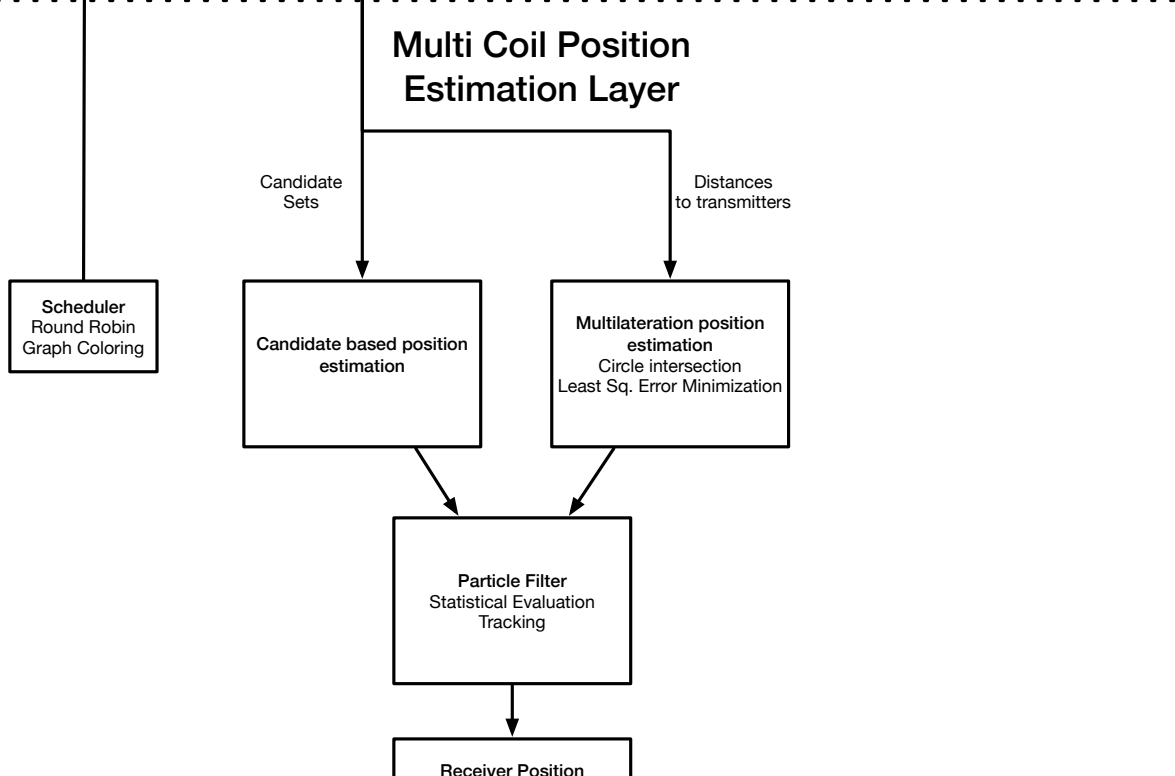
Physical Layer



Single Coil Position and Distance Estimation Layer



Multi Coil Position Estimation Layer

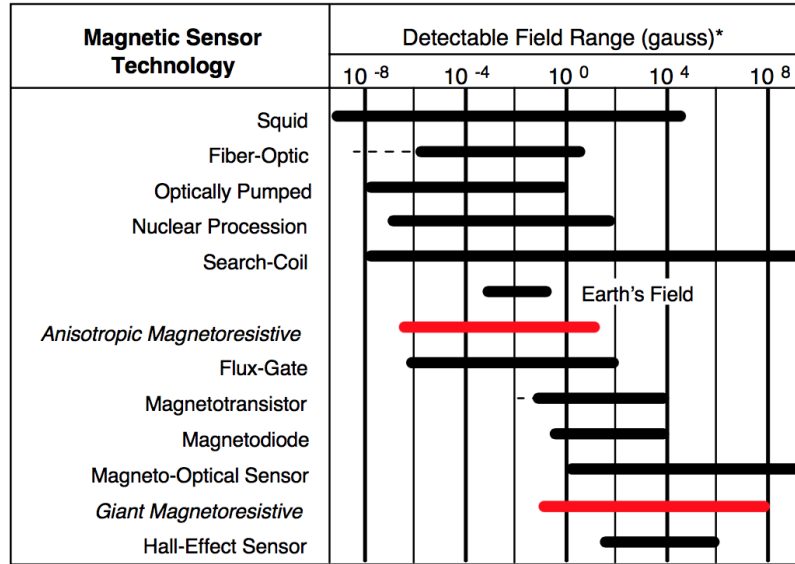


Physical Layer The physical layer manages the low-level functionalities of our localization system. The layer includes the control of the magnetic field generation on the transmitter side (frequency and correct time slot), whereas the receiver side performs signal detection, signal amplification, signal encoding and transfer to a central processing computer. Transmitters and receivers both have to be time synchronized to link the measurements to the correct Emitter coil axes.

Single Coil Positioning Layer On top of the physical layer, situated on a central processing computer, the single coil positioning layer performs a hardware abstraction step which shifts the different hardware related signal levels of the measurements to a standard level. The adjusted values are compared against theoretical magnetic field magnitude values to estimate position and distance. The model takes the three axes transmitter coil architecture into account which enables the system to calculate the position of a single receiver to a single point in each of the eight octants around a transmitter.

Multi Coil Position Layer The magnetic fields of a single transmitter do not provide sufficient information for unambiguous position estimations. To estimate the position of the receiver without ambiguity, measurements to several transmitters have to be performed and combined. This layer, therefore, consists of a scheduling algorithm which determines the trigger sequence of the emitter and a fusion algorithm which merges distance and position information to measured anchor points.

3.3 Available Magnetic Field-based Localization Systems



* Note: 1gauss = 10⁻⁴Tesla = 10⁵gamma

Figure 3.5: Overview of the different magnetic field sensing possibilities.

Taken from [CBSS98]. Our localisation system is a search coil-based approach.

Applications of magnetic fields are wide-spread, starting from measuring the power consumption of a device, over contact-less switches to accurate distance estimation. More demanding magnetic field applications can be found in aerospace, other parts of the industry, home entertainment and hospital environments mainly focusing on position or location estimation. A possible categorization of magnetic field based localization is either the usage of quasi-static or alternating/oscillating magnetic fields. It is also possible to distinguish between these systems whether they rely on the natural earth magnetic field and its fluctuations caused by environmental anomalies or on the usage of artificial magnetic fields. Another possibility covers the magnetic field detection mechanisms, the document [CBSS98] gives an overview of possible magnetic field sensing systems, their frequency bandwidth and the detectable magnetic field strengths. Figure 3.5 depicts the possible physical sensing modalities.

Our system is a search coil / magneto inductance based localization system using artificial alternating / oscillating magnetic fields for position estimation.

We now present different magnetic field based tracking systems. We also provide information about overlapping parts in the used techniques and algorithms but also go into the differences. The field of application covers medical areas, motion tracking environments and industrial and home entertainment applications which are presented in the next paragraphs. To reduce the size of the search coil, medical systems typically use single axis coils only, home entertainment,

3.3 Available Magnetic Field-based Localization Systems

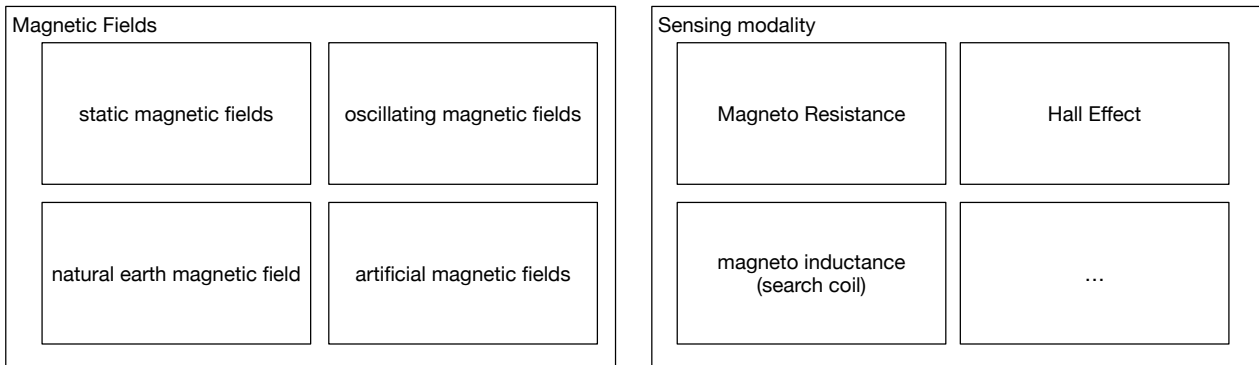


Figure 3.6: The magnetic field-based systems can be categorized by the type of magnetic fields the systems use to estimate the position of the receiver. The sensing modality is also a possible way to categorize the systems.

industrial and military applications require three axes receiver coils.

3.3.1 Medical Systems

Medical tracking systems often rely on magnetic fields due to their property to permeate the human body and therefore not requiring direct line-of-sight. Compared to optical marker systems, the search coils can be built smaller than the markers, reducing the weight and dimensions of the tracking device. Due to this, these medical systems support both, in-vitro and ex-vitro tracking applications. In contrast to our system, these systems are typically developed to work in specialized applications with highly accurate position estimations. All systems presented in this section are cable bound, a central signal acquisition and processing board is available for position estimation.

Several devices have been established in the medical market:

Polhemus Fastrack, Patriot This system uses low-frequency alternating magnetic fields to track up to 16 receiver coils. The range of the system is up to 3 meters. Only a single coil setup is possible; sub-mm accuracy is achievable. The system informs the user if there are interferences in the field. The main field of application is EEG Localization and neuroscience. The price of the device is above 2500 Euro. No information about the proprietary system concerning the synchronization is presented by the producer.

NDI Aurora System NDI Aurora is based on alternating magnetic fields, the tracking device achieves sub-mm accuracies and sub-degree orientation resolution. Up to 16 receiver devices can be tracked. The transmitter coils are either placed below the human body to track medical tools or placed next to the body to guide other sensors. Receiver coils can be located within the human body. The range is 50cm with a maximum update rate of 40 Hz. This system is mainly used in medical areas to support operations.

3 System Overview

Ascension Trak Star Ascension Trak Star is based on quasi-static magnetic fields emitted by one or more transmitter cubes. Depending on the necessary range, the cubes have a volume of 5cm^3 or 10cm^3 depending on the aimed measurement range. The accuracy lies below 1 mm. The orientation can be estimated with an accuracy below 1 degree. The sampling rate is 420 Hz for four receiver coils which are directly connected to the processing unit. The receiver probes are cable-bound.



Figure 3.7: Ascension Trakstar System with transmitter and receiver. The search coil is directly connected to the processing unit.

3.3.2 Motion Tracking

Motion tracking has become very popular in many situations in life: Scientists use magnetic field based systems as reference systems, airplane cockpits are equipped with magnetic field emitters to track the head position and bearing to adjust the virtual reality environment([G.11, p.56pp], [RBSJ79b]). Also entertainment products rely on motion tracking systems:

Ascension Flock of Birds Although being found in medical applications, Ascension provides a magnetic field based localization system suitable for motion tracking. The system has similar coverage, is cheaper than the medical system but is less accurate. The system is a single coil system [GLN09]. In contrast to our system, "Flock of Birds" is not suitable to cover larger areas and does not support multiple transmitters.

Sixsens Stem, motion tracking in entertainment Sixsens Stem is used as game input device (for example to control arm movements of virtual characters or monitor the skeleton of the character). The technique is comparable to our system. It uses alternating current to generate an artificial magnetic field. According to their website, the Stem system covers a living room. The accuracy is within several millimeters. To estimate the orientation of the input device a three axes receiver coil is used. The system has neither been developed to be used in different environments as industrial tracking approaches nor can it cover larger areas or supports multiple transmitters.

The sampling rate of the Stem system is around 20 Hz. The frequency of the generated oscillating magnetic field and its synchronization method is unknown.

3.3.3 Industrial Indoor Localization Systems and Tracking in Science

Particularly in demanding environments requiring stable and drift-less position and heading information, magnetic fields are often used for information extraction:

Helmet Tracking in airplanes In military and industrial applications it is necessary to provide information about the direction in which the person is looking. Particularly for head-up displays, head position and viewing direction are two important sources. Among other technologies like vision or IMU-based approaches, magnetic field systems are used to estimate this information. According to [G.11] these systems typically use oscillating magnetic fields at a frequency of around 10kHz, the mathematical background has already been described in 1979 by [RBSJ79a]. This system uses a single transmitter coil with three transmitter axes to estimate position and orientation.

Large scale industrial tracking of objects and vehicles in production lines Prigge ([PH04]) describes in his thesis a large scale tracking setup which can be used in industrial environments. In contrast to our system he uses a CDMA-based scheduling approach and describes in his work how to separate different magnetic field emitters and their magnetic fields in the measurements. Although relying on the artificial magnetic field, he uses extreme low-frequency magnetic fields to estimate the position of receivers. The coils are bigger than ours (diameter of 1 m), and 100W power is applied to the coils. Accuracy is within several cms.

Temperature distribution in fluid containers Temperature control is another application of magnetic field based localization: To achieve an even temperature distribution in the major fluid containers the location of floating sensor nodes with temperature sensors have to be estimated. To retrieve the position of the sensor nodes, Koenig et al. implemented a magnetic field based localization system [GTKKxn14]. Comparable to Prigge, they use quasi-static magnetic fields applied to circular coils to estimate the position. They also implement a calibration algorithm in [GTKKxn14] in which they compensate distance errors which arise due to model errors and environmental effects. They achieve an accuracy of several cms. The authors also rely on the so-called anisotropic magneto-resistive effect; the sensor material changes its resistance when magnetic fields are applied to the material. The change in resistance is measurable.

Tracking and Localization in science based on magnetic fields. In the biological research area, Markham et al. implemented in [MTEM10] a magnetic field based localization system. They track the life of underground animals. In addition to technical details they describe and evaluate the performance of their system when it is used to monitor animals living on the ground. The magnetic field, therefore, has to permeate the soil. In a test setup the coils were

3 System Overview

20cm times 30cm, the range was 4m, the position estimation achieves an accuracy of 40cm at the given resonant frequency of 130kHz. The transmitters are scheduled in a round-robin approach. In contrast to our system, the authors do not have to deal with dynamic influences of indoor environments and therefore can increase the resonance frequency of their coils. This also explains the higher accuracy.

Localization based on earth magnetic field measurements

Several researchers have developed and researched methods for indoor localization relying on the natural earth magnetic field and disturbances caused by indoor environments (see for example [GSDM11], [CDS⁺11] or Indoor Atlas¹). The systems use mobile phone sensors and the integrated electronic compasses to measure the field density of the earth magnetic field. As in WIFI based fingerprinting methods, the approaches need an excessive calibration step. In contrast to our system these methods do not generate static or oscillating *artificial* magnetic fields. According to indooratlas, the accuracy the system can achieve is below 2m² without any additional anchor points.

3.4 Conclusion

We discuss in the following sections the different layers of our magnetic field-based indoor localization system. The chapters cover signal related processing algorithms for signal gathering, synchronization of a single transmitter and receivers, hardware abstraction and single coil position and distance estimation and on top of this multi-transmitter position estimate including scheduling and distance / position fusion for localization and tracking. The system is evaluated in different environments and against an RF-based localization system to gather information about its repeatability and robustness in specific locations. Also, regions of interest and fusion with other sensor systems are discussed.

¹www.indooratlas.com

²https://www.indooratlas.com/static/magnetic_positioning_opus_jun2014.pdf, page 5, figure 3, last visited 6.3.2016

4 Physical Layer

The physical dependencies of oscillating magnetic fields and their influence on coils in the areas are well understood. The implementation of a localization system based on these effects still requires algorithms specifically designed for the generation and acquisition of magnetic fields and their physical nature. The combination of hardware implemented oscillating circuits reduces the effects of EM crosstalk on the receiver side and magnifies the power output of the transmitter coils when excitement voltages with the given resonant frequency are applied. These driver signals have to be carefully controlled about their rates as offsets lower the power output and thus reduce the maximum achievable range. On the receiver side, the sampling rates have to be adjusted correspondingly to achieve an accurate digital signal replicate. The magnetic field induced voltage comes with a **high dynamic range**: Close to the transmitter coil, the induced voltage is up to 3V, at the far end of the covered distance, the induced voltage only adds up to 2 to 3 mV.

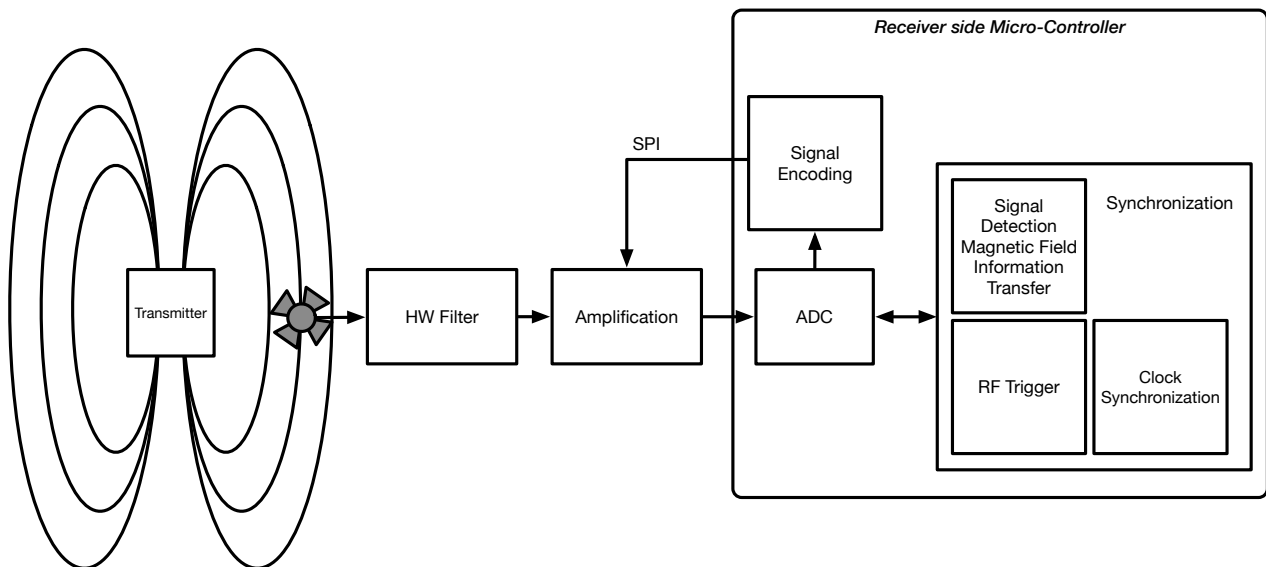


Figure 4.1: Schematic overview of the modules and tasks involved in low level signal gathering.

This effect results in a low signal-to-noise ratio at high distances which is additionally reduced by the inhomogeneity of the magnetic field: Depending on the position around the coil at a fixed distance, different voltage levels are induced depending on the angle. Therefore, especially in high distances, the receiver side signal detection mechanism has to be chosen carefully to maximize the covered area.

4 Physical Layer

The transmitter coil consists of three perpendicular coils which are sequentially excited. This approach provides magnetic field information which is then processed in the upper localization layers. This multi-axis approach introduces another topic: the **synchronization of transmitter and receiver**, as the receiver has to link the measurement to the correct emitter axis for further processing.

The physical layer addresses the **low level functions of the localization system**. It has to control the **magnetic field generation** on the transmitter side, the square shaped excitement signal on the coils and its frequency, and manages the **signal amplification, signal digitalization and representation of the induced voltage** on the receiver side. For both system components a strict **time synchronization** has to be established to correctly link the magnetic field measurements on the receiver side to the corresponding transmitter axes. The layer is the foundation for the position estimation. Estimation- and encoding errors and also noise caused by hardware or asynchronous sampling result in signal behavior which does not match the predicted magnetic field behavior at the receiver position. These errors strongly influence the position estimation accuracy.

4.1 Contribution

This chapter describes and evaluates methods which are integrated into the physical layer to provide a **stable representation of the induced voltage**. On the transmitter side, methods for a steady **oscillating magnetic field generation** with a given frequency are implemented and evaluated. In addition to RF-based synchronization between the transmitter and the receiver, the transmitter also implements a **uni-directional information transfer in the magnetic field** to provide a **robust synchronization mechanism** without RF data transfer.

The **signal gathering** considers the underlying physical laws of magnetic field generation and induction. Due to the high dynamic range and the cheap sampling hardware, the signal acquisition consists of a **software controlled amplification** step and a **DMA supported signal digitalization**. The receiver side oversamples the induced voltage trajectory and compares two successive sampling windows. Due to the repeating nature of the oscillating magnetic field, the signals result in a high correlation value even at a distance of 4.5m and a corresponding induced voltage level of below 4mV. **Different synchronization methods**, RF trigger messages, and magnetic field-based information transfer in combination with magnetic field detection have been implemented and evaluated in different scenarios about accuracy, power consumption, and position estimation rates. All these elements have been adapted and applied to work on microcontrollers with limited resources including the usage of digital signal processing supported commands.

4.2 Physical Background

In this section, we discuss the physical background upon which our localization system is built. This includes the magnetic field generation, the magnetic field behavior and the field density which is described by the law of Biot Savart. On the receiver side, the measured signal depends on the magnetic flux density. The law of Faraday relates the induced voltage depending on the receiver coil area and the magnetic field.

The magnetic flux density / magnetic field $\mathbf{B}(\mathbf{x}')$ is a vector with given length at position \mathbf{x}' , the magnetic field strength $\mathbf{H}(\mathbf{x}') = \frac{\mathbf{B}(\mathbf{x}')}{\mu}$ defines the direction and the length / strength of the magnetic field at the position. μ is the so called magnetic permeability.

4.2.1 Law of Biot Savart

The Law of Biot-Savart ([Hen04, p. 45, formular 2.21]) describes the magnetic field (or often also magnetic flux density) $\mathbf{b}(\mathbf{x}')$ at 3D position \mathbf{x}' which is generated by an infinitesimal small wire $d\mathbf{l}$ through which a current I flows:

$$\mathbf{b}^{d\mathbf{l}}(\mathbf{x}') = \frac{\mu_0}{4\pi} I d\mathbf{l} \times \frac{\mathbf{x} - \mathbf{x}'}{|\mathbf{x} - \mathbf{x}'|^3} \quad (4.1)$$

The used transmitter setup is a combination of frame-shaped coils. As depicted in figure 4.2 the current runs in the directions of the arrows around the wires of the frame.

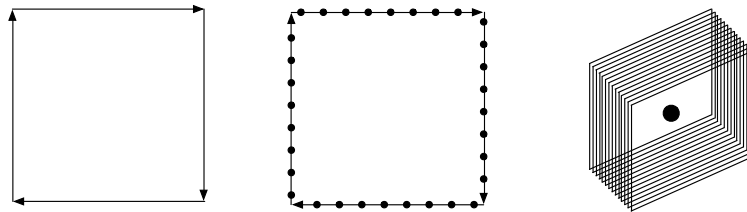


Figure 4.2: Left: Direction of the current along the frame, center: wire segment points used to approximate the magnetic field, right: model of a transmitter coil axis centered around the origin of the coordinate system.

To estimate the magnetic flux density $\mathbf{B}_i(\mathbf{x}')$ we apply a finite element method: The coil is represented by f frame coils (Fig. 4.2 right side, the coil axis itself is centered around the origin of the coordinate system), each frame consists of p infinitesimal small wire pieces (*points*) equally distributed on the frame coils (Fig 4.2 center). To reduce the processing complexity, the term $m = \frac{\mu_0}{4\pi} I$ is set to 1, in the calibration process, the term is then calculated. The direction of the wire segment is carefully evaluated as it strongly influences the direction of the resulting magnetic field vector.

4 Physical Layer

Let $\mathcal{L} = \{d\mathbf{l}_j \mid j \in 1, \dots, f * p\}$ be the set of the infinitesimal small wire pieces approximating the coil, the field strength $\mathbf{B}_i(\mathbf{x}')$ at the position \mathbf{x}' is then:

$$\mathbf{B}_i(\mathbf{x}') = \sum_{d\mathbf{l}_j \in \mathcal{L}} \mathbf{b}^{d\mathbf{l}_j}(\mathbf{x}') \quad (4.2)$$

Hereafter, the theoretical magnetic flux density has been calculated with the following values: As the transmitter coils consist of 300 windings, 300 frames are used ($f = 300$). Each side of the wire frame is approximated by 300 points, resulting in $p = 1200$ points per frame. We calculate the magnetic field around the coil in 5 cm steps between -450cm and 450cm , all positions closer than 30 cm are discarded. These values reflect the maximum covered distance of the system and the accuracy.

The field strength values of axis y and axis z orientation and, as the two axes are perpendicular to the x-axis, the coordinates are rotated around the corresponding axes, and the resulting field strength values are then used.

The data set contains 5929741 ($181 \times 181 \times 181$) $(\mathbf{B}_x(\mathbf{x}'), \mathbf{B}_y(\mathbf{x}'), \mathbf{B}_z(\mathbf{x}'))$ tuples, which are later used for the position estimation model.

Notice that there are effects that have not been modeled: self inductance of the perpendicular coils (this effect reduces the magnetic field strength at the positions) and cross talks between the perpendicular coils.

We do not consider the oscillation of the magnetic field which follows

$$B_{osc}(\mathbf{x}') \sim \sin(\omega t)$$

(Law of Faraday, see section 4.2.2), as mentioned, the crosstalk between the axes and the self induction of the coils have not been modeled.

Since we also implemented a sphere shaped transmitter coil with three transmitter axes, we performed similar steps to generate a theoretical magnetic field model for the sphere as well.

4.2.2 Law of Faraday

In the previous section, we calculated the magnetic field vectors $\mathbf{B}_i(\mathbf{x}')$ of the three transmitter axes in a 5 cm grid around the magnetic field emitter. The receiver measures the magnetic flux density using the induced voltage in 3 perpendicular receiver coils. The oscillating magnetic field, following a sinusoidal current, induces on the receiver side a voltage. This voltage can be described by the law of Faraday (see [KMR08, p. 391, Formula 27.27]:

$$U_{ind} = -N * \frac{d\Phi}{dt} \quad (4.3)$$

where N is the number of turns of the receiver coil, and $\Phi = \mathbf{B}(x') * A$, where $\mathbf{B}(x')$ is the magnetic flux density at position \mathbf{x}' and A is the area of the coil which is perpendicular to the magnetic field vectors at the position of the receiver coil. Φ is called magnetic flux.

As the applied current follows a cosine / sinusoidal trajectory, we describe U_{ind} as:
Let $\omega = 20kHz * 2\pi$

$$U_{ind} = -N * \frac{d\Phi}{dt} = -N * \mathbf{B}(x') * A * ((\cos(\omega t)) \frac{d}{dt}) \quad (4.4)$$

Therefore

$$U_{ind} = N * \mathbf{B}(x') * A * \omega * \sin(\omega t) \quad (4.5)$$

Applying the hardware calibration values of 20 kHz for the oscillating magnetic field this results in:

$$U_{ind} = N * \mathbf{B}(x') * A * 20kHz * 2\pi * \sin(20kHz * t * \omega) \quad (4.6)$$

We assume that the receiver coils are calibrated in such a way that the induced voltage of the 3 axes receiver coil is comparably of the same value as a theoretical point shaped receiver coil. As the receiver coils are in prototype state, the coils have different sensitivities which also have to be taken into account and estimated in the calibration process:

$$U_{ind}^i = -N * \mathbf{B}(x') * A * \omega * \sin(\omega t) * s_i$$

where s_i is a sensitivity factor of the receiver axis i .

Figure 4.5 and figure 4.9 depict the sinusoidal trajectory of the driving voltage on the transmitter coil and the induced voltage on the receiver side. The receiver side voltage follows $U_{ind} = N * \mathbf{B}(x') * A * 20kHz * 2\pi * |\sin(20kHz * t * \omega)|$. The absolute value of U_{ind} is caused by the used receiver amplification circuit. The calibration process has to take

$$N * A * 20kHz * 2\pi * |\sin(20kHz * t * \omega)|$$

into account.

4.3 Magnetic Field Generation

A transmitter consists of a micro-controller which is supervising three transmitter channels. Each of these circuits is responsible for a single transmitter axis and the generated magnetic field. The hardware consists of an H-bridge which continuously applies a cube-shaped signal to the transmitter coil. The Law of Biot Savart determines for each point around the transmitter coil the corresponding field density.

4.3.1 Hardware for Field Generation

The hardware is controlled by a DSPIC micro-controller whose main task is to supervise the magnetic field generation.

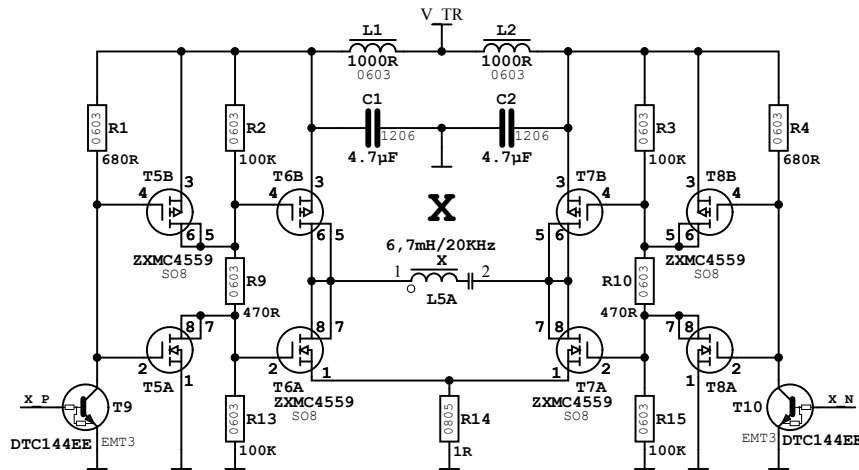


Figure 4.3: Schematics of a transmitter H-bridge channel. The bridge parts are actuated by the microcontroller; this includes the duty cycle of each side i_p and i_n and the base frequency of 20 kHz of the oscillating magnetic field. As the distribution of high power signals is complex, three similar channels are used for each transmitter coil.

Magnetic Field Generation

The magnetic field is generated by a three axes cube-shaped transmitter coil being sequentially excited. The dimension of the transmitter body is $18cm \times 18cm \times 18cm$. Each axis consists of 300 windings of 0.5 mm copper wire which are applied to the plastic coil body. Each transmitter axis is perpendicular to the other two axes. , Each coil is tuned to 20kHz by adapting the capacitor value of the attached serial oscillating circuit To increase the power output of the transmitter coils. The serial oscillating circuit filters out hardware related noises, the highest energy output of the coil is at its resonant frequency.



Figure 4.4: Different transmitter and receiver coil architectures left and center: cube shaped transmitter coils with three transmitter axes, right: circular transmitter coil with three transmitter axes and reduced crosstalk. Center front: 3D receiver coil with six conical axes, two coils are differentially amplified and sensed.

Although being more complex than a simple air coil, the three axes transmitter coil setup provides additional information: As each axis is perpendicular to the other two axes, the resulting magnetic field vectors of the transmitter coils are also perpendicular to each other. The magnetic field of a single coil is highly inhomogeneous but has ambiguous positions with comparable magnetic field magnitude values, a combination of three transmitter axes adds more information for a stable distance estimation and provides enough information to retrieve the position of the receiver in the octants around a single transmitter.

In contrast to quasi-static magnetic field systems, our system applies an alternating current to the transmitter coils. The result is a field following the excitement current. This can be thought of as expansion and retraction of the magnetic field according to the alternating current.

The underlying oscillation frequency is 20 kHz, 22 V peak to peak square shaped voltage and a 0.17 A current generate the magnetic field. The reason for choosing such a low frequency is that environmental effects (counter induction / magnetic fields) caused by the oscillating magnetic field strongly depend on the used frequency (see Law of Faraday, chapter 4.2.2), applying a lower frequency oscillation results in lower noisy effects.

An H-bridge circuit is used to generate a positive and negative energy flow at the transmitter coil. Each of the half bridges of this driver circuits is managed by a microcontroller pin separately. This control mechanism has been chosen to flexibly adjust the duty cycle of an emitter coil. This enables us, for example, to reduce the magnetic field strength if the receiver is very close to

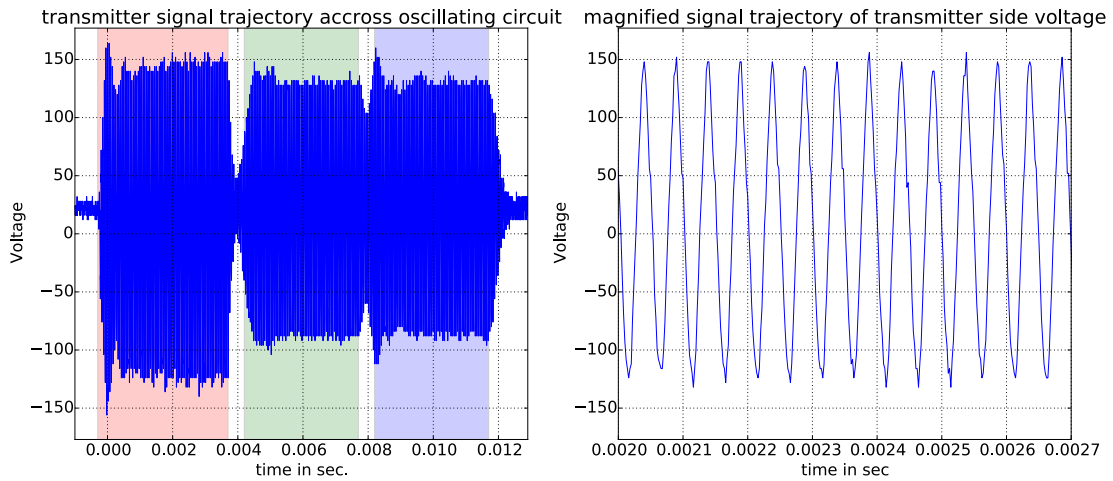


Figure 4.5: Voltage measured across the oscillating circuit at the transmitter side of a transmitter axis. Clearly visible is the crosstalk of the two other axis when an axis is emitting the magnetic field.

the transmitter coil. The low distance between the transmitter and the receiver causes a high induced voltage, possibly resulting in an overdriven amplification circuit on the receiver side. Reducing the duty cycle of the transmitter side bridge reduces the magnetic field and allows to measure the magnetic fields also at close distances. The period of each voltage direction is supervised in the micro-controller program.

The voltage trajectory of an excited transmitter coil, measured across the oscillating circuit, is depicted in figure 4.5. The magnetic field follows the current / voltage applied to the coil, the signal response of the transmitter coil is a sinusoidal shaped signal. A closer look at the signal shows that the circuit design with two micro-controller pins managing the square signals has a drawback: there is a short period where the states of the two micro-controller switches result in a high current peak. Because of the sequential processing of the transmitter program, the short circuit occurs when one output pin's state is switched, and the other control pin stays unchanged for one processor cycle. As the peak is not part of the 20 kHz spectrum, it will be filtered out or reduced on the receiver side's oscillating circuit.

As visible in figure 4.5, there is a crosstalk of the two muted axes. If an axis is excited, the other two coil axes act as capacitor plates also generating magnetic fields and therefore the generated magnetic field is reduced.

Instead of using a cube-shaped coil, we implemented a sphere shaped coil which will be discussed in section 4.3.2.

4.3.2 Behavior of different Transmitter Coil Architectures

For this evaluation, we measure the voltage across the L-C filter of the z-axis of both the cube-shaped coil and the spherical coil. In both coil variants, the y-axis is between the x and

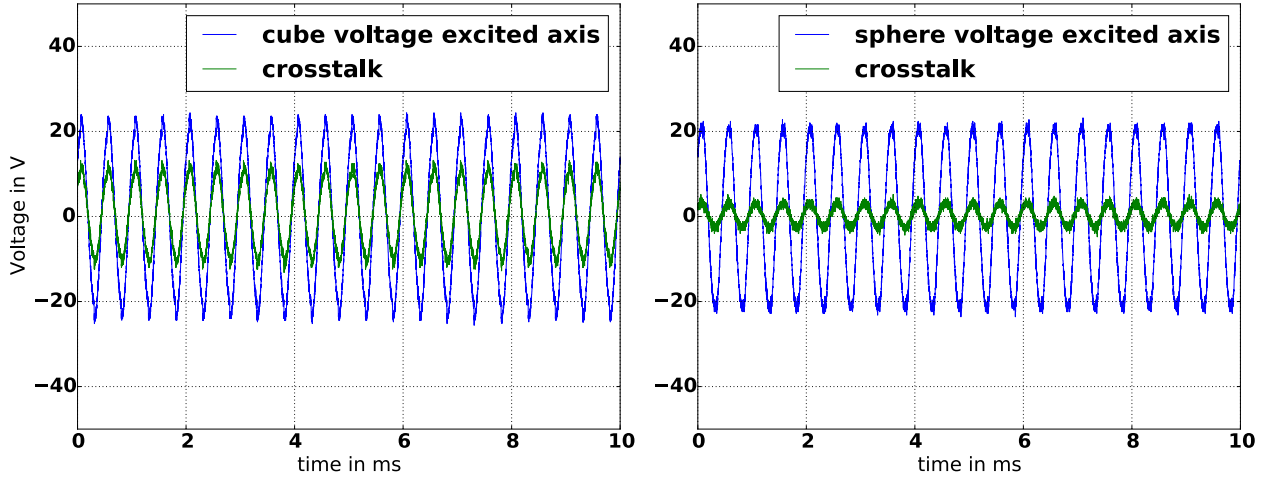


Figure 4.6: Excitement and crosstalk signal trajectories measured at a cube-shaped and a spherical transmitter coil. The crosstalk signal is measured at a perpendicular axis. The spherical transmitter coil has a lower crosstalk than the cube shaped one.

z-axis of the coil. The excitement voltage is in each measurement 2V peak to peak with an oscillating frequency of 20kHz. Both coil types are tuned to match this resonance frequency. The excitement signal and the crosstalk signal is measured simultaneously using an oscilloscope.

Figure 4.6 shows the raw signal of the cube-shaped coil and the spherical coil. It contains the crosstalk signal of the coils. The crosstalk voltage (**peak to peak**) of the cube-shaped coil is $u_{cross}^{cube} = 26V$, the spherical cube has a crosstalk of $u_{cross}^{sphere} = 10V$. For an excitement voltage of 20V peak to peak (the voltage used during typical operation), the crosstalk voltages are $u_{cross}^{cube} = 124V$ and $u_{cross}^{sphere} = 48V$.

The crosstalk on the non-active axis results in a counter magnetic field which reduces the magnetic field strength of the excited magnetic field axis. As the theoretical field model does not take this effect into account, the crosstalk negatively influences the position estimation using a single coil and the cube-shaped transmitter. The spherical cube has a reduced effect and therefore a better magnetic flux density representation. Due to the reduced crosstalk on the spherical coils, the calibration process of the spherical coil is less complex than the cube-shaped transmitter.

4.4 Hardware Calibration

In the hardware calibration step, the oscillating circuits are tuned to 20kHz. The frequency has been chosen because the frequency can be controlled by low-performance micro-controllers and the influence of environmental eddy magnetic fields generated by the artificial magnetic field is comparably low. Also, the tuning process of oscillating circuits is comparably easy, and the used capacitors are cheap. The reason for this filter approach is to reduce the effects of the environmental influences on the receiver side and to focus the output energy to the aimed frequency on the transmitter side.

The frequency of an oscillating circuit f_0 is defined by the inductivity L of the coil and the capacitance C :

$$f_0 = \frac{1}{2\pi\sqrt{L * C}} \quad (4.7)$$

The inductance of the transmitter coils lies in the magnitude of 20mH, the receiver coils of 12mH.

Transmitter Coil The driving voltage of the square shaped input signal can be adjusted using a voltage divider on the transmitter side board. We carefully tune the resistance ratio to reach the desired output voltage of 22 V. The oscillating circuit requires an adjustment of capacitors as the inductance of the transmitter coil is fixed. An oscilloscope measures the voltage across the capacitor; a signal generator excites the coil with a square-shaped signal at a specific frequency. The measured voltage across the capacitors depends on the excitement voltage and its frequency. If the resonance frequency of the oscillating circuit is applied, this results in a maximization of the measured voltage across the capacitors. We carefully estimate the L-C combinations of the transmitter axes to maximize the power output of the coil at 20 kHz.

Receiver Coil In contrast to the transmitter, the receiver coil is a serial oscillating circuit. Tuning the receiver coil requires a different calibration process: A transmitter coil, tuned to 20kHz, is placed at a fixed orientation and fixed distance relatively to the receiver axis. We measure the induced voltage across the receiver axis. The current resonance frequency of the receiver coil axis is defined by the frequency of the maximum induced voltage, the adjustment of the capacitor values is then comparable to the transmitter calibration process.

4.5 Receiver Side Magnetic Field Density Acquisition and Magnetic Field Representation

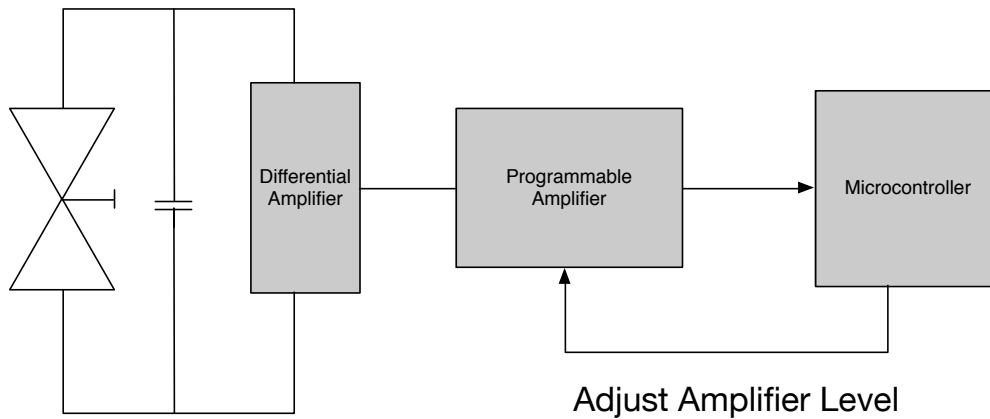


Figure 4.7: Schematic representation of the used receiver side processing circuit.

4.5.1 Sampling and Amplification Control

The wearable receiver device is measuring the oscillating magnetic field with a 3-axes coil. The dimension is $2\text{cm} \times 2\text{cm} \times 2\text{cm}$, each axis consists of two conical coils, which are connected to a differential amplifier. This chip amplifies the voltages of the two receiver coil parts in comparison to the center tap. A serial oscillating circuit is strictly tuned to 20kHz, which filters out signals generated by house installation and devices. Operational amplifiers and rectifiers pre-amplify the induced voltage. Programmable amplifiers regulate the signal level to overcome the high dynamic range of the magnetic field induced voltage. This also avoids overdriving the ADCs of the micro-controller. The absolute value of the voltage is implemented on the hardware side To cover the complete ADC range between 0V and 3.3V.

Similar to the transmitter side, a Microchip DSPIC33FJ128 microcontroller manages the functions of the boards. It is responsible for magnetic field detection, acquiring the raw magnetic field induced voltage signal, transmitter synchronization, amplification gain control and pre-processing of the measured induced voltage trajectory. An inertial measurement unit (IMU, Ivensense IMU 9150) is connected to the I2C bus. The IMU is periodically sampled between the magnetic field measurements and gathers information about the current acceleration, rotation rate and earth magnetic field. The compass integrated into the IMU is based on the Hall effect measurement principle and is not influenced by the oscillating magnetic field due to different frequency sensitivities. A low power ZigBee module provides either a peer to peer or star-shaped communication architecture between the transmitters to transfer the refined data to the location estimation computer. The Zigbee communication is bi-directional, information about the current scheduling and timing is exchanged between transmitters, processing computer and the receivers.

4 Physical Layer



Figure 4.8: Receiver module of the magnetic field localization system. The three axes receiver coil measures the magnetic flux at the current location of the receiver.

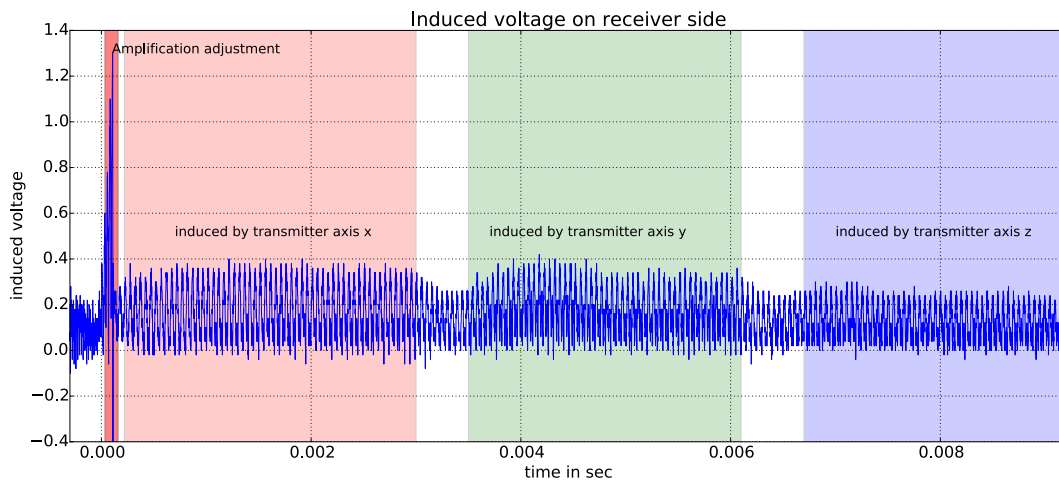


Figure 4.9: Raw voltage trajectory measured on the receiver side when a transmitter excites the three axis. Notice the different maximum amplitudes of the induced voltages of the three perpendicular transmitter axes.

Figure 4.9 depicts the signal trajectory measured on one channel on the receiver side. Three transmitter axes sequentially generate the magnetic field, the induced voltage of the magnetic fields are rectified and amplified on the receiver axes. Due to hardware tolerances of the receiver coils and the oscillating circuits, the maximum amplitudes of the three magnetic fields typically differ. Each receiver axis channel holds information about one component of the 3D magnetic field vector.

In this section, we explain the details of the signal gathering process on the receiver side, which includes triggering, amplification, digitalization, signal encoding and signal transfer for position estimation.

It is necessary to sample the induced voltage trajectory and process the information on the receiver side to provide accurate magnetic field position estimation. Although there is an RF transmission system attached to the receiver board, the transmission data rate is too low to

completely transfer the information to the computer for signal processing. Additionally, constant RF-based data streams create higher power consumption than the pre-processing step on the micro-controller. The calculated magnetic field induced voltage representation encoding is transferred to a central position estimation server for further processing (distance and position estimation). In the following parts we describe the different steps to ensure the most accurate signal acquisition and processing which is possible on the various components and the given hardware. The receiver board is equipped with a microcontroller to reduce the power with the goal to support at least 4 hours of continuous data recording and transfer. Due to the limited processing power of this device, including processor commands per second and available memory, the algorithms executed on the micro-controller are adjusted to work with the supported data types and their accuracies.

All steps described here are performed for all three receiver axes channels.

4.5.2 Receiverside Magnetic Field Representation

During the magnetic field generation, the receiver is recording the induced voltage trajectory of the magnetic field. The analog circuit contains a band-pass filter implemented in hardware and tuned to 20kHz and a two-step amplification part. The first step of the amplification sequence is a static differential amplifier, amplifying the induced voltage with a factor of 10. The second amplifier is a controllable amplifier. The amplification value is chosen in such a way that a maximum accuracy is achieved without overdriving the ADC. No hardware peak detector or envelop circuit is available.

The DSPIC micro-controller has a 12 bit onboard ADC which samples the trajectory with a sampling rate of 256kHz. As the device does not support the simultaneous recording of the three axes, each channel is recorded sequentially. The necessary sampling time for each signal has been adapted correspondingly. A DMA-based information transfer between the ADC and the memory is implemented to achieve this sampling rate. An interrupt-based processing step is performed after the digitalization of a full 20 kHz oscillation cycle is completed. This results in a trajectory of the magnetic field induced voltage which is then transferred to the processing computer. We adjusted the length of the transmitter axis pulse to both compensate the clock offsets on the transmitter and the receiver side and to be able to sample and process the induced voltage trajectory on the receiver. Including the time for excitement and settling of the coils, the minimum pulse interval is 4ms (1.3ms for digitalization of the signal of 3 axes and the additional time values).

The following part discusses different approaches representing the magnetic field induced voltage trajectory and therefore the magnetic field at the receiver's position. The signal trajectory of the induced voltage on the receiver side follows a rough sinusoidal trajectory, therefore the representation has to reflect this behavior.

The goal is to find a field representation which can deal with the high dynamic range of the induced voltage to support a range between 40 cm and 400 cm. The calculation of the representation has to be performed on a DSPIC micro-controller with 40 MHz clock rate without a

4 Physical Layer

floating point unit. This limits the possible magnetic flux density representations, as floating point operations take too long to support a good speed. The available onboard memory of the micro-controller is not sufficient to allow excessive use of lookup tables.

During the discussion of the approaches, we describe the transfer function $\mathcal{T}(s_i) \rightarrow b_i$ which transforms the signal representation s_i into the theoretical magnetic field component b_i . The transfer function gives information about the calibration process and the relation between the theoretical values and the measured values. Also, the maximum range of the field representation approach is given.

We start with the recording of raw induced voltage values on the receiver side. A magnetic field transmitter constantly excites one axis of the transmitter cube coils. The induced voltage values of the three receiver coil axes are recorded at different distances. We carefully place the receiver to avoid changes in its orientation. The receiver side micro-controller samples the three channels with a bit depth of 12 bit at a sampling rate of 170kHz. To achieve this, the direct memory access module is used which stores the values in three DMA buffers for further processing. The sampling rate has been chosen to gather two 20kHz signal oscillations with 128 values. After the three channels have been sampled, each sampling window w_i is transferred to the computer using a serial connection. The computer stores the data for later processing. In a mobile application, this approach is not usable, as the data rate of the sensor is too high to support wireless data transfer to the computer.

Because we record the induced voltage on the receiver side at different distances, the high dynamic range of the induced voltage is noticeable. Without relying on an amplification algorithm, the micro-controller sequentially steps through all amplification levels of each receiver channel and adds this amplification information to the window. In the analysis step, we choose for each distance the maximum amplification which does not overdrive the signal. Figure 4.10 depicts the signal trajectory of a single magnetic field oscillation which was induced on the receiver side at different distances.

Hereafter we discuss several possible signal representation:

- maximum value of the sampling window buffer
- mean value of the sampling window buffer
- amplitude of a sinusoidal fitting function
- correlation value of two successive sampling windows

Max Value

A simple and fast signal representation is the usage of the maximum value of a sampling window. This algorithm is in $\mathcal{O}(n)$ and consumes $\mathcal{O}(n)$ memory (the DMA buffers) where n is the sampling window buffer size. The approach can already be applied during the sampling phase. A drawback of this method is that the maximum value is prone to noise, electromagnetic sources like motors, power lines or on-board interferences strongly influence the signal especially when the receiver is far away from the transmitter coil and the magnetic field magnitude is low. The

measured noise has two sources, external EM sources, and the onboard amplification circuit. To reduce the onboard noise component, we increased the bit resolution of the ADC from 10 bit to 12 bit and reduced the amplification rate of the controllable amplifier by factor 4. This allowed us to distinguish the signal from noise up to a distance of 3.2 m.

$$s_{max} = \max\{\mathcal{W}\} \quad (4.8)$$

Mean Value

A signal representation consuming more processing time (as it introduces multiplications and a higher value domain) is the mean value of the sampling windows. The average value has the advantage that it is less prone to noise outliers.

$$s_{mean} = \frac{1}{|w_i|} \sum_{i=0}^{|w_i|} w_i[i] \quad (4.9)$$

The multiplication and accumulation (MAC) has been implemented in DSP-based Assembly commands (MAC, Multiply Accumulate Commands), resulting in an execution time of $200\mu s$ (compared to 5ms with standard processor commands) for a 128 word broad sampling window. The maximum range which still allows to distinguish the magnetic field induced voltage from the noise, lies between 3.5m and 3.8m depending on the orientation of the transmitter.

Let n be the sampling buffer window size.

$$Mean(t) = \sum \frac{U_{ind}(t)}{n} = \sum_t \frac{N * \mathbf{B}_i(\mathbf{x}) * A * 20kHz * 2\pi * \sin(20kHz * t * \pi)}{n} \quad (4.10)$$

$$Mean(t) = \frac{\mathbf{B}_i(\mathbf{x})}{n} * \sum_t N * A * 20kHz * 2\pi * \sin(20kHz * t * \pi) \quad (4.11)$$

This representation method therefore holds the information about the field strength at its position.

Sinusoidal Fitting Function

Taking the theoretical considerations of section 4.2.2 into account, the induced voltage follows a sinusoidal shaped trajectory. The harmonic function describing the voltage trajectory uses the amplitude κ , the frequency f ; the phase shift φ and the offset τ :

$$s(t) = \kappa * | \sin(f * t * 2\pi + \varphi) | + \tau \quad (4.12)$$

The absolute value of the sinusoidal function has to be applied as the hardware circuit rectifies the induced voltage value.

To determine the variables κ , φ and τ , we minimized the function $\Delta(t) = s(t) - \mathcal{W}_t$ using the

4 Physical Layer

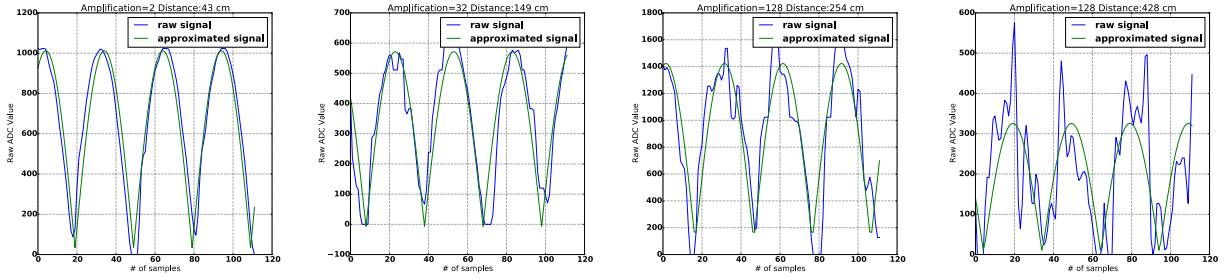


Figure 4.10: Sinusoidal-based approximation of the sampled magnetic field induced voltage. The Levenberg Marquardt algorithm has been used to minimize the difference between the measured signal and the approximated signal. Notice that the noise component of the signal rises with increased distance.

Levenberg Marquardt least square approach. κ is then the approximation of the field strength $\mathbf{B}_i(\mathbf{x})$.

This algorithm gives an approximation of the sampled signal. The amplitude κ can be used as a field descriptor. A drawback of the Levenberg Marquardt least square fitting algorithm is its excessive use of float and multiplication operations which cannot be implemented in an performant way on the receiver DSPIC micro-controller. Due to hardware limitations, a complete transfer of the DMA buffer to the processing computer is not possible.

This approach would allow to both approximate the field strength and hardware related issues as knowledge about the frequency is used and hardware offset values are included to minimize the voltage differences. The maximum distance achieved with this approach is 4.3m.

Correlation Value of two successive Sampling Windows

The basic idea behind the correlation value approach is that two successive sinusoidal shaped signals have a higher correlation value (similarity) than two sampling windows of white noise. Two sampling windows \mathcal{W}_1 and \mathcal{W}_2 are derived from the analog signal at the given sampling rate and bit depth. Let $n = |\mathcal{W}_i|$ be the buffer size of both windows.

$$\mathcal{K}_\tau = \sum_{i=0}^n \mathcal{W}_1[i] * \mathcal{W}_2[i + \tau] \quad (4.13)$$

$$\mathcal{K} = \max \mathcal{K}_\tau \quad (4.14)$$

Equation 4.13 calculates the correlation value with a given phase shift τ , equation 4.14 describes the field representation which is the maximum value of all \mathcal{K}_τ .

The transfer function reflects the magnetic field nature: As $\mathcal{K} = \max \mathcal{K}_\tau$ is the maximum value of all correlation values $\mathcal{K}(\tau)$ both sampling windows \mathcal{W}_1 and \mathcal{W}_2 are best synchronized. Both sinusoidal trajectories have equal values which is comparable to the mean root

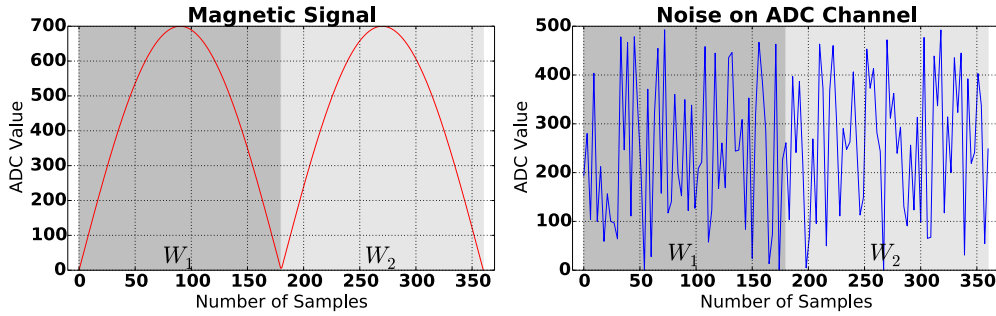


Figure 4.11: Applying a correlation algorithm to a sinusoidal shaped signal (left hand side) and noise signal (right hand side) results in a higher correlation value of the sinusoidal signal buffers compared to the noise signal.

square of a single sampling window. (Surface below the magnetic field induced voltage trajectory)

Although the calculation of \mathcal{K}_τ have been implemented using DSP-based MAC commands, the overall calculation of the \mathcal{K} value takes 1.4 ms for one channel on the DSP. The processing time of three transmitter axes and three receiver axes therefore is at least 12.6ms. In the test setup, we achieved a maximum range clearly above 4.5m.

4.5.3 Discussion

| Field repr. | Max. range | Processing time | Adv. | Disadv. |
|--------------|------------|-----------------|----------------------------|---------------------------------------|
| Max | 3.2m | 0.1ms per axis | Fast | prone to noise |
| Mean | 3.8m | 0.2ms per axis | easy to implement | no hardware information |
| least square | 4.3m | N.A. | reflects harmonic function | not suitable f. real time application |
| Cor. value | 4.5m | 4.5ms per axis | High range | long processing time |

Table 4.1: Overview of the magnetic flux density representation on the receiver side.

As discussed earlier, the limited resources of the receiver side DSPIC do not allow to use the least square approach which would be the most accurate approach for the field representation. Depicted in table 4.1, the correlation approach provides high accuracy and high range. A disadvantage is its high processing overhead as the algorithm lies in $\mathcal{O}(n^2)$ compared to the mean value field representation which lies in $\mathcal{O}(n)$. To still provide a sampling rate of 30 Hz, we suggest the following approaches:

- RF-based trigger synchronization or clock synchronization: mean value representation for three receivers and three transmitter axis resulting in a slot length of below 20 ms.
- threshold-based correlation signal detection for one transmitter axis and three receiver axes, magnetic field-based data transfer for transmitter id detection and mean value field representation with a slot length of 150 ms

The synchronization approaches are described later.

4.6 Amplification Control

The signal gathering sequence includes an amplification chain (a differential amplifier with a fixed rate of 10 and a dynamically adjustable amplifier between 1 and 128 times) and a 12 bit ADC with a reference voltage of 3.3V. The amplification level is controlled by the micro-controller. Particularly in positions with low signal levels, this improves the accuracy of the signal detection. A threshold-based algorithm evaluates the currently estimated ADC value to achieve the highest accuracy for a given position without overdriving the circuits. If the signal level is above the "high" threshold, the amplification gain is reduced by two, if the signal level is below the "min" threshold, the amplification gain is increased by two. The threshold values have to be chosen in such a way to avoid oscillations (periodically increasing and reduction of the amplification gain.). After the adjustment, the new amplification value is locally stored to be used in the next measurement cycle.

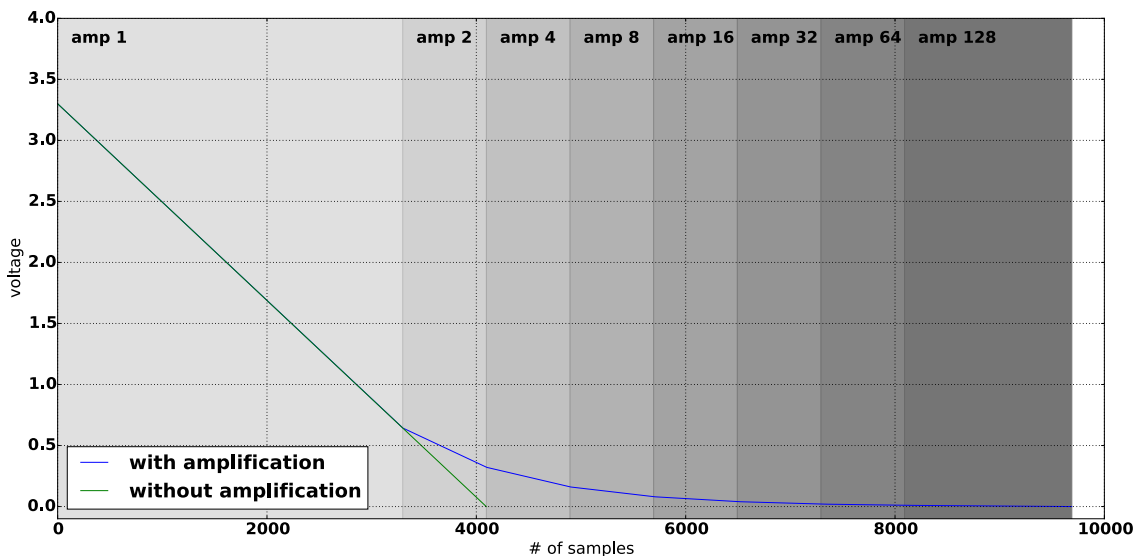


Figure 4.12: Increase of the accuracy of the 12 bit ADC when eight decades (1...128 times) programmable amplifier is used.

Figure 4.12 depicts the signal trajectory of a 12 bit ADC without additional amplification and with an eight decades programmable amplifier as integrated into our receiver circuit. Particularly in the low signal range, signal differences can be gathered. The figure also indicates the amplification intervals.

4.7 Transmitter-Receiver Synchronization

A strong synchronization between the magnetic field generator and the measurement unit has to be achieved to link the measured values with the three magnetic fields of the three transmitter coils. A cable bound would be the most accurate approach, but it is only acceptable if the system is used in a limited area and typically comes with reduced mobility. Therefore synchronization methods based on RF or magnetic fields are of better use.

4.7.1 RF Trigger Messages

RF communication typically involves transmission protocols to avoid packet collisions in the shared medium. Therefore RF network modules store packets in transmission buffers until the sending is possible and acknowledged. The storage time depends on the utilization of the channel and the number of nodes transmitting messages. In addition to the time in the buffer, propagation and processing delays on both the receiver and transmitter sides have to be taken into account. Especially in our system in which micro-controllers have to process multiple tasks (ADC sampling, I2C data transfer, data processing, magnetic field generation and RF stack service) the reduced resources introduce a processing delay of up to $2ms$ if the micro-controller is not able to immediately serve the RF module.

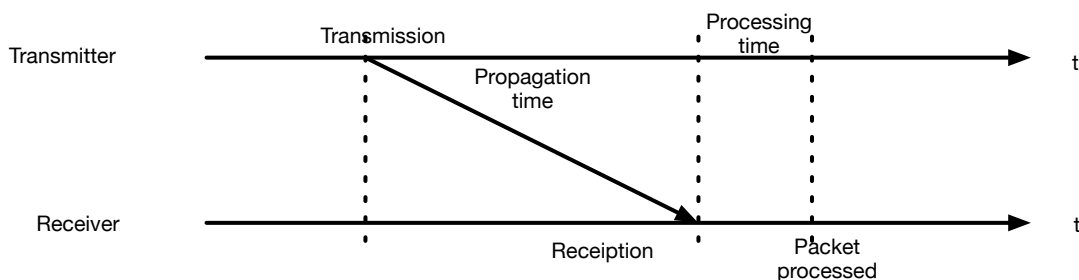


Figure 4.13: The accuracy of RF-based synchronization approaches rely on three components, the estimation of the packet buffer storage times, the propagation delay and the processing delays on the transmitter and receiver sides.

To keep these delays at a minimum level, we implemented interrupt callback functions being executed whenever a packet is transmitted or received. The callback functions then trigger the measurement cycle on the transmitter and receiver side. Interrupt priorities avoid error measurements during the ADC conversion cycle if the RF interrupt has a lower priority than the ADC DMA part. For information exchange and distributed algorithms, we implemented an RPC-based message processing chain. This chain is called on transmission and reception of packets to perform a specific task for the different packet types.

RF Timing Delays To estimate the timing delays of an RF trigger message we conduct the following experiment: a transmitter node periodically broadcasts a specific message type. On transmission and reception of the packets, the nodes perform a transition on a digital IO pin.

4 Physical Layer

Using an oscilloscope, we measure the combination of propagation and processing time on the receiver side.

In our test setup, the time difference between the trigger sender and the magnetic receiver board varied between $300\mu s$ and $450\mu s$, on the transmitter side the time values were between $200\mu s$ and $330\mu s$. The differences in the standard deviations of transmitter and receiver are related to the used Remote Procedure Call (RPC) mechanism implemented on top of the Zigbee RF stack and the other tasks to be served which are more complex on the receiver side.

The Zigbee information transfer supports up to 200 packets per seconds (60-byte payload) and introduces a packet loss rate of 4 to 5 percent depending on the environment. When several receivers are used for position estimation, and when acknowledged packets have been requested, it is possible that the number of packets which should be transferred in one second exceeds the maximum number of packets per second. Therefore different synchronization approaches have been considered trying to reduce the burden on the RF stack. Additionally, if the system is used in industrial environments, RF communication is error prone because of the EM emissions and disturbances (signal scattering). The result of the packet loss is that either the transmitter or the receiver is not aware of a measurement. If the transmitter misses the trigger packet, the magnetic field is not generated and therefore the receiver measures only the noise on the three channels. If the receiver misses the trigger event, a measurement is completely lost.

An additional message type is introduced to solve this problem: the trigger node sends a request to the corresponding transmitter which then broadcasts the trigger message informing the other nodes about its current magnetic field transmission.

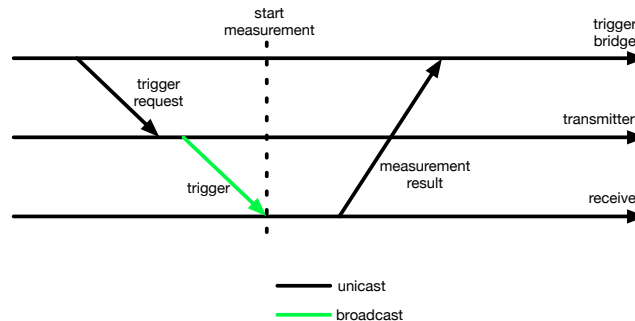


Figure 4.14: In order to remove measurements where the transmitter did not receive the trigger measurement resulting in "empty measurements", the triggering bridge requests a trigger message from the transmitter. If the transmitter does not receive this message, the receiver is not measuring.

If the transmitter does not receive the trigger request message, no measurement cycle is triggered on the receiver side as the transmitter itself does not send out the trigger message. This removes "outlier" messages containing only measurements of the receiver side noise level leading to position falsifications.

The drawback of this two-step triggering approach is that it puts additional burden on the RF channel. Twice as many packets have to be sent compared to the single step triggering approach.

An approach with a lower packet rate is, therefore, preferable.

4.7.2 Magnetic Field-based Synchronization

In this section, we propose a robust magnetic field synchronization method which does not rely on RF triggering messages and therefore reduce the amount of packets per measurement cycle. This includes the detection of oscillating magnetic fields with low magnetic field strength values, information modulation and demodulation in oscillating magnetic fields, synchronization of transmitter and receiver and measurements of the magnetic flux density by the receiver. As a side path, we apply the presented concepts to the field of smartwatches to detect regions of interests.

Synchronization and Data Transfer in Oscillating Magnetic Fields

As previously described, RF-based trigger messages can lead to packet loss and therefore to inconsistencies in the signal gathering process. The reason for these data corruptions is the possible packet loss in the localization RF networks which either results in measurements of the noise or missing measurements. In this section, we evaluate the possibility of using the oscillating magnetic fields to trigger measurements and how to transfer information between the transmitter and the receivers without the usage of RF communication modules. Particularly in industrial environments, the RF communication can be restricted by changing EM influences.

Influences of the receiver coil on the measured signal To obtain a stable, reliable and repeatable information representation, the physical properties of the coil types with regard to signal sensitivity (signal rise and range) and signal fall off have to be determined.

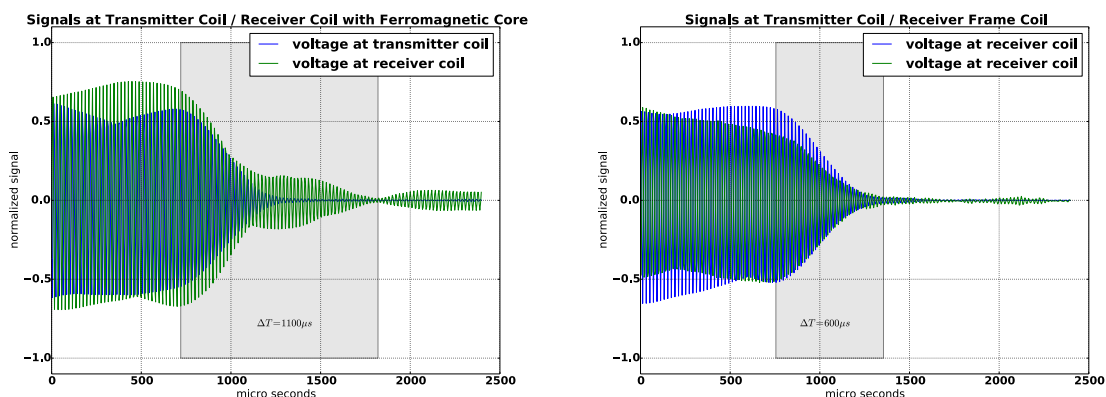


Figure 4.15: Signal behavior with and without a ferromagnetic core. The ferromagnetic core "magnifies" the magnetic field, therefore the coil is able to detect fields with lower magnetic field magnitude values.

4 Physical Layer

The induced voltage strongly depends on the distance between the transmitter and the receiver. To determine the minimum oscillation time of the transmitter, we measure the settling and falloff time on the receiver side coil. This evaluation should show that the signal falloff time varies with distance (the ferromagnetic core is "magnifying" the current magnetic field, and therefore the receiver side should be able to measure lower magnetic field magnitudes than the air coil. Additionally, ferromagnetic coils should also have a higher counter inductance.) and that ferromagnetic cores also extend the oscillation times on the receiver side. For comparison, we measure the signal trajectory on a transmitter coil (airframe coil with 300 windings) in the same manner as we do with the receiver coil. Both coil types have been tuned to a 20 kHz frequency band using oscillating circuits.

We recorded for both coils several oscillations of a transmitter coil at 20kHz with an amplitude of 22V peak to peak at 40cm and 250cm. Both coil types have been attached to receiver boards. We record the amplified induced voltage after the first amplification part. All signals have been digitalized at one mega sample per second using an oscilloscope. To estimate the fall off times of the different coil types, we record both coils, the transmitter and receiver coil. The oscillating magnetic field is generated by a transmitter board. Every 100 ms a transmitter axis is turned on for 30ms.

To reduce noise caused by other EM fields (in particular on the air coil), we apply an FFT-based bandpass filter on the raw voltage samples and remove all frequencies outside the interval of $[19500, 20500]kHz$. After this we normalize transmitter and the receiver voltage for easier comparability ($U_{norm} = \frac{U_{sample}}{U_{max}}$).

Figure ?? depicts the different signal fall off times: The ferromagnetic receiver coil takes twice as long as the nonferromagnetic coil, but has a more stable signal structure and is more sensitive to corresponding magnetic fields (which corresponds to higher ranges). When the excitement

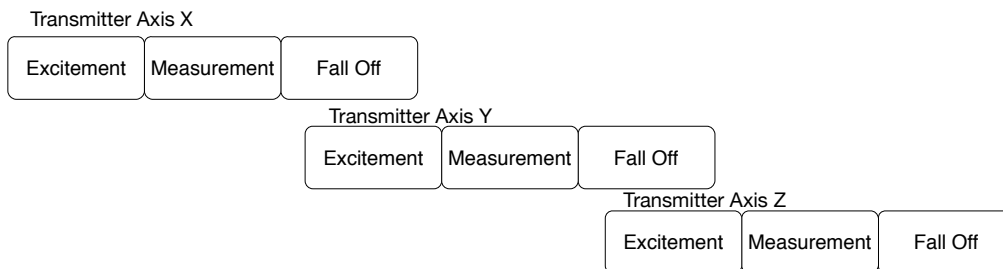


Figure 4.16: Schematic representation of a measurement slot on the receiver side

starts, the receiver signal nearly immediately follows the excitement voltage / magnetic field. The time until the maximum voltage is reached is $300\mu s$ for both coil types. The fall off time of the coil layouts differ, at 40cm the air coil has an approximately 50 percent lower fall off time of $600\mu s$ compared to the ferromagnetic coil which has a fall off time of $1100\mu s$. We saw in previous sections that the cube-shaped coil layout results in high crosstalk signals between the transmitter axes. A large fraction of the "falloff signal oscillations" are caused by the crosstalk of the coils. Also at 250cm the ferromagnetic coil has longer settlement times which is $900\mu s$

4.7 Transmitter-Receiver Synchronization

for the ferromagnetic coil and 500μ for the air coil. This effect is caused by the energy which is stored in the ferromagnetic material.

4 Physical Layer

The minimum excitement time depends on the used signal representation and its processing complexity, an excitement time of $10ms$ for each transmitter axis should be the goal.

Two successive measurement cycles should, therefore, be at least 0.9 ms apart ($900\mu s$ for signal fall off of the old signal and $300\mu s$ for excitement of the new signal) to achieve a clear reading of the induced voltage of a magnetic field transmitter axis on the receiver side. To reduce this time it is also possible to overlap the fall off time and the excitement time.

Correlation-based magnetic field detection In the previous section, we evaluated the excitement and fall off periods of the used receiver coils. This is necessary to define the minimum excitement times to detect information encoded in the magnetic fields. We implemented the magnetic field detection using the correlation approach as presented in chapter 4.5.2. The magnetic field is assumed to be sensed if this correlation value is above a given threshold.

To evaluate this approach, we implemented the correlation of two successive sampling windows in Assembly using MAC (multiply accumulate command) to reduce the processing of 3 receiver axes to below $1.5ms$ each ($12ms$ with common non-DSP commands). We refer to the chapter 4.5.2 for deeper insights and its detailed definition of κ .

A transmitter constantly excites one of its transmitter axes to estimate the maximum range of the correlation approach. The receiver samples two continuous magnetic field oscillations and calculates the corresponding correlation value of two buffers on the axis parallel to the emitter coil. We move the receiver along the major axis of the magnetic field and record for a set of discrete points the correlation values. Additionally, a measurement without magnetic field is performed to retrieve information about the noise behavior of the correlation approach. Because the transmitter is constantly generating the magnetic field, a synchronization algorithm is not used.

Figure 4.11 depicts the concept behind this: The correlation value of two sinusoidal-shaped signals is higher than the correlation value of two (white) noise trajectories.

As shown in figure 4.17 for the measurement positions, the estimated correlation value on the major receiver axis shows a higher correlation value than the noise signal. The signals measured at $86cm$ and $160cm$ differ from the typical magnetic field behavior, the falloff of the signals show a saturation effect: As no amplification adjustment algorithm is used in this data recording, the induced voltage overdrives the analog circuit and results in the saturation of the sampling window. After these two measurement points, the signal falloff is conforming to the magnetic field behavior, $\kappa \propto \frac{1}{d^3}$. Additionally with rising distance the signal's standard deviation increases. The explanation for this effect is that the reduced signal-to-noise ratio and the induced voltage are directly linked to the falling magnetic field magnitude values, and environmental influences which are overlapped by the magnetic field close to the transmitter but the effect weakens with growing distance.

Using this approach, we implemented a magnetic field detection mechanism which uses thresholds without any requirement of external trigger information: the receiver is constantly evaluating

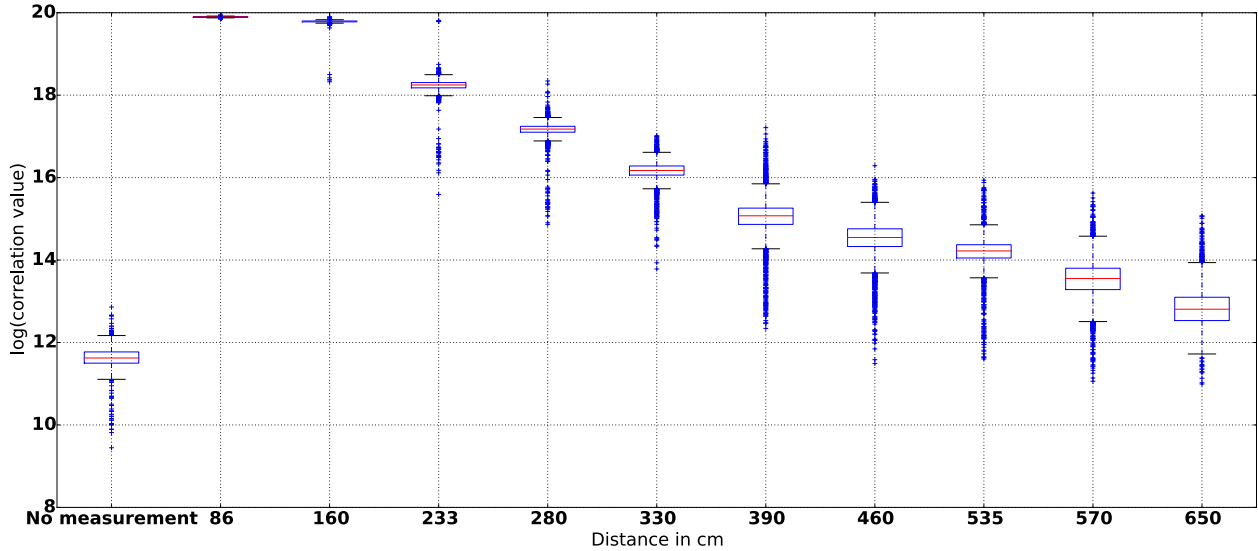


Figure 4.17: Correlation value of two successive sampling windows at different distances compared to the correlation value of the noise. With rising distance the correlation value drops but is still higher than the value of the noise. Especially at distances 80cm and 160cm the saturation effect of the induced voltage is visible, it is necessary to implement an amplification control protocol.

the correlation values of two successive sampling windows. If κ is above the threshold, the measurement of the magnetic field is started.

Correlation-based Signal Detection The signal detection mechanism evaluates two successive sampling buffers and shows a good performance with regard to coverage and range. We evaluate the signal detection mechanisms in several environments. The influence of electromagnetic field sources, for example, motor drivers, electric valves in industrial settings, microwaves, coffee machines or printers in office environments are to be evaluated. The interferences of this devices could trigger false measurements.

We initially record the correlation value of the analog circuit including the noise gathered by the coil, amplifiers, and rectifiers. Therefore the receiver collects 2000 samples of the correlation value. This signal is depicted in figure 4.18 on the left-hand side. The three receiver axes have different correlation noise levels, interesting is that one coil has a much higher basic correlation value (noise level) than the other two axes. This behavior is found on all prototype boards, and all receiver coils combinations.

For further evaluation, we recorded the noise correlation level in different environments. Figure 4.19 depicts the temporal progress of the various devices found in households. Another issue which is not addressed by a threshold-based triggering approach is that the temporal component of an EM influence is not covered by the approach.

4 Physical Layer

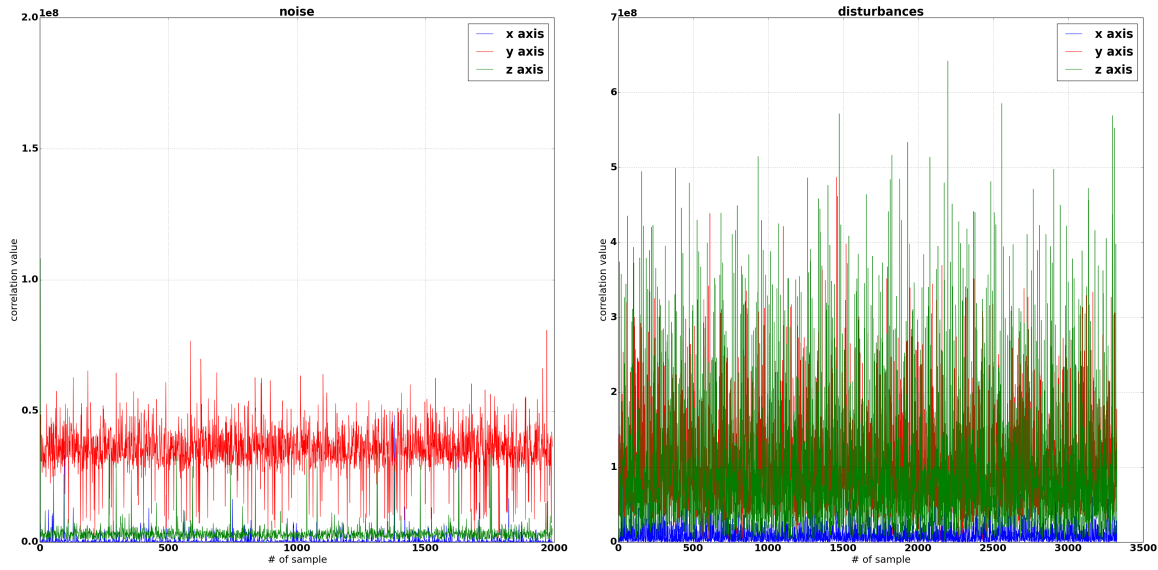


Figure 4.18: Correlation signal of the noise and electromagnetic disturbances (distance between receiver and motor driver 10cm), the disturbances are high enough to trigger false frame start events.

Figure 4.20 summarizes the different correlation values gathered in different environments. Compared to the noise correlation value of no electromagnetic sources, the values are much higher. A triggering approach solely using thresholds is only possible if the level is set to a correlation value κ_{thresh} which is higher than the values generated by the environments. Doing so also reduces the maximum range of the detection mechanism for magnetic field-based triggering. Therefore a more complex approach has to be applied and evaluated. In network communication, header and trailers enable the hardware to detect the start and end of packets on several transmission channels. Because of this, we implemented a transmission protocol for magnetic fields which encapsulates the id of the current transmitter provides a synchronization mechanism for the transmitters and receivers. The synchronization mechanism is be used in different applications such as AAL, offices or industrial production lines.

Figure 4.19 supports the header-based approach: Although generating higher correlation values on the receiver side, the artificial device signals can be distinguished from the magnetic field-based signals using a time-dependent sequence encoded in the magnetic field generation step.

Frame Layout A signal detection approach relying solely on thresholds is very error prone as different environments result in different threshold levels and therefore a reduced maximum distance. To support environments with high electromagnetic emissions (for example in industrial production environments) without reducing the maximum distance, a frame-based synchronization protocol is implemented. We present in the following part the requirements for such a protocol and how it can be implemented on top of the oscillating magnetic field to support synchronization and information transfer.

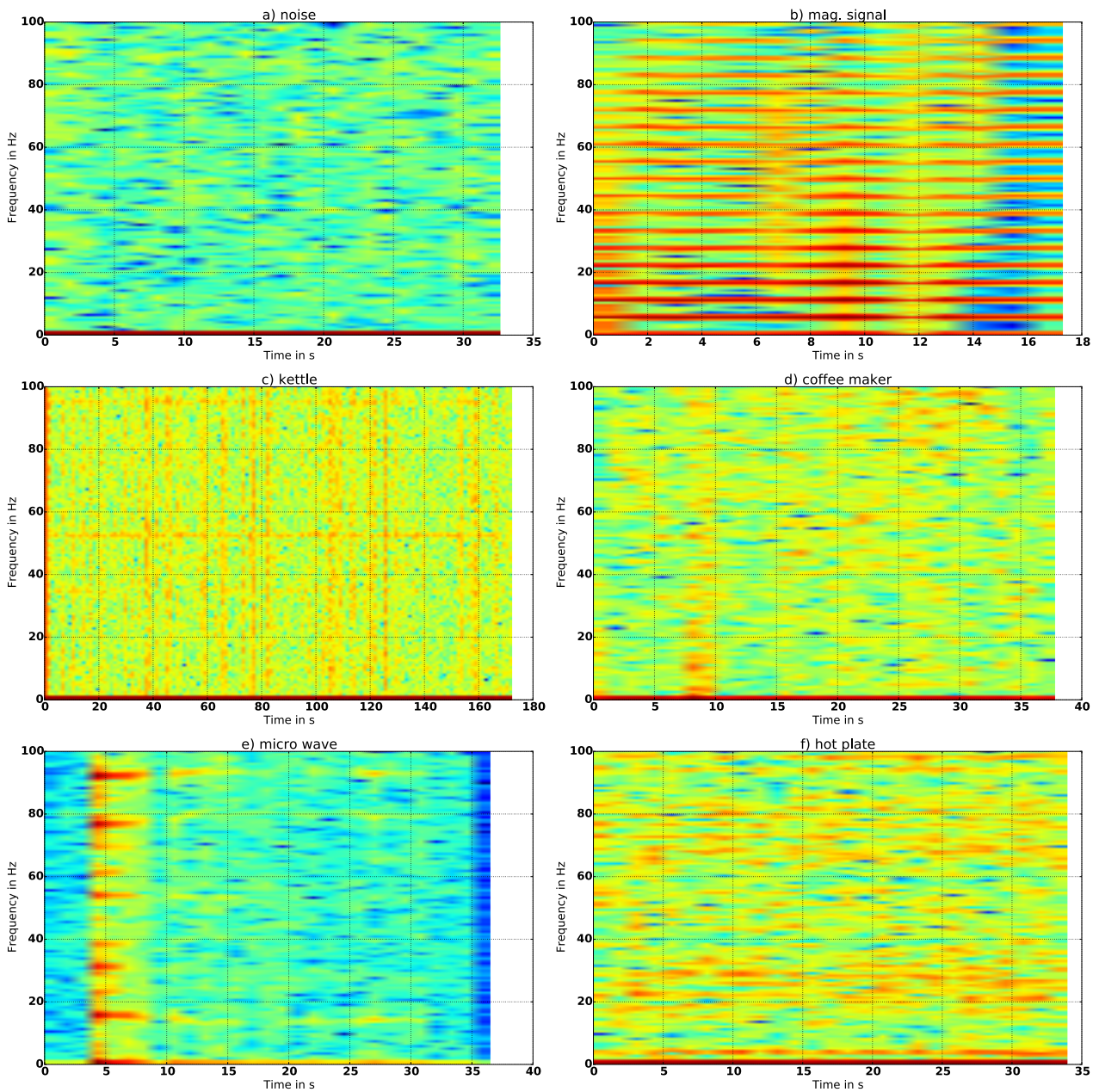


Figure 4.19: Spectrogram of the recorded correlation values of different environments including noise, oscillating magnetic fields, water boiler, coffee maker, microwave and hot plate of an oven.

Requirements The used protocol should be on the one hand robust against (periodic) electromagnetic interferences and signal changes, on the other hand simple enough to be implemented on the 40MHz microcontroller of the receiver board and support the high dynamics of the magnetic field along the transmission range. The signal encoding must support signal changes caused by movements (the signal level rises if the distance to the transmitter is reduced, the signal level drops if the distance to the transmitter is reduced.). Also, timing plays a role to

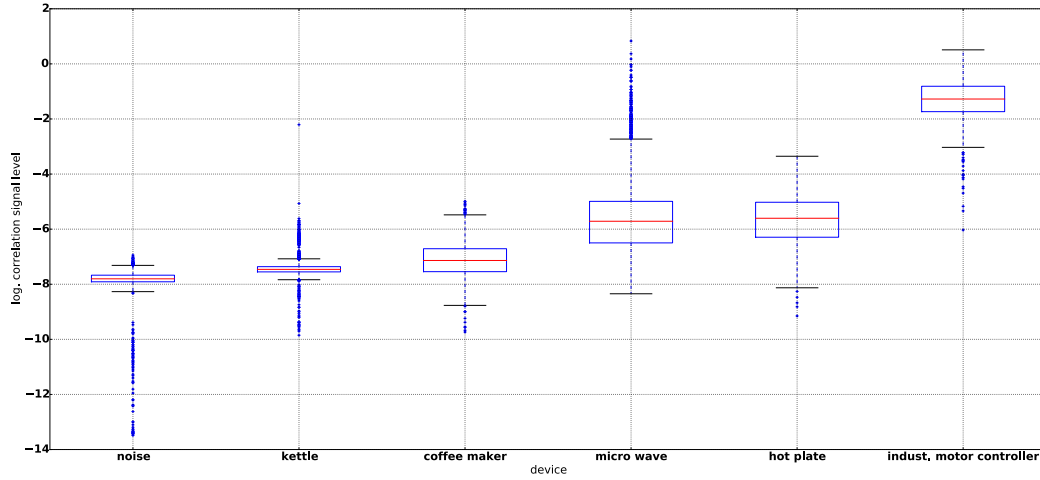


Figure 4.20: Correlation value distribution of different appliances.

support at least one position update per second in an eight transmitter setup.

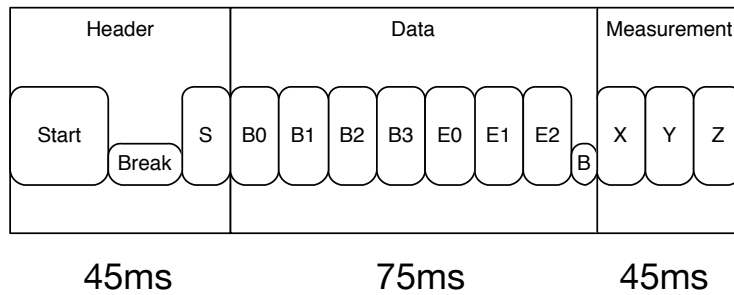


Figure 4.21: Frame layout for magnetic field-based data transfer. A header allows distinguishing the artificial magnetic field signal of the currently active transmitter from environmental signals. A data part encapsulates the transmitter id to link the measurement part with the currently active transmitter.

We, therefore, implemented a frame consisting of three parts: the header, the transmitter id encoded in the magnetic field, and the measurement part.

Header The header has to provide timing and synchronization information. Environmental EM emissions inducing voltages above the given start threshold have to be discarded to avoid false measurements. To achieve this, the header consists of a sequence of "magnetic field available" and "not available" intervals with different lengths: the first sequence part is used to detect the magnetic field using the correlation threshold and to adjust the amplification level to achieve optimum signal-to-noise ratio. As we are dealing with a time critical part, only three amplification levels are used (1, 16, 128), the amplification value is initially set to 128 and

automatically reduced if the signal is overdriven.

The header sequence is 40ms long, consisting of a 20ms long "start magnetic field", 10ms break where no magnetic field is generated and another 10ms long oscillating magnetic field. The length of this header sequence components provide enough information to filter out false measurements. The header signal sequence does not appear in the other frame parts to achieve time synchronization of the transmitter and the receiver. Even if the receiver starts sampling during a frame (e.g. after start-up), a frame is only recognized if the header sequence has been found. Therefore the receiver only needs to locate the header to be able to synchronize itself with the transmitter. The time interval is also long enough to measure the header sequence and to adjust the amplification level even if the receiver and transmitter are completely asynchronous.

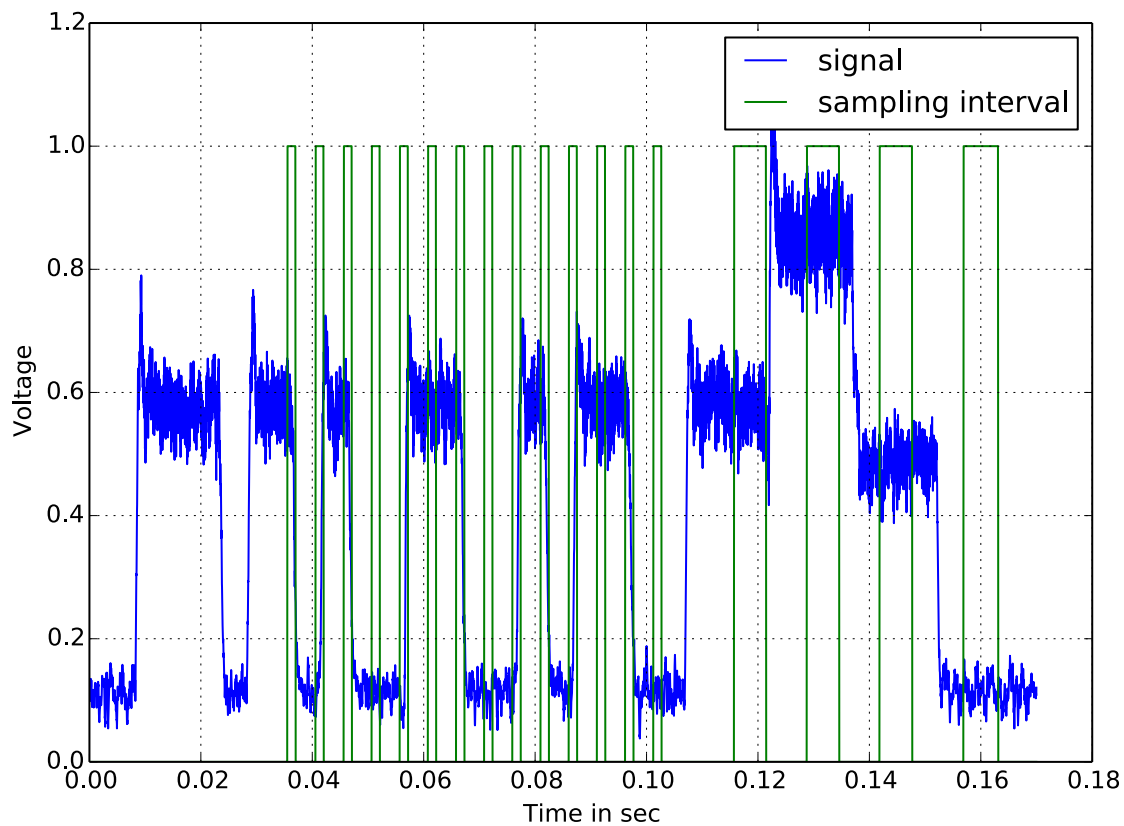


Figure 4.22: Manchester encoding of the transmitter id and measured on the receiver side, the receiver indicates the detection of a signal change by pulling a pin to logical high. The raw signal contains the encoded transmitter id and the magnetic field measurements of the transmitter axes (last three signal levels) which are simultaneously measured on the three receiver axes.

Transmitter id As already mentioned, in addition to the synchronization possibility, the protocol should provide information about the currently active transmitter. To achieve this, a 4-bit transmitter id is modulated in the magnetic field using Manchester encoding. After evaluating several encoding schemes (PWM, AM, Manchester), Manchester encoding was most

4 Physical Layer

stable with regard to movements (Movements increase or decrease the magnetic field induced voltage. Therefore PWM is prone to movements). Additionally, a 4 / 3 Hamming code is applied to detect bit errors and to be able to correct these errors.

Measurement After decoding and checking the transmitter id, the receiver starts the measurement of three receiver axes. The measurement cycle results in 9 correlation values representing the magnetic field vectors \mathbf{B}_x , \mathbf{B}_y , \mathbf{B}_z generated by the transmitter axes x , y , z . The length of the measurement cycle is 60ms for all three transmitter axes. Additionally, each transmitter axis measurement includes the adjustment of the amplification level.

Figure 4.22 depicts a raw magnetic field frame measured on the receiver side using an oscilloscope. The raw induced voltage shows the signal trajectory of the magnetic field data encoding for frame, transmitter id, and measurement. The sampling times for transmitter id detection and magnetic field measurements are included in the signal plot. Notice that the overall length of the frame is 180ms, the signal periods have been chosen to provide time buffers for inaccuracies caused by sampling and processing.

Evaluation, Range, Bit rate errors We tested the data transfer statically at discrete points at different distances. The analyses include the ratio of missed frames, the possible range and the bit error rates for different distances. We show that the bit error rate and frame detection rate depends on the distance between transmitter and receiver.

The transmitter is placed in the center of the measurement environment, a free area without any visible ferromagnetic materials or electromagnetic sources has been used.

The receiver is put in discrete positions along one transmitter axis between 40cm and 450cm, ten different positions have been recorded, 300 samples per measurement position have been evaluated. The transmitter modulates the numbers from 0 to 15 with a 200 ms delay between the modulations. We record for each demodulated value the time. Therefore it is possible to determine the packet loss of the system. Below 200 cm, the bit error rate of the system is 0 percent, also no packets are missed, we therefore exclude these values in the data plots. The overall packetloss rate in the measurement area is 5.2% (156 / 3000 packets have been missed) which is comparable to the packet loss rates of RF-based triggering. Visible in figure 4.23 on the right hand side, the packet loss rate increases with rising distance. The reason for this is that the signal-to-noise ratio is strongly influenced by the magnetic field which drops with $\frac{1}{d^6}$. The bit rate of correctly received values is 87.58%, the left hand signal plot of figure 4.23 depicts for each value the fraction of the different bit errors.

More of concern is the increasing number of lost packets, wrongly detected transmitter ids could be changed on the processing side which has knowledge about the triggering sequence.

Technical connectivity details The reason for the magnetic field-based synchronization and transmitter information encoding is to provide an accurate synchronization and information

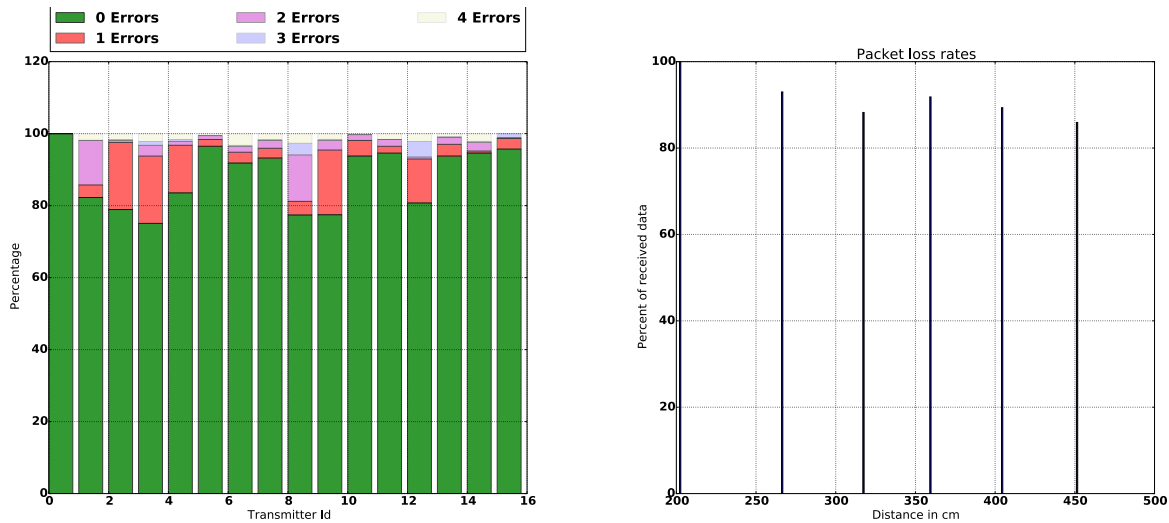


Figure 4.23: Combined Distance error rates for distances between 40cm to 451cm. Measurements have been stationary performed. 87.58 percent of the values have been correctly recognized. The packet loss rate increases with rising distance.

distribution mechanism. Until now we have not addressed the underlying transmitter control mechanism: For larger-scale setups, especially in industrial environments, RF communication needs additional measures to work and to reduce the packet loss rates (for example acknowledgment messages). Also making the system more reliable, these measures introduce extra time- and bandwidth burden. To avoid this, we trigger the transmitters using an Ethernet-based UDP¹ communication. Each transmitter is equipped with an Ethernet module and receives UDP trigger messages. After reception of a trigger message, the node begins with the magnetic field-based synchronization and data transfer as previously described.

Improvements of the signal-to-noise ratio During the synchronization and data transfer using the magnetic field, the receiver has to detect signal transitions and the lengths of the pulses. The coil architecture influences the overall magnetic field layout and therefore, the magnetic flux density is not evenly distributed. The data transfer using a single coil is therefore in some positions around the transmitter not always supported in its best way:

Depicted in figure 4.24 is the signal trajectory of two perpendicular cube shaped transmitter axes. The signals follow a sinusoidal trajectory and hold a phase shift. If a single transmitter axis is used for data transmission, the signal-to-noise ratio during data transfer strongly depends on the position around the transmitter. In order to reduce this effect, the header of the measurement frame is modulated on the transmitter axis which bears the highest magnetic field magnitude at the receiver side position. To achieve this, the estimated receiver position is taken into account to determine the relative angle against the transmitter. This angle is then used to determine the axis with the highest possible magnetic field at the receiver position. If several receivers

¹UDP has been chosen because compared to TCP UDP requires fewer resources and processing time to maintain communication. For real-time applications typically UDP is chosen.

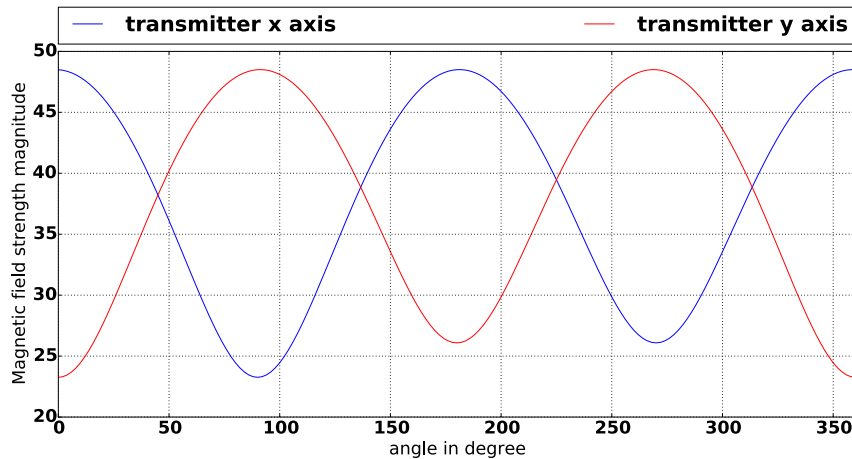


Figure 4.24: Magnetic field magnitudes of two perpendicular transmitter axes with regard around the transmitter coil. Clearly visible is a sinusoidal signal trajectory and a phase shift when comparing the two transmitter axes.

are within the transmitter's range, the receiver with the highest distance is considered as the magnetic flux density is lowest for this receiver.

4.7.3 Data Transfer in a quasi-static Magnetic Field

The magnetic field as information carrier has been proposed in [JFY⁺14]. The authors use a magnetic field to transfer data at short range between a transmitter coil and an IC-based magnetometer of a mobile phone. The magnetometer of cell phones usually supports a sampling rate below 100 Hz and is based on the so-called Hall effect. Hall effect-based sensors tend to be sensitive to strong magnetic fields with a low oscillation frequency. For higher frequencies, AMR-based sensors or magneto-inductive coils are typically used. In this chapter we show how to use low-frequency magnetic fields to detect regions of interests with a mobile phone or a wearable smartwatch, using their compasses over a longer range than 1cm (as in [JFY⁺14]). Additionally, data transmission and encoding in the magnetic field at higher frequencies (e.g. around 20kHz) with coil-based sensors are evaluated and combined with our magnetic field localization system to support a logistics scenario. The following part has been presented at the Body area networks conference 2015 ([PHCL15]).

Introduction

Many localization tasks do not require absolute coordinates; it is sufficient to gather proximity information. Regarding context and ubiquitous computing, proximity can be seen as part of the standard data vector. Due to the high availability of smart devices, for example, smartphones or smartwatches, we want to evaluate possibilities to detect proximity with these items. For a mobile consumer device and their users, location can in most cases be an identification of a room part such as a table, a drawer, a position in a shelf or a specific table, absolute coordinates

are typically not used which reduces the complexity of the localization system. Broadly used are in current days Bluetooth 4.0 (BLE) Beacons which can be seen as current state of the art in proximity detection. While the detailed accuracy of such systems depends on the specific setup and the environment, it is in general well above 1 m and thus unsuitable for higher precision applications as distinguishing between neighboring desks or doors, detecting which shelf someone is reaching for, or tracing hand positions when browsing through a rack of clothes.

We saw in the previous sections that magnetic fields could also be the information carrier. The magnetic field in this application has a much lower frequency (0 to 10 Hz) compared to the frequency of the oscillating magnetic field localization system as the fields are detected with the **integrated IC-based earth magnetic field sensors of the smart devices**. The described approach allows a generation of a **spatially limited magnetic field** with a maximum detectable range of 30 to 50 cm. Due to the simplicity of the hardware, proximity information can be easily integrated in the environment and therefore can be broadly used due to the high availability of smart devices with integrated magnetometers..

We discuss different physical modalities in section 2.3 about their deficiencies in indoor environment. Especially Bluetooth beacons, using RF waves, have a limited spatial resolution. Considering the behavior of RF waves - especially in the 2.5 GHz frequency spectrum - has several disadvantages:

- The RF signal is strongly influenced by human bodies; the signal amplitude is attenuated because the energy is absorbed by the flesh.
- Signal scattering resulting in a defraction of the RF signal.

Low-frequency magnetic fields in contrast to RF waves, permeate the human body almost without any influence, furniture and other appliances have either no or hardly any effect. Metal objects locally affect the magnetic field, but the influence of this eddy fields are locally limited and are distance dependent: the higher the distance, the lower the influence of the metal object. The density of the magnetic field is easily controllable by the current applied to the transmitter coil.

We want to examine how magnetic fields perform in typical close to reality applications. The goal is to benchmark the estimation of the system in different environments, see the limits of the system with regard to the limited range and how to apply well-known principles of magnetic field-based information transfer as we described them in the previous parts in the field of proximity detection.

Related Work

In this section, we want to give an overview of smart devices related influences in this research field. We already gave an overview of indoor localization system in section 2. Regarding the current chapter, smart devices with integrated sensor systems related works are of main concern (for example [DCC12]). Mainly WIFI-based systems [RS01], Bluetooth beacons [ZXM⁺14] and

4 Physical Layer

inertial sensors [LZD⁺12] are considered. Also, the fusion of these systems has been broadly examined [EM06]. Yet, these approaches are currently not able to achieve a proximity resolution of 30 to 50cm. The main problem is the inhomogeneity of the environment with the influence of furniture and persons on the RF signal propagation.

Considering magnetic field-based work, several approaches have been presented in research. The works cover magnetic field-based object tracking, positioning and proximity detection. Still, most of this work can hardly be applied to smartwatches and smartphones. Among others, passive tags are considered in [PHB01], different research topics cover passive RFID tags (currently no mobile phone comes with built-in RFID tag readers, not mentioning the smartwatch market) for example in [BDS08], [PFKP05], or position estimation system based on quasi-static magnetic fields [PH04] or oscillating magnetic fields as ours. In contrast to our magnetic field localization system (which uses 20kHz oscillations and therefore the smart devices cannot sense these fields), we apply an ultra low frequency to the transmitter coil and focus mainly on the data transmission part here. Additionally, using of-the-shelf hardware (both on the receiver and the transmitter side) reduce the costs of the systems.

For example in [JLC⁺12] a 125kHz oscillating magnetic field is used to detect proximities to given beacon emitters using magneto-inductive coils. The Location-log system described in [ZCC⁺12] is also based on 125kHz magnetic fields. The authors use a special purpose NFC hardware at 125kHz to measure the induced voltage in a receiver coil which is attached to the mobile phone. The external coil allows to measure magnetic fields with lower field strength values but requires more space and is not IC-based. Therefore inductance based techniques are not as widespread as electronic compass sensors which are basically in every smartphone. To retrieve information about objects persons currently interact with, a sensor modality attached to the hand or close to it is necessary. Gloves with integrated sensors (survey of this technology can be found for example in [DSD08]) or skeleton models [MBSS13] allow to gather this information; the additional hardware typically reduces social acceptance of these approaches. Sensor integrated into watch-like devices as in activity trackers or smartwatches are more and more common and therefore a good starting point.

In [PTA06] the fields generated by power lines embedded in walls are used for proximity estimation with special purpose sensors.

Closest to our work are approaches that rely on ambient magnetic flux density distributions for indoor localization as presented in [HK09]. The authors use the magnetic compass sensor attached to a robot to generate a map of the ambient magnetic field. In contrast to our proposed system the authors use the ambient magnetic field and the magnetic field anomalies arose due to disturbances: the accuracy was around 30 cm. The authors of [CDS⁺11] also use the ambient magnetic field to achieve a localization accuracy below 1 m.

Both approaches require elaborate fingerprinting and assume a static magnetic environment, which is a significant practical difference to our system.

On a technical level similar to our approach is the work by Jiang described in [JFY⁺14]. The authors use magnetic fields to transfer data between a computer and a mobile phone using the onboard compass sensor. The system covers data transfer in close range below 1 cm with a data rate of 44 bits per second. Similar range limitation applies to NFC technology included in many

modern smartphones. By contrast, we consider proximity detection on the range of 50 cm.

System Design and Implementation

Our system consists of three components:

an **RF-based iBeacon** for rough proximity detection to reduce the overall power consumption of the magnetic field coils,

a **magnetic field coil with attached driving hardware** to modulate the id of the region of interest, and,

a **mobile device** (either smartwatch or mobile phone equipped with a magnetic field sensor) sampling the environmental magnetic field to enable the demodulation of the id of the region of interest embedded in the artificial magnetic field. The iBeacon is not necessary for the overall functionality, the mobile phone app senses for the iBeacons, and starts the modulation state whenever the iBeacon is within close distance. Using iBeacons to distinguish the mBeacon cells helps to reduce the number of bits necessary to address different mBeacon coils which increase the data transfer rates.

Basic Principle The basic idea behind our approach is to mark the important regions of interest with magnetic beacons that are modulated with a region specific ID-code. An iBeacon scanner module in the app periodically checks the environment for known iBeacon ids; the measured RF signal strength triggers the initialization of the magnetic field generator. Using this approach also lowers the energy consumption on the mobile device side because the magnetic field compass has to be sampled only when the mBeacon is possibly in range. Whenever the user's phone or smartwatch comes within range of the magnetic field, it receives and recognizes the code. The range is determined by the peak density of the magnetic field $\mathbf{B}(d)$ and its density drops as the distance to the coil drops. (See section 5.4 for the overall physical background, the magnetic flux density follows the law of Biot Savart).

The design space of our system is given by the limitations of the magnetic field sensors incorporated in mobile consumer devices such as smartphones and smartwatches (e.g. compass sensor AKM AK8963). Typically, such sensors have a sampling rate of 10-20Hz and a measurement range between $\pm 1mT$ and $\pm 5mT$. The base signal that they continuously detect is the earth magnetic field ($30\mu T$ at the equator, $49\mu T$ in Europe).

To investigate the magnetic field behavior, we implemented a magnetic field FEM model as presented in the later chapters. We do so to determine the number of windings, the applied current, and the shape of the transmitter coil. This allows determining the maximum range with a given coil structure.

Hardware From the above considerations, the magnetic beacon utilizes a rectangular $40cm \times 30cm$ coil with 20 windings, which can be easily integrated into the environment. As magnetic fields permeate most materials, the coils can be hidden for example under a table, behind a

cupboard or within a door frame. The coil is driven by a current limited power supply which can deliver a peak current of about 4A at 15V.

Figure 4.27 depicts the field strength trajectory of a frame-shaped coil with $40 \times 30cm$ area to which a current of $I=4A$ is applied². Using this approach also assures that the generated magnetic field is not overdriving the compass sensors.

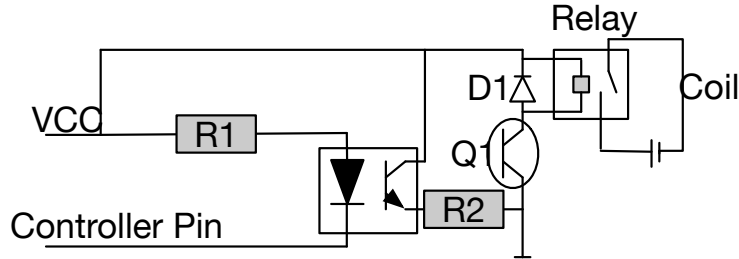


Figure 4.25: Schematics of the used coil driving circuit.

The current is modulated by a simple relay (or an appropriate transistor) controlled by a micro-controller. In our experiments, we use an off the shelf power supply (Grauppner 6458), a Sngle SRD-05vdc relay and an Arduino micro-controller board. The total cost of the components as we bought them is 75 Euro. We also implemented a four channel opto-relay-based system which ranges in the price interval of 20 euros. Note that although the peak power consumption is 60W since the system is not transmitting the whole time, the average value is close to 20W. To further reduce the power consumption we use Bluetooth beacons to determine when the user is in the rough proximity and only then switch on the magnetic beacon.

Mobile Device Detection Method The ID-code is modulated in the magnetic field using pulse width modulation (PWM). Taking the sampling rate of compass sensors of smartwatches and mobile phones into account, the minimum length of a magnetic field pulse should be around 150 ms. Notice that this interval also covers the transient oscillation of the coil. The modulated values are a multiple of the minimum pulse length ($l = n \times 150ms$).

The magnetic flux density is sampled using the on board Hall effect-based compass sensors of mobile phones and smartwatches. In our case, these were the Nexus 5 and One Plus One cell phone (compass sensor AKM AK8963) running under Android 5.0.1 and 4.4. Both phones supported a sampling rate of 17 Hz, for initial test the measurement vector $\mathbf{B}(x) = (m_x, m_y, m_z)$ was transferred to a computer using Wifi communication. The used smartwatch was the LG Watch R with similar performance. For the experiments, the processing sequence (as described in figure 4.28) was implemented on the watch and the phones.

We transform the measurement vectors \mathbf{B}_i into squared vector magnitudes, which automatically weights measurements with higher axis field strength (compared to the earth magnetic field

²Due to the temperature rise, the resistance of the coil increases, the applied current drops from 3.6A to 3.3A depending on the used coil at a voltage of 15 V.

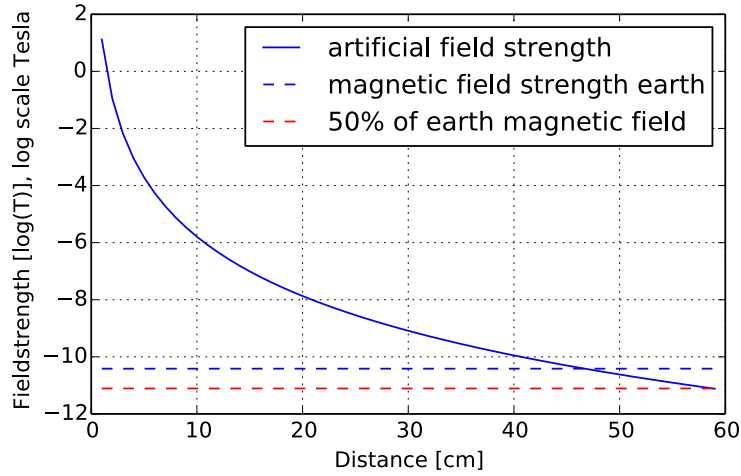


Figure 4.26: Theoretical field strength trajectory along the norm vector of the coil plain perpendicular to the diagonal intersection with distance d to the plain. Notice the logarithmic scale. It also includes the level of the earth magnetic field strength in Europe. The intersection of earth field strength level and the trajectory is seen as maximum range. (Model values: $N=20$, $a = 0.3\text{m}$, $b=0.4\text{m}$, $I = 5\text{A}$, frame shaped coil)

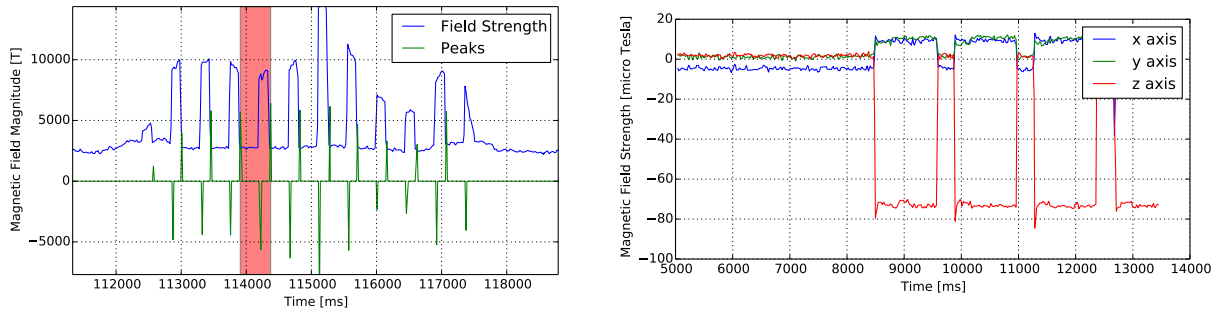


Figure 4.27: Left: Squared magnetic flux density with modulated coil id. The green peaks indicate the edges of the artificial magnetic fields. Right: Superposition of earth magnetic field and artificial magnetic field measured with a mobile phone.

vectors). The first order derivate of this parameter gives a good indication of the presence of artificial magnetic sources as the activation and deactivation process of the coil results in sharp edges. To suppress signal changes of the environmental magnetic field caused by movements, a median sliding window is applied to the sensor values. A peak detector finds the exact time when the coil is turned on and off. After detecting the length of the applied artificial field, we can use the direction change of the magnetic field vector to determine which side of the coil the sensor is. Therefore we compute at first the median environmental magnetic field density before the signal was applied. Then the difference of these two vectors is calculated. The sign of the largest component of the difference vector defines the side of the coil. The entire detection runs on the mobile device.

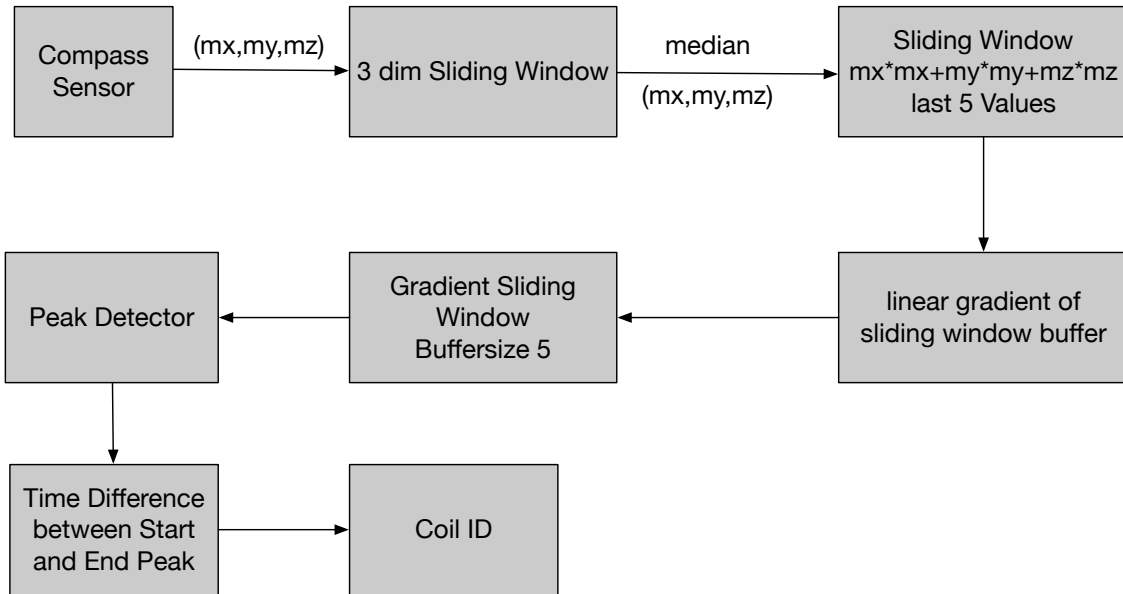


Figure 4.28: Processing sequence on the mobile device (smartwatch or cell phone).

Experiments

We evaluated our system in 5 different use cases in semi-naturalistic lab experiments inspired by different application domains (Figure 4.30). The first two (Figure 4.30 B) and D)) are motivated by a task tracking scenario where the top level task is determined by the table region at which a student is sitting while the individual steps involve interaction with devices placed at different regions on the table. The third use case (Figure 4.30 A)) is devoted to recognizing with a smartwatch from which shelf of a cabinet an object is taken. It is relevant for a variety of applications, from task tracking through shopping to the recognition of various activities of daily life. Along the same lines, the fourth use case (Figure 4.30 E)) deals with tracking user's hands when browsing through clothes hanging on a clothing rail. Finally, the fifth use case ((Figure 4.30 C)) shows that with the magnetic beacon embedded in the door or the door frame we can detect which door the user is opening with a key, even if the doors are just next to each other.

Workbench Sitting Location We attached four magnetic beacons below two workbenches (Figure 4.30 D)) to identify four different places next to each other where students can work or perform experiments. Each workbench has the dimension of $220\text{ cm} \times 120\text{ cm}$. We split each workbench into two workplaces (each of size $110 \times 120\text{ cm}$). The experiment is motivated by a task tracking scenario where the top level task is determined by the table region at which a student is sitting. While the individual steps involve interaction with devices placed at different regions on the table. Notice that it is a typical hardware workplace which includes machines, metal tools, power supplies and a large anti-static work mat. These influence the AC magnetic field either by reflection, absorption or generate electromagnetic field by itself.



Figure 4.29: Upper left picture: Transmitter coil attached and coiling frame to easily create a coil. Lower left picture: transmitter coil attached to metal door, right picture: Rack with four transmitter coils, the current of each coil has been tuned so that the magnetic fields do not influence each other.

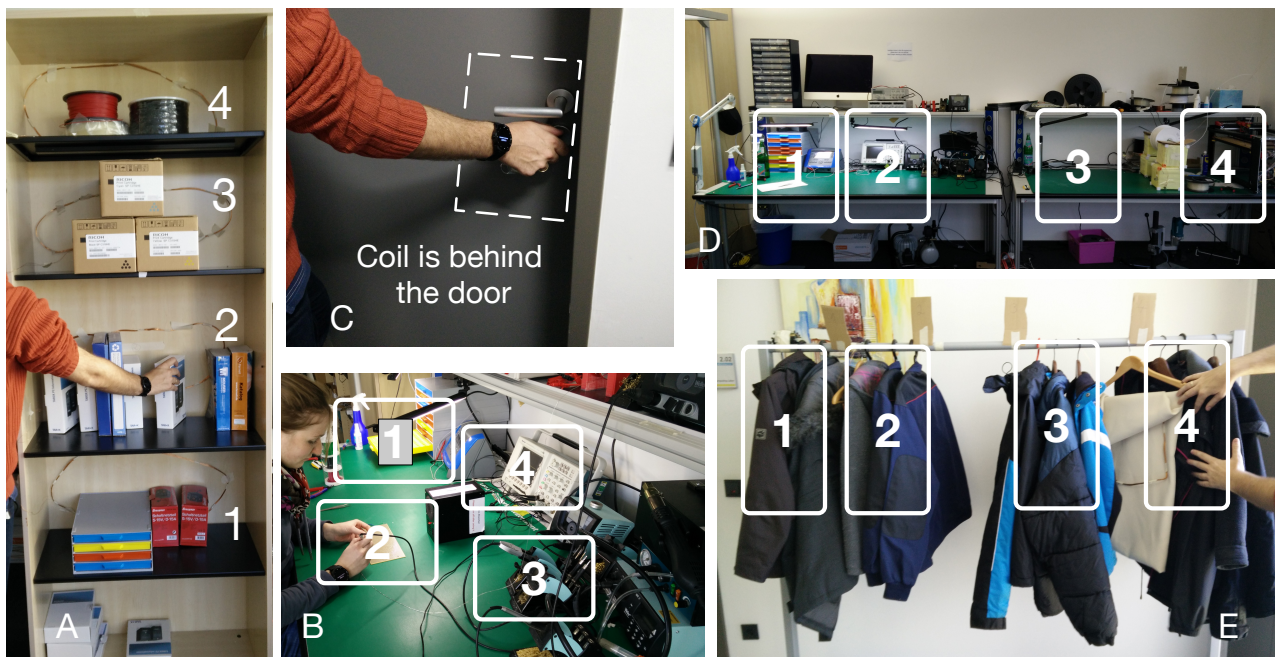


Figure 4.30: Different experimental setups. A) Picking equipment from different shelves B) A soldering task with different areas on the desk. C) Distinguishing between different doors. D) Estimating the position of a person at desks E) Finding a specific winter jacket at a cloth rail.

The experiments involved five student volunteers. Each subject was asked to sit down at one of the locations and perform a task of their choice for 10 seconds. This was repeated 15 times with a random selection of the four locations.

Interaction with Workbench Regions in a Soldering Task The workbench (Figure 4.30 B)) has been equipped with four coils, each coil covering a specific object or region which is used in a soldering task. The subjects were asked to solder a surface mounted device (SMD) resistor to a printed circuit board (PCB). This involves 1) placing a PCB on the workbench at location 2, 2) finding a specific resistor in the resistor set placed at position 3, 3) reaching for the soldering iron and changing the tip from big tip to small tip at location 1, and 4) adjust the multimeter to check the resistor value and test if the two contacts are connected at location (taking place at location 4). Five students volunteers wearing an LG Watch R smartwatch each performed the above tasks five times with no constraints except the above-described positions. The activities/positions were labeled manually by an observer. For the recognition algorithm, the wrist-worn smartwatch is of high importance as it retrieves the magnetic field information close to the hand. A drawback is that the hand typically moves fast from one location to the other and therefore either magnetic field information is missed or the magnitude the trajectory is mutilated resulting in invalid information.

4.7 Transmitter-Receiver Synchronization

| Id | Locations | | Cabinet Shelves | | Cloth Rail | | Opening Doors | | Work Bench, Soldering | | | |
|----|-----------|-------|-----------------|-------|------------|-------|---------------|-------|-----------------------|-------|------------------------------|---------------|
| | FbF | Event | FbF | Event | FbF | Event | FbF | Event | FbF | Event | Events longer than 3 Seconds | missed Events |
| 1 | 99.64 | 100 | 99.6 | 100 | 76.3 | 82.7 | 98.9 | 100 | 99.09 | 100 | 100 | 0 of 12 |
| 2 | 95.22 | 100 | 99.8 | 100 | 94.5 | 100 | 99.5 | 100 | 72.4 | 75 | 100 | 3 of 12 |
| 3 | 94.12 | 95.45 | 100 | 100 | 96.3 | 100 | | | 83.3 | 85 | 100 | 1 of 7 |
| 4 | 92.25 | 100 | 99.37 | 100 | 72.3 | 84.2 | | | 41.33 | 43 | 100 | 4 of 7 |

Table 4.2: Results of the different experiments. FbF - Frame by Frame. Notice that in the location experiment, there is one event in id 3 where a bluetooth burst disturbed the timing and therefore the length of the artificial magnetic field readings couldn't be correctly be determined.

Taking Objects from Cabinet Shelves A cabinet with four metal shelves (Figure 4.30 A)) was equipped with four magnetic beacons (one for each shelf). Initially, we planned to attach the coils below the metal shelves of the cabinet but the magnetic field was misshaped, and measurements were hardly possible. We, therefore, moved the coils to the back side of the shelves, superposition of the magnetic fields were reduced by lowering the applied current of the different shelves. This scenario also shows the advantage of magnetic fields; it is possible to adjust the applied current so that the magnetic field of a single coil only covers the corresponding bookshelf and does not influence the neighboring compartments. We randomly chose the shelf number and 4 subjects wearing an LG Watch R smartwatch were asked to reach for it. Each person reached 20 times for a randomly chosen shelf.

Cloth Rail We attached two coils to a 120 cm cloth rail (Figure 4.30 E)) and thus segmented the rail into four sections (on the left end right sides of the coils). 11 winter jackets were distributed randomly between the four sections. 5 participants were then asked to browse through the jackets checking the price (attached to the inner side of the jacket). An observer manually annotated when which participant was browsing through which section of the rail.

Opening doors In this scenario (Figure 4.30 C)) we attach two coils at two opposing doors that are 1.0 m apart. Within such a tight spacing, standard indoor location algorithms have very often problems in deciding in front of which door a person is standing. In the experiment one door is surrounded by a metal frame, another door opens into a meeting room which is surrounded by metal frames (Resulting in anomalies of the natural environmental earth magnetic field). Two subjects were asked to open a door 20 times. In each instance, the door is randomly chosen.

Health Considerations

As the system can be used in real-world applications, we also consider the influence of the magnetic field on the environment. According to measurements with the mobile phone, the maximum field density is 0.0012 T (1.2mT). The guidelines for electromagnetic fields (see [ABB⁺98] for details) limit the magnetic field strength to $800\mu T$ for a frequency of $7Hz$ (the duty cycle is 150 ms for a bit, therefore less than $7Hz$ is assumed for the field frequency) for general public

4 Physical Layer

exposure, occupational exposure is at $4081\mu T$. The magnetic field drops with $\frac{1}{d^3}$, therefore it is sufficient to place the coil in a box to prevent persons from touching the coil but still support magnetic field measurements. Figure 4.27 (right) depicts the influence of the generated artificial magnetic field of the transmitter coil at a distance of around 30 cm. The superposition results in a field strength of roughly $75\mu T$ which is in the safe field strength interval.

Results

All of the experiments were evaluated on frame by frame and event basis. Frame by frame evaluation refers to every single cycle in which the mobile device tries to decode an ID. Event evaluation was based on the majority of IDs recognized within the window labeled as belonging to a certain location.

As it can be seen in table 4.2 with three exceptions the frame by frame results are well over 90% and the event-based results are 100% correct. The first exception is the areas 2,3, and 4 of the workbench soldering experiment. The errors concern instances where the hand quickly reaches for an object without remaining in the area long enough for the ID to be correctly recognized. If we constrain the evaluation to events that are longer than 3 s then 100% are correct. The second exception is the first and last region in the clothes rail experiment. The errors occur when the user's hand is closer to the massive metal vertical rail than to the mBeacon. In those cases the ID is correctly recognized, however, the algorithm for recognizing which side of the coil the hand is on fails and returns the wrong side. Further improvements in the orientation algorithm are needed to address this problem. The third exception is class 3 in the workbench sitting experiment. Here the error is due to timing problems resulting caused by the task manager on the phone; the magnetic sensor readout is randomly interrupted by the mobile phone scheduler resulting in missing sensor values.

Conclusion

In this paper, we have shown that inexpensive and unobtrusive magnetic beacons allow mobile consumer devices such as smartwatches and smartphone to detect proximity to predefined regions of interest within a range that lies between Bluetooth beacons (in general more than $1m^2$ range) and standard NFC (a few centimeters). Key limitations are the temporal resolution and the power consumption of the beacons. Both are related to limits of the sampling frequency of the smartphone magnetic sensors (with higher temporal resolution shorter pulses are possible resulting in a lower power consumption). Future work needs to address intelligent power management of the mBeacons (e.g. synchronization with motion sensors of the mobile devices), more elaborate analysis of the orientation algorithms and investigation of more drivers coil setups (e.g. using more windings to reduce the current).

We developed a four channel mBeacon system, controlled by a microcontroller with integrated mBeacon system.

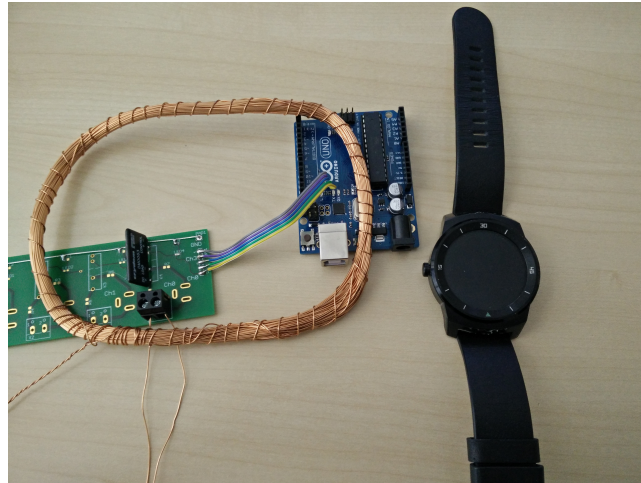


Figure 4.31: mBeacon base board with attached magnetic field coil. The micro-controller manages the information encoding in the magnetic field.

4.8 Conclusion

We presented in this chapter methods, algorithms, and approaches which utilize knowledge about the physical behavior of magnetic fields to provide a stable signal encoding of the generated magnetic field at the receiver side the position even at high distances. This part covers the synchronization of the components, transmitter, and receivers, either using RF communication or by encoding synchronization and transmitter id information in the generated magnetic field. Additionally, the signal gathering sequence on the receiver side has been described, and different signal encoding approaches have been evaluated with regard to signal stability, range (up to 4.5m) and the possibilities of implementation of a microcontroller with limited resources. The signal encoding uses the repeating nature of oscillating magnetic fields to distinguish artificial magnetic field signals from noises by applying a correlation approach. The result of this layer is signal encoding of the induced voltages of the three transmitter coils on the three receiver coil axes. This information is the input for the single coil position and distance estimation layer presented in the next chapter.

5 Signal to Position / Distance Estimation

The previous chapter presented a low-level architecture for a stable magnetic field representation up to a distance of 4.5m. Transferring the encoded magnetic field values of the three transmitter axes to a central processing unit allows more sophisticated transformation approaches than would be possible on the micro-controller side. Compared to ultrasound or other signal-runtime-based time-of-flight systems which solely rely on a linear signal dependency, magnetic field signal behavior-based localization or even just distance estimations between the transmitter and the receiver are more complicated to calculate: According to the law of Biot Savart, a wire generates a magnetic field if a current is applied. Multiple wires, as in coils, thus result in superposed magnetic fields, each of the wire components creates a fraction of the field. Typically, there is no analytic form for the generated magnetic field in the space around the coil. The reverse approach of estimating the exact position of a magnetic field value is even more complicated: In most coil setups the generated magnetic field is inhomogeneous; this means that if a receiver coil is rotated around a transmitter coil with fixed distance, the induced voltage trajectory follows a close-to-sinusoidal shaped function (We neglect that due to the movements additional voltage is induced). So for a single transmitter coil, multiple positions are possible solutions for a given magnetic field magnitude. A combination of three perpendicular transmitter coils, as implemented by our localization system reduces the possible points of residence to the points around the emitter coil which is equal to the measured field strength values of all three transmitter coils. Several issues have to be considered to retrieve the set of candidate positions defined by the measured voltage value tuples:

- , A **magnetic field model**, which allows retrieving the corresponding candidate set for a given measurement tuple by using information derived from magnetic fields of the three axes coil architecture.
- A method of how to **overcome hardware related tolerances on transmitter and receiver sides** to reduce the overall memory consumption and to avoid approaches comparable to fingerprinting. This relates to an approach which scales and shifts the signal intervals of the transmitters to a **common theoretical signal level**.
- An **efficient data structure for position and distance estimation** of multiple receivers against an emitter coil which can be used in different environments without the need for additional calibration.

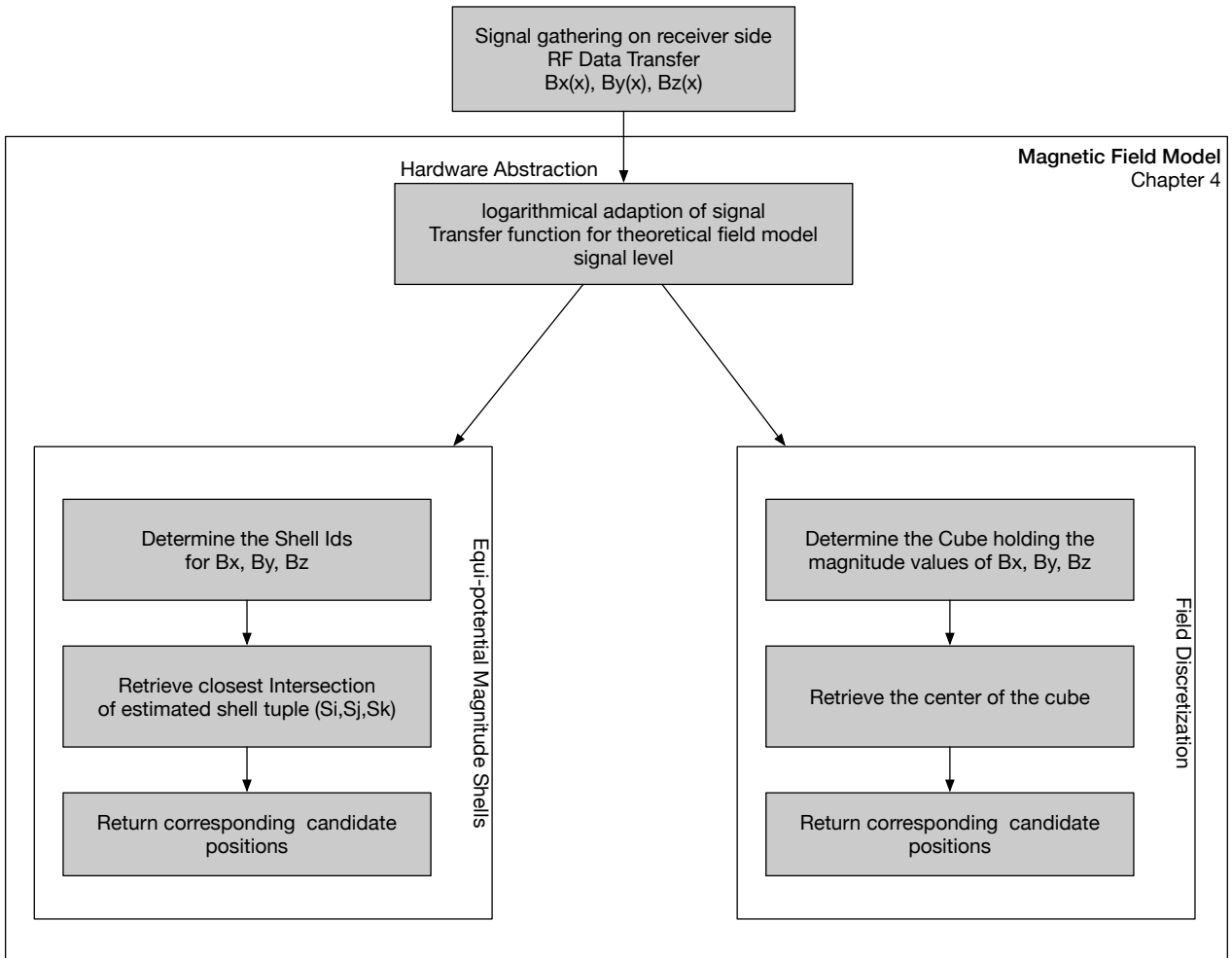


Figure 5.1: Sequence diagram of the position estimation using two different magnetic field model approaches.

5.1 Contributions

We describe in this chapter the **position estimation sequence to transform the raw magnetic field measurements into positions and distances** relative to the transmitter coil. Fundamental for the single coil position estimation is the availability of a **magnetic field model** describing the field behavior of different transmitter coil architectures, for example, the cube-shaped transmitter coil or the spherical shaped coil structure. Due to the high processing complexity and the lack of an analytical model describing the magnetic field, a pre-calculated **FEM model** has been implemented. **Transmitter precise calibration- and transfer-functions** scale and shift the raw signals to the signal level of the magnetic field model. The variables and parameters are determined in a **calibration step** by comparing the raw signal values of the receiver’s 3D coordinates to corresponding positions in the theoretical field model. Another issue addressed in this chapter is the **organization of the magnetic field model to support a robust and fast position and distance estimation**. Different approaches

have been evaluated concerning accuracy. This covers the **intersection of magnetic field magnitude shells** and the **3D space division by cubes**. The position estimation approaches are evaluated for both transmitter coil architectures. The mean position error for the cube shaped transmitter in a sphere with radius 4.5m is 117 cm, the average distance error is -2.3cm, for the spherical transmitters it is 70cm and 4cm.

5.2 Reference Measurements for the Magnetic Field Model and Calibration

As described, the shape of the magnetic field and specifically the field strength density values at their positions vary due to the manufacturing process and hardware related tolerances. Also, the receiver sensitivities sharply differ from coil to coil. We, therefore, perform a calibration process to scale and shift measured magnetic field values to the levels of the corresponding theoretical field values. The calibration process uses the camera-based OptiTrack motion tracking system to estimate the position and bearing of both transmitter and the receiver. Therefore infrared reflective markers are attached to the transmitter and the receiver. Eight cameras capture different sections of the calibration area. We carefully orient the various cameras of the system to cover each point of the calibration area by at least two cameras. This is necessary to estimate the 3D position of the markers.

After the required calibration process of the system, OptiTrack provides an accuracy below one centimeter and a sampling rate of 120 Hz in the monitored measurement area. The estimated raw positions of the markers are sent to the magnetic field system to be merged with the magnetic field measurements during the calibration process.

Data Recording Due to the limited visual range of the tracking system and to improve the stability of the optical position estimation, the calibration does not cover the complete magnetic field area, the transmitters are placed on a rotational table, and the data is gathered along rectangular sectors around the transmitter coil ($2\text{ m} \times 5.5\text{ m} \times 1.8\text{ m}$). We slowly walk in the specified recording area and record the corresponding coordinate / bearing information / magnetic field information. Also, different heights are taken into account. After 800 measurements, the transmitter coil is rotated around its z coordinate axis in 45-degree steps. This approach records at least 6000 data points (for each transmitter/receiver pair) for further processing. The schematic overview and an example of the recorded positions is given in figure 5.2.

Calibration Pre-processing

In a pre-processing step, the raw coordinates of the transmitter and receiver positions in the OptiTrack coordinate system are transformed to coordinates relative to the transmitter. This also takes the calibration sector into account. Figure 5.2 (right) depicts a complete point cloud of a processed calibration sequence of a single coil. The result is a set of coordinate/field

5 Signal to Position / Distance Estimation

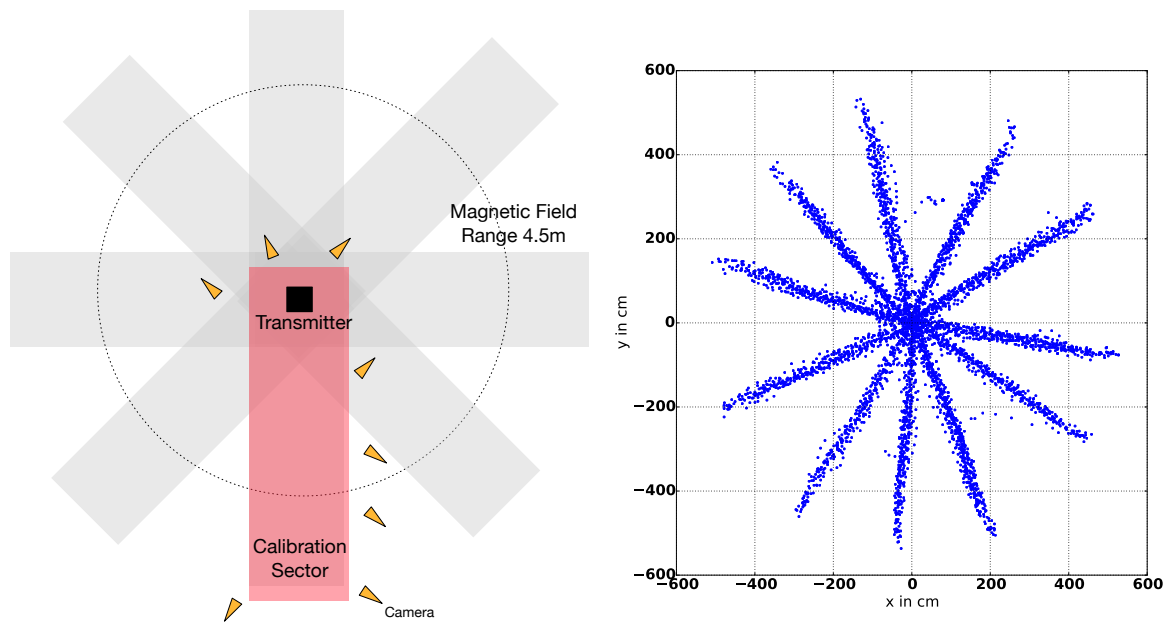


Figure 5.2: Schematic diagram of the calibration process and the positions of the camera, the red area indicates the tracking area covered by the optical tracking system. On the right hand side is a picture of the recorded positions from bird eyes view.

strength representation tuples describing the magnetic field. This information is then used to estimate transfer functions and to define values necessary for the magnetic field model and on-line position estimation steps.

5.3 Calibration and Common Signal Level

The first step of the position estimation is to shift and scale the measured raw voltages to the theoretical model values. A magnetic field model which is accurately estimated, meaning that all influences are modeled, allows transforming the measurement values with a low degree polynomial function (ideally a linear influence).

The transfer function has to adapt model values which were not part of the theoretical magnetic field model calculation, as the magnetic field permeability μ of the formula of Biot Savart or the frequency dependency of the voltage or the area of the receiver side coils as it is defined by the Law of Faraday. It also covers the sensitivities on the receiver side axes and the hardware related power output values on the transmitter side.

For the **cube-shaped transmitter** the calibration process has been previously described, figure 5.2 shows the positions which have been recorded with the cube shaped transmitter coil at 5000 different positions around the transmitter coil. The recording has to provide a set of measurement and 3D coordinate tuples. The 3D position is then used to retrieve the corresponding theoretical magnetic field model values.

Derived from [MTEM10], we use a logarithmic transformation approach:

In an initial step, we transform both the real world measurements and the corresponding model values to vector magnitudes for each transmitter axis measurement: Let $\mathcal{M} = ((v_x, v_y, v_z)_{t_x}, (v_x, v_y, v_z)_{t_y}, (v_x, v_y, v_z)_{t_z})$ be a measurement tuple of the induced voltage representation v_i of the receiver axes for transmitter axes t_i . Let $m_i = \sqrt{(v_x^2 + v_y^2 + v_z^2)}$ be the magnitude value of a transmitter axes measurement. Let M_i be the maximum value measured for this transmitter axes.

$$l_i = \log\left(\frac{m_i}{M_i}\right) \quad (5.1)$$

The transfer function \mathcal{P}_i , transforming the measurement (m_x, m_y, m_z) of transmitter axis i into the theoretical magnetic field magnitude, is a polynomial function:

$$t_i = \mathcal{P}_i^3(m_i) = a * l_i^3 + b * l_i^2 + c * l_i + d \quad (5.2)$$

The values of the polynomial function are estimated using a least square minimization approach and the calibration data set. The mean error of the scaled and shifted measurement values and the corresponding model magnitude values lie between -2.03 and +1.66 percent with a standard deviation between 8.15 and 11.06 percent points. These high variations occur due to the crosstalk between the excited transmitter axis and the two muted ones. This effect has not been modeled. Thus the created magnetic field shows a different behavior than modeled.

We also examined the distance error distributions. The results are given in picture ?? The approximation error is in most measurement points within a 10 percent interval; the mean error

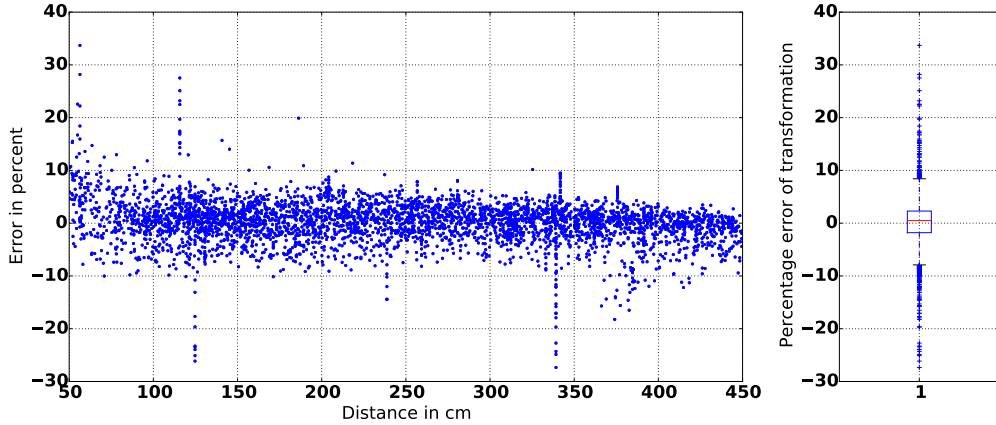


Figure 5.3: Distribution of the approximation error of the transfer function with regard to distance intervals.

is for all transmitters centered around 0.0, with a standard deviation between 4.2 to 4.6 percent points.

Cross talk model In chapter 4.3.2 we discussed the behavior of different coil architectures with regard to crosstalk and induced voltage on nonactive transmitter coils. The cross talk between the axes influences the generated magnetic field, as the two non-active coils produce noisy magnetic fields, superposing the desired magnetic field. This results in big differences of the modeled values with the measured values of the three transmitter axes.

We want to evaluate the possibility to describe the effects of the crosstalks by a linear combination of the axes' theoretical magnetic field magnitude values (t_x, t_y, t_z) at the estimated position: The theoretical magnetic field magnitude value derived from the linear combination is called t'_i :

$$t'_i = r_i \times t_x + p_i \times t_y + q_i \times t_z \quad (5.3)$$

Using again the Levenberg Marquardt least square minimization approach, we aim to evaluate for the calibration data set the polynomial coefficients and the "mixing values" (r_i, p_i, q_i) to be able to calculate the equation:

$$\mathcal{P}_i^3(l_i) = a * l_i^3 + b * l_i^2 + c * l_i + d = t'_i \quad (5.4)$$

The drawback of this approach is, that for each transmitter a separate model has to be calculated as the crosstalk of the transmitters differs and yet the results are still not satisfying.

The estimated transfer functions for the cube shaped coil (eq. 5.2) are used to adjust the raw measurement values of the receiver side coil to the signal level of the theoretical magnetic field model. As the mixing approach does not improve the approximation results (comparable error distribution and standard deviations), we neglect this and calculate for each transmitter-receiver combination the three transfer functions $(\mathcal{P}_z^3, \mathcal{P}_y^3, \mathcal{P}_x^3)$ as previously described.

Calibration and Signal Adaption of a Spherical Coil

In contrast to the cube-shaped transmitter coil, the spherical coil architecture showed a crosstalk twice as low as the cube coil. The sphere shaped coil body allows to lower the width of each transmitter axis and therefore the contact surface between the emitter coils. Doing so, the crosstalk is reduced from $u_{cross}^{cube} = 124V$ to $u_{cross}^{sphere} = 48V$. This also reduces the influence of magnetic fields of these axes.

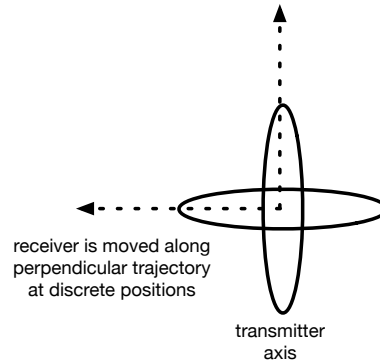


Figure 5.4: For all three transmitter axes, the receiver is moved along the norm vector of the coil plain. For a discrete set of positions, the measured magnetic field induced voltages are recorded and processed.

In contrast to the cube-shaped coil, which has corners resulting in magnetic flux density dents and therefore the uneven distribution of the density around the transmitter (Figure 5.9), the density of the spherical coil is evenly distributed around the coil axis (Figure 5.6). Thus the calibration process of this sphere is less complex as the angle around the coil can be neglected. For each transmitter axis, we record ten positions and the corresponding magnetic field measurements related to the spherical coil along a line. After data recording we estimate the values of the transfer function $\mathcal{P}_i^3(m_i)$ as described for equation 5.2. Figure 5.5 shows the results of the data recording, the raw value is scaled to overlay the theoretical values.

Due to the lower crosstalk, the magnetic field values are better approximated by the magnetic field model. This results in reduced noise and error on the approximation function side. The coil architecture has to be examined deeper, to reduce the position error in the future, but this is not part of this work.

5 Signal to Position / Distance Estimation

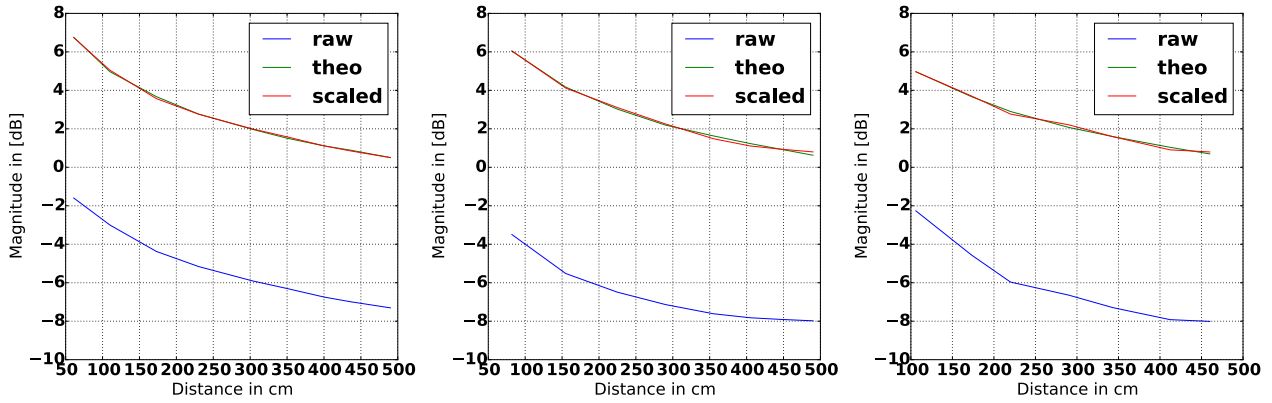


Figure 5.5: Calibration transfer functions for transmitter 8. The measured raw voltages are scaled and shifted to the signal level of the theoretical field model for the corresponding 3D positions.

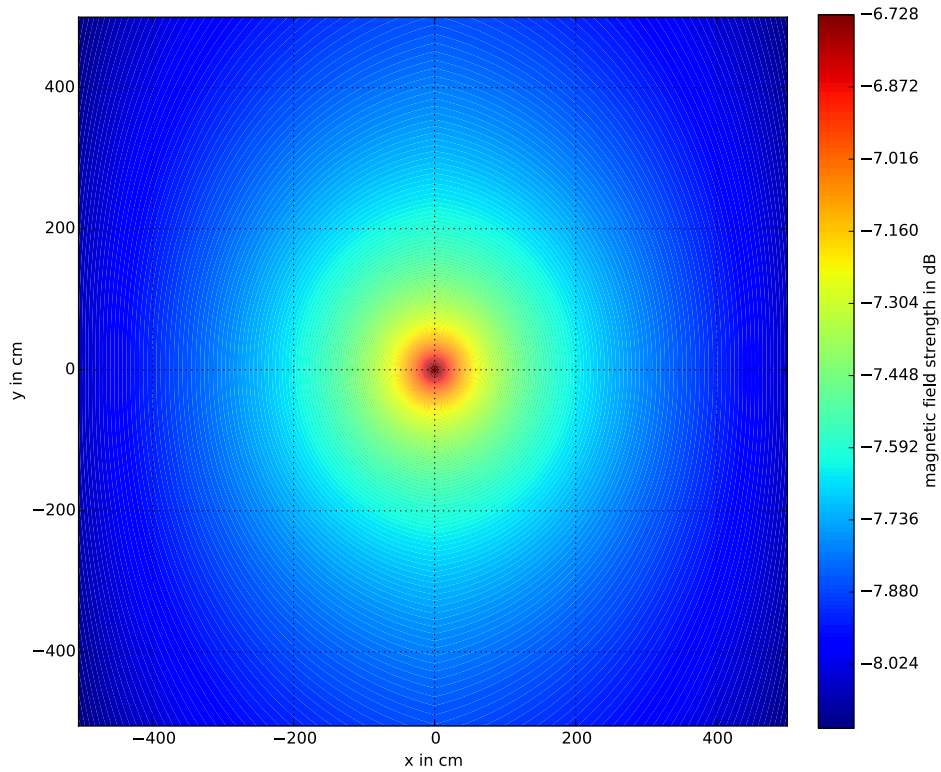


Figure 5.6: Signal distribution at $z=20\text{cm}$ for the spherical shaped coil and spherical shaped coil, both along the z -axis, not involving edges which influence the field density of the coil.

5.4 Theoretical Magnetic Field Model for Position and Distance Estimation

The behavior of magnetic fields is as in contrast to other sources such as ultra sonic-based position estimation approaches, highly nonlinear. The measured induced voltage on the receiver side follows $\frac{1}{d^3}$, it is therefore strongly dependent on the distance. Additionally, the transmitter coil architecture determines the shape of the generated magnetic field. This leads to the problem of inhomogeneity: rotating the receiver around the transmitter with a fixed distance results in different induced voltages as the magnetic field density (field lines) varies.

Thus the magnetic field model has to consider both the linearization of the signal and the inhomogeneity of the magnetic field. Additionally, the field approximation has to be resilient against magnetic field disturbances caused by the environment and measurement noise. Particularly in high distances, noise negatively influences the performance of the system. As we aim to support real-time applications, the model has to provide a fast position and distance estimation with a small memory consumption.

Due to the three axes transmitter coil setup, we describe a magnetic field model which provides position information of the receiver using a single transmitter within the eight octants around the transmitter with a standard deviation of the distance error below 32 cm and a mean position error below 120 cm. Using a spherical shaped coil architecture (and the corresponding magnetic field model), the standard deviation of the distance error is 27cm.

For most positions around the transmitter coil, the magnetic field strength cannot be calculated using analytic methods. A finite element method is applied to estimate the magnetic field generated by the three axes coil of the transmitter at discrete points. As the resulting data set for a $4.5m \times 4.5m \times 4.5m$ cube results in 729000 data points if the magnetic field values are calculated in a 10 cm grid around the coil, it is necessary to organize this data set to reduce the memory needed (For a 5 cm grid the number of tuples rises to above 5 million points). Also, a fast position lookup and an efficient calibration process, which does not require finger printing methods such as in WIFI-based approaches, has to be considered and evaluated. To reduce the magnetic field complexity caused by the number of positions/tuples, positions with similar magnetic field density magnitudes are aggregated. This reduces the sensitivity to measurement noise and variances from the theoretical magnetic field model. Additionally, two different coil architectures have been implemented and evaluated thus the magnetic field model should also support different coils models. Additionally the distance between the transmitter and the receiver can be derived from these candidate positions.

The positions with similar magnetic flux density values of a single coil form a cylindric geometrical volume around the transmitter coil. A transmitter axis magnetic field measurement of the receiver, therefore, is part of a corresponding volume. Taking into account that the receiver measures three emitter coils, this results in 3 volumes which are perpendicular to each other (because the generating magnetic field transmitter axes are also orthogonal to each other). Due to the missing direction of the magnetic field (the receiver circuit implements an absolute function) in combination with the magnitude of the vectors, the measurement of the receiver describes 8

points around the transmitter coil, each point in a different octant. Due to symmetrical effects, all candidate positions \mathbf{c}_i lie on a sphere with radius $d = \|\mathbf{c}_i\|$.

The estimated distance is therefore the distance between the candidate points and the transmitter coil.

5.4.1 Nearest Neighbor Lookup

Initially, we implemented a nearest neighbor lookup mechanism: For each theoretical field model position, we store the magnitude tuples (t_x, t_y, t_z) and its corresponding position in a KD-tree lookup data structure. After applying the calibration function to the raw measurements of the evaluation data set, the transformed magnitude tuple is used to retrieve the corresponding coordinate from the lookup tree. The results of this approach are depicted in figure 5.8. The distance estimation results in a mean error of -2.2 cm with a standard deviation of 35.76, the position error is 321.6 cm with a standard deviation of 184.7. Reducing the number of possible data points in the lookup tree (for example by changing the grid size of the theoretical field model coordinates) does not significantly reduce the position and distance error. Examining

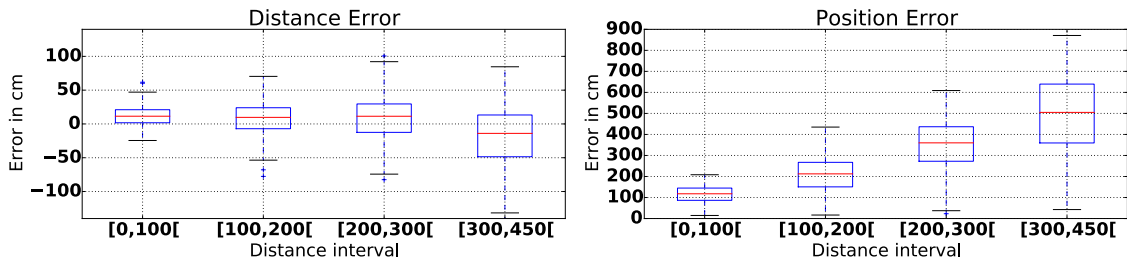


Figure 5.7: Result of naive magnitude lookup approach. Distance- and position errors of 4 different distance intervals around the transmitter. The distance estimation is less prone to errors than positions, although both have higher standard deviation values with rising distances.

the error distribution separated in distance intervals also shows a clear trend: the further away from a measurement point, the higher its position and distance error. The noise of the analog circuit is the main reason for this behavior.

The high error of the position estimation can be explained with the missing model for the transmitter coils crosstalk. The distance estimation takes three values magnitude values into account, outliers in the axes' values of the position estimation result in large coordinate offsets and errors. Figure 5.15 and latter sections discuss this problem more detailed.

5.4.2 Intersection of Equipotential Magnetic Field Shells

A possible way of retrieving the lateration and coordinate information can rely on the magnitude of the measured magnetic field vector at the position of the receiver. The (theoretical) magnitude $\|\mathbf{B}(\mathbf{x}')\|$ relies on the relative distance and orientation. The inhomogeneity of the field is clearly

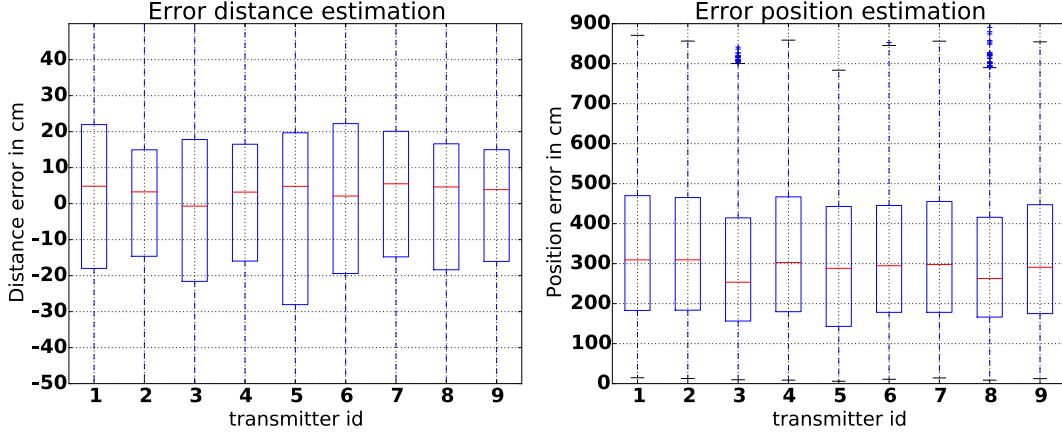


Figure 5.8: kd tree-based magnitude lookup, distance error: ($\mu = -2.26cm, \sigma = 34.77$) the position error is ($\mu = 321.60cm, \sigma = 184.74$). 75 percent of the distance estimation errors lie within an interval of $[-20cm, 20cm]$.

visible: keeping the distance constant and rotating the receiver around the transmitter results in a signal trajectory which is comparable to sinusoidal functions (see figure 4.24). A homogeneous behavior would result in a constant (or close to constant) signal value which is independent of the orientation.

To model this behavior, we combine positions around the transmitter coil which have comparable (theoretical) magnitudes. We, therefore, introduce the so called **equi potential shells**:

Let

$$\mathcal{S}_i^j = \{(x, y, z) \mid \|\mathbf{B}^j(x, y, z)\| \in I_i\} \quad (5.5)$$

be the i -th equipotential shell, a set of 3D positions around the magnetic field transmitter for axis j whose magnetic field density magnitude lies within the i -th magnitude interval. Notice that the shells describing the magnitude of the positions differ from magnetic field lines as field lines include the direction of the magnetic field and therefore have started at a pole and enter the coil at the opposite pole, the shells are an abstraction of the magnetic field density around the magnetic field coil.

The transmitter coil consists of three transmitter axes, thus a receiver side measurement describes the magnetic field density of $\mathbf{B}_x(\mathbf{x}')$, $\mathbf{B}_y(\mathbf{x}')$, $\mathbf{B}_z(\mathbf{x}')$. Thus the measured tuple $(\mathbf{B}_x(\mathbf{x}'), \mathbf{B}_y(\mathbf{x}'), \mathbf{B}_z(\mathbf{x}'))$ is an example of the intersection of three equi potential shells $(\mathcal{S}_x^k, \mathcal{S}_y^l, \mathcal{S}_z^m)$ where

$$\mathbf{B}_x(\mathbf{x}') \in \mathcal{S}_x^k \wedge \mathbf{B}_y(\mathbf{x}') \in \mathcal{S}_y^l \wedge \mathbf{B}_z(\mathbf{x}') \in \mathcal{S}_z^m$$

Figure 5.9 depicts an example of a magnetic equipotential field density shell. The shell is in most intervals hollow. The higher the distance between the shell and the transmitter, the more positions are part of the shell. Each shell can be described by its minimum and maximum magnitude value which allows a low memory consumption.

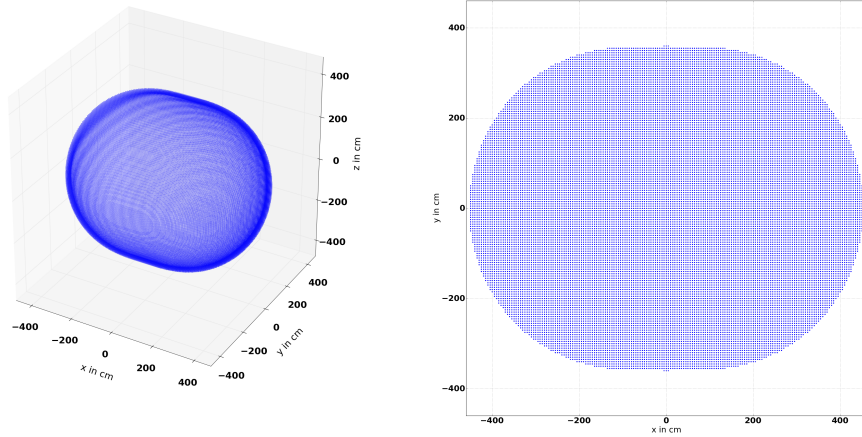


Figure 5.9: Example of an equi potential shell around the transmitter.

As we previously described, a measurement ($\|\mathbf{B}_x(x')\|, \|\mathbf{B}_y(x')\|, \|\mathbf{B}_z(x')\|$) can be linked to the three corresponding equi potential shells. The candidate positions lie in the intersection of

$$\mathcal{S}_x^k \cap \mathcal{S}_y^l \cap \mathcal{S}_z^m \quad (5.6)$$

Typically, the intersection of three shells (point sets) derived from the theoretical magnetic field model does not result in a single 3D position but is described by a volume. We calculate the center of this volume as an intersection representative. The sizes of the shells influence the granularity and position distribution of the intersections. We evaluate different possibilities how to organize the magnetic field model and how to choose the boundaries of the shells.

Magnetic field strength deviation We presented the concept of equipotential shells \mathcal{S}_i which combines a set of 3D positions with similar magnetic flux magnitude values. The field strength magnitude intervals have to be chosen in such a way to separate the 3D positions with regard to the signal falloff. Also, the sensitivity of the receiver circuit should be taken into account.

As neighboring 3D positions have comparable magnetic flux magnitudes, we sort the magnetic flux magnitudes of one axis in ascending order and removed those values occurring multiple times (symmetrical effects of the coils). As the simulation of the transmitter axes has a similar configuration (except the spatial orientation), the assumption drawn for this example are also valid for the other two axes.

Figure 5.11 depicts the signal path of the sorted data set. Positions with a low distance to the transmitter coil result in a very high magnitude value. Also visible is that the interval $[-14.3dB, -10.2dB]$ holds 90 percent of the regarded positions around the transmitter. This means, to accurately separate the positions, the interval aggregation strategy has to establish the interval boundaries mostly in these magnitude intervals for the equipotential shells \mathcal{S}_i .

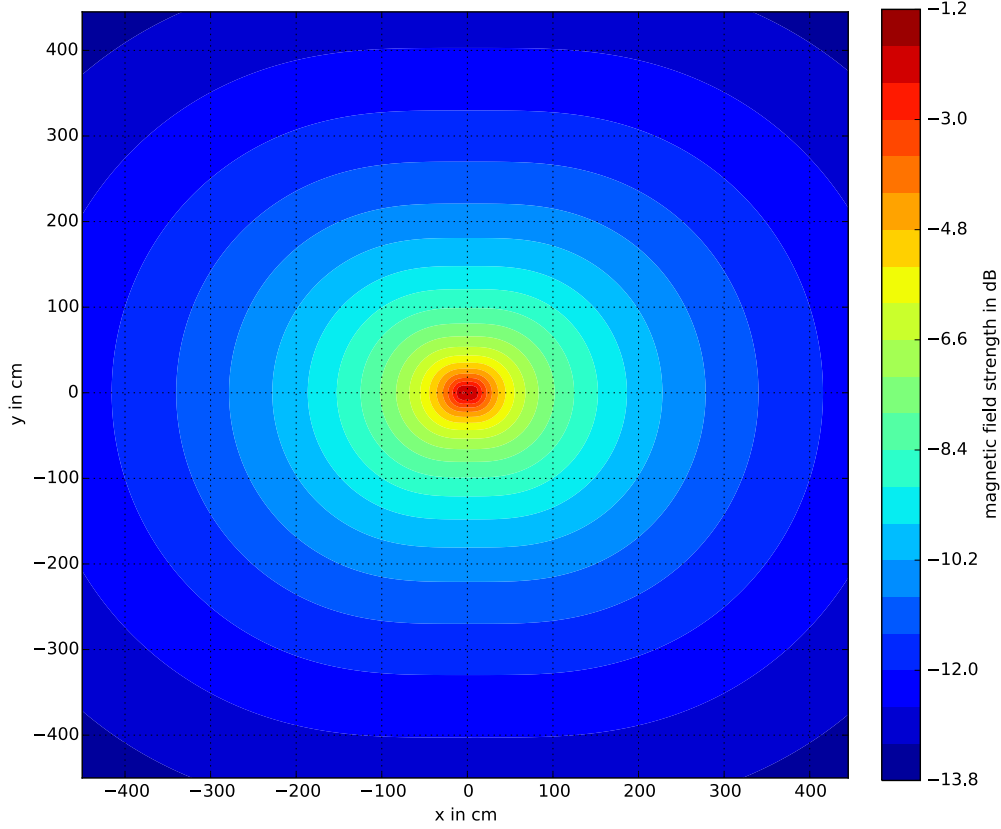


Figure 5.10: Equi potential shells of a transmitter axis. 20 different shells are displayed in this picture. Notice that the dimension of the shell shrinks the closer it gets to the coil.

We examine in the following part the different strategies for choosing the interval boundaries of the shells. For each evaluation, we apply the interval strategies to the theoretical magnetic field model and store the generated signal boundaries and magnitude shells. We estimate the three shell ids of the each 3D position by comparing the corresponding magnetic field magnitudes with the interval boundaries. If the magnitude is in the signal boundary, the corresponding shell is found and stored.

Position estimation sequence To evaluate the accuracy of the approaches, the data set of the calibration process is used. The data set consists of 9 transmitters and at least 5000 measurement points around the transmitter coils. To transform the raw field measurements into theoretical model values, we apply the calibration function \mathcal{P}_i of the corresponding transmitter axis from section 5.3. The resulting theoretical field value t_i is then used to determine $(\mathcal{S}_x, \mathcal{S}_y, \mathcal{S}_z)$ where $t_i \in \mathcal{I}_i, i \in x, y, z$. Because of measurement inaccuracies, errors in the transfer function

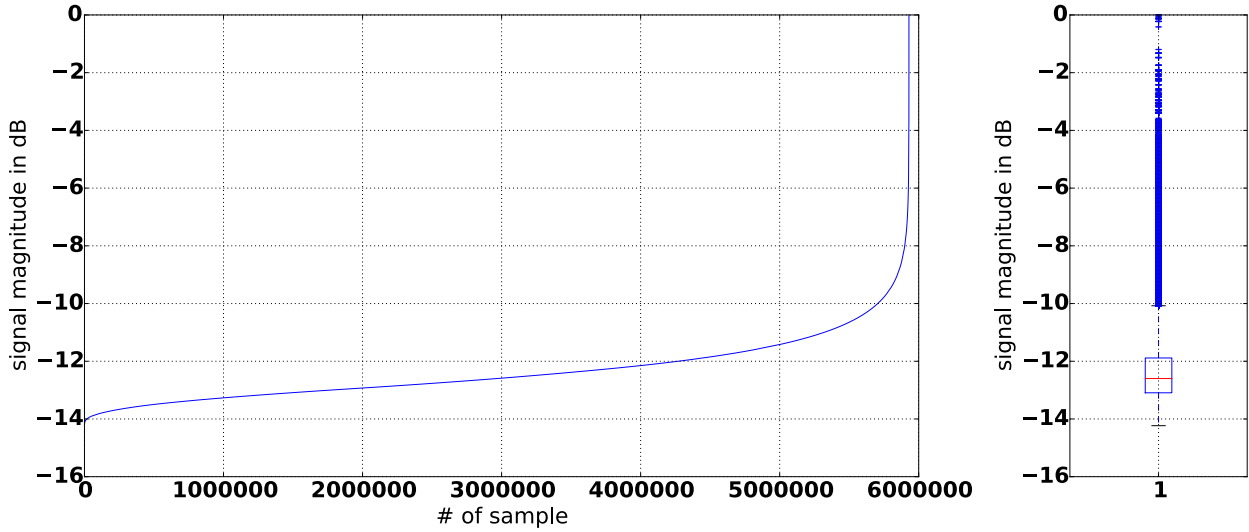


Figure 5.11: Magnitude distribution of the theoretical magnetic field data set of transmitter axis x . The trajectories main signal interval is $[-14.3dB, -10.2dB]$. The separation algorithm has to take this into account.

approximation, natural / environmental magnetic field disturbances, it is possible that the estimated tuple $(\mathcal{S}_x, \mathcal{S}_y, \mathcal{S}_z)$ does not result in an intersection. To solve this problem, we use the intersection which is closest to the estimated tuple. Using a Kd-Tree for fast nearest neighbor lookup allows retrieving the corresponding model coordinate \mathbf{x}_m which relates to $(\mathcal{S}_x, \mathcal{S}_y, \mathcal{S}_z)$.

After this, the position linked to the shell tuple is used as estimated position \mathbf{x}_m . As the magnetic field is symmetrical about the center of the coils, the magnetic field model only stores the coordinates of the first coordinates system octant. This helps to reduce the memory consumption. After position lookup, the eight positions of the different octants are returned as candidate positions.

We compare the estimated position \mathbf{x}_m to the reference position derived from the optical tracking system to calculate the absolute position and distance error. Also, notice that \mathbf{x}_m is a candidate position in the first octant of the transmitter coordinate system. For simplification, and without influencing the position estimation quality, the reference position is transferred in the first octant of the emitter coil coordinate system by applying the absolute function to the coordinate values.

Intervals based on a number of elements Initially we implemented this approach which subdivides the ordered magnitude set in intervals with a fixed number of items. This method favors the parts of the magnitude trajectory with a high number of features. In our case, this means that most signal intervals lie within $[-14.3dB, -10.2dB]$, which is a preferable result. It does not take the magnetic field behavior into account. As expected, the transmitters have different accuracies, the overall performance varies within 10 cm accuracy. The number of interval elements does influence the distance and position accuracy. Also visible is that the distance performance is more robust against calibration and modeling errors than the position estimation.

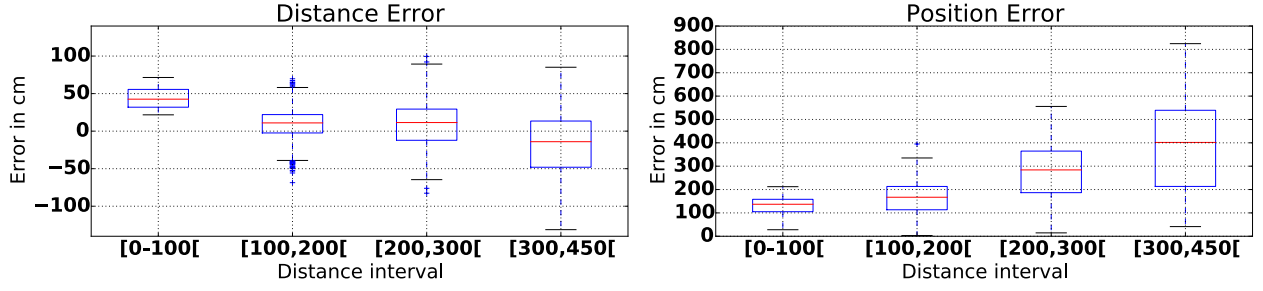


Figure 5.12: Error distribution of different distance intervals, the magnitude interval size is 30000 elements per interval. The position error is ($\mu = 168.2, \sigma = 92.7$), the distance error is ($\mu = -33.2, \sigma = 37.33$)

The position errors can be up to 900cm, which means that two coordinates are switched. We evaluated this approach with different interval sizes, the best results for the position estimation have been achieved if the interval size was 60k interval elements ($\mu = 168.2, \sigma = 92.7$), the distance estimation performs best with an interval size of 45k ($\mu = -33.3cm, \sigma = 37.33$) (see figure 5.12, figure 5.13).

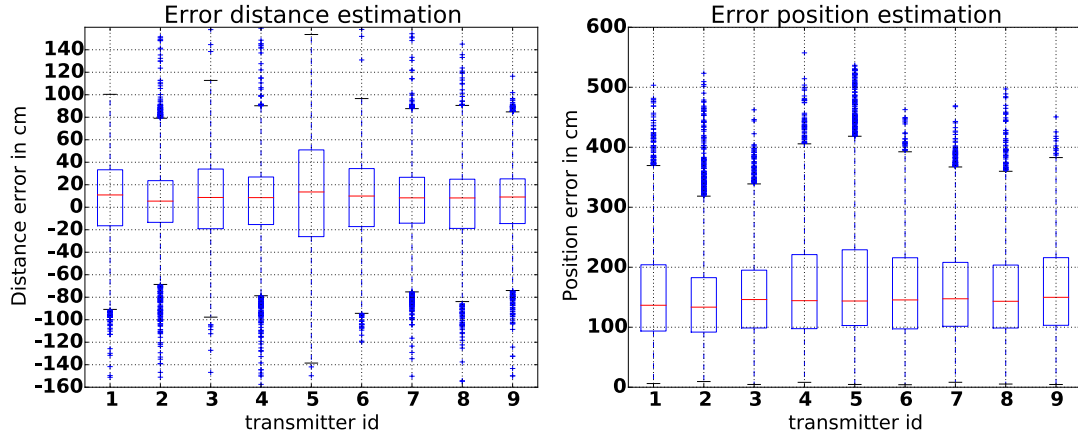


Figure 5.13: 45k elements per interval, distance error: ($\mu = 5.83cm, \sigma = 40.12$), position ($\mu = 159.50cm, \sigma = 84.17$)

Intervals based on the signal span In this approach the interval boundaries of \mathcal{S}_i are chosen in such a way that the span ($max - min$) of the magnitudes is below the gradient value. This means that the minimum value and the maximum value of the signal interval are at most the gradient value apart. Using this approach, it is possible to choose the intervals in such a way to guarantee the resolution of positions at high distances. Also, the signal to noise ratio and the noise resulting from the analog circuit can be taken into account. The best position results can be achieved with a gradient value of 0.08 dB ($\sigma = 149.02, \mu = 90.38$), the lowest distance errors are obtained with gradient value 0.11dB ($\sigma = -2.58, \mu = 34.9$) (see figure 5.14).

The shell-based approach shows several drawbacks about robustness against measurement and

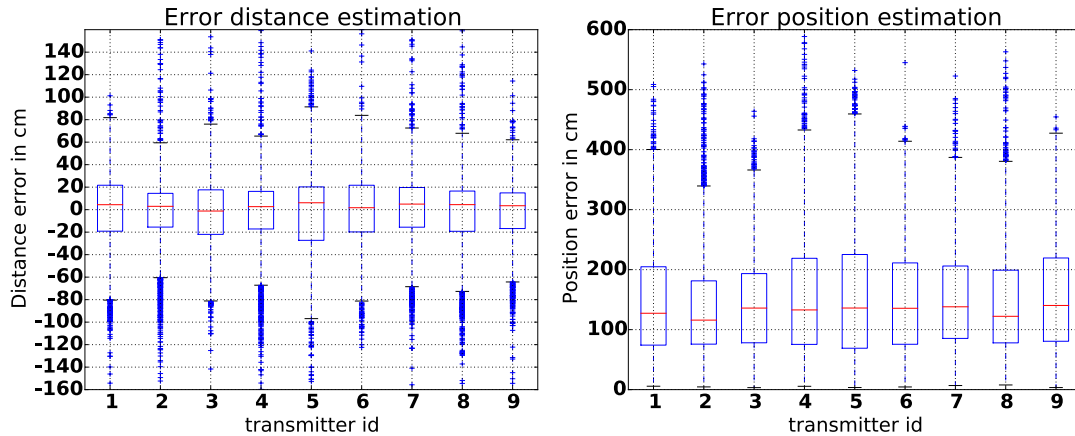


Figure 5.14: Distance and positioning error of the gradient approach, gradient 0.1 dB. Distance error: ($\mu = -5.60cm, \sigma = 37.86$), position error ($\mu = 168.71cm, \sigma = 102.28$)

modeling errors. Especially the position estimation using a single coil introduces large positioning errors. Also higher distances between the transmitter and the receiver strongly influence the error.

Figure 5.15 depicts and explains one problem arising from the shell approach: depending on the distance and the signal strength at the position, errors in the models (either the theoretical or the calibration functions) result in wrong shells. If a neighboring shell is chosen, this leads to an offset in the corresponding direction (a different shell intersection area is estimated) which can result in high position offsets. Choosing a wrong shell could also lead to a shell tuple which does not intersect at all. By returning the nearest tuple, this can result in error-prone position estimation which still yields good distance estimates.

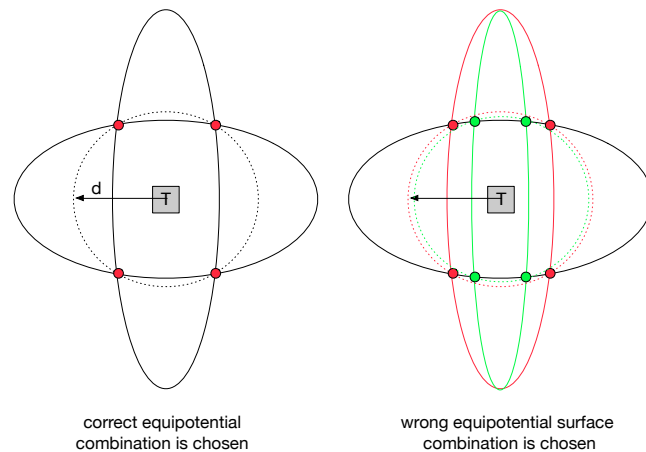


Figure 5.15: Schematic figure of the shell-based localization approach. The quality of position estimation drops when a wrong shell is chosen, as this results in wrong intersection values. Left: Correctly chosen shells result in a good approximation of the position (red points) and distance. Right: Due to measurement errors, errors in calibration or the model, a wrong shell is chosen. This results in a different intersection position and therefore a bigger position error. Estimation errors have lower influence on the distance estimation as the distance depends on three coordinates.

In contrast to the position errors (where a 3D position vector is determined by a 3D magnetic field magnitude vector), the distance errors are less prone to model and environmental effects, resulting in a better distance estimation with a mean error around 2 cm and a standard deviation of 37 as the distance is described by three values instead of one value.

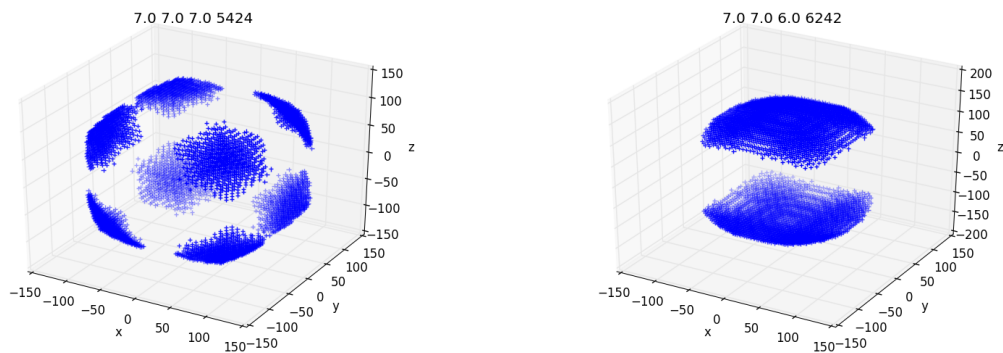


Figure 5.16: Two different intersection types of three shells. The left intersection set is approximated by the usage of the point center. The right intersection set is also mapped to the mean center of the set resulting in a high offset.

In addition to a more geometrical explanation approach, we also show another drawback of this shell-based approach: depicted in figure 5.16, the intersection of three shells does not always result in a small connected area of several cm^3 but can result in larger volumes which are not accurately mapped in the center of the intersection set. Returning the center of this

”sickle-shaped” volume can lead to huge offsets and therefore errors.

5.4.3 Cube-shaped 3D Division of Theoretical Magnetic Field Transmitter Space

In this approach, the volume around the transmitter coil is divided into cubes with given edge length. For each cube, we determine all positions of the magnetic field model which are included in this volume. The corresponding model magnitude values ($\|\mathbf{B}_x\|$, $\|\mathbf{B}_y\|$, $\|\mathbf{B}_z\|$) for the transmitter axes are then used to determine the signal range in this cube. This results in minimum and maximum values describing the magnetic field at the area around the center position of the volume.

Figure 5.17 depicts the centers of the sub-cubes of the evaluated magnetic field model. We also consider the sensor resolution and the calibration errors by adjusting the sub-cube edge length. In closer areas around the transmitter coil, a denser sub-cube placement with smaller cube edge lengths are used, starting from 20cm between 0 and 1m, to 30cm between 1m and 3m and 50cm above 3m. Considering the magnetic field symmetries, 814 volumes are found around the transmitter coil in one octant.

By using this kind of spatial separation, this approach also takes the signal-to-noise ratio of the circuit and the magnetic field behavior into account: The circuit can resolve more points in closer areas around the transmitters (high magnetic field density). Therefore the cubes are smaller than those in the outer regions.

Position and Distance Estimation The measurement evaluation consists of the usual raw value to theoretic value transformation and the magnitude calculation of the three transmitter axes magnetic fields. For the position estimation either an interval search data structure can be used or an $\mathcal{O}(n)$ comparison of the magnitudes and the signal intervals of the cubes. If no cube is found whose, signal intervals contain all three magnitude values, the nearest signal neighbor approach is applied. Both approaches result in a single cube and therefore a single estimated position.

Discussion We evaluated this approach with the given data sets. This approach results in position estimation errors below 120cm with a standard deviation of 88. The distance estimation has a mean error of -2.71cm with a standard deviation of 32.3.

5.4.4 Comparison

In this section, we give a comparison of the four different approaches. We look at distance and position estimation errors. Figure 5.19 depict the distance performances of the methods evaluated against different distance intervals. All methods present the results of the best parameters. Running the algorithms on a Intel corei7 with 2.8GHz shows that the approaches

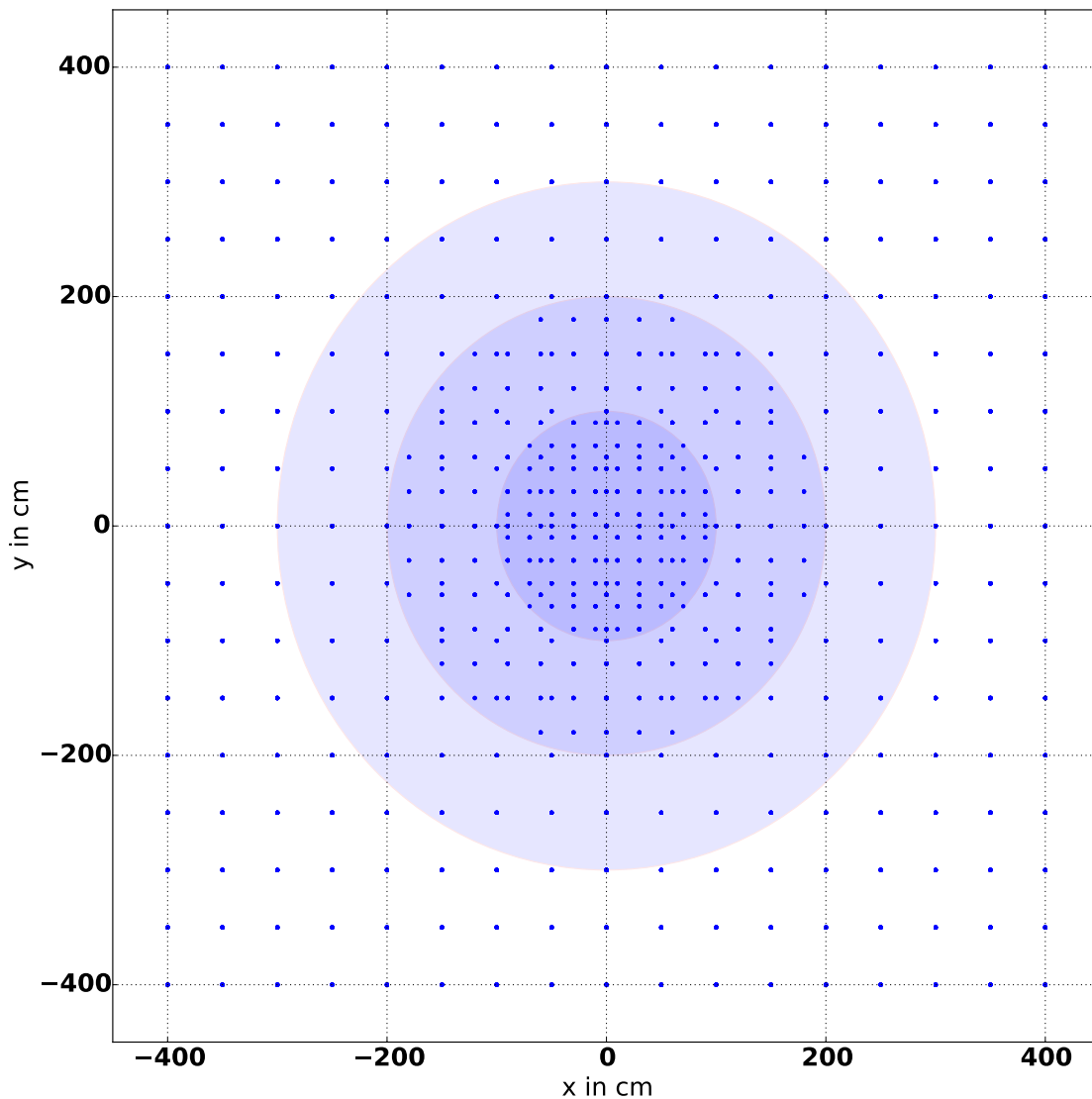


Figure 5.17: Centers of the cubes in x,y plane ($z=0$). The $450 \times 450 \times 450\text{cm}$ cube in which the theoretical magnetic field values are evaluated is discretized in 814 different volumes. Depending on the distance between the transmitter and the cube center, the sub-cube edge length is for 1m 20cm, between 1m and 3m 30cm and above 3m 50cm.

have similar complexity. The evaluation of a single magnetic field measurement takes around 5 ms.

In all cases, the distance performs better than the position estimation with a single coil. As already described in section 5.4.2, the distance estimation depends on the combination of three parameters, the 3D position vector also depends on three parameters, which makes it prone against disturbances. A better approximation of the magnetic field also helps to reduce the effect of intrinsic and extrinsic parameters as modeling and calibration errors or environmental effects. A more complex mapping of the magnetic field as we described in section 5.4.3 reduces both

5 Signal to Position / Distance Estimation

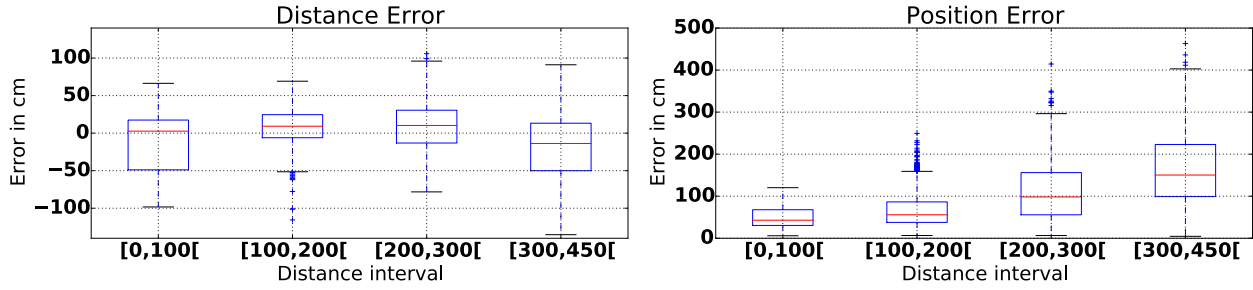


Figure 5.18: Results of the cube division-based position estimation. Position and error distribution of Transmitter 1. The position and distances are estimated using a cube shaped aggregation of model values.

| Approach | position error | distance error |
|-----------------------------|---|--|
| nearest neighbor | $\mu = 321.6 \text{ cm}, \sigma = 187.4$ | $\mu = -2.26 \text{ cm}, \sigma = 34.77$ |
| shell intersection interval | $\mu = 168.2 \text{ cm}, \sigma = 92.7$ | $\mu = -33.2 \text{ cm}, \sigma = 37.33$ |
| shell intersection gradient | $\mu = 149.02 \text{ cm}, \sigma = 90.38$ | $\mu = -2.58 \text{ cm}, \sigma = 34.9$ |
| cube-based | $\mu = 117.33 \text{ cm}, \sigma = 87.45$ | $\mu = -2.71 \text{ cm}, \sigma = 32.3$ |

Table 5.1: Distance and position estimation errors of a cube-shaped coil.

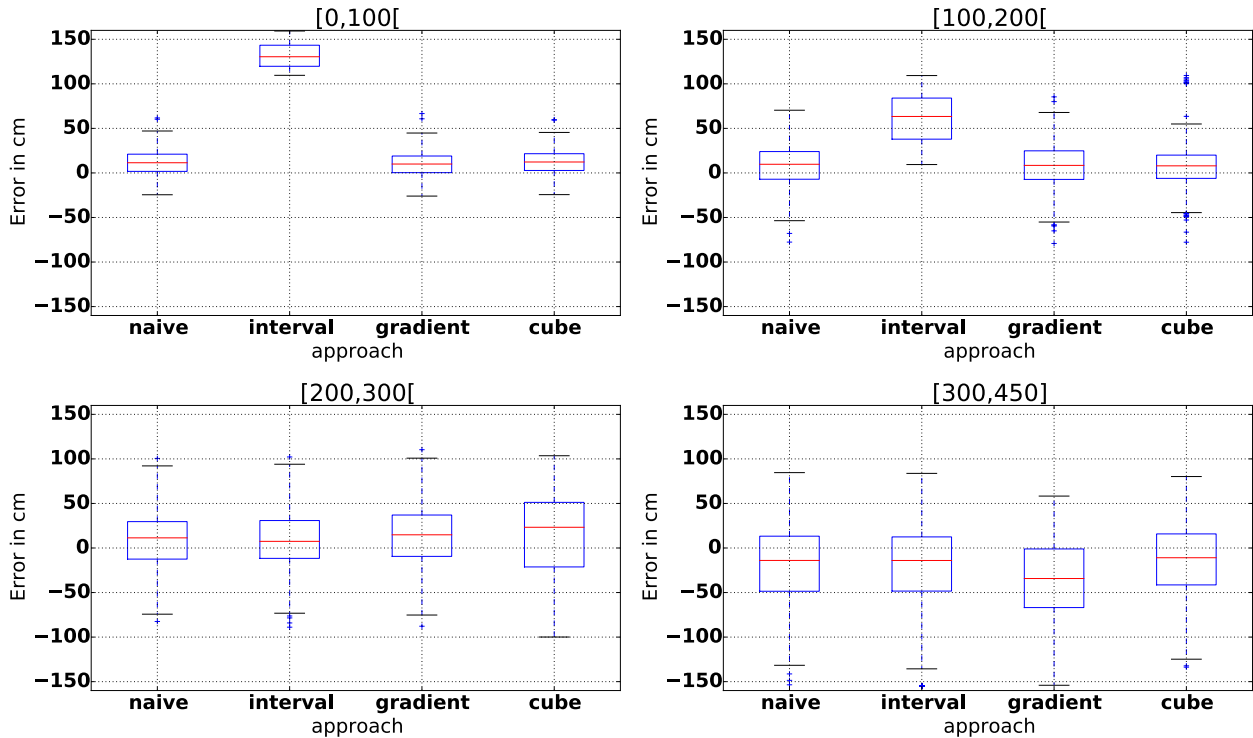


Figure 5.19: Distance performance evaluation of the four different approaches

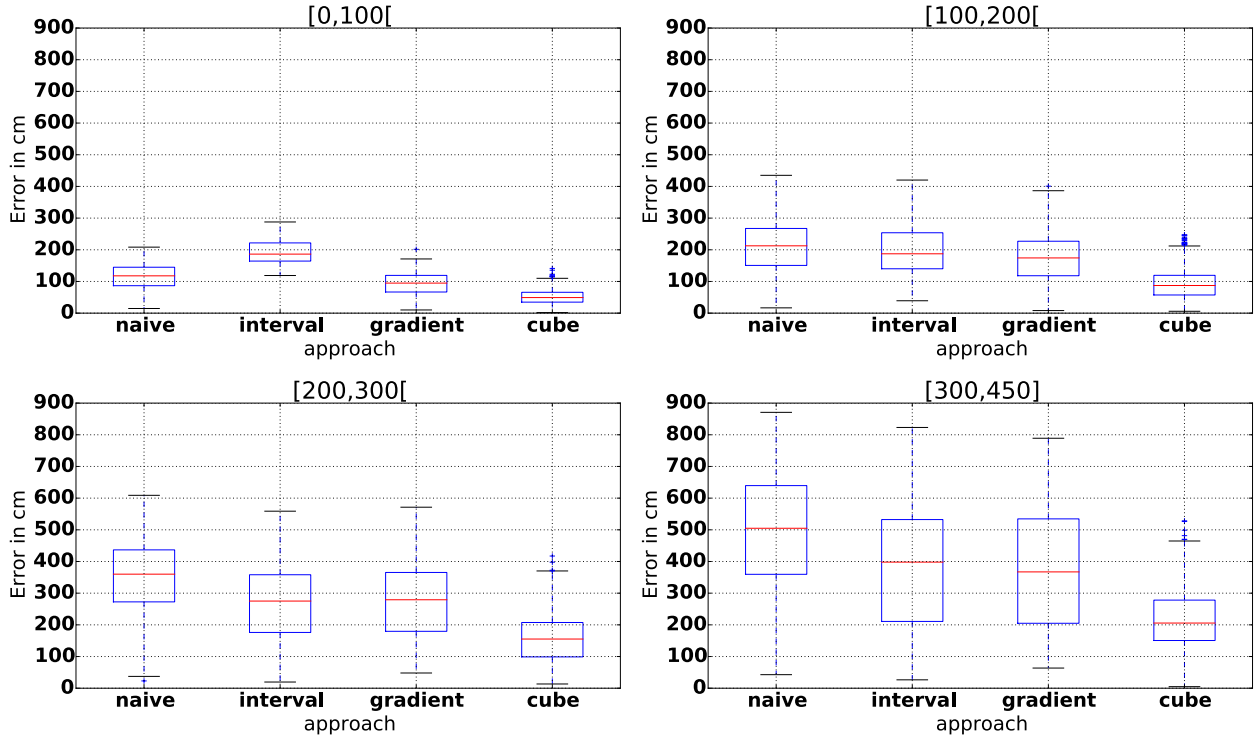


Figure 5.20: Position performance evaluation of the four different approaches

effects and also narrow the standard deviation of the measurement error and the related position estimation. Although being able to reduce the estimation errors, the position estimation relying on a single coil is not satisfactory. In most of the distance estimation intervals, the sub-cube approach outperforms the other approaches (the standard deviation is lower than the variation of the other algorithms), although it has a higher standard deviation in the interval between 200cm and 300cm.

As described in section 5.3 the cross talk of the transmitter coils influence the magnetic field on the physical level, an approximation or removal of the influence could not be achieved. A different three axes coil architecture with narrow coil axes reduces the crosstalk. In the following subsection, we evaluate the circular coil-shaped architecture as we did with the cube shaped coil.

Circular Coil Evaluation

The circular coil set up consists of 3 transmitter axes which are perpendicularly placed on a sphere. The coils are 1.5cm broad, the diameter of each axes circle is 12cm. Compared to the cube-shaped coil, the area of the coil is $0.011m^2$ against $0.032m^2$ which will result in a reduce range. 300 windings of 0.5mm copper wire have been attached to the coil body. After tuning

5 Signal to Position / Distance Estimation

the axes to 20kHz by adjusting capacitors of the LC circuit, transfer functions for each axis are calculated from 15 reference measurements along the axes. In this section, we want to show that a reduced crosstalk between the axes, and therefore a more accurate approximation of the magnetic field by the magnetic field model, leads to lower positioning and distance estimation errors. The transmitter coil design can still be improved by reducing the crosstalk furthermore but is not part of this work.

After estimating the transfer functions for the transmitter axes, we placed the transmitter coil in the same area. We randomly chose positions around the transmitter and measured the coordinates in the transmitter side coordinate system. For each measurement position we record at least 500 magnetic field measurements, RF-based synchronization is used. The cube-based approach was determined to be the most accurate approach for position estimation; we, therefore, apply this method to the recorded data.

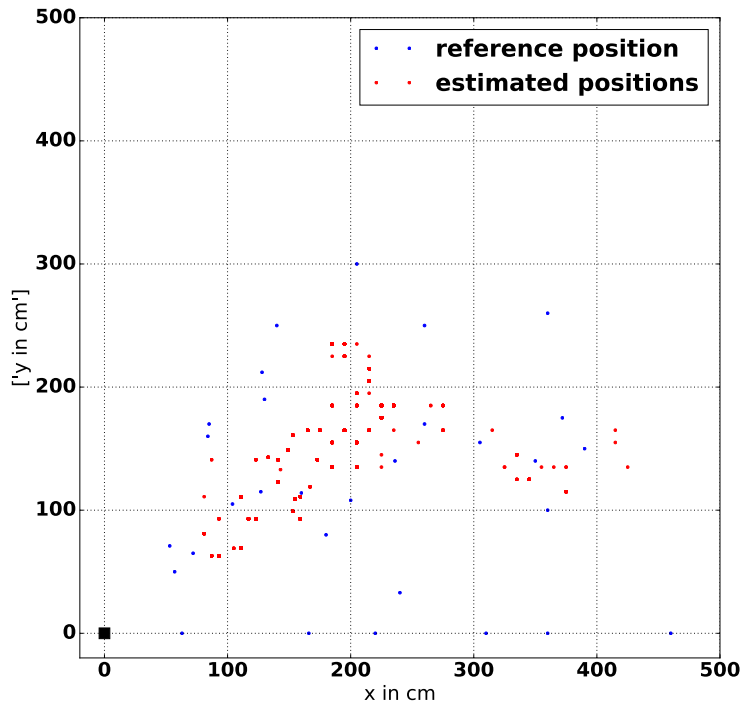


Figure 5.21: Reference positions and estimated positions of the spherical coil evaluation. points along the center of an axis result in poor position estimations.

Two issues are visible in the position and distance estimation:

1. The range of the coil is as expected reduced, the coverage of this setup is approximately 350cm. Using all positions results for the position estimation in ($\mu = 97.4\text{cm}, \sigma = 54.07$) and for the distance estimation ($\mu = -15.4\text{cm}, \sigma = 52.07$). Restricting the maximum range to 300cm (filtering out all reference positions further away) results in ($\sigma = 83.18, \mu = 43.66$) for the position error and ($\sigma = 4.67, \mu = 39.00$) for the distance error.

- Looking at the error distribution of the restricted data set shows a second property of the system: positions on the main axes of the transmitter coordinate system $(x + \epsilon, 0, 0)$, $(0, y + \epsilon, 0)$, $(0, 0, z + \epsilon)$ have an higher position and distance error. They are confused with points at around 10 to 15 degree of the axis being closer to the transmitter. If these positions are filtered out, the position error falls to $(\mu = 70.8cm, \sigma = 33.38)$ and the distance error to $(\mu = 4.67cm, \sigma = 27.85)$.

The reduction of the crosstalk of this coil type increases the quality of the position estimation. The distance estimation stays nearly at the same level compared to the cube shaped transmitter coils

| Method | mean error in cm | std deviation |
|------------------------------|------------------|---------------|
| cube shaped coil | 117cm | 87.45 |
| all positions | 97.4 | 54.07 |
| max distance 300cm | 83.18 | 43.66 |
| 300cm without points on axes | 70.8 | 33.38 |

Table 5.2: Position estimation errors of spherical coil

| Method | mean error in cm | std deviation |
|------------------------------|------------------|---------------|
| cube shaped coil | -2.71 | 32.3 |
| all positions | -15.4 | 52.07 |
| max distance 300cm | 4.67 | 39.00 |
| 300cm without points on axes | 4.67 | 27.85 |

Table 5.3: Distance estimation errors of spherical coil

5.5 Conclusion

In this chapter, we evaluated the different methodic approaches of estimating the candidate sets and the distances. The magnetic field generated by the transmitter coils is described by the law of Biot-Savart, we estimated the magnetic field density around a theoretical magnetic field transmitter as data set to build a magnetic field model for position and distance estimation. We implemented two different transmitter coil architectures with a three axes transmitter coil setup. This setup allows retrieving position information from the field density values of the three transmitter axes in addition to the relative distance. A cube-shaped transmitter coil is easier to produce, but has a higher coil crosstalk and therefore a bigger error for position and distance estimation. The spherical coil is more complex to produce but has a lower crosstalk and therefore a higher accuracy.

We described the processing sequence of how to deduce position and distance information from the magnetic field information. In addition to low memory consumption and lookup speed, different coil architectures should be easily integrated into the model.

5 Signal to Position / Distance Estimation

Using this physical knowledge allows us to implement a calibration process for various magnetic field transmitter coils taking the magnetic field behaviors of these coils into account. The calibration abstracts on the receiver side the different sensitivity factors of the receiver coils and compensates hardware related tolerances on transmitter and receiver side. After converting the measured signal to the signal level of the theoretical magnetic field model, we presented three different approaches how to organize the magnetic field information.

The magnetic field model supports, on the one hand, an information (position and distance) retrieval in $\mathcal{O}(\log(n))$ (where n is the number of model elements) with a memory consumption of $\mathcal{O}(n)$, on the other hand an organization scheme taking the non-linear behavior of the magnetic field and the falling sensitivity of the analog receiver side circuit with rising distance into account. The magnetic field model also retrieves the receiver position with a single transmitter coil by evaluating the magnetic field density of the three perpendicular magnetic transmitter coils. The best position and distance results have been achieved if the magnetic field volume of a transmitter is subdivided into cubes. Depending on the distance between the cube and the transmitter, the edge length can be adjusted to represent the sensitivity of the receiver circuit and the magnetic field density which fall both with rising distance. Therefore the edge length have to be increased. Doing so, we achieve a position accuracy of $(\mu = 117cm, \sigma = 87.45)$ and a distance accuracy of $(\mu = 2.71cm, \sigma = 32.3)$.

The position estimation quality rises if a different coil architecture is used as we showed by using a spherical shaped coil setup. The position error drops to 70cm with a standard deviation of 33. The distance estimation accuracy stays nearly unchanged. This shows that the stability of the distance is less error prone than the position estimation about model and calibration errors.

6 Multi Coil Position Estimation

The previous chapter gave insights of how to determine the position of a receiver relatively to a transmitter. Due to the underlying measurement principle and the receiver side hardware circuit, the approach results in symmetrical ambiguous positions around the transmitter. Additionally, the position estimation is error prone as the 3D coordinate relies on three magnetic field measurements. Small offsets in the highly dynamic induced voltage signal result in high outliers. Thus the distance estimation performs better. This chapter covers the **combination of several transmitters to estimate the receiver position**. As the system now relies on several transmitters, it is possible that two or more transmitters have intersecting magnetic field areas. Uncontrolled generation of two or more transmitters, therefore, results in a superposition of the magnetic fields, which would falsify the measurements to each of the transmitters. Thus it is necessary to **determine a schedule of transmitters** to manage the generation of magnetic fields. Also, a **common time or synchronization** between the transmitters is required to determine the start of the transmitter measurement slots.

After this, a **fusion algorithm which takes both, the stable distance estimation and the error-prone candidate position estimations** into account, has to be established. Especially measurement cycles with only one or two valid transmitters can benefit from this fusion algorithm as the candidate positions provide (rough) direction information. Also, questions about **tracking and statistical modeling of the error** arise. The performance of the localization system with regard to regions of interest detection and the evaluation in different areas has to be considered. A comparison against commercially available systems shows the overall position estimation accuracy and problems arising in indoor environments. Additionally, it is interesting to compare our localization system against RF-based systems, especially in demanding environments.

6.1 Contribution

To avoid superposition of magnetic fields of different transmitters, we evaluated **round robin-based scheduling algorithms** and we transferred the problem of **graph coloring to the scheduling problem** of transmitters. The scheduling algorithm based on graph coloring reduces the number of triggering slots by simultaneously triggering transmitters which do not influence each other.

6 Multi Coil Position Estimation

A common time has to be established to link the measurement slot to a specific time. Therefore different **centralized and distributed time synchronization and triggering algorithms** are presented and evaluated.

We evaluate **localization fusion algorithms** combining distance and position measurements from different transmitters to estimate and track the absolute position of a receiver. The distance measurements are applied to a **circle intersection algorithm** and a **least square error minimization algorithm**, the candidate position sets are filtered in such a way to choose the element from each set which is closest to the others. A **particle filter for tracking and position stabilization** has been implemented which additionally weights the positions statistically. We **evaluate the localization in different environments** with regard to **regions of interest**. In large scale setups the system allows to determine regions which are more than 50 cm apart, in small scale industrial setups (in which the coils are maximum 2 m apart), the distance between the regions have to be above 20 cm. **Compared to commercially available Bluetooth-based localization systems** with a mean position error of 67 cm, our prototype system has a mean position error of 77 cm and provides in contrast to the RF system in all measurement points a position estimation.

6.2 Synchronization of the components

The oscillating magnetic field localization system applies a time division multiple access scheme to measure the field strengths of the different transmitters.

To be able to link the measurements to the correct transmitter which is generating the magnetic field, it is necessary for each sensor node to 1) know the pulsing sequence of the transmitters and 2) to know the exact start time of the magnetic field generation process. To achieve this, the nodes have to be time synchronized or notified about the opening of a measurement slot. The accuracy of the synchronization process strongly influences the noise level and the achievable data rates. Asynchronous real time clocks caused by the process can only be compensated by increasing the duty cycle of each axis. This, on the other hand, reduces the overall sampling rate.

Synchronization in sensor networks have broadly been researched in literature: Examples for synchronization algorithms can be found in [SV03], [GR03] or [Awe85]. Also ideas from the network time protocol ([Mil92]) or Cristian's algorithm ([Cri89]) can be used. Several approaches for node synchronization, and centralized/decentralized information exchange for sensor network maintenance will be presented in the following sections.

6.2.1 Trigger Messages

The simplest way of synchronizing the components of our localization system is the transmission of trigger messages. In section 4.7 we already described the RF signal trigger. The trigger can be a signal transition on a wire or RF messages transmitted by a central service. Each of the transmitters is sequentially addressed; the receivers are also informed about the start and the transmitter which is currently generating the magnetic field. Although this scheme allows to implement a strict time synchronization ($10\mu s$ for the cable synchronization and $340\mu s$ for RF-based synchronization), the star shaped approach introduces a single point of failure. Additionally, the cable-based synchronization setup is complex and obstructs the user. RF trigger systems like Zigbee-based systems have a packet loss rate of 2% to 5% which results in measuring errors or in missing measurement results. This has to be considered during algorithm development.

Centralized vs. Decentralized Approach Depending on the field of application which has to be covered moreover, the number of transmitter nodes, the triggering mechanism can either be centralized (a single node broadcasts trigger messages to the nodes) or decentralized (the transmitter nodes create a ring which defines the order of the trigger sequence). In the centralized approach, a node holds the list of available transmitter nodes and sequentially broadcasts trigger messages with the corresponding transmitter id. On reception, the selected transmitter and all receivers start their measurement cycle.

In contrast to the centralized approach, the decentralized approach does not have a designated trigger node, but the triggering algorithm is performed on each node of the sensor network: The algorithm consists of 2 steps, the organization of the triggering ring (node discovery) and the

triggering cycles. This is discussed in the next section. Although not a new field of research we describe this approach for completeness.

Transmitter Node Discovery In a distributed network, information has to be exchanged using messages; no shared memory is available. To discover all transmitters of our magnetic field localization system, the transmitter nodes perform message exchanges to distribute information about their local RF neighborhood. The receivers do not actively transmit discovery messages; they only store the received information to hold the same data set and therefore the same version of the transmitter ring.

This discovery algorithm is periodically called or when a new transmitter node enters the sensor network.

A discovery message $m_d = (sn_d, t_{startTime}, \{t_1, t_2, \dots\})$ holds the discovery sequence number sn_d and a list of transmitter ids t_i found in the sensor network. Additionally a time stamp $t_{startTime}$ indicates the time when the first trigger sequence should start. Whenever a transmitter receives this broadcast message, it checks the local discovery sequence number sn_d , and $t_{startTime}$. If sn_d changed, it discards the local list of discovered transmitter ids and uses the latest list received. Since it is possible in a distributed system to start the discovery mechanism from different times, sn_d is also used to detect and merge multiple discovery processes.

If multiple discovery sequences exist, the nodes order the sequences in ascending starting time order and use the sequence with the smallest start time. Additionally, the start time has to be higher than the locally stored start time of the current transmitter discovery list.

On reception of a discovery message, the transmitter merges the local transmitter list with the received transmitter list.

The discovery algorithm terminates when there are no changes in the received local discovery list. The transmitters (and the receivers which also receive these discovery messages) sort the transmitter id list in ascending order. When the start time is reached, the sequence list is used to start the triggering cycle according to the local list. The message exchange can either be done using RF-based Zigbee communication or Ethernet communication.

Assuming that all nodes have received the full set of transmitters in the sensor network, the transmitter nodes can start the synchronization process:

The scheduling sequence is organized in a round-robin way, the length of each transmission slot is known, transmitter t_i therefore can estimate its own triggering time: $t_{trigger} = t_{startTime} + i \times t_{slotlength}$. When the transmitter starts a measurement, it broadcasts a trigger message. All other nodes can, therefore, synchronize their local clocks and re-adjust their next measurement start times.

Using this decentralized approach has several advantages: The number of transmitters can dynamically be changed as the transmitter ring will automatically be re-adjusted. The system has no single point of failure.

```

Members:
TransmitterList = {t0, ..., ti}, initially empty
input : Empty Transmitter Id List
output: Each transmitter has list of transmitterIds

On reception of Transmitter List Message
bool transmitLocalList = False;
for i ← 0 to len(TransmitterListRF) do
  | if TransmitterIdListlocal.notContains(ti) then
  | | TransmitterIdListlocal.append(ti);
  | | transmitLocalList = true;
  | end
end
if transmitLocalList then
  | RFBroadcast(TransmitterIdListlocal);
end

```

Algorithm 1: Transmitter Node Discovery Algorithm

The ring requires additional organization messages which is a disadvantage as it introduces extra burden to the transmission channel. Also packet loss and additional complexity for the detection and triggering algorithm has to be taken into account (especially processing time, extra power consumption for the packets and memory on the micro-controllers). The distributed version of the triggering algorithm also introduces jitter to the triggering process. Longer measurement slots are compensating the inaccuracies induced by transmission and processing delays.

Summarizing: a distributed algorithm for node discovery in combination with a trigger algorithm implements a system which can be used in dynamic environments. It can automatically integrate new transmitter upon startup. A request-response trigger mechanism provides accurate synchronization of the transmitter and receiver nodes and can be implemented in such a way to avoid "noise" measurements (see figure 4.14). However, still, RF specific problems have to be dealt with.

6.2.2 Distributed Algorithm for Clock Synchronization

We noticed an increase of packet loss and therefore an inaccurate synchronization when the distributed approach is used in larger scale setups (10 transmitters in an area of 200m²), This problem could only be solved by doubling the slot length of the measurement cycles and therefore a reduction of the position estimation rate. Another possibility for stable measurements is to synchronize the local clocks of the sensor network components.

The node discovery algorithm stays unchanged. The clock synchronization algorithm is a combination of ideas of the NTP and Cristian's Algorithm. This work has been part of the peer reviewed Ubicomp 2012 submission [PL12].

Local Time Server Estimation and Time Synchronization

In literature time synchronization can be achieved through message exchange. Many research groups presented their work for (WIFI) network-based time synchronization: An overview is given in [SY04] and [ASSC02], different approaches are described in [EGE02], [SBK05], [LC10], [MKSL04], [VGR03], [GKS03], each of these protocols focus on sensor networks and their limited resources and power requirements.

We use a combination of ideas described in Cristian's algorithm [Cri89] and NTP [Mil92]. To achieve a sufficient clock synchronization accuracy, the RF transmission, propagation and the processing time on the time server side has to be estimated. The RF transmission/propagation time in Zigbee sensor networks is constant, the processing time on the server side depends on the workload of the micro-controller.

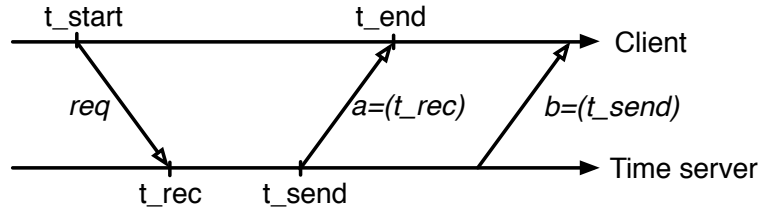


Figure 6.1: Schematic description of the time synchronization message exchange sequence.

The client sends a time request to the time server and stores the local start time (t_{start}) when the message is transmitted. The server stores its local time (t_{rec}) when the request is received and returns t_{rec} as a response to the client. As the emission of the packet takes time (data transfer from the micro-controller to the RF unit, processing, collision detection), there is a time difference between putting the response in the transmission buffer and the actual emission time. When the response is sent, the server stores the local time t_{send} and transfers this message to the requesting client. When the client receives the response message, it stores its local time as t_{end} , after receiving the t_{send} time, the time synchronization can be performed:

$$t_{procServer} = t_{send} - t_{rec} \quad (6.1)$$

$$t_{RoundTripTime} = t_{end} - t_{start} \quad (6.2)$$

$$t_{propagationTime} = 0.5 * (t_{RoundTripTime} - t_{procServer}) \quad (6.3)$$

$$t_{newTime} = t_{send} + t_{propagationTime} + (t_{currentTime} - t_{end}) \quad (6.4)$$

With this approach, we achieve a clock synchronization between the client and the time server of below $200\mu s$, due to the clock drift, delayed RTC update calls (magnetic field generation and sampling have higher interrupt priorities than the RTC), the synchronization process needs to be triggered every 4 s.

Large scale Time synchronization In larger-scale setups, like offices, households or industrial environments, it is not always possible to directly receive/transmit data from and to the time server. We, therefore, implemented a distributed algorithm which automatically determines the global connectivity graph and the node which allows achieving the most accurate time synchronization.

A connectivity graph

$$\mathcal{G}_c = \{e_k = (t_i, t_j) \mid t_i, t_j \in \mathcal{T}, t_i \in rfRange(t_j)\} \quad (6.5)$$

is a graph structure representing the RF connections between the nodes of the sensor network. An edge between two nodes indicates that messages between the nodes are directly sent and received.

Similar to the discovery of transmitters, the nodes collect information about the local neighborhood:

In the first step, the transmitter nodes periodically search their local neighborhood to discover their RF neighbors. The transmitter nodes then start adding this information to their local connectivity graph which is then broadcasted and locally updated (procedure comparable to the transmitter node discover algorithm previously presented).

After the exchange of this connectivity graph is finished, a tree structure is created:

The root of the tree is the node with the highest number of adjacent nodes and the smallest transmitter id (center of the graph). Starting from the center of the graph, we apply the breadth-first search algorithm resulting in a hierarchical tree with the minimum distance to the center of the graph. A node synchronizes with the neighboring node which is closest (level in the tree) to the center node/root of the tree. If several neighbors have the same distance to the root, the transmitter node with the smallest id is used for synchronization.

We manually evaluated the time offset introduced by each level of the tree: We created a synchronization tree which is comparable to a list.

After the time synchronization algorithm was performed, we measured the time difference between the root node and the node at level i of the list using an oscilloscope. Every second both nodes changed the value of an output pin, and we measured the time difference between the two edges of the signal. Each level in the tree introduces a clock offset of approximately $60\mu s$. Due to the limited range of the magnetic field, even larger time offsets would not influence the measurements, as there is no superposition of magnetic fields. (The RF transmission range is much higher than the magnetic field range).

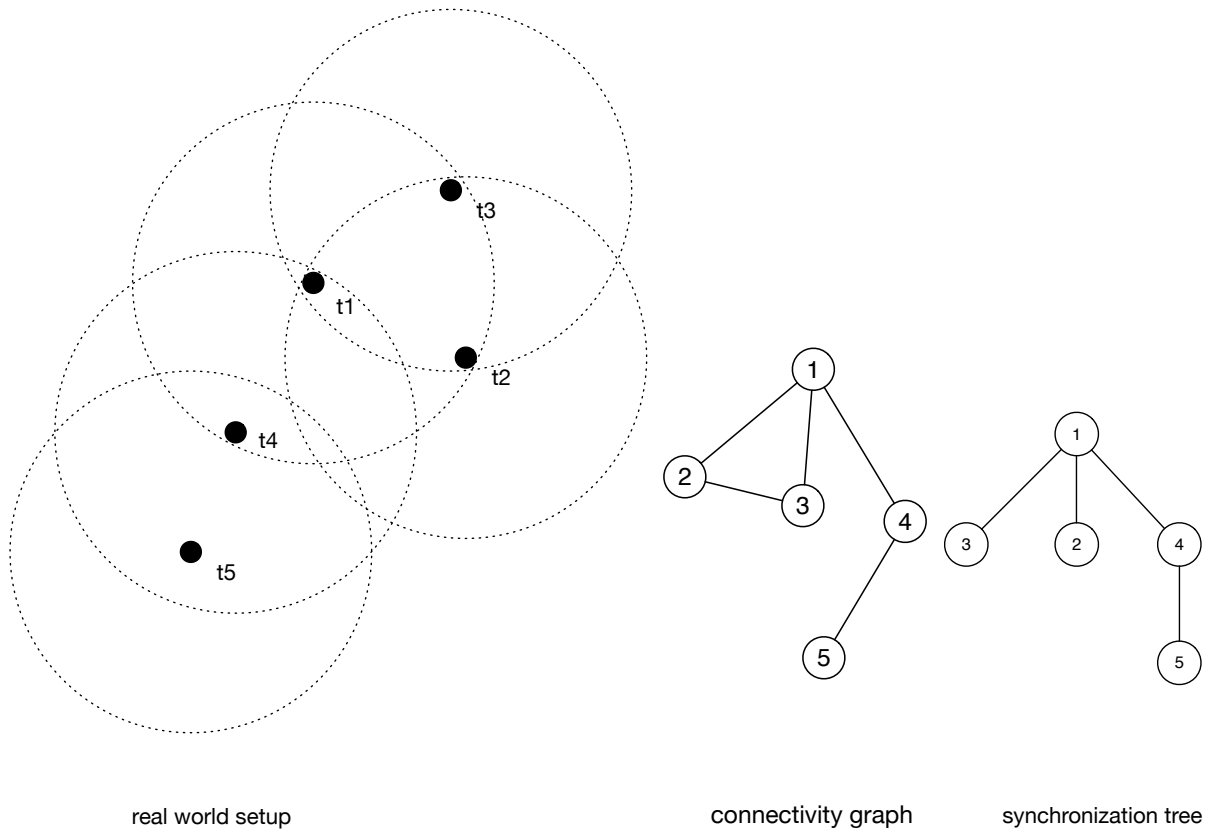


Figure 6.2: Real world position of sensor network nodes with their RF transmission range on the left hand side, in the center the corresponding connectivity graph, the estimated synchronization tree on the right hand side.

After the time synchronization algorithm has been finished, the measurement cycle is performed on the nodes. The transmitters estimate the start times of their measurement slots using the transmitter list derived from the transmitter node discovery algorithm. The receiver estimates the start times of all transmitters. All nodes start the sampling as calculated and corresponding to their local clocks.

In [PL12] we explained and evaluated this synchronization approach, in larger scale setups or hazardous environments (RF signals are attenuated by walls alternatively, persons), the message exchange of the distributed algorithms are hindered or distorted resulting in packet losses.

This leads to inconsistencies in the time server related data structures and the local transmitter sequence data structures. Due to this, the local clocks are not correctly set, and nonvalid



Figure 6.3: Deformed tree to estimate the timing offset introduced by using a hierarchical synchronization approach. The nodes t_i synchronize their clocks with t_{i-1} , t_1 with t_{Center} .

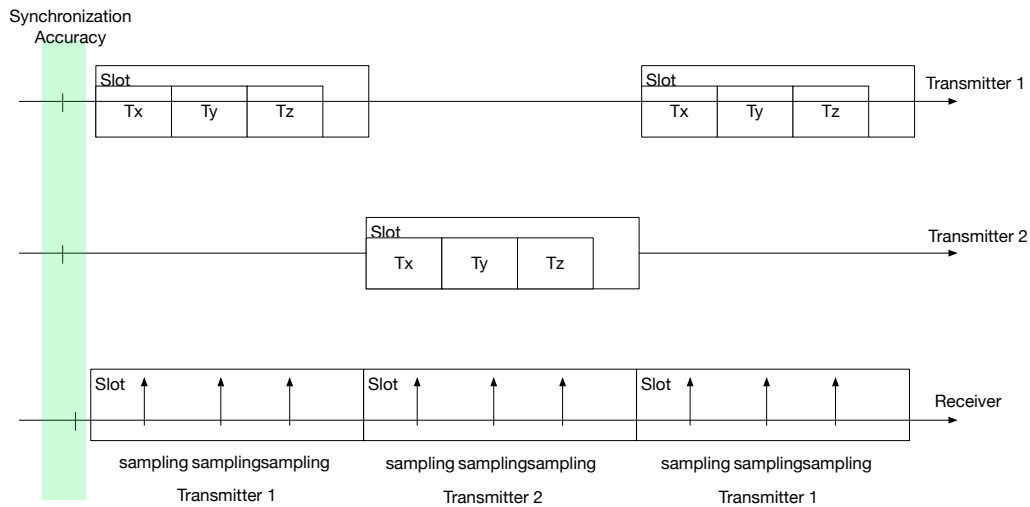


Figure 6.4: Sampling procedure for two transmitters and one receiver. The nodes have synchronized their real time clocks and achieved the synchronization accuracy as shown by the green area. The nodes estimate their start times of the measurement slots and generate the magnetic fields correspondingly. The receiver also estimates the start times and links the sampled values to the transmitter using the information derived from the node discovery algorithm.

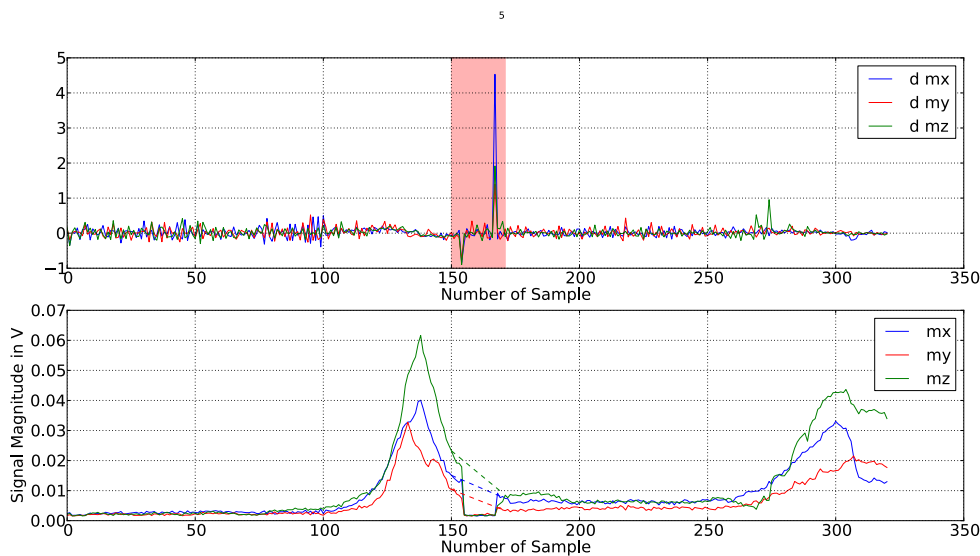


Figure 6.5: Due to information inconsistencies in the information exchange caused by missing or delayed messages, the local clocks of the nodes are not correctly synchronized and cause signal interruptions (lower signal plot). Using the first derivative (upper signal plot) of the signals allows to detect the peaks and then discard the measurements.

magnetic measurements are performed. Looking at the trajectories of successive measurements to certain transmitters show that there are signal interruptions which can be detected in the first signal derivative. An example of this problem is presented in figure 6.5.

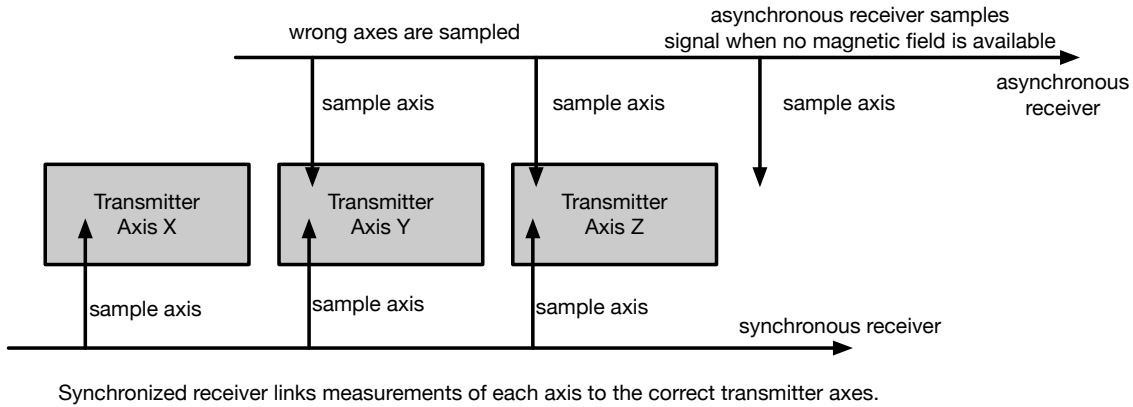


Figure 6.6: If a receiver is asynchronous to the transmitter, this results in timing offsets of the sampling times. In extreme cases, it is possible that one or more sampling buffers cover areas outside the correct transmitter axes and therefore result in wrong measurements.

Although achieving good results in the estimation of regions of interest (see publication [PL12]), inaccuracies in the signal detection and synchronization mechanisms arise from these problems:

Information Inconsistencies The message exchange is based on data collection (node discovery), if transmitters cannot estimate the correct set of transmitters \mathcal{T} which are currently in the sensor network, they will start their magnetic field generation at the wrong time slots. The same effect is achieved on the receiver side, the receiver links measurements to wrong transmitters and therefore return incorrect measurements.

Time Synchronization The system requires a synchronization of the nodes' real time clocks to about $200\mu s$ to $300\mu s$. Although additional safety values have been added to the measurement cycles, the overall slot length of $20ms$ is not long enough to suppress the effects of asynchronous clocks. If the RTC of transmitters are asynchronous, the transmitters generate magnetic fields at wrong times. This results in superposition of neighboring transmitters' magnetic fields. It is also possible that the sampling time at the receiver side is not within the artificial magnetic field time interval as depicted in figure 6.6.

Scalability Due to the high number of broadcast messages, the RF channel will be overloaded if a large scale setup is used. The Zigbee module allows transmitting around 200 messages (when no other task is run on the microcontroller). If additional tasks have to be executed in addition to the RF module service, the number of messages transmitted drops to 100. This means, that the micro-controller of the time-server can handle up to around 15 nodes assuming six packets per time synchronization sequence. Also, the request response-based time synchronization mechanism is prone to this. Also, the memory consumption on the transmitter side increases as the connectivity graph and the sampling sequence has to be maintained.

6.2.3 Conclusion

We discussed in this section and chapter 4.7 different synchronization approaches to achieve a clean separation of different transmitter measurement slots. The synchronization approaches are required to determine the correct transmitter axis signal link on the receiver side. We presented RF-based and magnetic field-based approaches. All approaches have to deal with similar packet loss rates of up to 5 percent, the central RF-based trigger approach can achieve the highest position estimation rate but introduces a single point of failure. Decentralized / distributed algorithms for triggering and clock synchronization have been described; they can reach similar position estimation rates than the centralized RF trigger algorithm, but they put the extra burden on the transmission channel as the distributed approaches have to maintain local information about the sensor sets.

A different approach, solely relying on magnetic fields, encodes synchronization and transmitter id information in the magnetic field and therefore does not require any RF communication between the transmitters and the receivers. A drawback is that the measurement slots have to be widened as the information and synchronization approach require more time.

For small scale setups (several rooms) with low RF influences, the centralized RF trigger approach is preferable, in larger setups like in industrial environments introducing many unpredictable influences, the magnetic field-based synchronization moreover, triggering approach is more reliable but reduces the position estimation rate.

6.3 Transmitter Scheduling

Using magnetic fields for position estimation requires dedicated measurement slots for information modulation and data consistency. A key requirement in ubiquitous and pervasive applications is a minimum position update rate of 1 Hz. To avoid superposition of magnetic fields from different transmitters, scheduling algorithms have to organize the access to the medium. The used scheduling algorithm has, as already mentioned in the previous chapters, to take the reduced memory, processing power and bandwidth of the sensor nodes into account. Additionally, the algorithms influence the provided sampling rates.

6.3.1 Round Robin

In our eyes, the simplest scheduling algorithm in sensor networks which avoids the superposition of magnetic fields is the round robin algorithm (see for example [Tan07]). It exclusively allocates the time slot for a single transmitter and can be implemented using a token passing approach. The round robin scheduling does neither use any information about the spatial setup nor magnetic field coverage of the magnetic field localization system; it only requires the number of transmitters and their ids to relate the sampling slots to the corresponding transmitters. A measurement cycle consists of the sequence of m measurement slots (with m

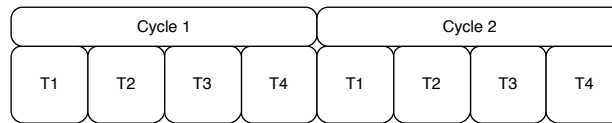


Figure 6.7: An example of two measurement cycles for a round robin-based schedule. In each slot a single transmitter is triggered.

unique transmitters), each of the slots is exclusively and explicitly assigned to a transmitter. A cycle therefore takes $m \times t_{slot}$. The position update rate of the round-robin-based scheduling approach is $\frac{1s}{m \times t_{slot}} Hz$ where m is the number of active transmitters in the localization system.

In applications with a small number of transmitters, this approach is preferable as the application room is covered by multiple transmitters which require separate measurements slots.

Increasing the number of transmitters and the covered area leads to lower position update rates as the position estimation frequency is directly linked to the number of transmitters. Thus for larger setups, it is not possible to ensure a minimum position estimation rate of 1 Hz, as the cycle time linearly rises with the number of transmitters used in the setup. Both memory and processing resources are low. This algorithm has been implemented on the transmitter micro-controllers. In a distributed way, the algorithm detects new transmitter nodes and the disappearance of nodes as presented in the previous chapter. Messages collecting information about currently available nodes are passed between the nodes, the transmitters build up a token ring, the scheduling order can, for example, be sorted according to rising transmitter ids.

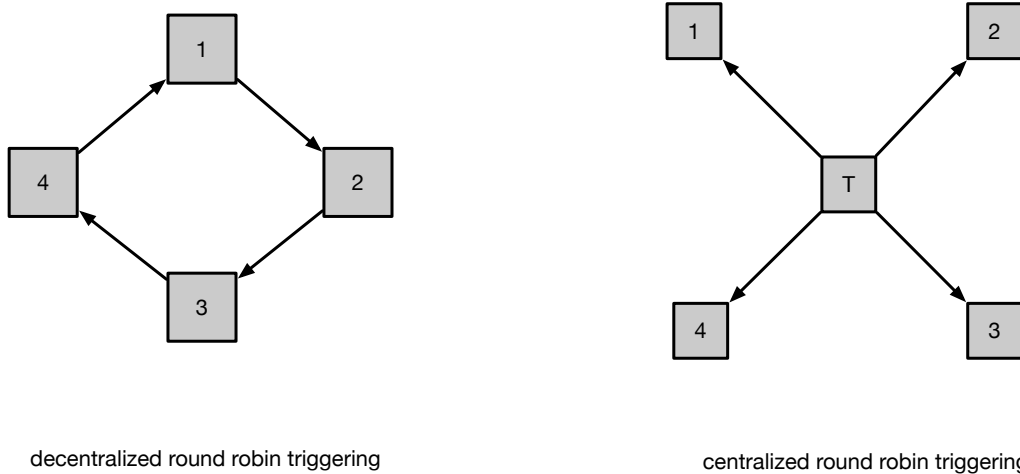


Figure 6.8: Round robin-based scheduling. Left: a decentralized token ring. The nodes pass a message to the neighbor, the node currently holding the message is allowed to generate the magnetic field. Right: centralized round robin approach, a trigger node holds a list of the transmitters and sends a message to the current transmitter.

To reduce the communication effort, we also implemented a centralized round-robin scheme in which a central node holds a list of the active transmitters and triggers the transmitter nodes according to the scheduling sequence.

6.3.2 Graph Coloring-based Scheduling

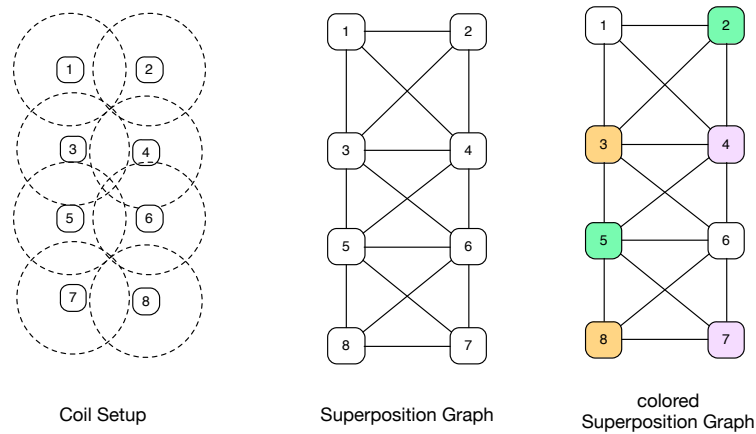


Figure 6.9: Example of a real world setup, the corresponding Superposition graph and its colored version. Compared to the round-robin approach (8 measurement slots), the graph coloring scheduling only uses four measurement slots in a cycle to perform the position estimation.

The round robin approach showed limitations with regard to the position estimation rate. To solve these limitations, the limited range of magnetic fields and spatial arrangement of transmitters are taken into account. The magnetic field emitters support a maximum range of 4

6 Multi Coil Position Estimation

- 4.5m. The basic idea of the following algorithm is to simultaneously trigger transmitters if their generated magnetic fields do not superpose. To avoid this, the transmission ranges of the transmitters must not overlap each other.

In the first step the spatial setup (positions of the transmitters) are considered and used to calculate the so called **Superposition Graph** \mathcal{S} . The Superposition Graph $\mathcal{S} = (\mathcal{N}, \mathcal{E})$ consists of the transmitters (Nodes) $\mathcal{N} = \{t_i \mid t_i \in \mathcal{T}\}$ and edges between the nodes if these nodes share overlapping transmission areas $\mathcal{E} = \{(t_i, t_j) \mid \|\mathbf{p}_{t_i} - \mathbf{p}_{t_j}\| < 2 \times d_{max}\}$, where \mathbf{p}_{t_i} is the position of the transmitter t_i .

The Superposition Graph is then used to generate a schedule of the transmitters: We transfer the scheduling problem of magnetic field emitters to the issue of graph coloring. The graph coloring problem is an \mathcal{NP} hard problem which tries to efficiently color the nodes in such a way that all neighboring nodes of a node have other colors than the currently chosen node. Among other properties of the coloring problem, the number of different colors (chromatic number) is limited by the maximum numbers of neighbors of a node. As the problem is \mathcal{NP} hard, only heuristics are available to solve the coloring problem (for example [Klo02]).

Even for our small scaled setups with only up to 20 nodes, it is not possible to use the brute force approach to color the node. Therefore we apply the following algorithm, which is faster but is not returning in all cases an optimal coloring of the graph:

The **center** of a graph is the node which has the highest number of neighbors.

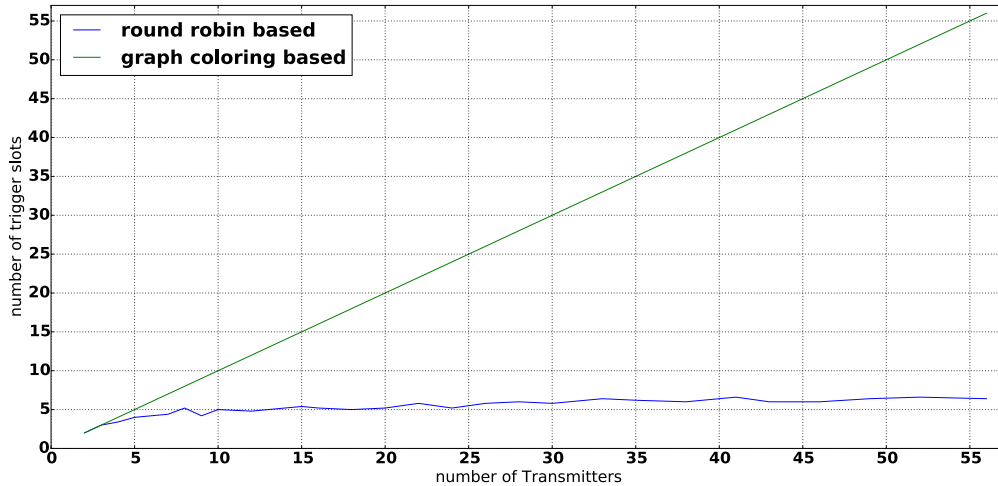


Figure 6.10: Comparison of round-robin-based scheduling and Superposition graph coloring-based scheduling. Especially in large setup, the graph coloring-based approach requires a low number of measurement slot and therefore allows higher position estimation rates than the round-robin-based scheduling.

Nodes with the same color are then simultaneously triggered, therefore a speedup in the position estimation due to the reduction of the number of measurement slots in the cycle can be achieved in most real world cases.


```

Members:
 $\mathcal{S} = (\mathcal{N}, \mathcal{E})$ , Superposition Graph
 $\mathcal{N} = \{t_i \mid t_i \in \mathcal{T}\}$  Transmitters in the setup
 $\mathcal{E} = \{(t_i, t_j) \mid \mathbf{p}_{t_i} - \mathbf{p}_{t_j} \mid < 2 \times d_{max}\}$  Edges between transmitters
 $\mathcal{C}_{\mathcal{N}} = \{c_0, \dots, c_n\}$  colors of the transmitters. nodesToColor List of nodes which are currently in
the coloring process
input :  $\mathcal{C}$ 
,initially each color set to -1
output :  $\mathcal{C}$ 
,a correct color list, each neighbor node is differently colored.

for each strongly connected subgraph
for each strongly connected subgraph do
    estimate the center C of the graph and the number of neighbors of the center C
     $C.color = 0$ 
    add all neighbor nodes to the nodesToColor list
    while  $len(nodesToColor) \neq 0$  do
         $n = pop(nodesToColor)$ ; // remove the first element get the smallest color  $c_s$  which is
        not used in the n.neighbor
         $n.color = c_s$ 
        add all uncolored neighbors of n to the nodesToColor
    end
end

```

Algorithm 2: Graph Coloring-based Scheduling, (comparable to Sequential Coloring [Klo02],chapter 3)

Figure 6.9 provides an example of a schedule generated using the graph coloring approach. Notice that in a graph with eight nodes two or more nodes can simultaneously be pulsed.

A simulation has been implemented to compare the performance of the round-robin-based approach with the graph coloring scheduling approach. We define a measurement area A_e . Each transmitter has a circular transmission area defined as $A_t = d_{maxRange}^2 * \pi$. To uniquely estimate the position of the receiver, three transmitters are necessary. The number of transmitters for the simulation area is therefore given by $\mathcal{T} = 3 \times \lceil \frac{A_e}{A_t} \rceil$. The transmitters are then randomly positions in the measurement area. Setups which make no sense (high number of transmitters close to each other...) are filtered out, the positions of the transmitters have to be at least 80 percent of the maximum transmission range apart and within the transmission range of the transmitter a maximum of 2 other nodes are allowed. If these restrictions cannot be fulfilled a new measurement area is generated and transmitters are again randomly spread over the area.

After this, the Superposition Graph of this environment is generated as previously described. We apply the coloring heuristic and compare the results against the round-robin-based approach. The measurement area is a cube-shaped area, with edge length between 5m and 35m, which is increased in 1m steps.

Figure 6.10 shows the result of the simulation. The number of triggering slots for a round-robin-

based schedule linearly rises with the number of transmitters in the environment. For larger environments, the graph coloring-based scheduler returns schedules are much faster than the round-robin-based approach.

6.4 Multi Coil Localization Approaches

In chapter 2.1.3 we saw different larger scale localization approaches suitable for multilateration systems. These systems depend either on lateration or angulation algorithms. To stabilize the position estimation, different filter methods such as Kalman filters or Monte Carlo methods are applied.

Our localization system also depends on magnetic field derived distance information to different magnetic field transmitter anchor points. We describe and evaluate in this different chapter approaches which are suitable for position estimation. This covers fingerprinting on raw signal values (without the need for generating a magnetic field model), multilateration and candidate algorithms for position estimation and regions of interest estimation based on distance and positions. The fusion of the different position estimation algorithms achieves a mean position error of 62.7cm.

The estimation of regions of interest provides semantic proximity information; the lateration-based localization algorithms give higher resolution without the setup and calibration complexity of fingerprinting approaches. In contrast to regions of interest where a discrete number of ROIs are defined and usable, the Cartesian positions are not only linked to the semantic regions but are available in the complete covered area.

6.4.1 Data Set for Position Accuracy Evaluation

For qualitative position error estimation using multilateration and candidate algorithms, we recorded a data set in the ambient assisted living lab BAALL. 6 magnetic field transmitters (cube coils) have been placed in the apartment at the corners of the simulation environment. The positions of the transmitters have been chosen in such a way to guarantee at least two transmitters visible during a measurement.

We place the receiver at 20 different, randomly chosen positions in the $12m \times 8m$ area. The heights of the reference positions are also varied. The exact coordinates are measured using a laser meter. At least 300 measurement rounds (all six transmitters are triggered) are recorded at each measurement position. The system is RF triggered and centrally controlled. After data recording, the measured induced voltages are transformed into candidate position information and distances as presented in the previous chapter. The data set is then applied to the different position estimation algorithms. Evaluation against the reference positions allows to determine mean position error and standard deviation of the different approaches.

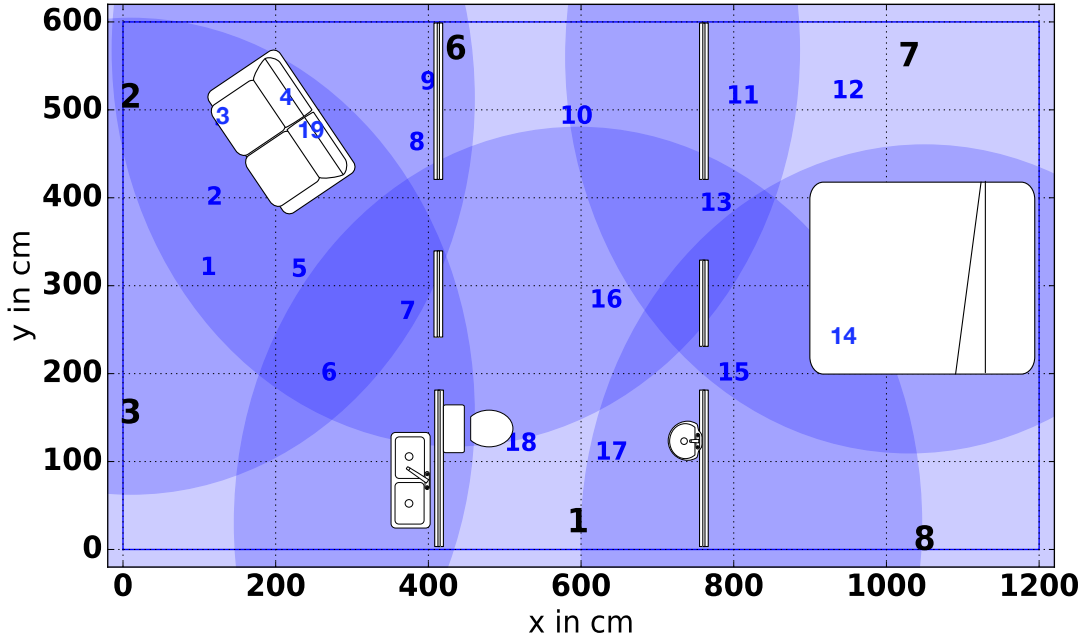


Figure 6.11: Room layout out and position of the transmitters in the assisted living lab in Bremen. The positions of the transmitters should support in each point of the environment at least two visible transmitters.

6.4.2 Candidate Points

The architecture of the transmitter coils restrict the position to 8 points around the transmitter coil in the eight octants each. Although the accuracy is restricted ($(\mu = 117cm, \sigma = 87.45)$ for the cube-based approach), we want to evaluate if the candidate sets can be used for position estimation. Especially when only a low number of magnetic field measurements in a measurement cycle is available, the usage of candidate positions is interesting although being inaccurate.

Geometrical Approach

The candidate sets have an advantage compared to the distance or angle-based localization approaches: The relative position against a transmitter coil is already available. Combining the candidate sets from different transmitters can therefore be implemented more efficiently compared to for example lateration approaches. The basic idea of the geometrical approach is to find a candidate position from each transmitter measurement set which is closest to the receiver position. This means, that the chosen candidates themselves have minimum distance to each other.

Let $\mathcal{T} = \{t_i\}$ be the set of transmitters where valid measurements are available. Let $\mathcal{C}_i = \{\mathbf{c}_i \mid i \in 1 \dots 8 \wedge t \in \mathcal{T}\}$ be the candidate set of transmitter t in the world coordinate system. $\mathcal{C} = \{\mathcal{C}_j \mid j \in \mathcal{T}\}$ is the set of valid candidate sets of the current measurement round. Let

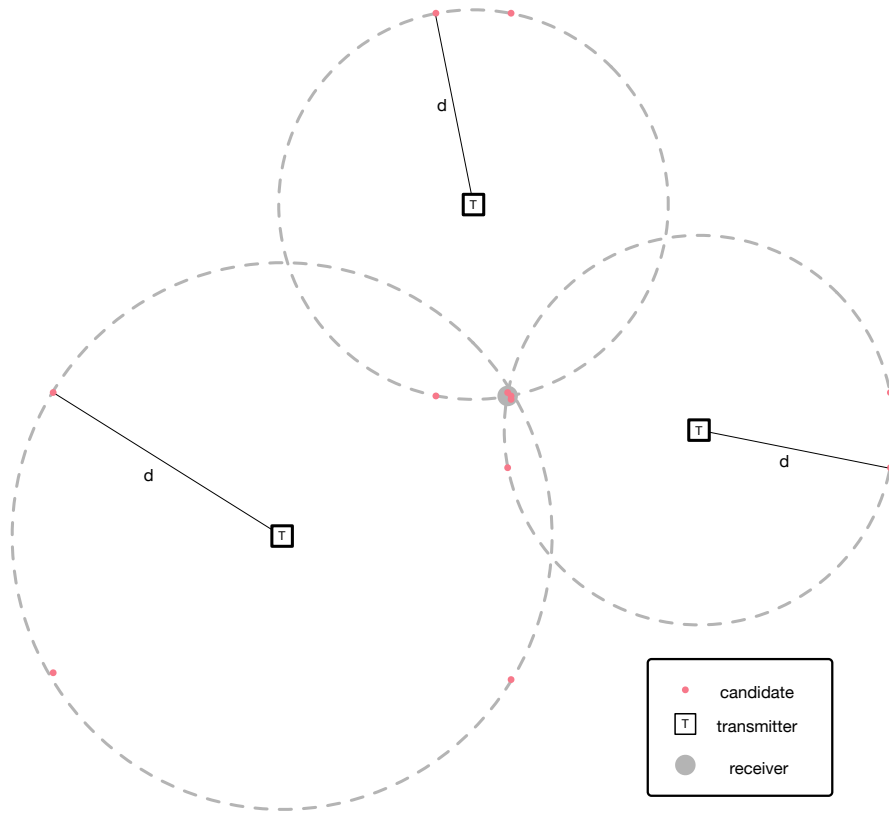


Figure 6.12: Position estimation using candidate and distance information.

$\mathcal{I} = \{a, b, c, \dots, n \mid n = |\mathcal{C}|\}$ be the indexes of the currently chosen candidate positions of each candidate set $c_a^t \in \mathcal{C}_t$ of the current measurement. Let

$$\mathbf{z}_{\mathcal{I}} = \frac{\sum_{i=0}^n \mathbf{c}_i}{|\mathcal{C}|}$$

be the center of the currently chosen candidates. The measure for choosing the best candidates is

$$d_{sum} = \sum_{i=0}^n \|\mathbf{z}_{\mathcal{I}} - \mathbf{c}_i\|$$

By evaluating each combination of the elements of the different candidate sets, we find the combination of candidates of the different transmitters which have the minimum distance to their center $\mathbf{z}_{\mathcal{I}}$ and therefore to each other. The center \mathbf{z} is also the estimated position using the candidate localization.

Figure 6.12 depicts an example of this approach, the estimated candidates are situated around their transmitters, the gray circle indicates the position of the receiver. The three candidates close to the receiver would be chosen by our algorithm.

Evaluating the data set presented in section 6.4.1 results in a poor localization quality: the mean error $\mu = 186.07cm$ with a standard deviation of $\sigma = 90.93$.

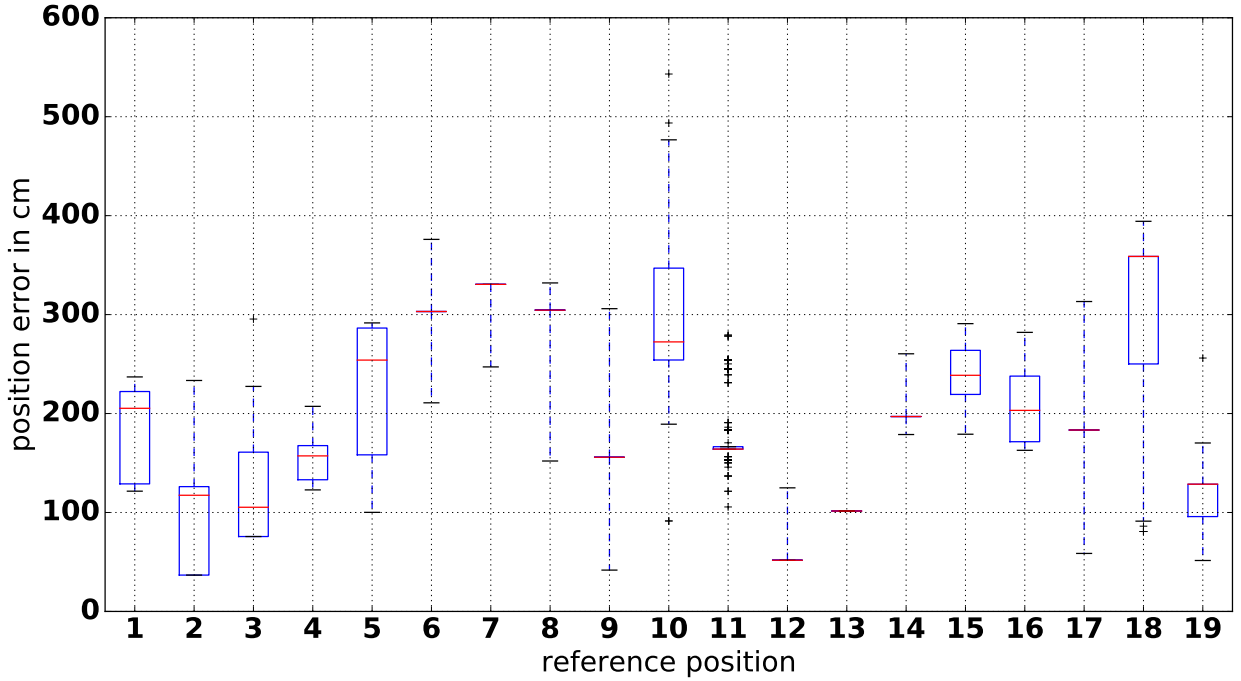


Figure 6.13: The candidate position estimation has a mean error of $\mu = 186.07cm$, $\sigma = 90.93$

The high position errors are the results of two issues:

In a cycle with a single valid transmitter measurement, the wrong candidate is chosen.

If we choose the closest candidate to the reference position this reduces the position error to $\mu = 176.86cm$, $\sigma = 87.95$.

The high candidate position error strongly influences the position of the center of the chosen candidates. Angular offsets (when the position is described by spherical coordinates relatively to the transmitter) are not considered. A function which favors smaller distances is $d' = (1 - \frac{d}{\sum d_i}) * d$. This still does not significantly reduce the error rate: $\mu = 180.12cm$, $\sigma = 84.33$.

Probabilistic Approach

Another possibility of estimating the receiver position is the usage of statistical methods. In the model evaluation we estimated the position error distribution of the candidates. We assume that the error is normally distributed $\mathcal{N}(\mu = 117cm, \sigma = 87.45)$.

Let \mathbf{x} be a 3D coordinate in the measurement environment,

$$p(\mathbf{x}) = \prod_{i=0}^n \mathcal{N}(\|\mathbf{x} - \mathbf{c}_i\|, \mu, \sigma)$$

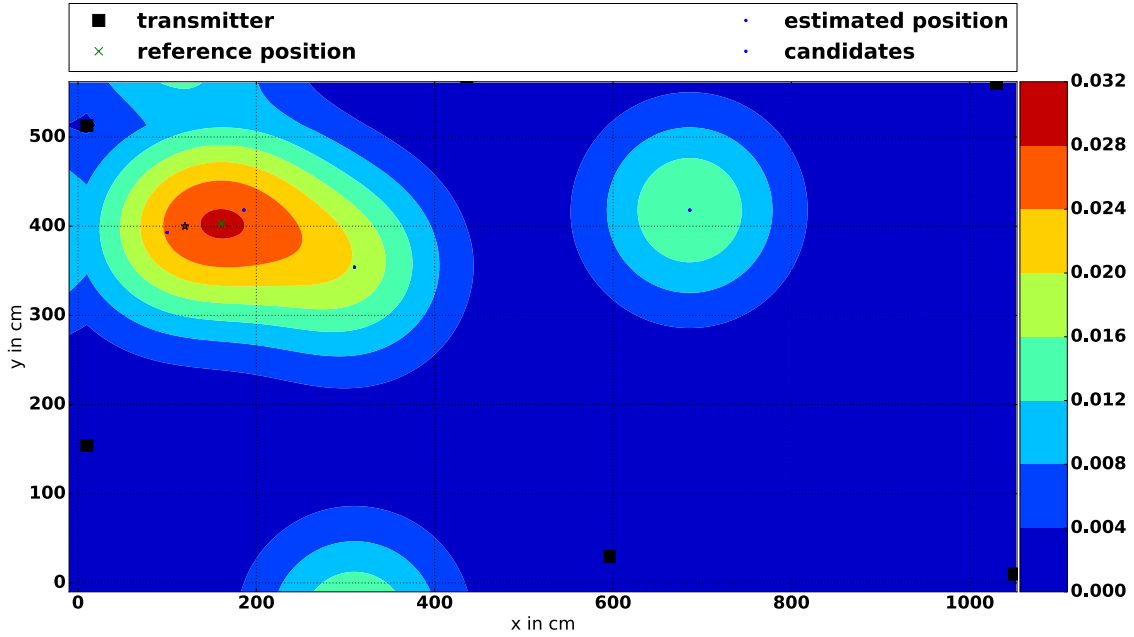


Figure 6.14: Example of a probability distribution of candidate sets. Position error 41.1cm.

describes the probability of the position being the position of the receiver. The position of the receiver is then the maximum probability p_{max} :

$$p_{max} = \max(p(\mathbf{x})), \mathbf{x} \in Environment$$

The evaluation of this mixture of Gaussians for a large environment is time-consuming as the maximum probability has to be found. A brute force algorithm has been used to estimate the positions of the test data set. The accuracy of the position estimation was slightly better than the geometrical approach: ($\mu = 170.2cm, \sigma = 84.3$). Due to the high processing effort, we favored the geometrical approach.

The evaluation of the data set with the described algorithm showed that the position estimation accuracy depending on candidate sets is not that accurate as the estimation using multilateration algorithms. Neither distance weighting nor information derived from statistical evaluation helps to reduce the positioning error.

Still, there is a field of application: The multilateration algorithm requires measurements from two or more transmitters, a measurement round with a single measurement therefore only reduces the position to a sphere around the transmitter. The candidate approach, in combination with a tracking algorithm, can, therefore, provide more information in a single coil measurement cycle than the pure distance-based approach.

6.4.3 Multilateration

Chapter 5.4.3 describes the magnetic field-based distance estimation. In contrast to the candidate 3D positioning, the distance estimation is more stable and introduces less error in addition to a lower standard deviation. Especially in an area with a dense transmitter placement, allowing to determine the distance to at least two transmitters, distance-based localization offers a robust 3D positioning and tracking of the wearable receivers.

In this section we describe three approaches, namely **the least square minimization approach** and a **particle filter-based on distance estimations** and an **approach utilizing circle intersections**. In the case of the Monte Carlo method, we describe the weight function taking the statistical evaluation of the previous chapter into account. Additionally, the algorithms are evaluated with regard to accuracy and repeatability.

Probabilistic Approach

A method often found in literature depends on probabilistic methods. We implemented a Monte-Carlo method with 150 particles using the known error distribution of the distance estimations derived from the calibration process. We combine the distance estimations of a measurement round to estimate the receiver's position.

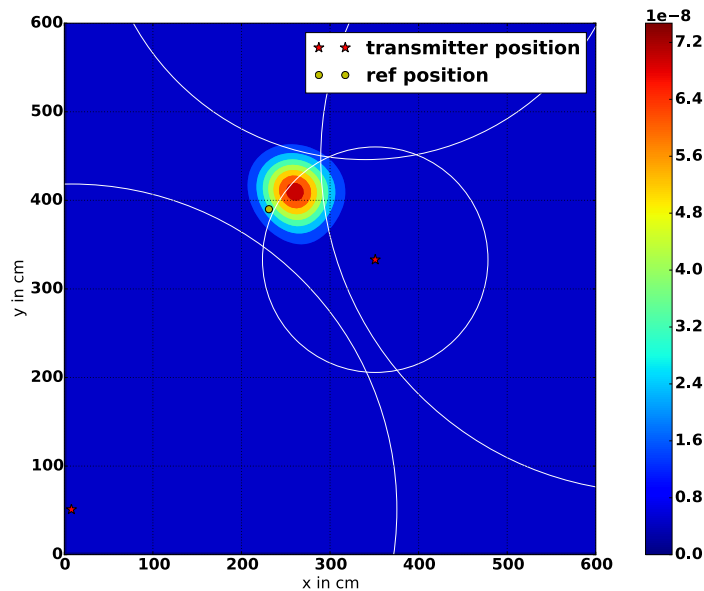


Figure 6.15: Maximum likelihood estimation of 4 transmitters with given distances to the transmitters. The used mean error of the distance estimation is 0, the standard deviation is 40. All transmitters are equally favored.

The used particle filter $\mathcal{P} = \{p_i \mid i = 1 \dots n\}$ consists of a set of particles $p = (x, y, z, v, \rho)$ describing the position (x, y, z) of the particle, its speed v and absolute heading ρ in the world's

coordinate system.

Initialization Initially, the positions and the heading of the particles are randomly chosen. The positions of the particles lie within the boundary of the measurement environment; the heading angle is in $[0, 360]$ degree.

Particle Movement Before the particle evaluation can take place, the particles are moved according to their internal speed and heading state. Both variables are also adapted using a random Gaussian value distribution to represent measurement noise.

Distance Processing The set of magnetic field distance estimations $\mathcal{D} = \{d_i \mid \|\mathbf{t}_i - \mathbf{r}\| = d_i, i \in [0, n]\}$ holds all distances derived from the receiver side position \mathbf{r} to the transmitters \mathbf{t}_i which are within the sensing range of the magnetic field receiver.

We evaluate all particles against the distance set \mathcal{D} :

Let \mathcal{W}_j be the provability of particle j for the given distance set \mathcal{D} , where \mathcal{W}_j is:

$$\mathcal{W}_j = \prod_{i=0}^n \mathcal{N}(\|p_j - \mathbf{t}_i\| - d_i, \mu_i, \sigma_i) \quad (6.6)$$

Equation 6.6 is the initial form of the particle probability function used in our particle filter. It evaluates each particle whether its position and therefore its distance to the transmitter t_i fits the estimated distance d_i . The center μ of the Gaussian probability function $\mathcal{N}_{(\mu, \sigma)}$ describes the mean distance error of the transmitter t_i .

As the distance estimation errors vary over die distances, we implemented a more complex evaluation function, which represents the distance error functions of the transmitters more accurately:

$$\mathcal{W}_j = \prod_{i=0}^n \mathcal{N}(\|p_j - \mathbf{t}_i\| - d_i, \mu_i = 0.3 \times d_i, \sigma_i = 0.1 \times d_i) \quad (6.7)$$

$$\mathcal{W}_j = \prod_{i=0}^n \mathcal{N}(\|p_j - \mathbf{t}_i\| - d_i, \mu_i = 0.0, \sigma_i = 0.1 \times d_i) \quad (6.8)$$

Equations 6.7 favors particle positions which are further away than the estimated distance, this probability function is applied if the estimated distance is below $1m$, if the estimated distance is above $1m$, equation 6.8 is used, which broadens probability ring around the transmitter depending on the distance. We intentionally do not normalize the probability of each distance estimations in order to favor closer distance values which are more accurate than the ones further away.

Figure 6.16 depicts the result of the two equations eq. 6.7 and eq. 6.8. The contour of the probability function is shifted towards the transmitter with lower distance (which is more reliable than the transmitter which is further away).

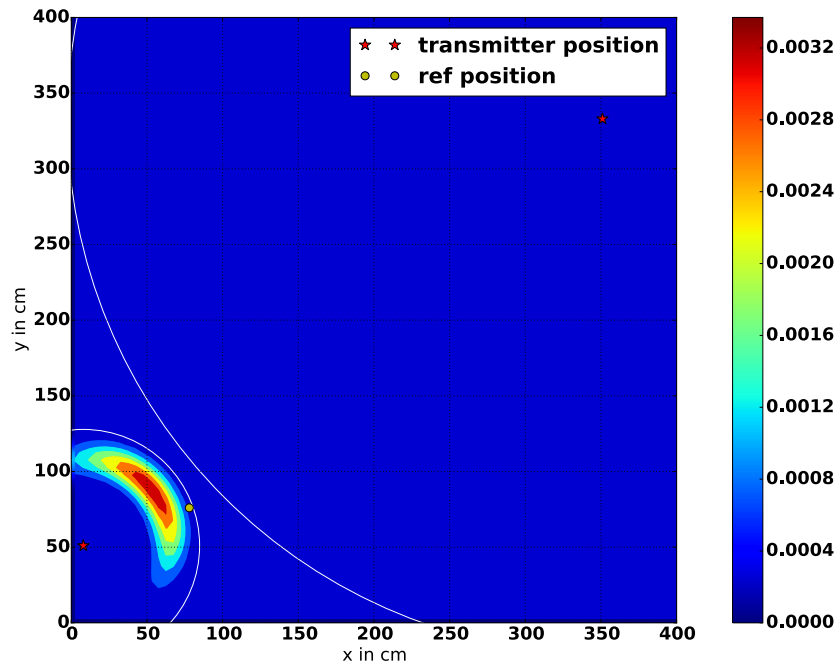


Figure 6.16: More complex probability distribution of the scene. Transmitters with lower distance values are favored for higher distance transmitters.

After the probability evaluation of all particles, the state of the particle filter is updated: the current position is the weighted mean value of the 20 best particles.

Resampling In the resampling phase, the weighted particles are sorted in ascending order and half of the particle set is randomly cloned. The 25 best particles are cloned as well. After this, the particle set is again order according to the particle weights. Finally, the supernumerary particles (the particles with low probability) are removed.

We create for each measurement point a new particle filter with randomly initialized particle positions. The overall mean error of the lateration particle filter is ($\mu = 172.30cm, \sigma = 66.16$). The reasons for the error rate is:

If single distance measurement cycles are used, the distance results in a probability ring around the corresponding transmitter. Particles which accidentally have the corresponding distance to the transmitter are weighted with comparably high probability as the particles which correspond to the real position of the receiver. Also, two distance estimations can result in a faulty positions guess: The particle distribution can lead to cases in which the estimated position jumps between the two intersections of the distance circles as one intersection is as likely as the other (pos. 7 and 14). Therefore a tracking algorithm should be used relying on the combination of all available information (intersections + distance estimations) moreover, which converges faster and therefore avoids the oscillation between the two intersections of two distance measurements.

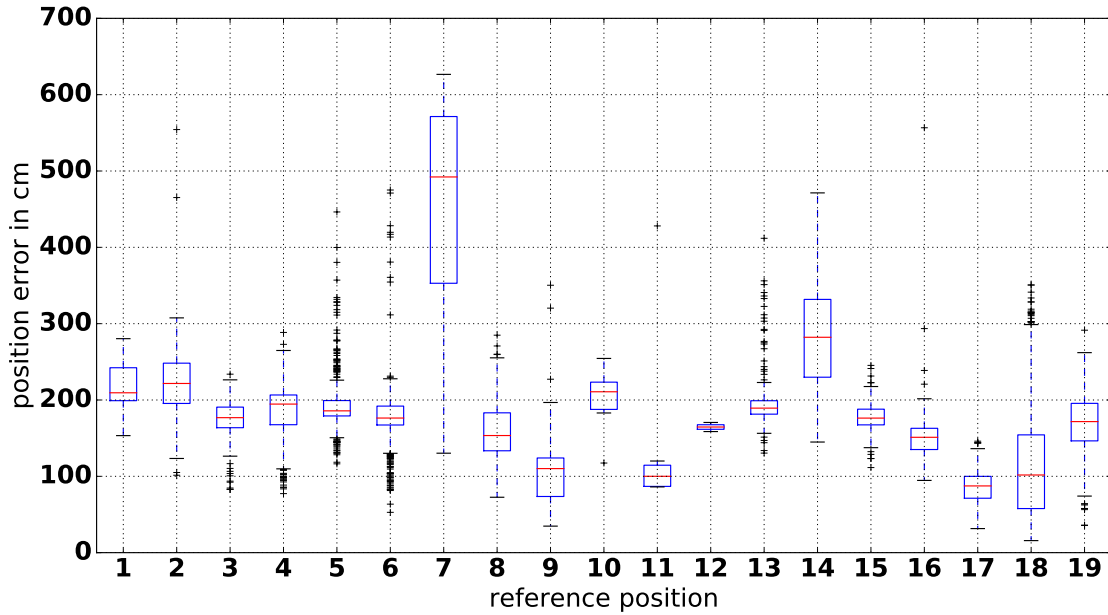


Figure 6.17: Error distribution of the lateration particle filter. The overall mean error and standard deviation is ($\mu = 172.30\text{cm}$, $\sigma = 66.16$),

Least Square Error Minimization Methods

Multilateration algorithms rely on distance estimations between anchor points and the measurement devices. In our approach, the magnetic field measurement is transformed into distance estimations between the magnetic field transmitter and the magnetic field receiver. Each distance estimation limits the possible position of the receiver to a circle (in 2D) or a sphere (in 3D) around the transmitter anchor point. Multiple distance estimations result then in a single point if all distance restrictions are taken into account. Due to environmental effects, model inaccuracies, magnetic field distortions and hardware related false measurements, it is possible that the estimated circles do not intersect in a single point, either because of distances being too big or too small.

To overcome this problem we describe a least square optimization algorithm (Levenberg Marquardt-based), which tries to find a point in space whose distance fits best to the distance estimations against the transmitters:

Let $\mathbf{r} = (x, y, z)$ be the position of the receiver, $\mathcal{T} = \{\mathbf{t}_i = (x, y, z)_i\}$ be the set of transmitter positions, $\mathcal{M} = \{d_i \mid d_i = \|\mathbf{r} - \mathbf{t}_i\|, t_i \in \mathcal{T}\}$ the set of estimated (faulty) distances between the magnetic field receiver and the transmitters. The residual function which should floor plans is

$$\mathcal{R}(\mathbf{r})_{\mathcal{M}} = \sum_{d_i \in \mathcal{M}} \left| \|\mathbf{t}_i - \mathbf{r}\| - d_i \right| \quad (6.9)$$

where \mathbf{r} is a position which is evaluated against the measured distances.

As the least square minimization algorithm itself does not support tracking, the start position

of the algorithm is the result of the previous measurement cycle.

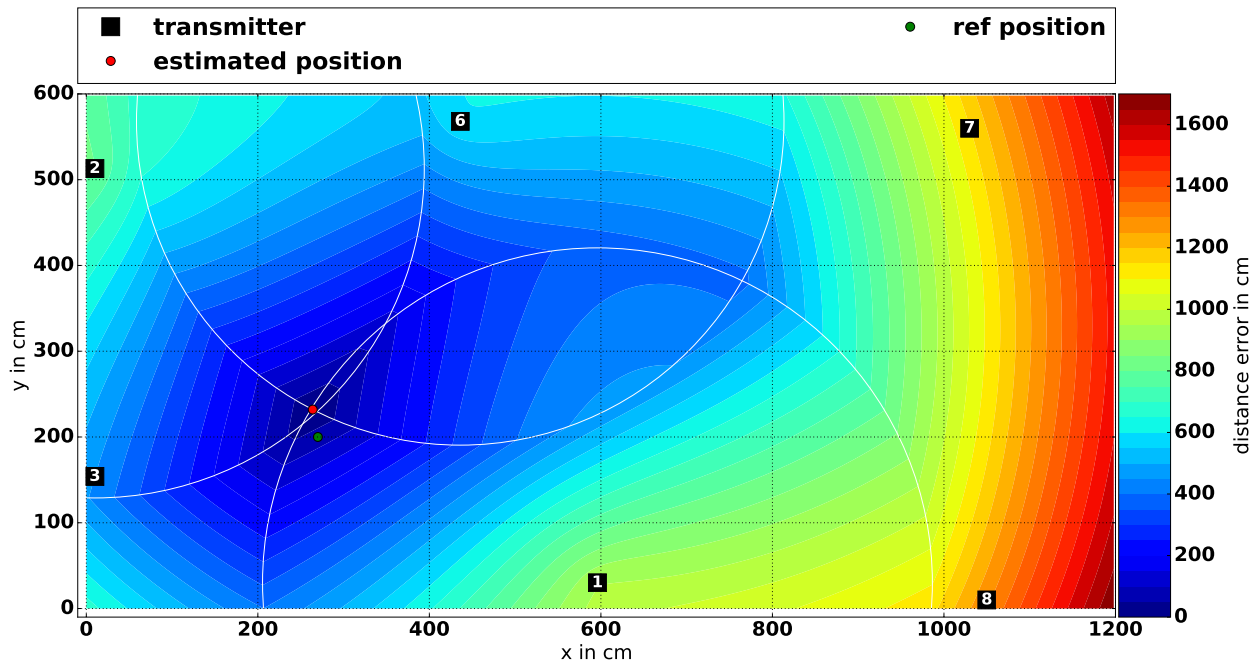


Figure 6.18: Example of the error distribution described by equation 6.9. The the three distance estimations restrict the position of the receiver to the minimum of the error function. In this example the position error is 33.52cm.

Compared to the candidate-based position estimation, both, the overall position error and its standard deviation are reduced. Depicted in the figures 6.18 and figure 6.19, the model evaluation showed a mean distance error of ($\mu = 140.14\text{cm}, \sigma = 164.82$) when all measurement rounds (including single distance measurement rounds) are considered. Filtering these positions out results in a mean error of ($\mu = 98.56\text{cm}, \sigma = 80.97$). Although using the position of the previous measurement round as start point of the minimization algorithm, high position errors are visible. Due to missing tracking abilities, the estimated position is not restricted to close regions around the previous position estimation. Considering the intersection of the two circles described by the distance estimations, it is possible that the wrong intersection point is chosen. This is, for example, the reason for the high position error of reference positions 14 or 11.

Intersection of Circles

If two or more distance estimations to different transmitters are available, the position of the receiver is limited to the position of one of the intersecting points. As previously mentioned, false measurements, errors caused by environmental effects or magnetic field model inaccuracies lead to offsets in the distance estimation. Still calculations of the intersections (figure 6.20) are

6 Multi Coil Position Estimation

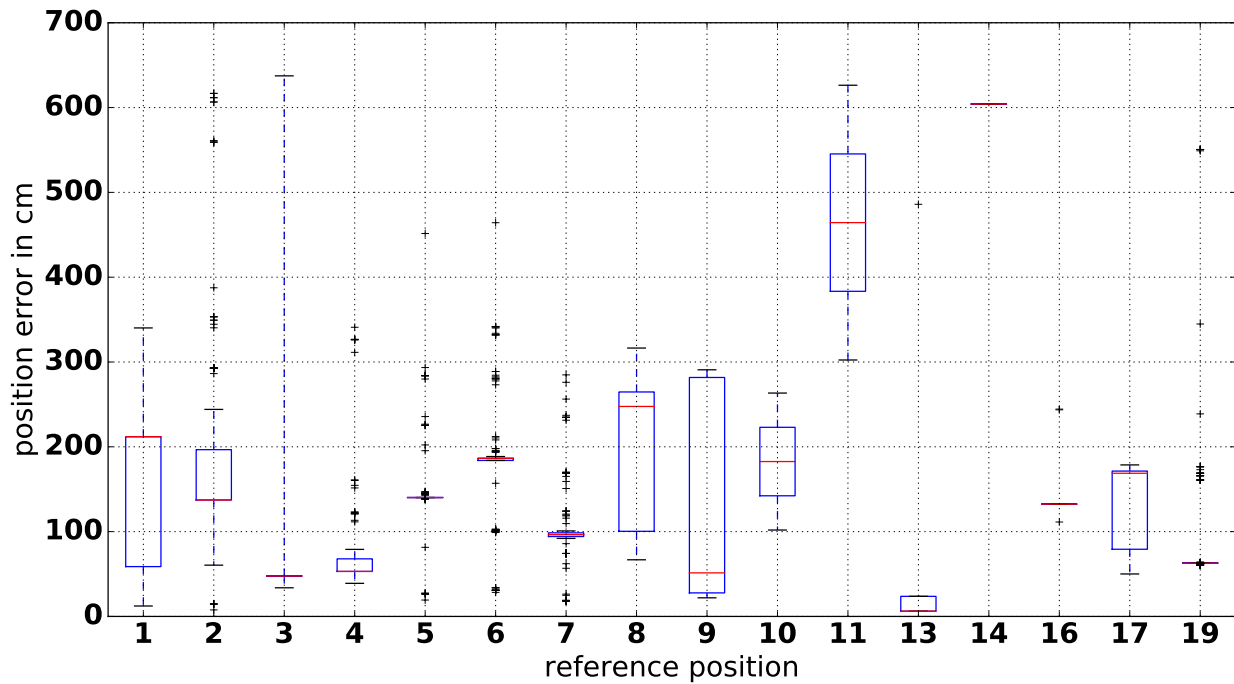


Figure 6.19: Results of the least square minimization algorithm. The mean error and the standard deviation for 3D position estimation is ($\mu = 140.14cm, \sigma = 164.82$) for all measurement cycles including also those with a single distance measurement. Removing those single distance measurement rounds reduces the error to ($\mu = 98.56cm, \sigma = 80.97$). Single transmitter measurements have been removed, therefore reference points are missing.

possible:

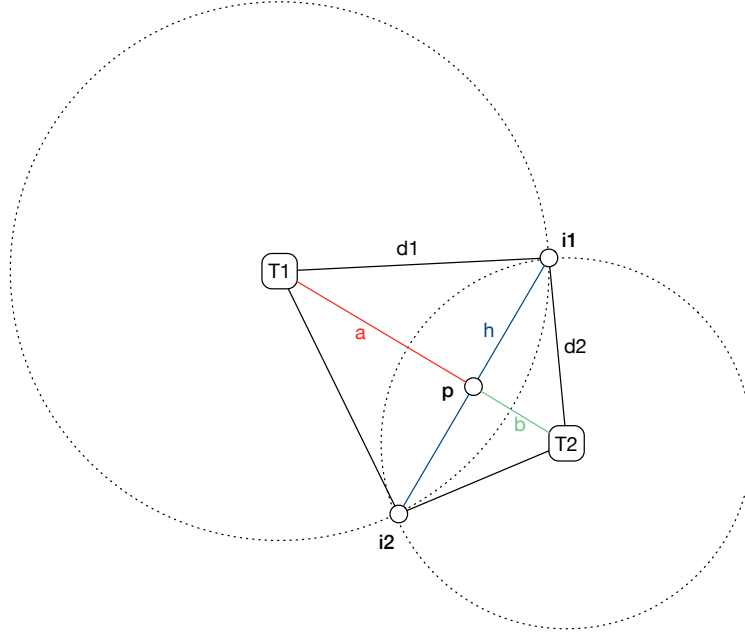


Figure 6.20: Schematic view on the circle intersection problem. Comparable approaches are for example described by Paul Bourke [Pou97]

Let t_1 and t_2 be the transmitters measured with corresponding distances d_1 and d_2 . Let $\mathbf{t}_1 = (x_1, y_1)$ and $\mathbf{t}_2 = (x_2, y_2)$ be the coordinates of the transmitters, $d = \|\mathbf{t}_1 - \mathbf{t}_2\|$ be the distance between the transmitters.

$$a = \frac{d_1^2 - d_2^2 + d^2}{2d} \quad (6.10)$$

$$h = d_1^2 - a^2 \quad (6.11)$$

$$\mathbf{p} = (x, y) = \mathbf{t}_1 + \frac{a(\mathbf{t}_2 - \mathbf{t}_1)}{d} \quad (6.12)$$

The intersections of the two circles therefore are:

$$\mathbf{i}_1 = \left(x + \frac{h(y_1 - y_0)}{d}, y + \frac{h(x_1 - x_0)}{d} \right) \quad (6.13)$$

$$\mathbf{i}_2 = \left(x - \frac{h(y_1 - y_0)}{d}, y - \frac{h(x_1 - x_0)}{d} \right) \quad (6.14)$$

We consider for each measurement round the intersections \mathbf{i}_l of two transmitter measurements (d_i, d_j) , $j \neq i$, where $\|\mathbf{x}_l - \mathbf{t}_i\| = d_i$ and $\|\mathbf{x}_l - \mathbf{t}_j\| = d_j$.

Three cases can occur: there is a single intersection if the two circles touch each other, no intersection, if $d_i + d_j < \|\mathbf{t}_i - \mathbf{t}_j\|$ or two intersections otherwise.

When the two circles do not intersect, we add three additional positions (see figure 6.21) to the intersection list instead of discarding this tuple:

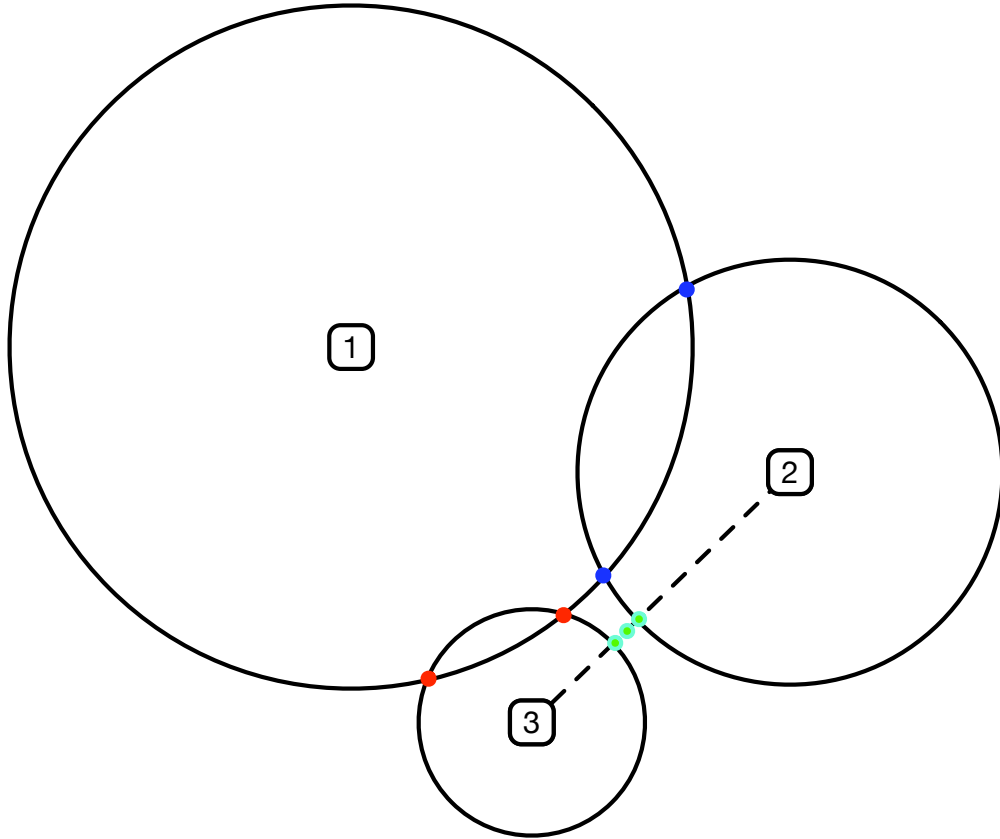


Figure 6.21: Different cases of the intersection of the circles around the corresponding transmitters. The green positions are added when circles would not intersect.

Consider the connection of the two transmitters; two positions are defined by the intersection of the two circle with the connection, the third one is the center of these two positions.

As previously defined, $\mathcal{T} = \{\mathbf{t}_i = (x, y, z)_i\}$ is the set of transmitter positions, $\mathcal{M} = \{d_i \mid d_i = \|\mathbf{r} - \mathbf{t}_i\|, \mathbf{t}_i \in \mathcal{T}\}$ is the magnetic field-based distance measurement set, $|\mathcal{M}| > 1$.

For each transmitter pair $(t_i, t_j), i \neq j$ we define

$$\mathcal{S}(i, j) = \{\mathbf{s}_k \mid \|\mathbf{s}_k - \mathbf{t}_i\| = d_i \wedge \|\mathbf{s}_k - \mathbf{t}_j\| = d_j\}$$

if $d_i + d_j > \|\mathbf{t}_i - \mathbf{t}_j\|$

$$\mathcal{S}(i, j) = \{\mathbf{s}_i, \mathbf{s}_j, \mathbf{s}_m\}$$

where

$$\begin{aligned} \mathbf{s}_i &= \mathbf{t}_i + d_i * (\mathbf{t}_j - \mathbf{t}_i), \\ \mathbf{s}_j &= \mathbf{t}_j - d_j * (\mathbf{t}_j - \mathbf{t}_i) \text{ and} \\ \mathbf{s}_m &= \mathbf{t}_i + 0.5 * (\mathbf{t}_j - \mathbf{t}_i) \end{aligned}$$

$$\mathcal{S} = \{\mathcal{S}(i, j) \mid i \neq j, i, j \in \mathcal{T}\}$$

For each transmitter pair, we, therefore, calculate at most three candidate positions for the receiver position. As with the candidate sets retrieved from the magnetic field model, it would be possible to calculate the combination of intersection points minimizing the distance to their combined centers.

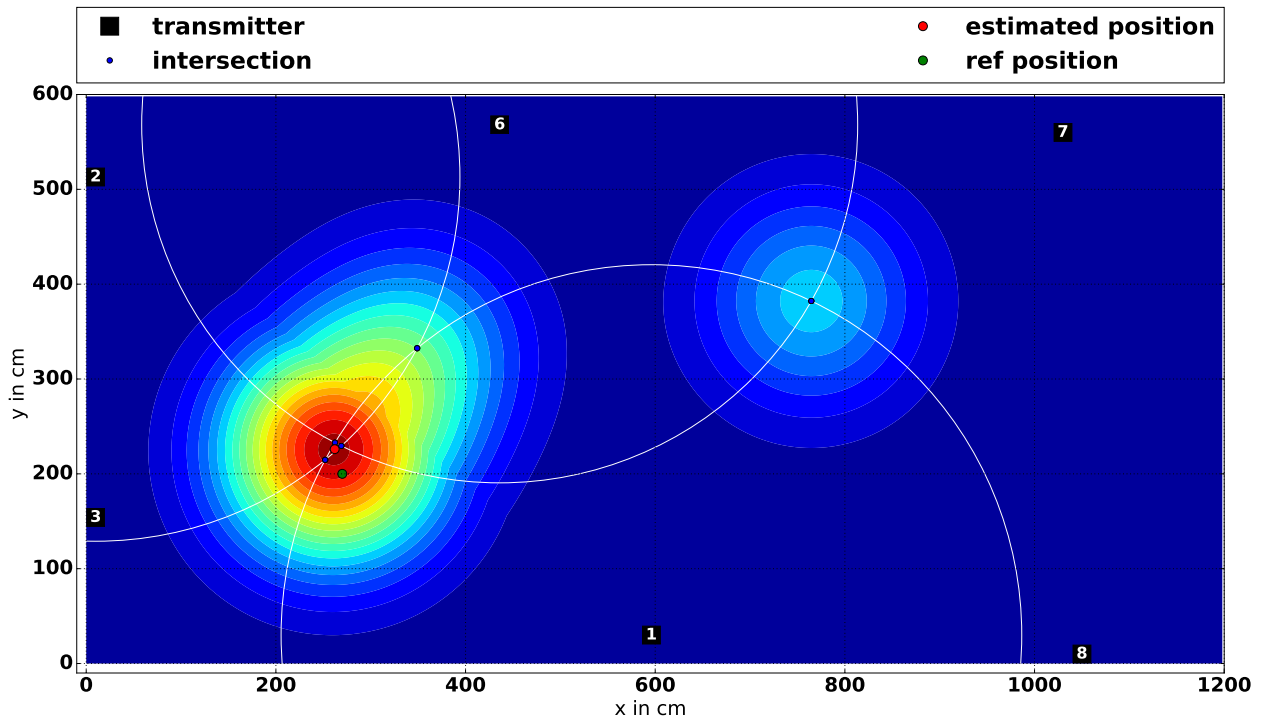


Figure 6.22: Probability distribution of the intersections in the surveilled area.

To provide tracking possibilities, we implemented a particle filter. Let \mathbf{p}_o be the position of the particle o . The weight function is defined as:

$$p(\mathbf{p}_o) = \sum_{\mathcal{S}_i \in \mathcal{S}} \max_{\mathbf{s}_l \in \mathcal{S}_i} \mathcal{N}(\|\mathbf{s}_l - \mathbf{p}_o\|, \mu, \sigma) \quad (6.15)$$

Figure 6.22 depicts the probability distribution of a three measurement estimation. The maximum of this function is clearly visible close to the reference point. We also included the estimated intersections. It is clearly visible that there are offsets in the intersects not resulting in a single intersecting position.

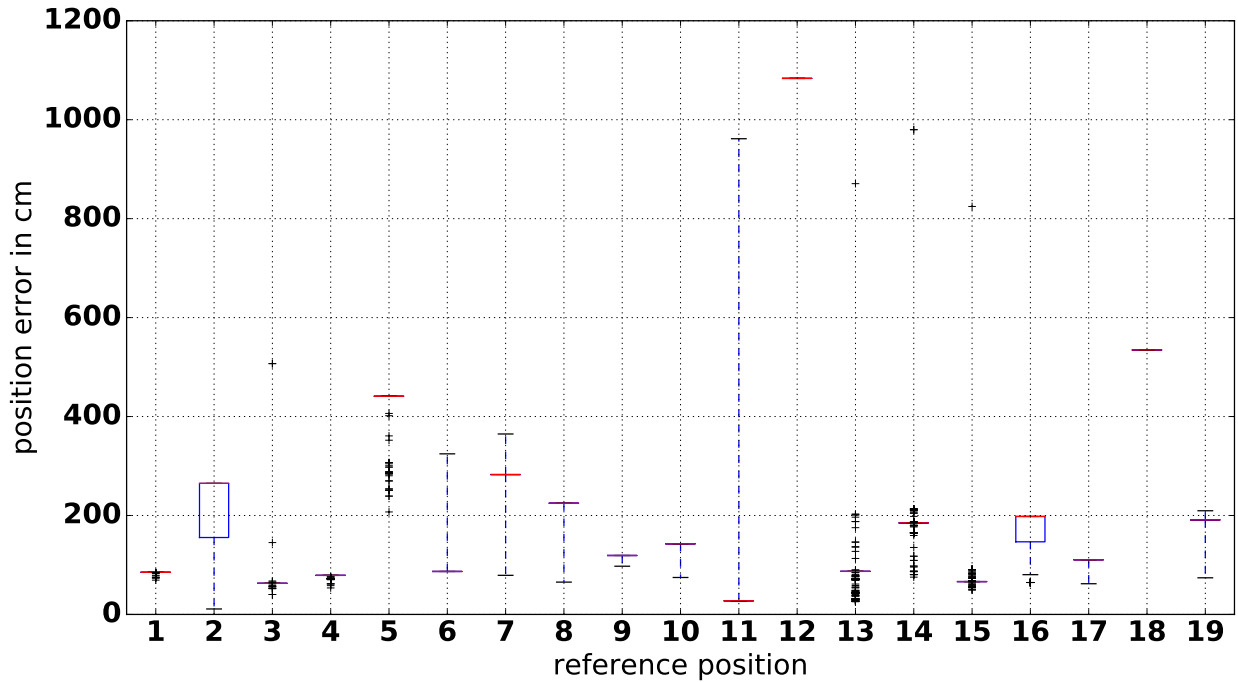


Figure 6.23: Results of the intersection of distance related circles around the corresponding transmitters. The position error is ($\mu = 119.13\text{cm}$, $\sigma = 234.97$).

To avoid the effects of ambiguous measurement cycles with two or one measurements, a particle filter has been applied. The particle movement strategy and the resampling stay unchanged. Unfortunately, this approach does not work for every situation: If the measurement cycle consists of a single estimation, no intersection is provided. In this case, we skip the evaluation.

Figure 6.23 combines the position error results of the 19 reference positions. The reference position 12 lies in an area covered only by a single magnetic field transmitter. The intersection-based particle filter cannot estimate the position. The position error arises due to the overall distance error noise on top of the signal. The mean position error is 119.13cm , the standard deviation is, due to the reference position 12, 234.97 . Although the position error is reduced, this approach does not use the complete "picture" described by the measurements because each intersection set just use measurements to 2 transmitters. The least square approach would use the "whole picture" and should, therefore, be more accurate.

Due to random start conditions of the particle filter, it is possible that the wrong intersection side of two intersections is chosen, in some reference positions, only single distance pairs are available.

In the next section, we present a fusion of all these position estimation algorithms which use lateration and candidate set information for position estimation.

6.4.4 Fusion of Point- and Distance-based Algorithms

In the previous sections, we presented distance-based and candidate set-based algorithms for position estimation of the receiver. Several issues have been found: The candidate-based localization approach is inaccurate. Due to its ambiguous candidate positions around the transmitters, a tracking algorithm is necessary to choose among the eight positions. This also applies to the algorithms based on circle intersection or distance error functions: measurements to 2 transmitters result in ambiguous positions which only can be determined by a tracking algorithm. The distance-based algorithms show, in contrast to the candidate algorithms, a lower positioning error. We, therefore, fused the approaches to achieve a mean position error below 65cm.

The fusion algorithm can be divided into a tracking part and a position estimation part.

Particle Filter-based Tracking

The tracking algorithm uses the Monte Carlo method. The particles define the state as the possible position of the receiver $\mathbf{p}_i = (x, y, z)_i$. Several input parameters can be applied to the filter: Candidate sets of different transmitters, intersection sets of multiple distance estimations or single positions (derived from the least square lateration localizer). Each position in the applied list is evaluated against the probability function defined by equation 6.15. Resampling and movement models stay unchanged and work as previously described.

Position estimation

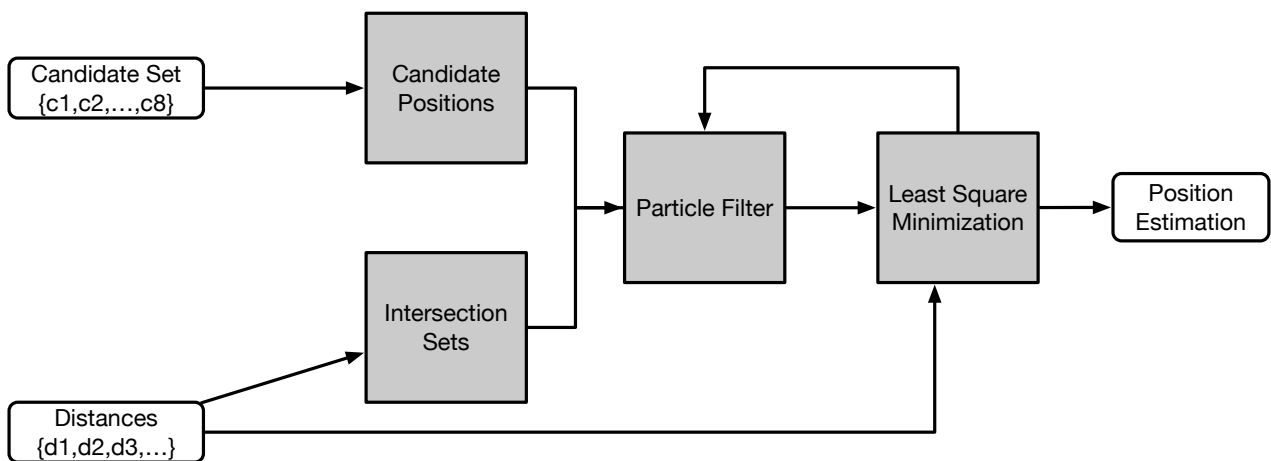


Figure 6.24: Processing sequence of the fusion of the different position estimation algorithms. The output of the particle filter is used as start position of the least square minimization estimation.

The position estimation part of the fusion algorithm (figure 6.24) depends on the number of available measurements. If a single measurement is found, the corresponding candidate positions

6 Multi Coil Position Estimation

are applied to the particle filter. If there are two or more measurements, the corresponding distances are used to estimate the intersection points as described in section 6.4.3. The intersection set \mathcal{S} is then applied to the particle filter and evaluated against the particle set. After resampling and state update, the particle filtered position is returned.

We already mentioned that the intersection approach only uses parts of the overall available information, the least square lateration approach, using all measurements at once but strongly relies on the start position in the error function and often terminates in local minima positions. When a stable position estimation is presented to the least square localizing algorithm, the position estimation is accurate. After the calculation, the estimated position; the to the particle filter for processing.

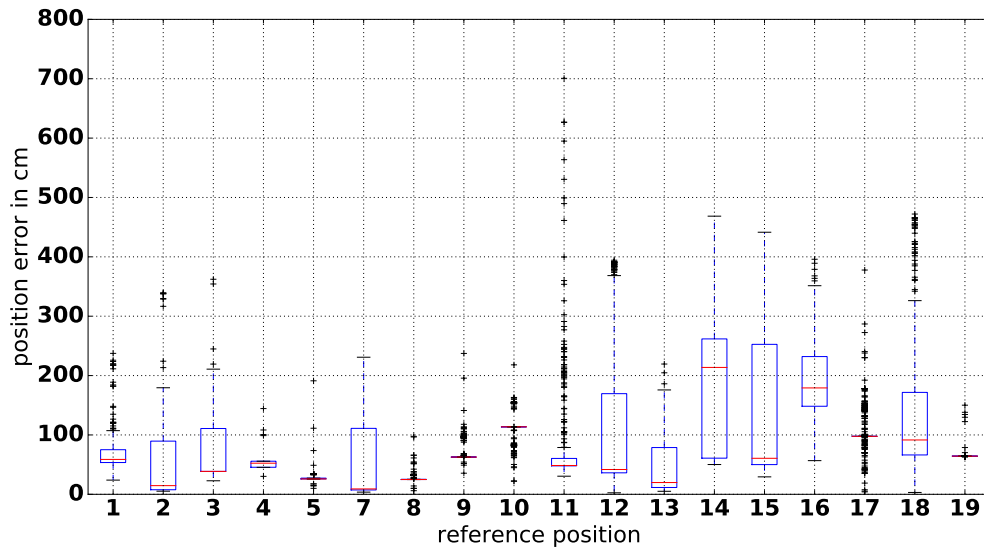


Figure 6.25: Position error of the fusion algorithm. The mean position error is ($\mu = 62.73cm, \sigma = 82.8$).

The fusion of distance-based and candidate-based approaches results in a localization accuracy of $\mu = 62.73cm, \sigma = 82.8$, (details in figure 6.25). Compared to the lateration localization approach, the fusion algorithm has both a reduced mean error and standard deviation. Although applying sliding windows to filter out outliers in the raw signal, there are still reference positions with high position fluctuations. This is a typical result when the receiver is far away, and the signal is unstable.

6.5 Comparison against an RF-based Localization System

We evaluated the particle filter localization algorithm in several environments. The magnetic transmitters have been set up to achieve a corresponding coverage to support distance measurements from at least two transmitters in each point of the experiment area. In addition to the magnetic field locations, we record Bluetooth-based location information from the Quupa localization system which has been installed in the IRL (Innovative Retail Laboratory of the DFKI in St. Wendel). The IRL is located in an office complex built of concrete. The

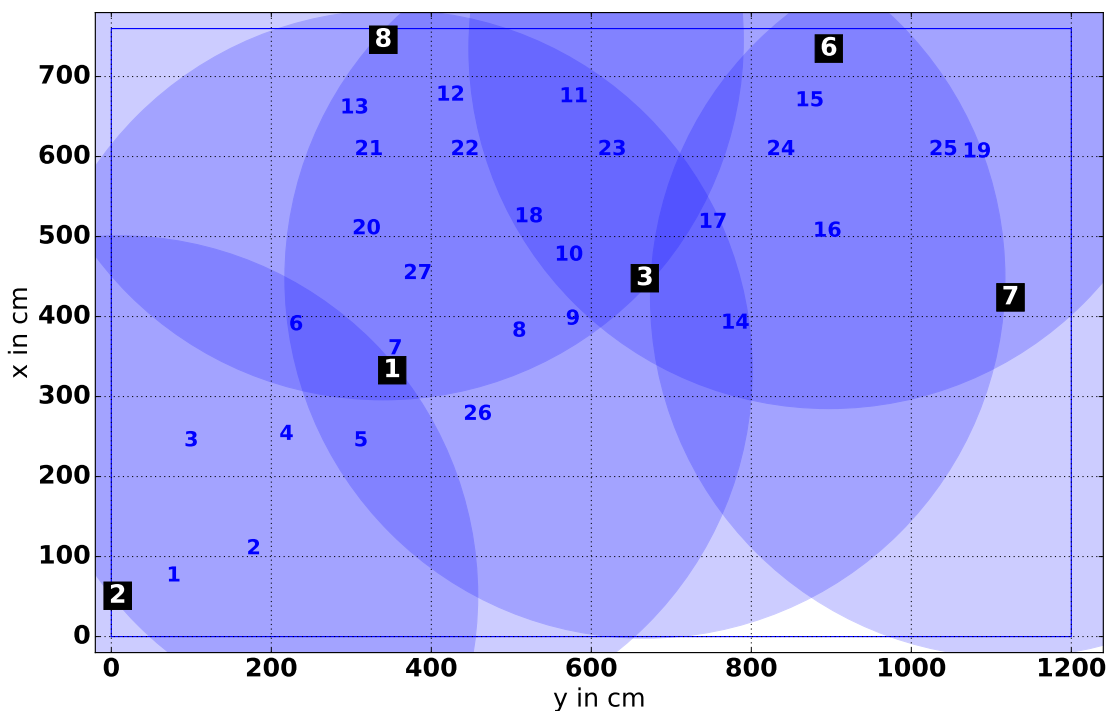


Figure 6.26: Setup of the localization system in the IRL shopping environment.

laboratory is $10 \times 14m$, in the center area, lightweighted construction elements with metal frames, metal moreover, wooden shelves. Additionally, sales related equipment like a vending machine, a security antenna and RFID readers in the 100kHz frequency spectrum can be found. We recorded 27 different reference positions with six transmitters. The positions have been randomly chosen, the positions of the transmitters are on the ground, several reference positions introduce disturbances by walls or metal cooling sales counters.

6.5.1 Evaluation

Figure 6.26 depicts the position of the transmitters and the reference positions. Notice that there are several positions which are only served by two transmitter coils. We record for Quupa and the magnetic field localization system the raw values for post processing and accuracy evaluation.

The magnetic field measurements are transformed into distance estimations. Each measurement cycle (with the given distance set \mathcal{D} is presented to the position fusion algorithm). The estimated positions of both systems are stored and compared. As the environment is demanding, it is possible that no position estimations were possible in a position. **In this case, we add the highest position estimation error of the corresponding localization system to the evaluation data set.**

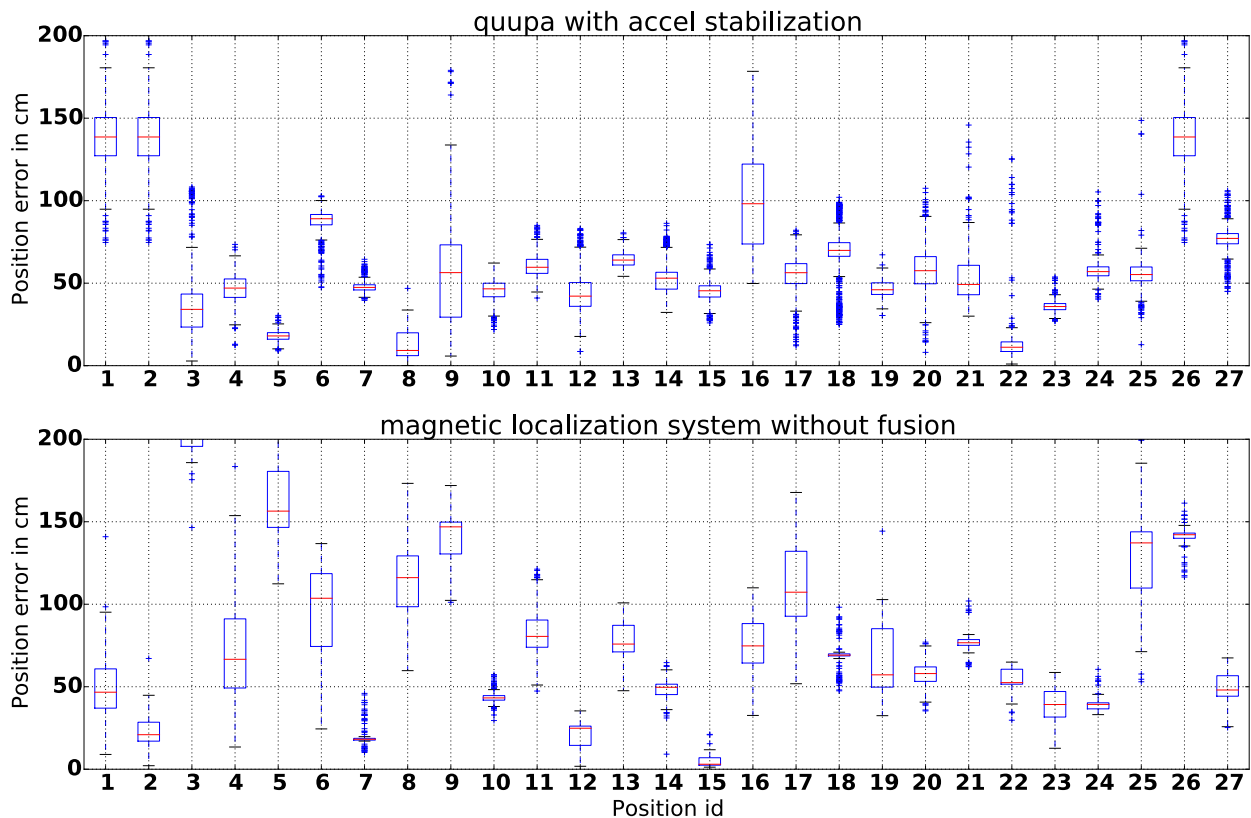


Figure 6.27: Comparison of the Quupa bluetooth localization system and the magnetic field localization system in the IRL shopping environment. Mean error and standard deviation of the Quupa system is for 27 positions, for the magnetic field system this is ($\mu = 77.20, \sigma = 45.83$) is and ($\mu = 66.49, \sigma = 51.91$) for Quupa.

In this environment the oscillating magnetic field indoor localization system achieves a mean error of 77.2cm compared to 66.49cm of the Quupa system (Details see figure 6.27). Compared to the Bluetooth system, our system performs less accurate, although we provide in each reference

position measurements and locations. The Quupa system is commercially available; the system consists of several combs covering only small parts of the surveilled area. The antennas are attached to the ceiling to provide line-of-sight. Currently, nine persons are developing this system, in contrast to a single researcher working on the magnetic field localization system.

Particularly in the reference positions 1 and 2, two positions below a metal cooling counter, our system performs a position accuracy below 50cm, the RF system is not able to retrieve any position information. The Quupa system used for this setup six antenna groups which have been attached to the ceiling and cover defined areas. For these cells, line-of-sight signal propagation was necessary and aimed. Our system, in contrast, has been placed next to the room elements to cover both sides of the separating parts. Additionally, the Quupa locations are IMU filtered (integrated into the Bluetooth beacon), our system only uses raw magnetic field information for position estimation.

6.6 Detection of Regions of Interest

6.6.1 Large Scale Transmitter Setup in different Environments

The fusion of WIFI and the inertial-based system often rely on fingerprinting methods. These approaches usually try to gather signal information from which a longer term signal behavior in the immediate environment is derived. For RF-based systems, the disadvantages discussed in 2.3.1 often require heavy signal filtering in combination with multiple data recordings. Fingerprinting approaches to avoid the need for modeling the signal behavior, which can be complex in indoor environments especially close to metal objects. Being not the main focus of this work, our magnetic field localization system has been evaluated in several environments using region of interest determination based on fingerprinting: Because the magnetic fields are only locally influenced by obstacles and EM sources, the repeatability of the signal is extremely high. Thus we want to evaluate in this section whether a fingerprinting / classification approach with raw magnetic field derived signal information, and a simple one step data recording is sufficient to distinguish a high number of regions. Also, the minimum distance between the ROIS is of interest.

| Location | Events with Synch errors | Events | Percent |
|-------------|--------------------------|--------|---------|
| Office | 123 | 292 | 42.12 |
| Apartment | 65 | 186 | 34.94 |
| Living Area | 130 | 427 | 30.44 |
| Cellar | 131 | 424 | 30.90 |

Table 6.1: Statistics for Synchronization errors at different locations

A big advantage of magnetic fields compared to RF systems is that those dynamic indoor elements have only limited influence on the magnetic field signal and therefore less maintenance

is necessary.

Parts of this work have been submitted to Ubicomp 2013 ([PL13]).

This evaluation has been conducted in the early stages of the development of our localization system. Therefore, synchronization approaches have not been researched. During the experiments the disadvantages of RF-based clock synchronization have been visible: Due to missing synchronization packets, the clocks have been asynchronous in some measurement cycles resulting in signal "gaps".

We applied a detection algorithm which marked those signal intervals as not usable (example signal trajectory in figure 6.5). Table 6.1 holds information about the synchronization problems in the different environments.

We evaluate the quality of regions of interest detection in different larger scale environments. This includes an apartment ($70m^2$ with six transmitter coils), a living area in a house ($95m^2$, seven transmitters), a cellar in the same building ($95m^2$, seven transmitters) moreover, an office environment with $245m^2$ and eight transmitters. Three persons sequentially were told to randomly enter the defined regions of interests.

Figure 6.28 and figure 6.29 depict the floor plans of the different environments and the defined regions of interest. In some cases, the neighboring regions of interest could not be separated due to missing orientation information; we, therefore, aggregate those regions to bigger ones. Notice that these environments include demanding sections which would strongly influence the detection accuracy of RF systems as well: ROIs have been defined **in metal bath tubes**, showers, around metal heating systems or in metal storage shelves.

Also keep in mind, that the transmitters have been placed next to walls. This means that the generated magnetic field permeates the wall and therefore also provides position information to regions in the room on the other side of the wall.

Data recording and evaluation

We record the raw magnetic field measurements of the sequentially triggered magnetic field transmitters for off-line processing. The magnetic field receiver has been attached to a belt at the hip and was pointing in the walking direction of the person. Three female and four male subjects conducted the experiments; we told them to stay in the regions of interest in a human understandable way ("stand next to the wardrobe") instead of measuring their absolute coordinates. The subjects were requested to stand for at least 20 seconds at these positions.

We extract from the gathered raw data the magnetic field magnitudes (m_x, m_y, m_z) and the axes ratios $t_x = \frac{m_x}{m_y}$, $t_y = \frac{m_y}{m_z}$ and $t_z = \frac{m_z}{m_x}$.

$r_x = \frac{v_x^x}{v_x^y}$, $r_y = \frac{v_y^y}{v_y^z}$ and $r_z = \frac{v_z^z}{v_z^x}$ describe the relative orientation of the receiver in the magnetic

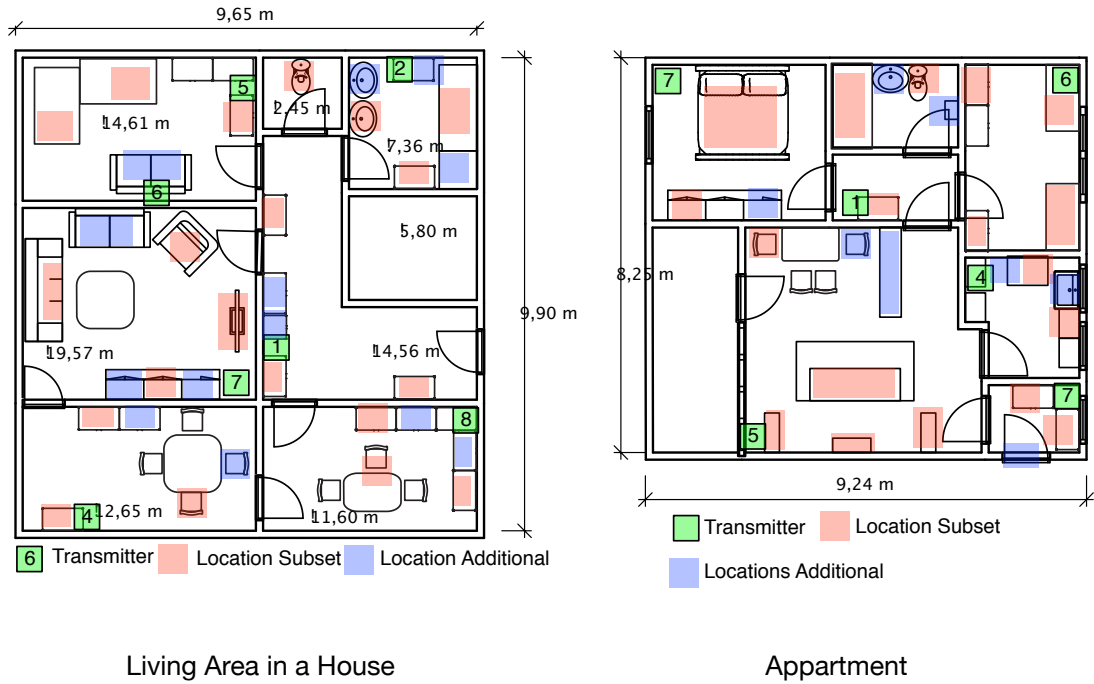


Figure 6.28: Regions of interests defined in different everyday living environments in addition to the position of the transmitters. Notice that the transmitters also permeate walls and furniture and therefore a lower number of transmitters is necessary to cover the environment.

fields of the transmitter. v_i^j is the voltage measured by the receiver axis i when transmitter axis j generated the magnetic field. The defined feature vector is:

$$(m_x, m_y, m_z, t_x, t_y, t_z, r_x, r_y, r_z)$$

Due to the early stage of development, we used these features to train a decision tree (CART) containing the different regions of interests and their corresponding features.

m_i, t_i describe the relative position of the receiver to the transmitter (you can think of polar coordinates with angle and distance), the bearing of the receiver is described by r_i . **We used the data of one person to train the classifier, the data sets of the other persons have been used to evaluate the classifier.**

Discussion

We achieve in these environments a classification rate of 81.4% for the living area of the house (full data set), 94.4% for the cellar and 92.17% for the office environment. The overall classification rate is 88.2% for all regions of interest in the house.

A combination the regions of interests to a more realistic setup raises the classification rates to 87.2% for the house and 97.1% for the office.

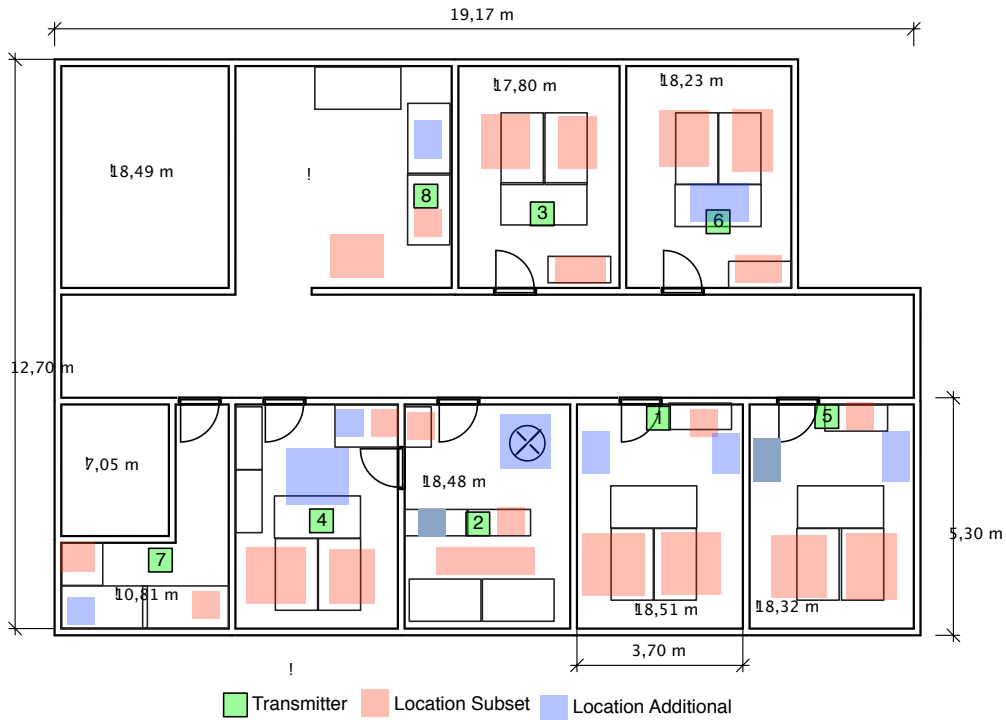


Figure 6.29: Definition of regions of interest in an office environment.

Figure 6.30 depicts the confusion matrix of the data recordings in the office environment. The classification results for the other environment show similar behavior in the frame-by-frame classification approach. Especially regions of interests being close (smaller than 50cm) are confused with regions close to the class. Although adding the receiver axes ratios r_i to the feature set, which should describe the orientation of the receiver and therefore should provide limited heading information, is not sufficient enough to separate those regions. We assume that orientation information is less stable because it relies on 2 out of 9 measurement values instead of 6 (compared to magnitudes m_i). Little changes in heading and position of the receiver in a ROI strongly influences the induced axes voltage and therefore lead to different feature vector values. To overcome this effect, we merge neighboring regions of interest requiring heading information to be distinguished.

In nearly all classes feature vectors are misclassified as null class elements. To some extent, this happens because of synchronization effects which have not been recognized by our detection algorithm, some items are effects by annotation errors, when the annotation value has been assigned too early or too late.

The system also performs well in demanding areas with a lot of metal parts as being found in heating systems or metal bath tubes. The true positive rate is also above 87 percent. Except for the RF synchronization problems which are visible in all environments, influences caused by small dynamic changes in the environment (for example opening of drawers, wardrobes or changes of materials on the desktop) are not visible in the data sets. We performed the data recording during a typical workday where workers were in their offices and worked on their

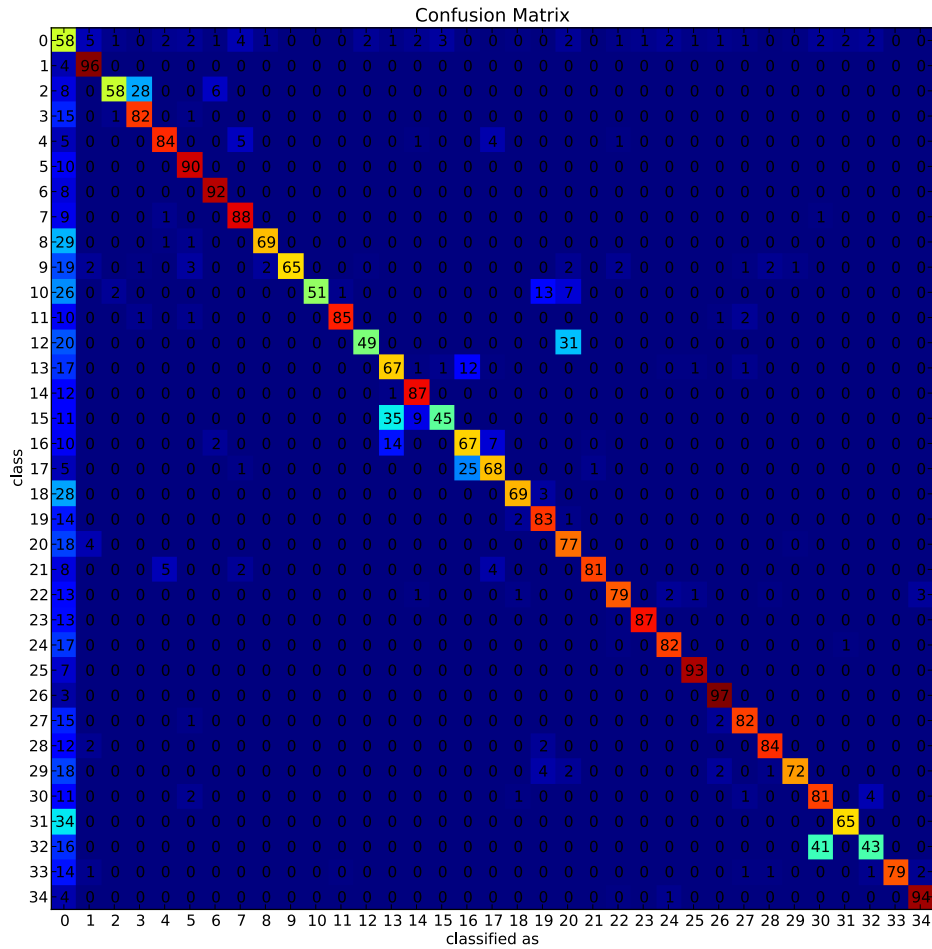


Figure 6.30: Classification result of the frame-by-frame-based classification in the office environment. Neighboring regions are often confused.

computers.

Although the number of transmitters varied in the different environments (from a relatively dense transmitter setting in the 70 square meter apartment to a relatively sparse setting in the office environment, the regions of interests could be determined when they were at least 50cm apart. The approach of the configuration of the regions of interest is limited to placing the receiver in the specific area. Compared to for example the RADAR approach of Microsoft, where influences by humans are recorded, the definition of a region of interest in our system is only a data recording at this area.

6.6.2 Small Scale Transmitter Setup for Industrial Maintenance Tasks

Maintenance in industrial environments is a demanding task: Besides localization of the machine to maintain, the maintenance task usually has to follow specific workflow sequences and different parts (and therefore locations) of the machine. The worker has to turn off the power, often in specific orders not to damage electronics or motors, close valves, adjust and configure the speed of mixing devices or simply just change filters. In these modules, many different regions have to be specified, identified and found. We saw in the beginning that regions of interest could be addressed using the raw magnetic field estimations and a simple fingerprinting approach. This has been evaluated in different larger scale setups.

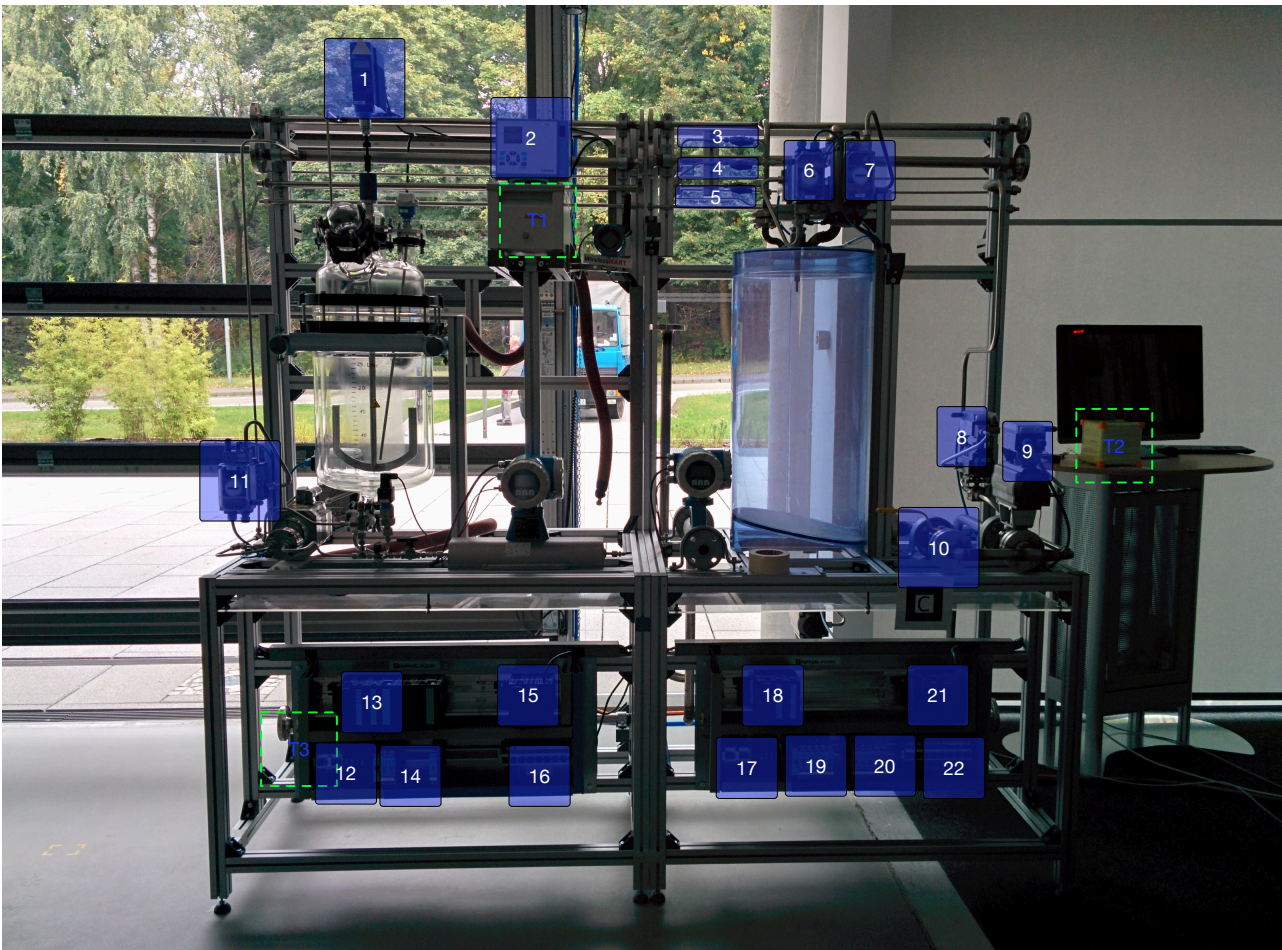


Figure 6.31: Small scale ROI evaluation in an industrial environment. The red and green areas indicate the definitions of the regions of interest for transmitter 1 and 2. The ROIs are in some cases less than 10cm apart. The transmitters are attached to the metal frame, their positions are indicated by the green dashed rectangles. 22 different ROIs are defined and should be differentiated.

We performed a close to reality experiment in an industrial show production line at the SmartFactory in Kaiserslautern. The module is $220\text{cm} \times 80\text{cm} \times 240\text{cm}$ big, we attached three transmitters at different positions and levels. We defined 22 different regions of interests which

would be part of a maintenance task. The main focus here was the possibility to interact with the module (for example removing the filter or opening or closing a valve). Figure 6.31 depicts the defined regions of interest. We argue that, although the overall position error of our system is above 60cm , the repeatability of the signal allows to define and recognize regions of interests which are less than 20cm apart. For regions which should be less than 20cm apart, the quasi-static approach described in section 4.7.3 can be applied.

Data recording and evaluation Three transmitters have been attached to the metal frame of the production module in such a way to not hinder the subjects in their grabbing tasks. Secondary, the production module can easily be moved, a definition of the regions of interest in the absolute world coordinate system is not useful. In contrast to the large scale setups, we use an RF-based centralized triggering scheme which avoids the synchronization problems of the last data recordings. One transmitter has been placed at 220cm height, another at 120cm and the last one was put behind the element on the floor. All transmitters are fixed to the frame. The goal of the evaluation is to estimate the recognition rate of our magnetic field localization system concerning regions of interest based on distance and position estimation. Both, frame-by-frame and event-based rates are of interest. After defining 22 regions of interest which are related to actions being performed during production and maintenance, we record for each of the two receivers coils the magnetic field readings at the different regions.

ROI detection algorithm In chapter ?? the accuracy evaluation showed that the position is comparably stable. This effect is even stronger if the distance between the transmitters and the receiver is low moreover, therefore the magnetic field signal high.

The estimated positions and the corresponding errors, both caused by environmental and model influences, are either repeatable or locally bound.

Using the recorded data from the setup-phase, we use the estimated distance tuples of a measurement round and the estimated position to specify the closest region of interest.

$$(x, y, z, d_1, d_2, d_3)$$

If a measurement to a transmitter resulted in a nonvalid distance estimation, -1 was used to indicate this. To eliminate outliers in distance measurements, a sliding window with buffer size 5 has been used (the sliding window size corresponds to 1s). Each region of interest is defined by the mean position and mean distances derived from the setup data recording. In the experiment phase, a K-dim tree is used to retrieve the nearest region of interest of the estimated position. If the distance between the estimated position and the center of the region of interest is smaller than 15cm , the algorithm returns the id of the region of interest, the null class is returned otherwise.

Experiment In the experiment, two persons carry the receivers and were randomly told to interact with the corresponding regions of interests. 60 randomly chosen regions of interests have been used. A second person annotates the time of entrance and leaving of the receiver as

6 Multi Coil Position Estimation

ground truth information. Notice that due to hardware and model tolerances, two setup steps (for each receiver one) are necessary.

Discussion Figure 6.32 depicts the results of the **frame-by-frame** region of interest estimation. We recorded in the data set over 8000 measurements against labeled regions of interest. 73.4% of the frame-by-frame estimations have been correctly related to the regions of interest. Especially the regions 3,4,5 perform badly; they are too close to each other and also close to regions 6 and 7. 3,4,5 have all three a recognition rate below 50 percent.

Also clearly visible are the incorrect regions 12 - 16 and 17 to 22, all of these are close to each other.

Looking at the different distances of the regions to the transmitters, the classification rate directly correlates with the proximity to the transmitter: If a region of interest is close to a transmitter, the rate is high. As already discussed, low distances result in a very stable position estimation (including stable and continuous readings) compared to distances at higher ranges, which tend to be unstable and intermittent.

| Region of Interest | overall count | correct | TP Rate |
|--------------------|---------------|---------|---------|
| 3 | 3 | 2 | 66% |
| 4 | 2 | 1 | 50% |
| 5 | 1 | 0 | 0% |
| 13 | 2 | 1 | 50% |
| 14 | 3 | 2 | 66% |
| 17 | 3 | 2 | 66% |
| 18 | 3 | 2 | 66% |
| 21 | 3 | 2 | 66% |

Table 6.2: Results of the majority decision. 8 events of 60 regions of interest have been misclassified. 86.7% have been correctly classified.

If we perform a majority decision on each event, 8 of 60 regions of interests are not correctly detected:

Only regions 3,4,5 and 13,14 and 17,18,21 have recognition rates below 100 percent. In the cases of the valve regions (3,4,5) the defined regions are too close together to be separated, the other regions are in the electrical section of the production module where a lot of metal components, wires and motor drivers are situated. The metal components generate eddy magnetic fields influencing the induced voltage and therefore the classification results. Due to the inhomogeneous distribution of both wanted and eddy magnetic fields the estimated positions and distances are not as stable as wished.

A combination of regions 3,4,5 (which are only 7 to 10 cm apart each) increases the true positive rate to 92%.

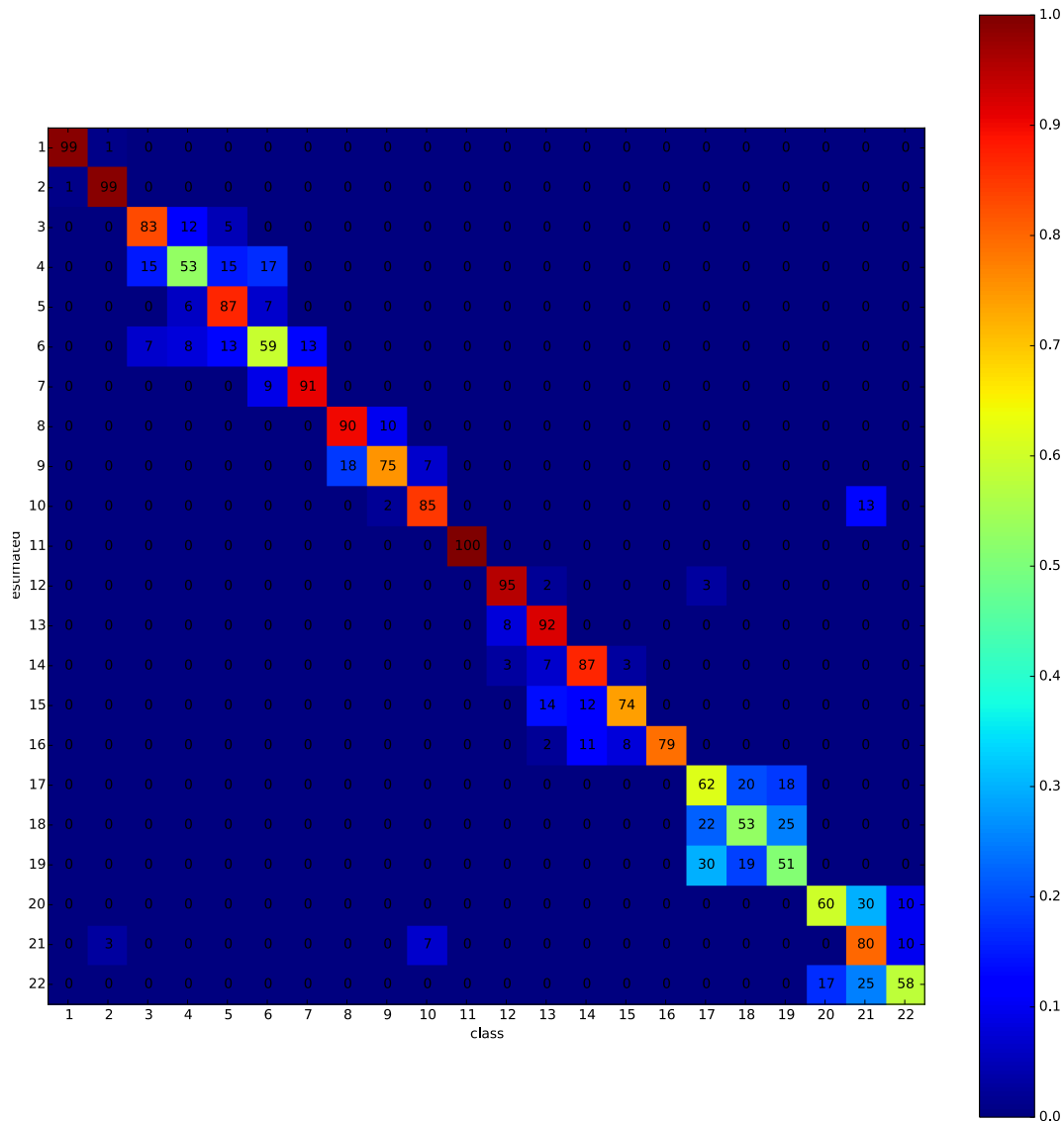


Figure 6.32: Overall combined frame-by-frame detection rates of subject one and two. Regions of interests, which are close to each other (distance lower than 15 cm) are often confused, regions close to the transmitters perform better.

Conclusion The estimation of regions of interest has been evaluated in different environments, starting from typical everyday life environments like apartments, living areas in houses, cellars or office environments. The advantage of magnetic fields compared to light- or sound-based systems are used to reduce the number of necessary anchor points. In contrast to other physical modalities, magnetic fields are hardly influenced by walls, furniture or humans. Placed next to walls allows a transmitter to serve in the nearby rooms. We presented a raw signal-based classification approach to distinguish between regions of interest being at least 50cm apart. A region of interest detection relying on distances and positions in a close-to-reality industrial environment allows distinguishing areas which are more than 15 to 20cm apart. The stability of

the magnetic field influences the minimum space between regions of interest. The closer the region of interest is to a transmitter; the less space has to be considered.

6.6.3 Combination of Magnetic Field-based Localization and mBeacon-based ROIs

In addition to the previous proof of concept evaluations, we also considered the combination of quasistatic magnetic field beacons and our oscillating magnetic field localization system. For industrial applications it is often necessary to retrieve information about the devices a person is interacting with. Especially information about the hand is important (to for example detect the interaction with material or with control panels.). Due to influences caused by industrial installations as high voltage motors, driving circuits or bus systems, the magnetic field localization system is affected and cannot provide position information which is accurate enough to distinguish between regions of interest which are closer than $20cm$. The tracking and large scale position estimation of workers is performed by the oscillating magnetic field system, small scale interactions with significant objects are performed using the mBeacons. To achieve this, we installed several coils as described in section 4.7.3.

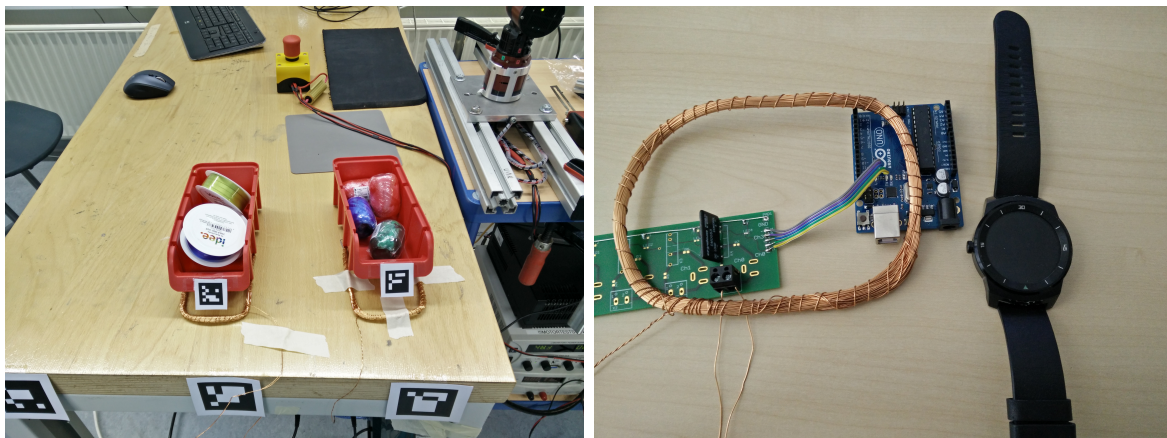


Figure 6.33: mBeacon in industrial environments. Left: mBeacon system for storage management. Right: mBeacon controller circuit and detector smart watch

In the scenario, the worker is using an IMU sensor attached to the wrist, as it provides a higher update rate for acceleration, gyroscope, and magnetic field sensors than smartwatches. Additionally, the fusion of this sensor information allows to retrieve bearing information of the hand.

The industrial environment contains several devices which are equipped with the mBeacon system: To detect interactions with control panels, mBeacon coils have been attached behind control panels, whenever the worker interacts with the panel this can be detected. Placing the mBeacon coils below storage boxes can be used to implement a stock holding system: If the person reaches for an item stored in a box, the magnetic field encoded information is sensed by

the IMU and is used to reduce the number of elements in the box. The recognition/detection rates are comparable to the results presented in the previous chapter.

6.7 Conclusion

This chapter presented and evaluated approaches which are necessary to achieve a multi coil position estimation. This covers, on the one hand, the synchronization of the transmitters and receivers, the scheduling of the transmitters and on the other hand the fusion of the position and distance information between the receiver and the different transmitters.

Several synchronization algorithms, either centralized or decentralized have been described, implemented and evaluated with regard to stability and information exchange complexity. Scheduling algorithms can either provide a naive round robin based schedule or if they take the spatial relations of transmitters and the limited range of magnetic fields into account, which then reduces the number of measurement slots.

| Approach | Subapproach | Mean error | Standard deviation |
|------------------------|---------------------|------------|--------------------|
| <i>Candidate-based</i> | | | |
| | geometrical | 186.07 cm | 90.93 |
| | probabilistic | 170.2 cm | 84.3 |
| <i>Distance-based</i> | | | |
| | probabilistic | 172.30 cm | 66.16 |
| | least square | 140.14cm | 164.82 |
| | circle intersection | 119.13 cm | 234.97 |
| <i>Fusion</i> | | 62.73cm | 82.8 |

We presented and evaluated in this chapter different localization approaches with regard to position stability and accuracy. Two different algorithmic approaches have been introduced working with different information sources: Derived from the three axes transmitter architecture, candidate sets provide (rough) position information even if only a single transmitter is sensed. A combination of candidate sets of different transmitters results in a position error of 180cm. The errors rates in the single coil position estimation also dominates the accuracy in this approach.

The usage of distances as information carrier shows similar behavior as in the model section compared to the candidate approach: all approaches show lower position errors. Especially when only two measurements are available, the lateration approaches fluctuate between the two ambiguous positions (the two possible intersections of the circles defined by the measured distances).

A fusion algorithm, using a particle filter for tracking, the candidate-based approach for single coil position estimation, the circle intersection approach for multi-coil measurements and the least square minimization approach for overall position estimation reduces the position error to 62.7cm with a standard deviation of 82.8.

6 *Multi Coil Position Estimation*

Using raw magnetic field information for a fingerprinting approach can be applied to large scale localization setups. We were able to distinguish up to 30 different regions of interest in environments up to $200m^2$ using simply the raw magnetic field information.

Applying a similar approach to the estimated distance and position information derived from the magnetic field model has been tested in a close to reality industrial environment. Here we were able to separate regions which are at least 20 cm apart. In both cases, the errors caused by the environment and in the later additionally by the model and localization algorithms are stable and result in low feature vector variations leading to accurate detection results for regions of interest.

7 Fusion of Magnetic Field Distance Estimations and LIDAR-based Position Estimations

Industrial applications require highly accurate position estimation approaches to retrieve information about the environment for mapping and self-localization. Typically optical localization systems based on cameras or Time-of-Flight cameras achieve the aimed accuracy. This position estimation usually requires complex algorithms and introduces high data rates. Also, laser scanners are often used to enable a mobile robot to perform self-localization. These systems then rely on point clouds derived from a 3D 360-degree line scan at high sampling rates. These approaches are not usable if wearable systems have to be supported as the algorithms require high processing and memory resources which are typically not available in low power systems.

To solve this problem we propose four single beam laser distance measurement units ("LIDAR-Lite") with an accuracy of 2.5 cm. The units are attached to a helmet and point in each of the four (local) cardinal points. Obstacles, like walls, reflect the light pulse and the distance between the unit and the obstacle can be estimated. This system is interesting in the fields of construction sights as the sensors can be attached to a helmet. In combination with an IMU, the laser distance measurements provide sufficient information to perform a position estimation. This chapter discusses the challenges of the system; several questions arise from this approach:

- How can a position be estimated from four single laser beams with a partially known environmental map as it is found on construction sites? (**Lidar Lite-based position estimation**)
- What is the **accuracy** of such a system? How do **discrepancies in the map** influence the position accuracy (for example what happens if a wardrobe is not part of the map model?) which results in higher or lower distance estimations? How do errors on the heading signal influence the position estimation?
- How can a magnetic field-based anchor point be integrated into such a system? (**Fusion with magnetic field distance information**)
- Is it possible to estimate the position of an anchor point on the fly by relying on the previously estimated position and relative distance measurements to the anchor point? (**dynamic anchor point position estimation**)

7.1 Contribution

We present in this chapter a **prototype helmet** for indoor position estimation utilizing a low number of lidar distance measurement beams in combination with an integrated IMU. An algorithm for **low resource position estimation in a known environment** (a map of the environment is available) is presented relying on geometrical considerations. Ambiguous position estimations arise due to symmetrical effects caused by parallel and perpendicular walls which are cleared by **combining distance measurements to sparsely placed magnetic field transmitters with the laser position estimations**. The mean position error of the LIDAR-based algorithm is below 8cm. The algorithm for position estimation runs on an Intel Edison with 500 MHz; the overall architecture runs for more than 8 hours. Additionally, we propose an algorithm for dynamical position estimation of a newly added magnetic field transmitter coil with an accuracy of below 50cm.

7.2 Related Work

Light detection and ranging (LIDAR)-based sensors and robust and accurate algorithms for processing have been developed in different fields of research. With ongoing developments in autonomous driving, sensor costs need to be reduced and therefore cheap but still accurate singled beam sensors cost around 140 Euros. LIDAR-based localization is described in many research works, among others, [WE14] describe the estimation of the 3D position of vehicles using complex LIDAR cloud point information. A comparable system has been used by [LCC⁺10] to provide indoor localization; the scientists equipped a backpack with several laser scanners, IMUs, and cameras to generate a floorplan of the environment. They achieve an accuracy of below 30cm. The authors of [BZF12] implemented a handheld laser scanner IMU system which is usable to generate an indoor map. Closest to this work is [PS16]. The authors describe how IMU-based pedestrian dead reckoning can be stabilized using laser distance measurements to nearby walls. They study the effect of doors and obstacles but do not provide a separate algorithm based on laser distance estimations.

7.3 LIDAR Helmet

The wearable sensor helmet consists of a processing unit (Intel Edison, two cores 500 MHz each), 4 to 6 LIDAR Lite sensors which are attached to an Atmel ATmega328P-AU micro-controller for 2D or 3D position estimation, and an LSM9DS0 9 degree of freedom IMU sensor for gathering acceleration, gyroscope, and earth magnetic field Information for bearing estimation. The time synchronized sensors sample at 45 Hz. The system is battery powered and runs with a LIPO Battery pack for 8 hours.

A LIDAR Lite sensor provides distance information with a rate of 45Hz with a maximum distance range of 60m. According to the producer, the distance accuracy is 2.5cm. For 2D



Figure 7.1: Photograph of the LIDAR helmet. The four laser-based distance measurement units point 4 different directions.

position estimation, we attached 4 LIDAR sensors at the helmet, pointing to north, south, west and east. 3D position estimation requires at least one additional sensor pointing either to the ceiling or the floor.

The IMU sensor is sampled at 100 Hz; a Kalman filter estimates the orientation of the helmet in the world coordinate frame. The Kalman filter automatically discards earth-magnetic field measurements which are not within a given magnetic field strength interval.

For 2D position estimation, we are interested in the heading information, 3D position estimation also requires roll and pitch. We attached the IMU and the sensors in such a way that the north sensor points correlates with 0-degree heading, the other sensors correspondingly point to the other directions (90-degree steps).

Figure 7.1 and figure 7.2 depict the wearable helmet with attached LIDAR Lite sensors and the basic idea of the data gathering: Each sensor is the start point of a vector/beam with given direction and length (heading and relative sensor orientation, distance estimation).

7.4 LIDAR-based Localization

During the design phase, we carefully placed the LIDAR sensors on a plane, the relative orientations of the LIDAR sensors are known. For easier understanding, the sensors are addressed according to the cardinal points: north, south, west and east. A measurement cycle consists of a distance estimation of each of the LIDAR measurement sensors d_i and an IMU

heading Ψ update $(d_n, d_s, d_w, d_e, \Psi)$.

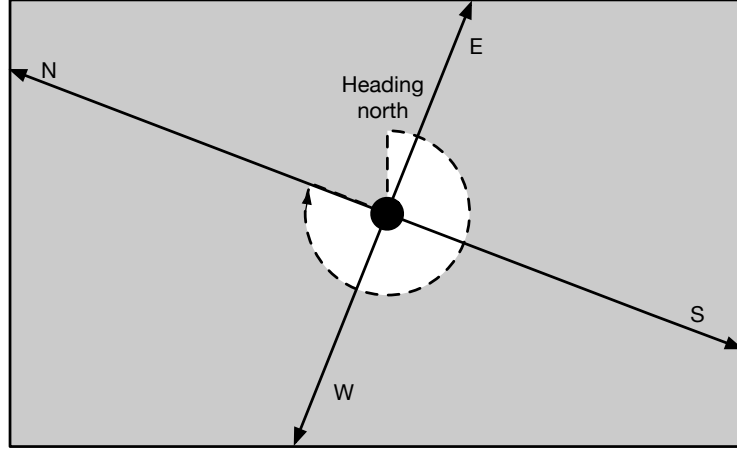


Figure 7.2: 4 LIDAR Lite distance measurement sensors are attached to a helmet pointing in 4 perpendicular directions. An obstacle in the path of the beam reflects the laser pulse, the runtime between emission and reflection is used to estimate the absolute time of flight and therefore the distance between the sensor and the obstacle. Using an IMU allows us to estimate the heading of the helmet.

As we estimate the heading error with around 10 to 15 degrees, the position estimation of the LIDAR helmet also considers the error prone heading. For easier explanation, we regard a simple room layout, a rectangular room with $700\text{cm} \times 1500\text{cm}$ length and breadth. If we now look at a single LIDAR distance measurement, for simplification the north sensor corresponding with the heading angle Ψ , the LIDAR sensor's position is restricted:

As the LIDAR system measures the runtime of the laser pulse between the sensor and the reflection of the laser pulse, the valid occupied area - or correctly a line - must fulfill two restrictions: the distance d between the LIDAR helmet at position $\mathbf{x} = (x, y)$ and the reflected point $\mathbf{r} = (r_x, r_y)$ must be equal to the estimated distance d_i and $\angle(\mathbf{r}, \mathbf{x}) \in \{\Psi - \epsilon, \Psi + \epsilon\}$:

$$\mathcal{P} = \{(x, y) \mid \|(x, y) - \mathbf{x}\| = d_i \cap \angle((x, y), \mathbf{x}) \in \{\Psi - \epsilon, \Psi + \epsilon\}\} \quad (7.1)$$

In the computational implementation, we regard each wall or obstacle of the room and estimate the position of the LIDAR sensor relatively to these points:

Each wall is described by two points $W = ((x_1, y_1), (x_2, y_2))$ defining the corners of the wall. The LIDAR sensor provides distance information d_n to the obstacle with the known heading Ψ . The position of the helmet can be described by two points on the wall. Namely, the position

of the reflection A (causing the distance) and the foot point D of the helmet's position B , the projection of the position on the wall.

Figure 7.3 contains two schematics, the left-hand side plot depicts the names and positions of the base points and the helmet in addition to the angle and distance estimation, the right-hand side figure shows the possible positions lying on parallel lines to the wall. Therefore it is sufficient to look at the corners of the wall: In the following part, we refer the names of the variables to the figure 7.3.

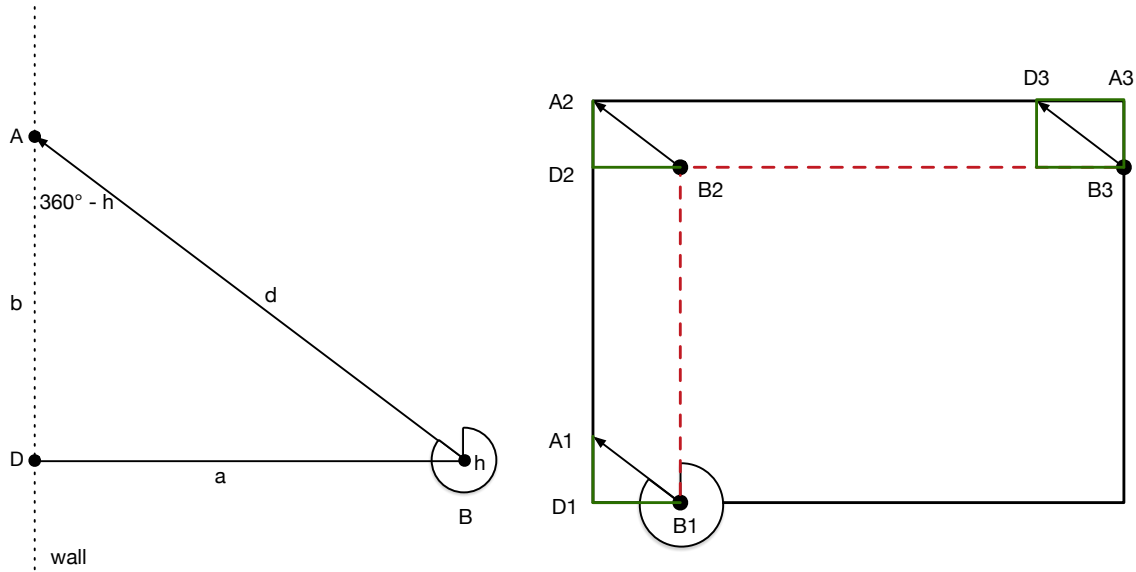


Figure 7.3: Estimation of one base point B_i . Depending on the heading angle quadrant, D or A is the corner of the wall.

Three cases have to be considered:

1. (A_1, B_1, D_1) B_1 is on the wall of the perpendicular wall, D_1 is the base point of the triangle which is also the corner of the walls.
2. (A_2, B_2, D_2) A_2 is the second corner of the wall, D_2 lies on the wall between A_1 and A_2
3. (A_3, B_3, D_3) A_3 is the corner of the second wall, B_3 is on the third wall.

Note that all three cases involve right angle triangles, therefore the distances can be calculated using the theorem of Pythagoras.

$$b = \cos(h) * d = \cos(\Psi) * d \tag{7.2}$$

$$a = \sqrt{d^2 - b^2} \tag{7.3}$$

Depending on the heading angle Ψ the vector $\vec{d} = (a, b)$ differs:

$$\begin{aligned} \vec{d}_{90} &= (a, b), \\ \vec{d}_{180} &= (a, b), \\ \vec{d}_{270} &= (a, -b), \end{aligned}$$

7 Fusion of Magnetic Field Distance Estimations and LIDAR-based Position Estimations

$$\vec{d}_{360} = (a, -b).$$

The positions of the LIDAR helmet for cases 1)-3) are:

$$B_1 = D_1 + (a, 0),$$

$$B_2 = A_2 + \vec{d}_i,$$

$$B_3 = A_3 + (0, -b)$$

The resulting lines:

$$l_1^{north} = (B_1 + k * \Delta(B_2 - B_1)) \quad (7.4)$$

$$l_2^{north} = (B_2 + k * \Delta(B_3 - B_2)) \quad (7.5)$$

are used from now on.

Each of the LIDAR sensors attached to the helmet describes the position of the helmet from a different point of view, resulting in 8 different lines:

$$l_1^{north}, l_2^{north}, l_1^{south}, l_2^{south}, l_1^{west}, l_2^{west}, l_1^{east}, l_2^{east}$$

The heading angles for the different sensor orientations have been considered and adapted correspondingly. The position of the helmet lies on the intersection of one of the two lines of each sensor. We, therefore, intersect each line l_i^j with the other lines of the other sensors:

$$p_{i,j}^{l,m} = \{(x, y) \mid (x, y) \in l_i^l \wedge (x, y) \in l_j^m, l \neq m, i \neq j\} \quad (7.6)$$

moreover, store the results. **The position of the helmet is the intersection point which occurs the most times in the list of intersection points.**

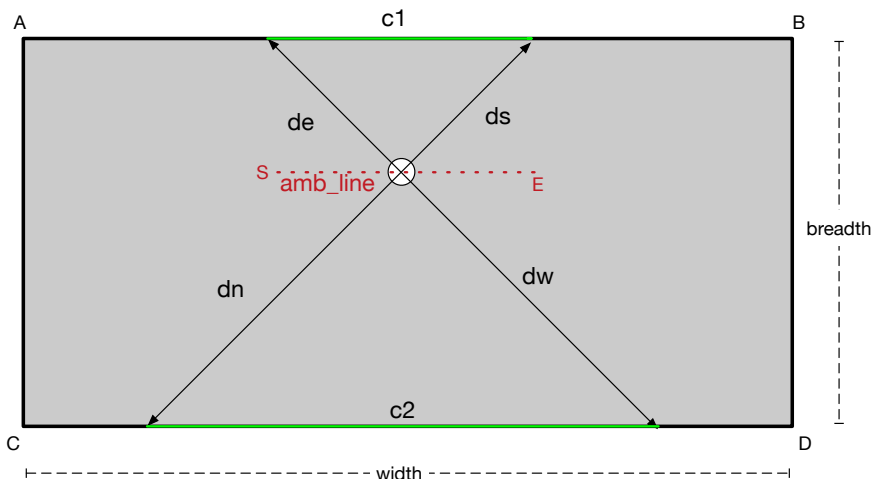


Figure 7.4: If the hypotenuses of the two opposite triangles lie on opposing walls, the ambiguous case occurs: The lines of residence do not intersect but superpose, an ambiguous line is the result for this case.

7 Fusion of Magnetic Field Distance Estimations and LIDAR-based Position Estimations

Although providing 4 degrees of freedom in the 2D case, there are positions in which the actual position cannot uniquely be derived from the measured distances:

Two neighboring distance beams form a right-angled triangle where the adjacent and the opposite sides' length are determined by the distance measurements. The absolute orientation in space is ruled by the heading information. The position estimation is distinct when the corners of the hypotenuse are on different walls. If the two corners are on the same wall (and on the opposing side of the room is a parallel wall where also both points are on the same wall), the position estimation results in an ambiguous case (figure 7.4):

Both hypotenuses are on opposing walls, the position of the LIDAR helmet cannot be reduced to a single point in 2D space but deforms into an ambiguous line. The exact mathematical description of the ambiguous line is: (referring to the variables of figure 7.4):

Let $c_1 = \sqrt{d_e^2 + d_s^2}$ and $c_2 = \sqrt{d_n^2 + d_w^2}$ be the length of the hypotenuses on the walls. The dimensions of the room are determined by the height h and the breadth b . The length $l_{amb} = b - \max c_1, c_2$. The start point \vec{S} of the ambiguous line is $\vec{S} = \vec{C} - \vec{d}_n$, the end point \vec{E} is defined as $\vec{E} = \vec{D} - \vec{d}_w$.

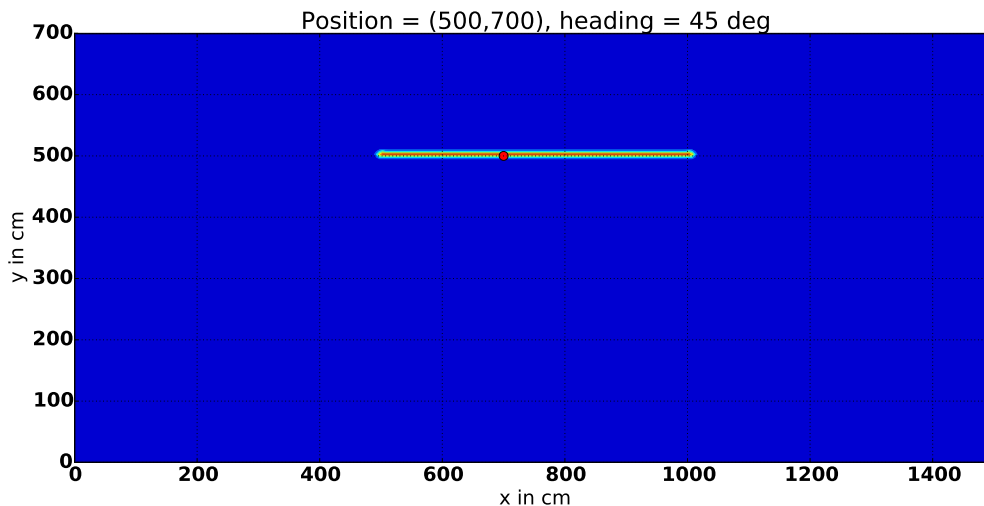


Figure 7.5: Propability distribution in a $700 \times 1500cm$ room. The position is $(400,700)$, the heading is 45 degree. Clearly visible is the ambiguous line of the possible positions with comparable distance.

To solve this problem, it is either necessary to attach more LIDAR Lite sensors with different relative orientations or to use an additional sensor modality to provide additional proximity information. Thus we use the magnetic field indoor localization system.

Figure ?? depicts the results when the distance estimations of the LIDAR sensors is compared against a 5 cm grid in the room. The more equal the distance tuple is compared to the reference position, the higher the probability. It is clearly visible that this position cannot be distinguished solely from the LIDAR distance measurements. Adding a magnetic field transmitter reduces the number of ambiguous positions to two intersections as depicted in figure 7.6.

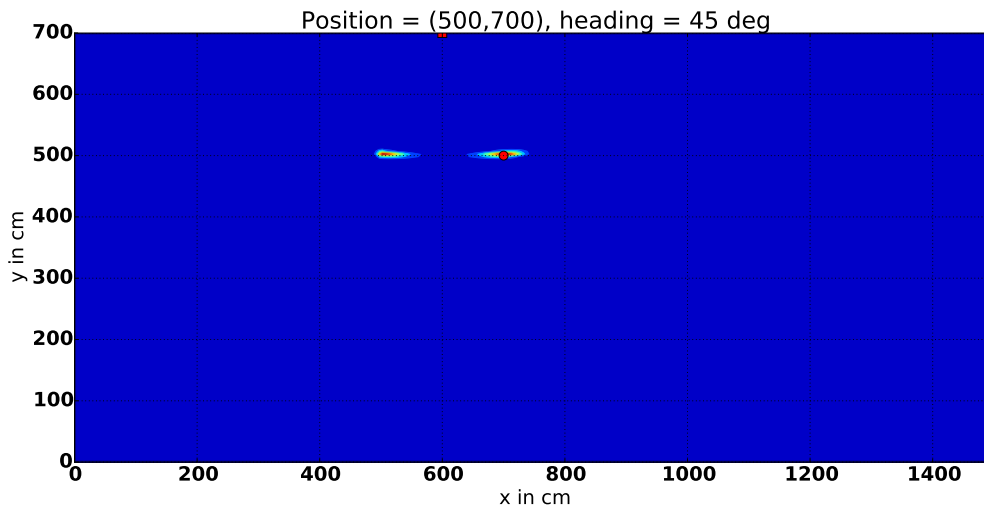


Figure 7.6: Same scene as in figure 7.5 but with single magnetic field transmitter and corresponding distance measurement. This additional anchor point reduces the ambiguous line to two possible positions, which could for example be determined by a particle filter and its tracking possibilities.

7.5 Influence of Distance, Heading and Map Errors on LIDAR Position Accuracy

In the previous section, we mathematically described the LIDAR Lite-based position estimation. In contrast to expensive LIDAR scanners, which provide a full 360 degree scan of the environment, we use an IMU to link the estimated distances and the angular information. As the IMU fuses gyroscope, earth magnetic field information and acceleration data to estimate the bearing information of the sensors, disturbances in the raw sensor data lead to errors in the angular information. Especially anomalies in the earth magnetic fields result in heading errors. The combination of distance and heading information in LIDAR position estimation therefore propagates these errors in the self-localization part.

Obstacles in the environment which are not part of the map, typically the result in lower distance measurements, as the laser pulse is reflected by the obstacle instead of the wall. On the other hand, windows or glass installations lead to higher distances as the laser pulse permeates the glass and the pulse is reflected by obstacles behind the glass.

To study the effects of heading errors and changed distances, we simulate the effects by adding normally distributed error values to randomly chosen position moreover, heading values in a $15m \times 7m$ big rectangular-shaped room for 1000 positions for each error value. Heading values resulting in ambiguous cases (described in the previous section) have been discarded.

Figure 7.7 depicts the effects of heading errors on the localization accuracy. Heading errors have effects on all 4 directions, and therefore the lines of residence are estimated wrong. With growing heading error this effect rises. Due to a number of outliers the mean error value is

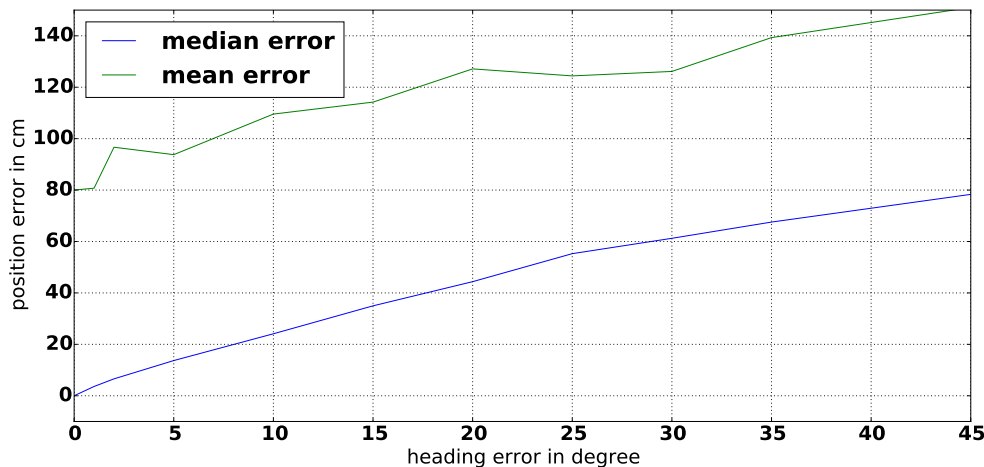


Figure 7.7: Mean and median LIDAR position error caused by heading errors. 8 degree heading error result in a median error of 20cm.

significantly higher than the median error value.

Figure 7.8 depicts the error distribution with an heading error in the interval of ± 15 degrees. The median error of 1000 samples is 36.8cm. Also visible is the high number of outliers. A fraction of outliers results due to ambiguity of the distances / heading tuple, the estimated lines of residence intersect for at least two points in the same number of lines. Therefore it is not possible to distinguish between these points without additional information. Supplemental, the sample set also contains exotic positions where at least one coordinate component is very close to the wall. The outcome of this is degraded lines of residence with multiple but indistinguishable intersections.

The position estimation of the helmet is not only influenced by error-prone heading information but by defective distance measurements. The producer estimated the distance accuracy of the sensor to be around 2.5cm. Environments with unmodelled obstacles such as wardrobes, plants or wall elements result in different distance estimations. The distances do not match the stored map and therefore influencing the quality of the position estimation. We simulate these effects by randomly adding additional error values to the correct distances.

Although evaluating different error intervals, the most interesting error interval is around 40 cm as this is the typical size of furnitures like wardrobes. Figure 7.9 depicts the error distribution of 1000 randomly chosen samples. Compared to erroronouse heading information, the distance estimation errors have lower effects on the position estimation quality than the heading information.

Consequently, unmodelled environmental elements have a lower effect on the position errors than heading errors caused by metal objects.

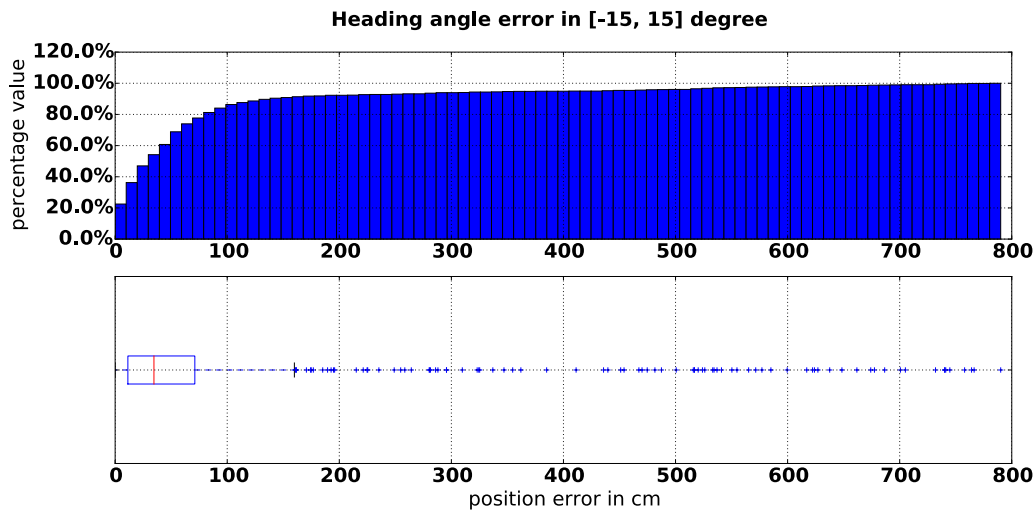


Figure 7.8: Median LIDAR position error, when the heading error lies within ± 15 degree. Median Error of 1000 randomly chosen position and heading tuples is 36.8 cm.

7.6 Fusion of Magnetic Field Distance Information and LIDAR Positions

We discussed in the previous section the influence of heading- and the distance measurement errors on the quality of the position estimation. Also the quality of the "reflection map", which allows to derive the lines of residence and the intersection points, influence the estimation quality. Additionally, depending on the orientation of the LIDAR sensor system, there are cases where the orientation results in ambiguous lines. In these cases, it is not possible to retrieve the unique position of the LIDAR sensor.

7.6.1 Experiment and Evaluation

To evaluate the sensor system we recorded 25 positions in a $6.46 \times 8.7m$ rectangular shaped room. The room has two panorama window sides; we used the installed blinds as reflecting obstacles. The room dimensions have been adapted correspondingly. The helmet was placed on a tripod for uninterrupted measurements. As also visible in figure 7.11 we placed magnetic field transmitters in the environment. The magnetic field system allows to limit the positions of the LIDAR helmet and remove ambiguous positions. At least 1000 measurements have been recorded at each measurement point.

Due to obstacles like plants, storage cupboards or chairs, which have not been part of the room model, in addition to error prone heading information, the estimated LIDAR position derived from the LIDAR distance measurements, does not result in a single point but several intersections. To choose the correct intersection, we fuse the magnetic field distance information with the LIDAR positions.

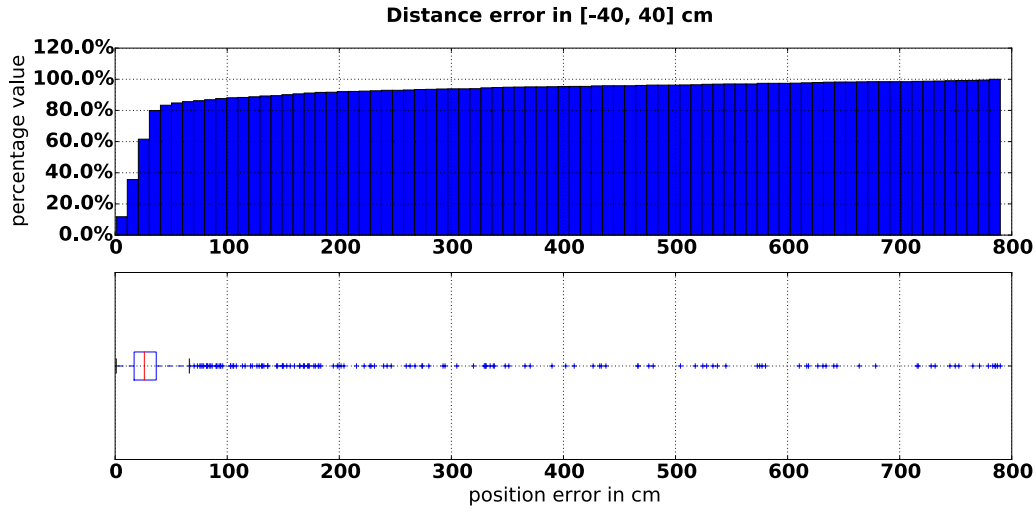


Figure 7.9: Error distribution with an heading error in the interval of ± 5 degree and an distance error in the interval of ± 40 cm. The distance error is interesting as wardrobes usually range is this area, if the map does not indicate this obstacle, this errors can be found.

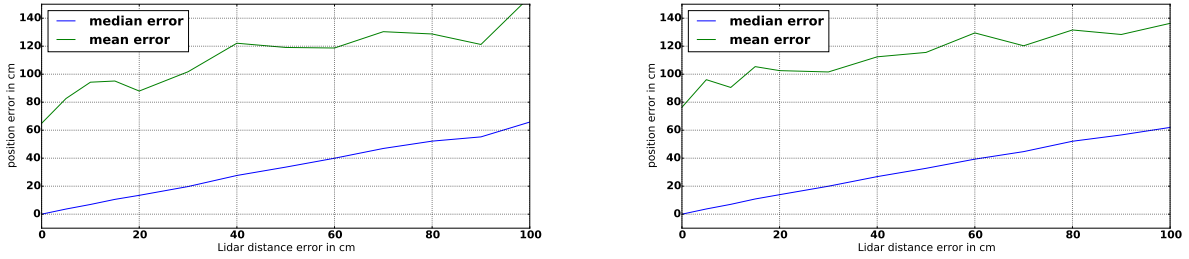


Figure 7.10: Position error dependency relatively to distance errors. Left hand side: Simulation with no heading error, right hand side: Simulation with additional heading error $\epsilon \pm 5$ degree.

The lower boxplot of figure 7.13 depicts the accuracy of the LIDAR-based position estimation when the intersection closest to the reference position is chosen. The median error lies below 8cm.

As the magnetic field receiver and the LIDAR helmet are considered to be at the same point, the distance between the helmet and the magnetic field transmitter is considered to be the same as measured by the magnetic field receiver.

Let $\mathcal{D} = \{d_i\}$ be the set of magnetic field distance measurements to the transmitters t_i . Let $\mathcal{I} = \{\mathbf{p}_i\}$ be the set of possible LIDAR positions, the intersections derived from the LIDAR algorithm.

We compare the distance

$$d_{int} = \|\mathbf{p}_{intersection} - \mathbf{t}_i\| \quad (7.7)$$

between the intersection \mathbf{k} and the transmitter t_i against the measured magnetic field distance d_i :

$$\epsilon_{(i,k)} = d_{int} - d_i \quad (7.8)$$

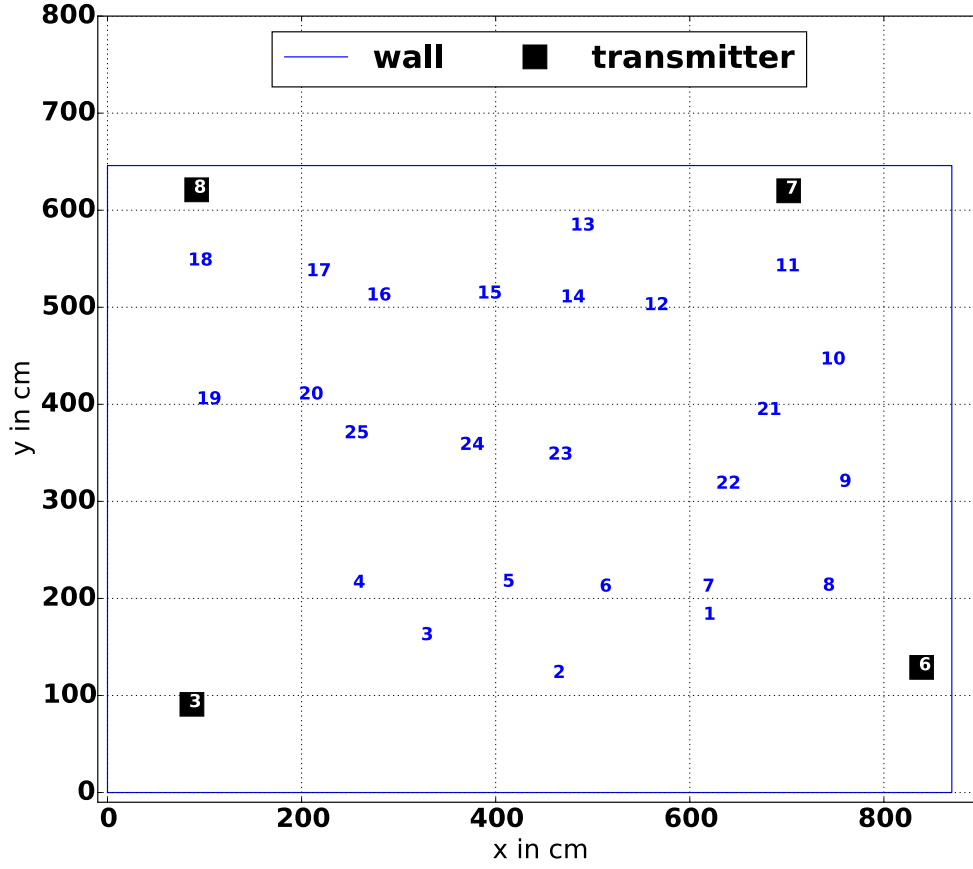


Figure 7.11: Room layout with positions of the transmitters and the measurement positions of the test environment. The magnetic field transmitters have been placed close to the walls.

Using a normal distribution $\mathcal{N}(0\text{ cm}, 40)$ (accuracy value of the magnetic field distance evaluation) allows to estimate the probability of an intersection representing the reference position with corresponding magnetic distances:

$$p_{(i,k)} = \mathcal{N}(\epsilon_{(i,k)}, 0\text{cm}, 40) \quad (7.9)$$

If several magnetic field measurements are available, the probability p_k is

$$p_k = \prod_{i \in \mathcal{D}} p_{(i,k)} \quad (7.10)$$

The intersection with the highest probability is then chosen as result.

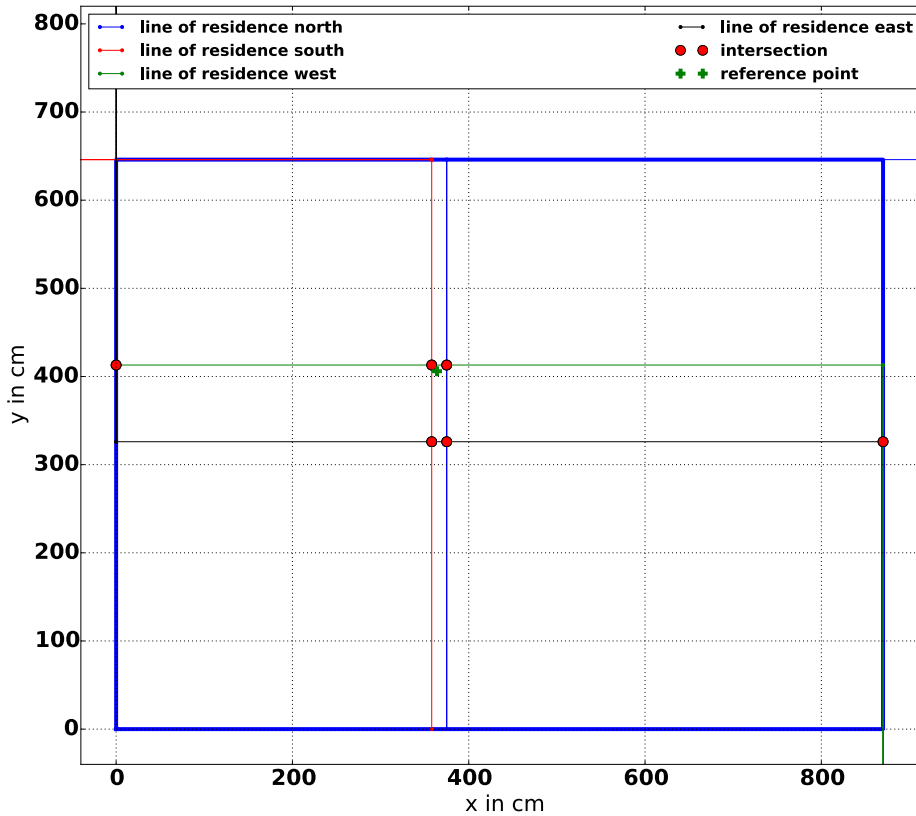


Figure 7.12: Estimated lines of residence for a LIDAR-based helmet position estimation. The 4 LIDAR distance estimations determine 8 lines which intersect in several points in space. The position of the helmet is determined by the highest count of intersections.

We use the weighting function of equation 7.10 to implement a particle filter, the movement, and resampling algorithms are presented in the localization chapter 6.4.3. To allow the filter to settle, we remove the first 20 measurement cycles after the first magnetic field distance measurement.

Figure 7.13 holds the result of the probabilistic LIDAR magnetic field distance fusion algorithm. The median position error is 7.82cm , several outliers positions lead to a high standard deviation of 72.87 and a mean position error of 36.98 cm . Without outliers, the median position error is 5.88cm and a standard deviation of 17.3 . The figure also allows the comparison against the best intersections: Using the best intersection results in a mean and median error below 4cm with a very low standard deviation of 3.1 .

The high variance of the position estimation error in several positions of the LIDAR test is an effect, where the magnetic field signal of a transmitter is unstable. This results in cases, where different intersecting positions are chosen due to their higher probability. This is a drawback of this approach, additional fusion with accelerometer information will reduce this effect

7.7 LIDAR supported Estimation of Magnetic Field Transmitter Positions

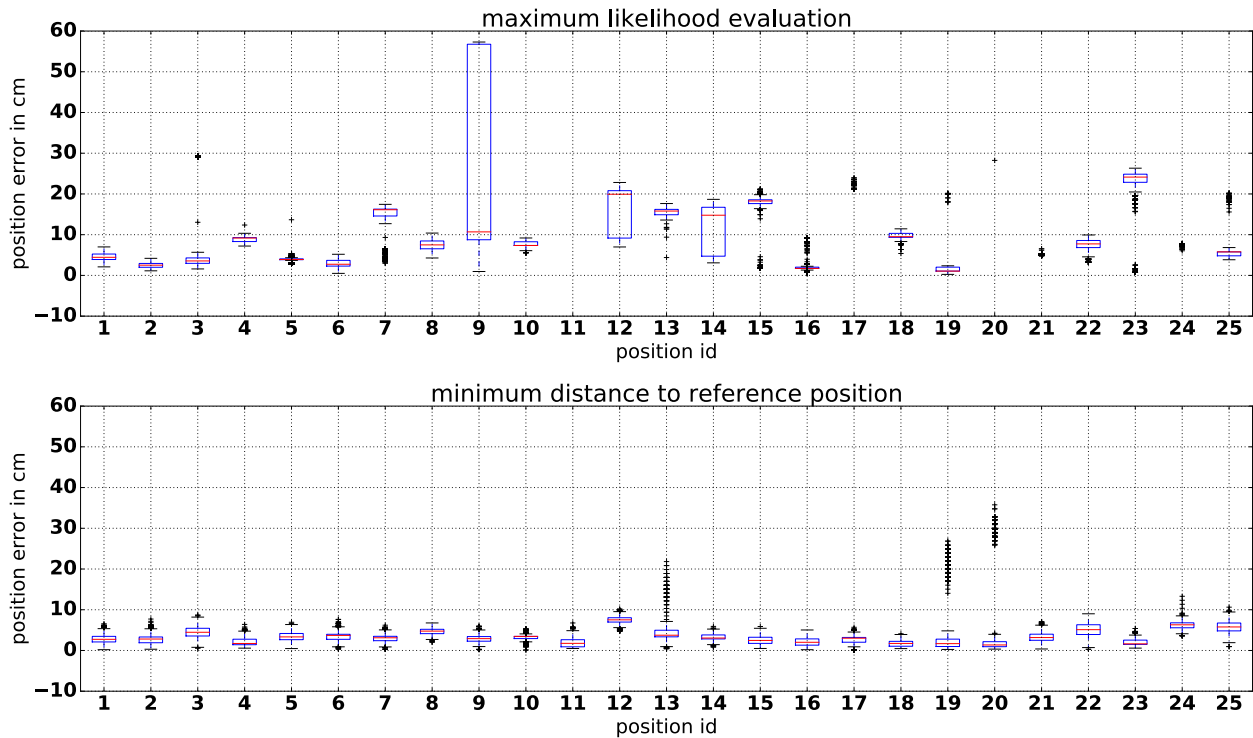


Figure 7.13: Top plot: Error distribution using maximum likelihood and magnetic field distance fusion algorithm for position estimation. The position error distribution over all positions: ($\mu = 36.98, \sigma = 72.87$), median error is 7.82cm. Bottom plot: Intersection with minimum distance to the reference position is chosen. ($\mu = 3.81, \sigma = 3.1$).

7.7 LIDAR supported Estimation of Magnetic Field Transmitter Positions

We already argued, that oscillating magnetic fields have advantages in indoor environments as they permeate obstacles and walls. In [PMF⁺12] we describe algorithms and approaches to support rescue teams in unknown indoor environments using RF and ultrasound information. The rescue teams carry mobile anchor points with them, which are placed along the rescue team's path. The actual position of these anchor points is described and calculated on the fly when the nodes are deployed.

We show in this section a similar approach which uses magnetic field distance estimations and accurate LIDAR positions to describe the unknown position of a new magnetic field transmitter. In contrast to ultra sound-based distance estimations, magnetic field transmitters can also be used in wet/hot environments, they do not require direct line-of-sight and also work when environmental noises (e.g. noises of a burning house) occur. As they permeate structures, a lower number of transmitter positions needs to be deployed.

The following algorithm covers two problems: the first problem is the **position estimation of newly added magnetic field transmitters** and the second problem is how to detect **changes**

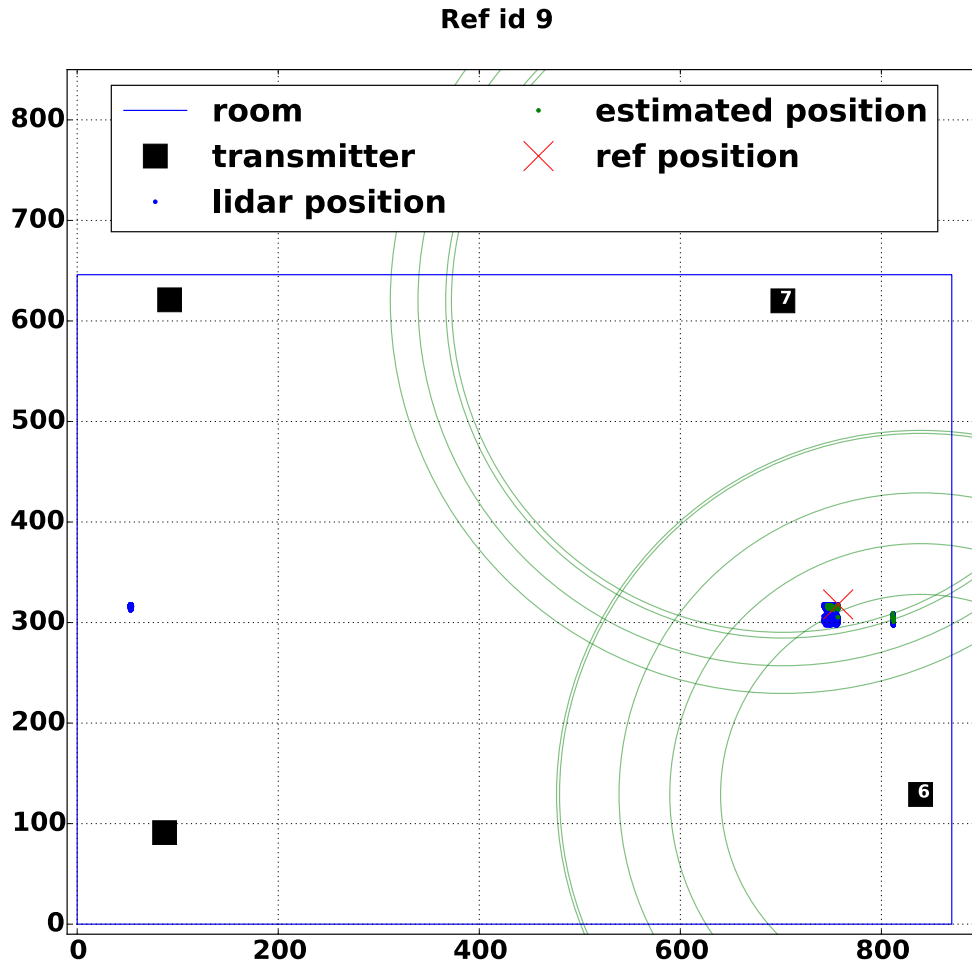


Figure 7.14: Result of the position estimation of reference point 9. Due to changing magnetic field distance estimations, the best intersection point "jumps" from the right intersection cluster to the center cluster and back.

of magnetic transmitter positions. We argue that the second problem can be solved by the first one: the algorithm can periodically run on the gathered information, estimating the positions of the transmitters and compare the estimated position against the stored anchor point position. If there is an offset which is outside a given boundary, the position of the transmitter has been changed.

Keep in mind that we rely on two sources of information: the LIDAR-based position estimation of the helmet (which uses the magnetic field distance information to restrict the possible positions) and the magnetic field distance estimations to the newly added transmitter anchor point.

We use the data set of the previous section 7.6. To follow our argumentation, we only use LIDAR positions which rely on at least two different magnetic field transmitters (one anchor point of whom we assume that the position is known and a transmitter with an unknown position to be estimated.).

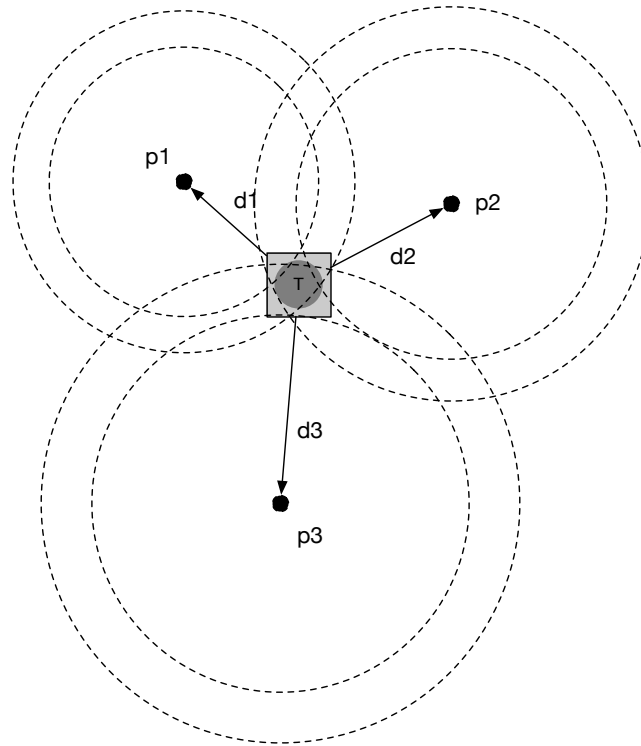


Figure 7.15: Estimation of the transmitter position using 3 position estimations and 3 distance estimations relatively to this transmitter. The position of the transmitter T is derived from the estimated LIDAR-based positions p_i and the magnetic distances d_i measured during the position estimation using the least square position estimation approach as presented in the previous chapter.

Figure 7.15 depicts the idea of our approach: The magnetic-field-based distance estimations from the different LIDAR positions around the magnetic field transmitter are considered to be error prone with an error of up to 40 cm. Each of the LIDAR positions and magnetic field tuples restrict the position of the unknown transmitter to a circular belt around the LIDAR position. A combination of different LIDAR/magnetic distance tuples can, therefore, be used to determine the position of the new transmitter.

Least Square minimization approach For initial tests, we used the same position estimation approach as described in section 6.4.3. The algorithm tries to find a coordinate which minimizes the difference between its distances to the anchor points and the corresponding magnetic field distance measurements. In the simulation, the performance was promising, applying this approach to the real world data set showed its drawback: In most cases, the local minima of the error function was not the absolute minimum. Typically the positions of transmitters are in the corners of rooms. In the data set, the (filtered) LIDAR positions did not allow to fully determine the position of the new, unknown transmitter resulting in inaccurate transmitter positions. The more position distance tuples are available **around** the new transmitter coil, the more accurately an anchor point can be estimated.

Probabilistic approach A more reliable approach is based on statistical evaluation of positions against the LIDAR anchor point / magnetic distance measurements. As in the least square minimization approach, the LIDAR anchor points and the magnetic field distance measurements allow to statistically evaluate each coordinate about its feasibility of being the transmitter position.

Let $\mathcal{L} = \{\mathbf{l}_i \mid i = 0 \dots n\}$ be the set of LIDAR estimated positions, $\mathcal{D} = \{d_i \mid i = 0 \dots n\}$ are the corresponding magnetic field-based distance estimations. Let $\mathbf{p} = (x, y)$ be a possible position of the magnetic field transmitter.

$$\epsilon_i(\mathbf{p}) = \|\mathbf{l}_i - \mathbf{p}\| - d_i$$

The offset $\epsilon_i(\mathbf{p})$ is then statistically evaluated using a normal distribution:

$$\mathcal{W}_{\mathbf{p}} = \sum_{i=0}^n \mathcal{N}(\epsilon_i(\mathbf{p}), 0, 40)$$

In a brute force approach we evaluate each position on a 5cm grid in room and store the probability of each position.

As depicted in figure 7.16 the probability function has its maximum within the room boundary and close to real world position of the transmitter. The results of the position estimation is presented in table 7.1.

| | T1 | T2 | T3 | mean error |
|---------------------|---------|---------|--------|------------|
| reduced data set | 121.4cm | 24.59cm | 113cm | 86cm |
| all LIDAR positions | 26.4cm | 27.5cm | 68.9cm | 40.9cm |

Table 7.1: Position estimation error of an unknown magnetic field transmitter using a combination of LIDAR and magnetic field distance information. The reduced data set requires at least two magnetic field distance measurements (one to a known magnetic field transmitter and one to the unknown magnetic field transmitter to restrict the LIDAR positions as described in the previous section), in the second approach all LIDAR positions are used assuming that the LIDAR position can be estimated using a tracking algorithm.

The position estimation of the newly added transmitter is strongly determined by the spatial relative positions of the LIDAR positions, the measured magnetic field distances and the number of measurements. Low distances restrict the position more than those further away. The variance of the position estimations of t_1, t_2, t_3 are directly linked to the distributions of the distances as depicted in figure 7.17. The mean position error of the transmitter position estimation is 86cm; the minimum error was 25cm. If we assume that we can determine the LIDAR intersections using a tracking algorithm, we can use also those LIDAR positions which only have magnetic field distance measurements to the unknown transmitter; the mean error drops to 40.9cm with a minimum error of 26.4cm.

We saw that the estimation of transmitter positions could be performed by fusing information from LIDAR and magnetic field sensors with an accuracy below 80 cm.

7.7 LIDAR supported Estimation of Magnetic Field Transmitter Positions

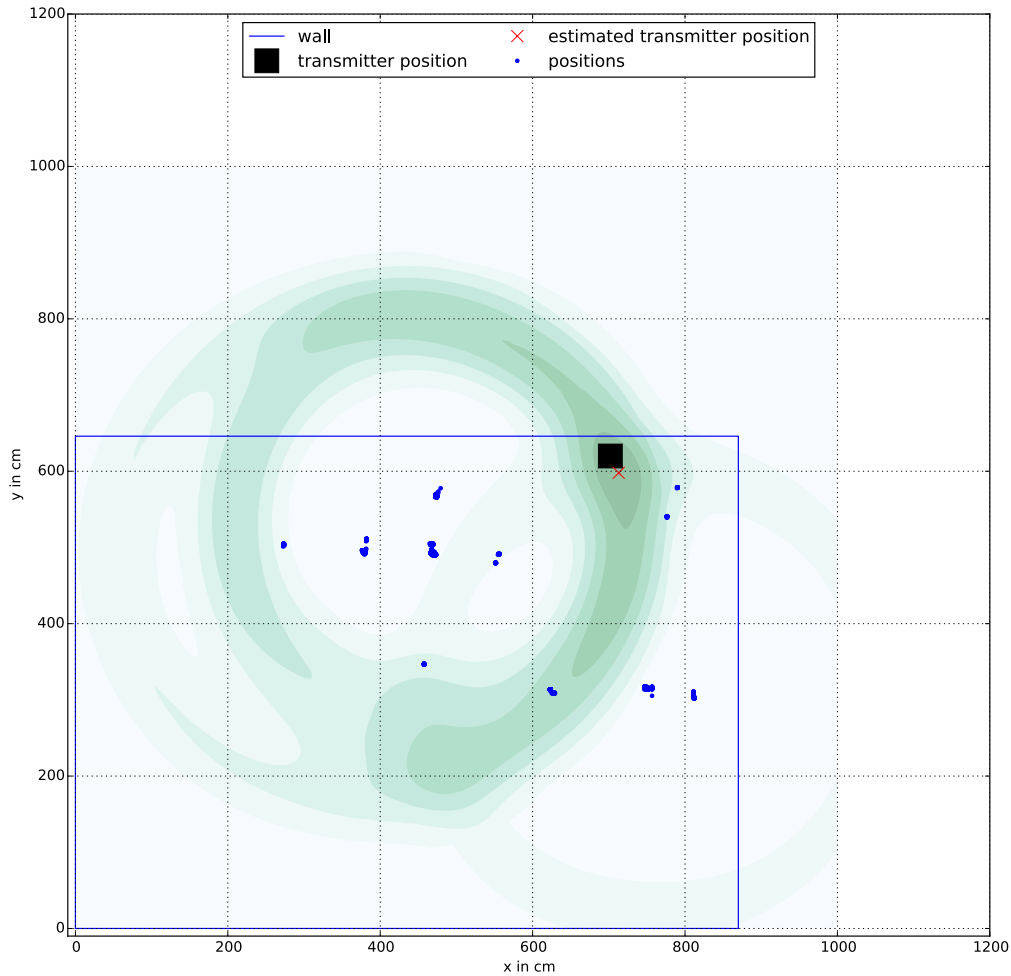


Figure 7.16: Using the magnetic distance information and the LIDAR derived positions at different locations allows to accurately estimate the position of unknown transmitters. The accuracy of the transmitter position increases if distances between the LIDAR and the magnetic transmitter is estimated from different positions around the position.

The approach can, for example, be used on a construction site, where due to the progress of the construction, new anchor points have to be added and their positions have to be estimated.

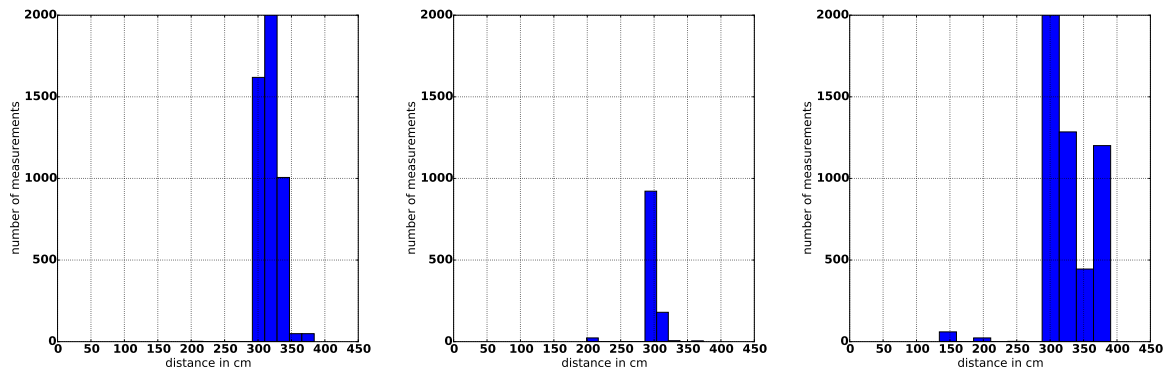


Figure 7.17: Distance distributions of the three transmitter position estimations.

7.8 Conclusion

This chapter described an LIDAR-based localization system. The system is integrated into a helmet, so an application on a construction site is possible. The helmet includes the four LIDAR distance measurement units, an IMU to determine the bearing of the helmet and therefore the directions of the LIDAR beams and an Intel Edison processing unit. The overall position estimation algorithm relies on four distance measurement beams and the heading of the system. Each LIDAR measurement describes lines of residence parallel to the walls. Intersections of these lines then result in the position of the helmet. Due to the comparably low information, special cases can occur in which a distinct position estimation is not possible. Thus we presented the mathematical problem description for these ambiguous cases and a magnetic field distance-supported fusion algorithm to estimate the correct position. In a static evaluation, the combination of magnetic field and LIDAR information used for position estimation achieves a mean position error of 36 cm; the median error is 7.82 applying a maximum likelihood approach. The estimation of the position of magnetic field-based anchor points has been evaluated, the position can be estimated with a mean error of 86 cm when measurements to two magnetic field transmitters are requested, if also single measurements to the transmitter to be position are used, the positioning error drops to 40.9 cm.

8 Conclusion

In this dissertation, we described a localization system based on oscillating magnetic fields. The system consists of two components, stationary magnetic field transmitters, and wearable magnetic field receivers. Compared to other physical localization modalities, the magnetic field signal interaction with the environment is either nonexistent or locally restricted. We presented a processing architecture which utilizes the physical behavior of magnetic fields to provide a stable, reliable and accurate position and distance estimation. The architecture covers the **physical layer**, the **position and distance estimation against a single transmitter** and the **multi coil position estimation** against all transmitters. The system has been evaluated in different environments about accuracy and spatial resolution (detection of regions of interest). The approaches also cover the repeatability of the signal. In environments with a high ratio of metal devices, which strongly influences RF-based localization systems, the advantage of magnetic fields is visible: RF systems are either not able to determine positions or are strongly influenced, our approach still retrieves the location information.

Physical Layer The physical layer of the system deals with hardware related methods covering magnetic field generation and information encoding on the transmitter side, transmitter-receiver synchronization, signal gathering, amplification and signal encoding on the receiver side. The tasks are implemented on a DSPIC micro-controller, utilize special digital signal processing commands to speed up the tasks and also consider the magnetic field's properties, as its high dynamic range.

Single coil position and distance estimation This single coil position and distance estimation layer implements a hardware abstraction layer to transform the hardware specific magnetic field signals of the receivers to a common signal level of the magnetic field model to reduce memory consumption. On top of this, a magnetic field model reflects the shape and behavior of the magnetic field in the environment. It enables the system to retrieve a (rough) position (mean error of 108cm) of the receiver using a three coil transmitter architecture; the distances have a mean error of 40 cm within the maximum range of 4.5m.

Multi coil position estimation A combination of measurements to multiple transmitters requires scheduling, time synchronization algorithms and a localization algorithm based on the estimated candidate sets and the distances to the anchor points. Two scheduling algorithms have been evaluated. A round-robin-based approach permeates furniture for small scale setups. For a higher number of transmitters, we described a scheduling algorithm which includes the spatial

8 Conclusion

distribution of the transmitters and simultaneously triggers transmitters whose magnetic fields do not superpose. This problem has been transferred to graph theory, and by applying a graph coloring approach, it was possible to determine a valid schedule without superposing magnetic fields to speed up the scheduling process and therefore to increase the position estimation rates. The localization fusion algorithm covers multilateration approaches using the distance estimations (circle intersection, least square error minimization), the candidate sets are evaluated by finding the candidates who are closest to each other. On top of these algorithms, a particle filter performs tracking and filtering.

Evaluation and applications The described indoor localization system allows a position estimation with a mean error of 65cm to 75cm (in an area of $8m \times 10m$) depending on the evaluated environment. For comparison, a commercially available Bluetooth RF localization system has been tested in a shopping environment ($12m \times 8m$) with a mean position error of 67cm, our prototype system reached a mean position error of 77cm in the same environment. Although performing worse than the RF system, the magnetic field-based localization system was able to retrieve a position in each reference position, whereas the RF system was not able to estimate a position below metal shopping counters.

Additionally different region of interest detection approaches have been evaluated in office, living and industrial environments, all utilizing raw magnetic field information and distance/position information derived from the magnetic field model. For large scale setups (8 coils in $20m \times 10m$) the regions have to be at least 50cm apart, a small scale coil setup (3 coils in $2m \times 3m \times 0.8m$) requires at least 15 to 20cm proximity between the ROIs.

LIDAR / Magnetic field Distance Fusion The magnetic field localization system has also been used to support a LIDAR localization system. We described the position estimation based on four laser distance measurements against walls and possible constraints arising due to the low number of information. A fusion algorithm of magnetic field derived distances, and LIDAR-based positions have also been presented. It solves ambiguous positions and support the overall position estimation. The mean position error of the fused LIDAR system is 8cm.

Summary *We presented in this dissertation an indoor localization system based on oscillating magnetic fields. We specified the processing architecture, identified layer specific problems and presented, researched, implemented and evaluated approaches solving these problems. Additionally, concepts, especially on the lower level layers of the processing architecture, take the magnetic field behavior into account. The oscillating magnetic field localization system provides distance estimations with a mean error of 40cm against the stationary magnetic field anchor points; the overall position accuracy is between 60 and 70 cm depending on the environment. The system has been evaluated in key environments about accuracy and the ability to separate regions of interest. Comparing our prototype system against a commercially available RF-based localization system showed the advantages of magnetic fields about obstacles: Our system estimated positions below metal objects, the RF-based system was not able to determine these points. This shows that magnetic fields are a good alternative source of information in indoor environments. Compared to other physical measurement principles, the magnetic field permeates furniture, walls, persons and electronic devices and therefore the installation effort is lowered as no line-of-sight is required. Particularly in the field of ubiquitous computing and AAL, this system allows a nonintrusive installation as it can be integrated into the environment, for example within the raised floor or in a cupboard. Publications of this localization system have been submitted and peer reviewed at well-known conferences and journals covering the fields of indoor localization([PHCL15], [PMF⁺12], [PKLF11]), wearable computing ([PSKL08]), ubiquitous computing([PL12]) and Ambient assisted living ([PBA⁺10], [PL13]) and was also used to generate data sets for gesture recognition ([PLB⁺10]).*

Future Work

The research on the localization system holds several topics which are either addressed in current projects (for example "HiMagiac" funded by Stiftung Rheinland-Pfalz) which can be addressed in future works:

The underlying hardware can be improved; this covers the used **coil architecture** moreover, the transmitter and receiver side circuits. We already showed that different coil shapes have different crosstalk values and therefore different performances. As the crosstalk strongly influences the generated magnetic field, a crosstalk reduction leads to a range extension on the one hand, and an improvement in position estimation accuracy in the currently covered area on the other hand.

On the receiver side a reduction of the hardware noise level in combination with auto-logarithmical amplifiers and 24bit ADCs can **improve the sensitivity of the signal gathering** approach. Due to the fast signal decline (high distance dependency), this only works in combination with stronger magnetic fields.

Not addressed in this work is the **orientation estimation** relying on magnetic fields. The generated magnetic fields in addition to the receiver side three axis coil provide sufficient information to describe the relative bearing of the receiver coil.

We described an initial calibration process to transform the hardware related signal levels to a common theoretical magnetic field signal level. Magnetic field distortions caused by the environment (for example metal objects) can and should be part of the calibration process when the system is set up in a new environment. Therefore environmental models or fingerprinting-based lookup tables are suitable approaches and can improve the localization accuracy.

A **fusion of the magnetic field positions with acceleration information** is an option to reduce the position noise when in a stationary state or to increase the accuracy of the tracking algorithm when the receiver is moved. The integration of the acceleration information can be part of the already described particle filter.

Several **applications** for this indoor localization system are of interest: Due to the permeating nature of the magnetic fields, the system can be used in industrial production lines to provide absolute position information for a transport robot. Applications in hospital environments with a very dynamic and varying environment are also possible, the magnetic field-based localization system can track movements of nurses and other groups to provide information about cooperations and interactions.

Bibliography

- [ABB⁺98] A Ahlbom, U Bergqvist, JH Bernhardt, JP Cesarini, M Grandolfo, M Hietanen, AF Mckinlay, MH Repacholi, DH Sliney, JAJ Stolwijk, et al. Guidelines for limiting exposure to time-varying electric, magnetic, and electromagnetic fields (up to 300 ghz). international commission on non-ionizing radiation protection. *Health Phys*, 74(4):494–522, 1998.
- [ACD⁺11] Salah Azzouzi, Markus Cremer, Uwe Dettmar, Thomas Knie, and Rainer Kronberger. Improved aoa based localization of uhf rfid tags using spatial diversity. In *RFID-Technologies and Applications (RFID-TA), 2011 IEEE International Conference on*, pages 174–180. IEEE, 2011.
- [ACRC09] Martin Azizyan, Ionut Constandache, and Romit Roy Choudhury. Surroundsense: Mobile phone localization via ambience fingerprinting. In *Proceedings of the 15th Annual International Conference on Mobile Computing and Networking, MobiCom '09*, pages 261–272, New York, NY, USA, 2009. ACM.
- [AFD07] Abdalkarim Awad, Thorsten Frunzke, and Falko Dressler. Adaptive distance estimation and localization in wsn using rssi measures. In *Digital System Design Architectures, Methods and Tools, 2007. DSD 2007. 10th Euromicro Conference on*, pages 471–478. IEEE, 2007.
- [ASS⁺09] Sameer Agarwal, Noah Snavely, Ian Simon, Steven M. Seitz, and Richard Szeliski. Building rome in a day. In *Twelfth IEEE International Conference on Computer Vision (ICCV 2009)*, Kyoto, Japan, September 2009. IEEE.
- [ASSC02] Ian F Akyildiz, Weilian Su, Yogesh Sankarasubramaniam, and Erdal Cayirci. A survey on sensor networks. *Communications magazine, IEEE*, 40(8):102–114, 2002.
- [AV04] Cesare Alippi and Giovanni Vanini. Wireless sensor networks and radio localization: a metrological analysis of the mica2 received signal strength indicator. In *37th Annual IEEE Conference on Local Computer Networks*, pages 579–582. IEEE Computer Society, 2004.
- [Awe85] Baruch Awerbuch. A new distributed depth-first-search algorithm. *Inf. Process. Lett.*, 20(3):147–150, 1985.
- [AZ01] Parham Aarabi and Safwat Zaky. Robust sound localization using multi-source audiovisual information fusion. *Information Fusion*, 2(3):209 – 223, 2001.

Bibliography

- [BDS08] Mathieu Bouet and Aldri L Dos Santos. Rfid tags: Positioning principles and localization techniques. In *Wireless Days, 2008. WD'08. 1st IFIP*, pages 1–5. IEEE, 2008.
- [BJ09] Melvin L Barnes Jr. System, method, and computer program product for providing location based services and mobile e-commerce, February 3 2009. US Patent 7,487,112.
- [BJRGN11] Francisco Borrego-Jaraba, Irene Luque Ruiz, and Miguel Ángel Gómez-Nieto. A nfc-based pervasive solution for city touristic surfing. *Personal and ubiquitous Computing*, 15(7):731–742, 2011.
- [BK88] Johann Borenstein and Yoram Koren. Obstacle avoidance with ultrasonic sensors. *Robotics and Automation, IEEE Journal of*, 4(2):213–218, 1988.
- [BK12] C. Beder and M. Klepal. Fingerprinting based localisation revisited: A rigorous approach for comparing rssi measurements coping with missed access points and differing antenna attenuations. In *Indoor Positioning and Indoor Navigation (IPIN), 2012 International Conference on*, pages 1–7, Nov 2012.
- [BMB⁺13] Andreas Baak, Meinard Müller, Gaurav Bharaj, Hans-Peter Seidel, and Christian Theobalt. A data-driven approach for real-time full body pose reconstruction from a depth camera. In *Consumer Depth Cameras for Computer Vision*, pages 71–98. Springer, 2013.
- [BMPC08] Karl Benkic, Marko Malajner, P Planinsic, and Z Cucej. Using rssi value for distance estimation in wireless sensor networks based on zigbee. In *Systems, Signals and Image Processing, 2008. IWSSIP 2008. 15th International Conference on*, pages 303–306. IEEE, 2008.
- [Boe] Wolfgang Boehler. Investigating laser scanner accuracy.
- [BP00] Paramvir Bahl and Venkata N Padmanabhan. Radar: An in-building rf-based user location and tracking system. In *INFOCOM 2000. Nineteenth Annual Joint Conference of the IEEE Computer and Communications Societies. Proceedings. IEEE*, volume 2, pages 775–784. Ieee, 2000.
- [BSM07] Abdelmoula Bekkali, Horacio Sanson, and Mitsuji Matsumoto. Rfid indoor positioning based on probabilistic rfid map and kalman filtering. In *Wireless and Mobile Computing, Networking and Communications, 2007. WiMOB 2007. Third IEEE International Conference on*, pages 21–21. IEEE, 2007.
- [BZF12] Michael Bosse, Robert Zlot, and Paul Flick. Zebedee: Design of a spring-mounted 3-d range sensor with application to mobile mapping. *Robotics, IEEE Transactions on*, 28(5):1104–1119, 2012.
- [CBK⁺11] David M Chen, Georges Baatz, K Koser, Sam S Tsai, Ramakrishna Vedantham, Timo Pylvanainen, Kimmo Roimela, Xin Chen, Jeff Bach, Marc Pollefeys, et al. City-scale landmark identification on mobile devices. In *Computer Vision and*

- Pattern Recognition (CVPR), 2011 IEEE Conference on*, pages 737–744. IEEE, 2011.
- [CBSS98] Michael J Caruso, Tamara Bratland, Carl H Smith, and Robert Schneider. A new perspective on magnetic field sensing. *SENSORS-PETERBOROUGH-*, 15:34–47, 1998.
- [CCG] Min Chen, Fred Cheng, and Ram Gudavalli. Precision and accuracy in an indoor localization system.
- [CDS⁺11] Jaewoo Chung, Matt Donahoe, Chris Schmandt, Ig-Jae Kim, Pedram Razavai, and Micaela Wiseman. Indoor location sensing using geo-magnetism. In *Proceedings of the 9th international conference on Mobile systems, applications, and services*, pages 141–154. ACM, 2011.
- [CKBH00] G.K.M. Cheung, T. Kanade, J.-Y. Bouguet, and M. Holler. A real time system for robust 3d voxel reconstruction of human motions. In *Computer Vision and Pattern Recognition, 2000. Proceedings. IEEE Conference on*, volume 2, pages 714–720 vol.2, 2000.
- [CLZ⁺13] Lina Chen, Binghao Li, Kai Zhao, Chris Rizos, and Zhengqi Zheng. An improved algorithm to generate a wi-fi fingerprint database for indoor positioning. *Sensors*, 13(8):11085–11096, 2013.
- [CN08] Mark Cummins and Paul Newman. Fab-map: Probabilistic localization and mapping in the space of appearance. *The International Journal of Robotics Research*, 27(6):647–665, 2008.
- [COSH11] David Crandall, Andrew Owens, Noah Snavely, and Dan Huttenlocher. Discrete-continuous optimization for large-scale structure from motion. In *Computer Vision and Pattern Recognition (CVPR), 2011 IEEE Conference on*, pages 3001–3008. IEEE, 2011.
- [Cri89] Flaviu Cristian. Probabilistic clock synchronization. *Distributed Computing*, 3(3):146–158, 1989.
- [DCC12] Gabriel Deak, Kevin Curran, and Joan Condell. A survey of active and passive indoor localisation systems. *Computer Communications*, 35(16):1939–1954, 2012.
- [DCFPF11] Dan Ding, Rory A Cooper, Paul F Pasquina, and Lavinia Fici-Pasquina. Sensor technology for smart homes. *Maturitas*, 69(2):131–136, June 2011.
- [DCR10] Rafael Lima De Carvalho and Paulo Fernando Ferreira Rosa. Identification system for smart homes using footstep sounds. In *Industrial Electronics (ISIE), 2010 IEEE International Symposium on*, pages 1639–1644. IEEE, 2010.
- [DSD08] Laura Dipietro, Angelo M Sabatini, and Paolo Dario. A survey of glove-based systems and their applications. *Systems, Man, and Cybernetics, Part C: Applications and Reviews, IEEE Transactions on*, 38(4):461–482, 2008.

Bibliography

- [ED06] Ethan Eade and Tom Drummond. Scalable monocular slam. In *Computer Vision and Pattern Recognition, 2006 IEEE Computer Society Conference on*, volume 1, pages 469–476. IEEE, 2006.
- [EGE02] Jeremy Elson, Lewis Girod, and Deborah Estrin. Fine-grained network time synchronization using reference broadcasts. *ACM SIGOPS Operating Systems Review*, 36(SI):147–163, 2002.
- [EM06] Frédéric Evennou and François Marx. Advanced integration of wifi and inertial navigation systems for indoor mobile positioning. *Eurasip journal on applied signal processing*, 2006:164–164, 2006.
- [FFGG⁺10] Jan-Michael Frahm, Pierre Fite-Georgel, David Gallup, Tim Johnson, Rahul Raguram, Changchang Wu, Yi-Hung Jen, Enrique Dunn, Brian Clipp, Svetlana Lazebnik, et al. Building rome on a cloudless day. In *Computer Vision–ECCV 2010*, pages 368–381. Springer, 2010.
- [FNI13] Zahid Farid, Rosdiadee Nordin, and Mahamod Ismail. Recent advances in wireless indoor localization techniques and system. *Journal of Computer Networks and Communications*, 2013, 2013.
- [G.11] Collinson R. P. G. *Introduction to avionics systems*. Springer, 2011.
- [GBG⁺09] J. González, J.L. Blanco, C. Galindo, A. Ortiz de Galisteo, J.A. Fernández-Madrigal, F.A. Moreno, and J.L. Martínez. Mobile robot localization based on ultra-wide-band ranging: A particle filter approach. *Robotics and Autonomous Systems*, 57(5):496 – 507, 2009.
- [GG03] Fredrik Gustafsson and Fredrik Gunnarsson. Positioning using time-difference of arrival measurements. In *Acoustics, Speech, and Signal Processing, 2003. Proceedings. (ICASSP'03). 2003 IEEE International Conference on*, volume 6, pages VI–553. IEEE, 2003.
- [GH05] André Günther and Christian Hoene. Measuring round trip times to determine the distance between wlan nodes. In *NETWORKING 2005. Networking Technologies, Services, and Protocols; Performance of Computer and Communication Networks; Mobile and Wireless Communications Systems*, pages 768–779. Springer, 2005.
- [GKS03] Saurabh Ganeriwal, Ram Kumar, and Mani B Srivastava. Timing-sync protocol for sensor networks. In *Proceedings of the 1st international conference on Embedded networked sensor systems*, pages 138–149. ACM, 2003.
- [GLN09] Yanying Gu, A. Lo, and I. Niemegeers. A survey of indoor positioning systems for wireless personal networks. *Communications Surveys Tutorials, IEEE*, 11(1):13–32, First 2009.
- [GO02] David B Green and AS Obaidat. An accurate line of sight propagation performance model for ad-hoc 802.11 wireless lan (wlan) devices. In *Communications, 2002. ICC 2002. IEEE International Conference on*, volume 5, pages 3424–3428. IEEE, 2002.

- [GR03] Jana Van Gruenen and Jan Rabaey. Lightweight time synchronization for sensor networks. In *WSNA*, 2003.
- [GSDM11] Brandon Gozick, Kalyan Pathapati Subbu, Ram Dantu, and Tomyo Maeshiro. Magnetic maps for indoor navigation. *Instrumentation and Measurement, IEEE Transactions on*, 60(12):3883–3891, 2011.
- [GTKKxn14] Dennis Groben, Kittikhun Thongpull, Abhaya Chandra Kammara, and Andreas K xF6 nig. Neural Virtual Sensors for Adaptive Magnetic Localization of Autonomous Dataloggers. *Advances in Artificial Neural Systems*, 2014:17, 2014.
- [Har13] Robert Harle. A survey of indoor inertial positioning systems for pedestrians. *IEEE Communications Surveys & Tutorials*, (15):1281–1293, 2013.
- [Has93] Homayoun Hashemi. The indoor radio propagation channel. *Proceedings of the IEEE*, 81(7):943–968, 1993.
- [HB01] Jeffrey Hightower and Gaetano Borriello. Location systems for ubiquitous computing. *Computer*, 34(8):57–66, 2001.
- [HE04] Lingxuan Hu and David Evans. Localization for mobile sensor networks. In *Proceedings of the 10th annual international conference on Mobile computing and networking*, pages 45–57. ACM, 2004.
- [Hen04] Heino Henke. *Elektromagnetische Felder: Theorie und Anwendung*. Engineering online library. Springer, 2004.
- [HGRL08] Friedrich Hanser, Agnes Gruenerbl, Clemens Rodegast, and Paul Lukowicz. Design and real life deployment of a pervasive monitoring system for dementia patients. In *Pervasive Computing Technologies for Healthcare, 2008. . International ICST Conference on Pervasive Computing Technologies for Healthcare (Pervasive Health-2008), 2nd, January 30 - February 1, Tampere, Finland*. IEEE, 2008. Feb. 1 2008 Page(s): 279-280 Digital Object Identifier 10. 1109 / PCTHEALTH. 2008. 4571090.
- [HHB⁺03] Tian He, Chengdu Huang, Brian M Blum, John A Stankovic, and Tarek Abdelzaher. Range-free localization schemes for large scale sensor networks. In *Proceedings of the 9th annual international conference on Mobile computing and networking*, pages 81–95. ACM, 2003.
- [HHZN12] Omran Al Hammadi, Ahmed Al Hebsi, M Jamal Zemerly, and Jason WP Ng. Indoor localization and guidance using portable smartphones. In *Proceedings of the The 2012 IEEE/WIC/ACM International Joint Conferences on Web Intelligence and Intelligent Agent Technology-Volume 03*, pages 337–341. IEEE Computer Society, 2012.
- [HK09] Janne Haverinen and Anssi Kemppainen. Global indoor self-localization based on the ambient magnetic field. *Robotics and Autonomous Systems*, 57(10):1028–1035, 2009.

Bibliography

- [HKH⁺10] Peter Henry, Michael Krainin, Evan Herbst, Xiaofeng Ren, and Dieter Fox. Rgb-d mapping: Using depth cameras for dense 3d modeling of indoor environments. In *In the 12th International Symposium on Experimental Robotics (ISER)*, 2010.
- [HLCH12] Miles Hansard, Seungkyu Lee, Ouk Choi, and Radu Patrice Horaud. *Time-of-flight cameras: principles, methods and applications*. Springer Science & Business Media, 2012.
- [HTP10] Michal Havlena, Akihiko Torii, and Tomáš Pajdla. Efficient structure from motion by graph optimization. In *Computer Vision—ECCV 2010*, pages 100–113. Springer, 2010.
- [HTU09] S. Hijikata, K. Terabayashi, and K. Umeda. A simple indoor self-localization system using infrared leds. In *Networked Sensing Systems (INSS), 2009 Sixth International Conference on*, pages 1–7, June 2009.
- [HW02] Mike Hazas and Andy Ward. A novel broadband ultrasonic location system. In *UbiComp 2002: Ubiquitous Computing*, pages 264–280. Springer, 2002.
- [HWB00] Jeffrey Hightower, Roy Want, and Gaetano Borriello. Spoton: An indoor 3d location sensing technology based on rf signal strength. *UW CSE 00-02-02, University of Washington, Department of Computer Science and Engineering, Seattle, WA*, 1, 2000.
- [IHQ04] S.J. Ingram, D. Harmer, and M. Quinlan. Ultrawideband indoor positioning systems and their use in emergencies. In *Position Location and Navigation Symposium, 2004. PLANS 2004*, pages 706–715, April 2004.
- [IKH⁺11] Shahram Izadi, David Kim, Otmar Hilliges, David Molyneaux, Richard Newcombe, Pushmeet Kohli, Jamie Shotton, Steve Hodges, Dustin Freeman, Andrew Davison, et al. Kinectfusion: real-time 3d reconstruction and interaction using a moving depth camera. In *Proceedings of the 24th annual ACM symposium on User interface software and technology*, pages 559–568. ACM, 2011.
- [IZFB09] Arnold Irschara, Christopher Zach, J-M Frahm, and Horst Bischof. From structure-from-motion point clouds to fast location recognition. In *Computer Vision and Pattern Recognition, 2009. CVPR 2009. IEEE Conference on*, pages 2599–2606. IEEE, 2009.
- [JFY⁺14] Weiwei Jiang, Denzil Ferreira, Jani Ylioja, Jorge Goncalves, and Vassilis Kostakos. Pulse: Low bitrate wireless magnetic communication for smartphones. In *Proceedings of the 2014 ACM International Joint Conference on Pervasive and Ubiquitous Computing, UbiComp '14*, pages 261–265, New York, NY, USA, 2014. ACM.
- [JLC⁺12] Xiaofan Jiang, Chieh-Jan Mike Liang, Kaifei Chen, Ben Zhang, Jeff Hsu, Jie Liu, Bin Cao, and Feng Zhao. Design and evaluation of a wireless magnetic-based proximity detection platform for indoor applications. In *Proceedings of the 11th*

international conference on Information Processing in Sensor Networks, pages 221–232. ACM, 2012.

- [JLP06] Guang-yao Jin, Xiao-yi Lu, and Myong-Soon Park. An indoor localization mechanism using active rfid tag. In *Sensor Networks, Ubiquitous, and Trustworthy Computing, 2006. IEEE International Conference on*, volume 1, pages 4–pp. IEEE, 2006.
- [KL08] Jürgen Kemper and Holger Linde. Challenges of passive infrared indoor localization. In *Positioning, Navigation and Communication, 2008. WPNC 2008. 5th Workshop on*, pages 63–70. IEEE, 2008.
- [Klo02] Walter Klotz. Graph coloring algorithms. *Mathematics Report*, 5(2002):1–9, 2002.
- [KMR08] Karl Küpfmüller, Wolfgang Mathis, and Albrecht Reibiger. *Theoretische Elektrotechnik*. Springer-Lehrbuch. Springer, 2008.
- [KN04] T. Komine and M. Nakagawa. Fundamental analysis for visible-light communication system using led lights. *Consumer Electronics, IEEE Transactions on*, 50(1):100–107, Feb 2004.
- [KVPV14] Tero Kivimäki, Timo Vuorela, Pekka Peltola, and Jukka Vanhala. A review on device-free passive indoor positioning methods. *International Journal of Smart Home*, 8(1):71–94, 2014.
- [KZM⁺08] Michael Kuhn, Cemin Zhang, Brandon Merkl, Depeng Yang, Yazhou Wang, Mohamed Mahfouz, and Aly Fathy. High accuracy uwb localization in dense indoor environments. In *Ultra-Wideband, 2008. ICUWB 2008. IEEE International Conference on*, volume 2, pages 129–132. IEEE, 2008.
- [LC10] Sami M Lasassmeh and James M Conrad. Time synchronization in wireless sensor networks: A survey. In *IEEE SoutheastCon 2010 (SoutheastCon), Proceedings of the*, pages 242–245. IEEE, 2010.
- [LCC⁺10] T. Liu, M. Carlberg, G. Chen, J. Chen, J. Kua, and A. Zakhor. Indoor localization and visualization using a human-operated backpack system. In *Indoor Positioning and Indoor Navigation (IPIN), 2010 International Conference on*, pages 1–10, Sept 2010.
- [LCCVG07] Bastian Leibe, Nico Cornelis, Kurt Cornelis, and Luc Van Gool. Dynamic 3d scene analysis from a moving vehicle. In *Computer Vision and Pattern Recognition, 2007. CVPR'07. IEEE Conference on*, pages 1–8. IEEE, 2007.
- [LDBL07] Hui Liu, Houshang Darabi, Pat Banerjee, and Jing Liu. Survey of wireless indoor positioning techniques and systems. *Systems, Man, and Cybernetics, Part C: Applications and Reviews, IEEE Transactions on*, 37(6):1067–1080, 2007.
- [LHP⁺14] Liqun Li, Pan Hu, Chunyi Peng, Guobin Shen, and Feng Zhao. Epsilon: a visible light based positioning system. In *Proceedings of the 11th USENIX Conference*

Bibliography

- on Networked Systems Design and Implementation*, pages 331–343. USENIX Association, 2014.
- [Li] Larry Li. Time-of-flight camera—an introduction.
- [LR12] Patrick Lazik and Anthony Rowe. Indoor pseudo-ranging of mobile devices using ultrasonic chirps. In *Proceedings of the 10th ACM Conference on Embedded Network Sensor Systems*, pages 99–112. ACM, 2012.
- [LS07] Sooyong Lee and Jae-Bok Song. Mobile robot localization using infrared light reflecting landmarks. In *Control, Automation and Systems, 2007. ICCAS '07. International Conference on*, pages 674–677, Oct 2007.
- [LUV⁺11] Meiling Luo, Dmitry Umansky, Guillaume Villemaud, Marc Lafort, Jean-Marie Gorce, et al. Estimating channel fading statistics based on radio wave propagation predicted with deterministic mrfdpf method. In *European Conference on Antennas and Propagation 2011*, 2011.
- [LZD⁺12] Fan Li, Chunshui Zhao, Guanzhong Ding, Jian Gong, Chenxing Liu, and Feng Zhao. A reliable and accurate indoor localization method using phone inertial sensors. In *Proceedings of the 2012 ACM Conference on Ubiquitous Computing*, pages 421–430. ACM, 2012.
- [Mau12] Rainer Mautz. *Indoor positioning technologies*. PhD thesis, Habilitationsschrift ETH Zürich, 2012, 2012.
- [MBSS13] Sarvenaz Salehi Mourkani, Gabriele Bleser, Norbert Schmitz, and Didier Stricker. A low-cost and light-weight motion tracking suit. In *IEEE International Conference on Ubiquitous Intelligence and Computing . International Conference on Ubiquitous Intelligence and Computing (UIC-2013), December 18-20, Vietri sul Mare, Italy*. o.A., 12 2013.
- [MHV11] S.O.H. Madgwick, A.J.L. Harrison, and R. Vaidyanathan. Estimation of imu and marg orientation using a gradient descent algorithm. In *Rehabilitation Robotics (ICORR), 2011 IEEE International Conference on*, pages 1–7, June 2011.
- [Mil92] D. Mills. Network time protocol (version 3) specification, implementation, 1992.
- [MJF⁺08] Domenico A Maisano, Jafar Jamshidi, Fiorenzo Franceschini, Paul G Maropoulos, Luca Mastrogiacomo, Antony Mileham, and Geraint Owen. Indoor gps: system functionality and initial performance evaluation. *International Journal of Manufacturing Research*, 3(3):335–349, 2008.
- [MKSL04] Miklós Maróti, Branislav Kusy, Gyula Simon, and Ákos Lédeczi. The flooding time synchronization protocol. In *Proceedings of the 2nd international conference on Embedded networked sensor systems*, pages 39–49. ACM, 2004.
- [MLG08] A Mathias, M Leonardi, and G Galati. An efficient multilateration algorithm. In *Digital Communications-Enhanced Surveillance of Aircraft and Vehicles, 2008*.

- TIWDC/ESAV 2008. Tyrrhenian International Workshop on*, pages 1–6. IEEE, 2008.
- [MLH05] Kavitha Muthukrishnan, Maria Lijding, and Paul Havinga. *Towards smart surroundings: Enabling techniques and technologies for localization*. Springer, 2005.
- [MMWKH14] Piotr Mirowski, Dimitrios Milioris, Philip Whiting, and Tin Kam Ho. Probabilistic radio-frequency fingerprinting and localization on the run. *Bell Labs Technical Journal*, 18(4):111–133, 2014.
- [MS11] Gerald F Marshall and Glenn E Stutz. *Handbook of optical and laser scanning*. CRC Press, 2011.
- [MSDIT13] Carlos Medina, José Carlos Segura, and Angel De la Torre. Ultrasound indoor positioning system based on a low-power wireless sensor network providing sub-centimeter accuracy. *Sensors*, 13(3):3501–3526, 2013.
- [MT11] R. Mautz and S. Tilch. Survey of optical indoor positioning systems. In *Indoor Positioning and Indoor Navigation (IPIN), 2011 International Conference on*, pages 1–7, Sept 2011.
- [MTEM10] Andrew Markham, Niki Trigoni, Stephen A Ellwood, and David W Macdonald. Revealing the hidden lives of underground animals using magneto-inductive tracking. In *Proceedings of the 8th ACM Conference on Embedded Networked Sensor Systems*, pages 281–294. ACM, 2010.
- [MVFB10] Eladio Martin, Oriol Vinyals, Gerald Friedland, and Ruzena Bajcsy. Precise indoor localization using smart phones. In *Proceedings of the international conference on Multimedia*, pages 787–790. ACM, 2010.
- [MWBS09] Alessandro Mulloni, Daniel Wagner, Istvan Barakonyi, and D. Schmalstieg. Indoor positioning and navigation with camera phones. *Pervasive Computing, IEEE*, 8(2):22–31, April 2009.
- [NMR⁺10] Pavel V Nikitin, Rene Martinez, Shashi Ramamurthy, Hunter Leland, Gary Spiess, and KVS Rao. Phase based spatial identification of uhf rfid tags. In *RFID, 2010 IEEE International Conference on*, pages 102–109. IEEE, 2010.
- [OKL14] Jung H Oh, Doojin Kim, and Beom H Lee. An indoor localization system for mobile robots using an active infrared positioning sensor. *Journal of Industrial and Intelligent Information Vol*, 2(1), 2014.
- [PAK⁺05] Neal Patwari, Joshua N Ash, Spyros Kyperountas, Alfred O Hero III, Randolph L Moses, and Neiyer S Correal. Locating the nodes: cooperative localization in wireless sensor networks. *Signal Processing Magazine, IEEE*, 22(4):54–69, 2005.
- [PAY07] Sang Young Park, Hyo-Sung Ahn, and Wonpil Yu. Round-trip time-based wireless positioning without time synchronization. In *Control, Automation and Systems, 2007. ICCAS'07. International Conference on*, pages 2323–2326. IEEE, 2007.

Bibliography

- [PBA⁺10] Gerald Pirkel, David Bannach, Oliver Amft, Matthias Kreil, and Paul Lukowicz. Towards wearable sensing-based assessment of fluid intake. In *Eighth Annual IEEE International Conference on Pervasive Computing and Communications, PerCom 2010, March 29 - April 2, 2010, Mannheim, Germany, Workshop Proceedings*, pages 298–303, 2010.
- [PFKP05] Donald J Patterson, Dieter Fox, Henry Kautz, and Matthai Philipose. Fine-grained activity recognition by aggregating abstract object usage. In *Wearable Computers, 2005. Proceedings. Ninth IEEE International Symposium on*, pages 44–51. IEEE, 2005.
- [PH04] Eric A Prigge and Jonathan P How. Signal architecture for a distributed magnetic local positioning system. *Sensors Journal, IEEE*, 4(6):864–873, 2004.
- [PHB01] Joseph A Paradiso, Kai-yuh Hsiao, and Ari Benbasat. Tangible music interfaces using passive magnetic tags. In *Proceedings of the 2001 conference on New interfaces for musical expression*, pages 1–4. National University of Singapore, 2001.
- [PHCL15] Gerald Pirkel, Peter Hevesi, Jingyuan Cheng, and Paul Lukowicz. mbeacon: Accurate, robust proximity detection with smart phones and smart watches using low frequency modulated magnetic fields. In *Proceedings of the 10th EAI International Conference on Body Area Networks, BodyNets '15*, pages 186–191, ICST, Brussels, Belgium, Belgium, 2015. ICST (Institute for Computer Sciences, Social-Informatics and Telecommunications Engineering).
- [PHW⁺14] Gerald Pirkel, Peter Hevesi, Sebastian Wille, Norbert Wehn, and Paul Lukowicz. Monitoring household activities and user location with a cheap, unobtrusive thermal sensor array. In *Proceedings of the 2014 ACM International Joint Conference on Pervasive and Ubiquitous Computing. International Conference on Ubiquitous Computing (Ubicomp), Seattle, WA, USA, USA, UbiComp '14 Adjunct*, pages 141–145. ACM, 9 2014.
- [PKLF11] Gerald Pirkel, Kamil Kloch, Paul Lukowicz, and Carl Fischer. Emergent behaviour in collaborative indoor localisation: An example of self-organisation in ubiquitous sensing systems. In *Architecture of Computing Systems - ARCS 2011 - 24th International Conference, Como, Italy, February 24-25, 2011. Proceedings*, pages 207–218, 2011.
- [PL12] Gerald Pirkel and Paul Lukowicz. Robust, low cost indoor positioning using magnetic resonant coupling. In *The 2012 ACM Conference on Ubiquitous Computing, UbiComp '12, Pittsburgh, PA, USA, September 5-8, 2012*, pages 431–440, 2012.
- [PL13] Gerald Pirkel and Paul Lukowicz. Indoor localization based on resonant oscillating magnetic fields for aal applications. In Juan A. Botía, Juan Antonio Álvarez Garcia, Kaori Fujinami, Paolo Barsocchi, and Till Riedel, editors, *Evaluating AAL Systems Through Competitive Benchmarking*, volume 386 of *Communications in*

Computer and Information Science, pages 128–140. Springer, Berlin - Heidelberg, 2013.

- [PLB⁺10] Gerald Pirkel, Paul Lukowicz, David Bannach, Florian Wagner, Alberto Calatroni, Kilian Förster, Thomas Holleczeck, Mirco Rossi, Daniel Roggen, Gerhard Tröster, Jakob Doppler, Clemens Holzmann, Andreas Riener, Alois Ferscha, and Ricardo Chavarriaga. Recording a complex, multi modal activity data set for context recognition. In *ARCS '10 - 23th International Conference on Architecture of Computing Systems 2010, Workshop Proceedings, February 22-23, 2010, Hannover, Germany*, pages 161–166, 2010.
- [PMF⁺12] Gerald Pirkel, Widyawan Daniele Munaretto, Carl Fischer, Chunlei An, Paul Lukowicz, Martin Klepal, Andreas Timm-Giel, Joerg Widmer, Dirk Pesch, and Hans Gellersen. Virtual lifeline: Multimodal sensor data fusion for robust navigation in unknown environments. *Pervasive and Mobile Computing*, 8(3):388–401, 2012.
- [Pou97] Paul Bourke. Intersection of two circles. <http://paulbourke.net/geometry/circlesphere/>, 1997. [Online; accessed 6.3.2016].
- [Pri05] Nissanka Bodhi Priyantha. *The cricket indoor location system*. PhD thesis, Massachusetts Institute of Technology, 2005.
- [PS10] A. Povalac and J. Sebesta. Phase of arrival ranging method for uhf rfid tags using instantaneous frequency measurement. In *ICECom, 2010 Conference Proceedings*, pages 1–4, Sept 2010.
- [PS11] A. Povalac and J. Sebesta. Phase difference of arrival distance estimation for rfid tags in frequency domain. In *RFID-Technologies and Applications (RFID-TA), 2011 IEEE International Conference on*, pages 188–193, Sept 2011.
- [PS16] Duy Duong Pham and Young Soo Suh. Pedestrian navigation using foot-mounted inertial sensor and lidar. *Sensors*, 16(1):120, 2016.
- [PSKL08] Gerald Pirkel, Karl Stockinger, Kai S. Kunze, and Paul Lukowicz. Adapting magnetic resonant coupling based relative positioning technology for wearable activity recognition. In *12th IEEE International Symposium on Wearable Computers (ISWC 2008), September 28 - October 1, 2008, Pittsburgh, PA, USA*, pages 47–54, 2008.
- [PSP13] Smitha Paulose, Elizabeth Sebastian, and Babu Paul. Acoustic source localization. *International Journal of Advanced Research in Electrical, Electronics and Instrumentation Engineering*, 2(2):933–9, 2013.
- [PTA06] Shwetak N Patel, Khai N Truong, and Gregory D Abowd. Powerline positioning: A practical sub-room-level indoor location system for domestic use. In *UbiComp 2006: Ubiquitous Computing*, pages 441–458. Springer, 2006.
- [PWH12] A.R. Pratama, Widyawan, and R. Hidayat. Smartphone-based pedestrian dead

Bibliography

- reckoning as an indoor positioning system. In *System Engineering and Technology (ICSET), 2012 International Conference on*, pages 1–6, Sept 2012.
- [QHZ⁺] Lanxin Qiu, Zhangqin Huang, Shaohua Zhang, Cheng Jing, Hao Li, and Shuyao Li. Multifrequency Phase Difference of Arrival Range Measurement: Principle, Implementation, and Evaluation. *International Journal of Distributed Sensor Networks*.
- [Rap01] Theodore Rappaport. *Wireless Communications: Principles and Practice*. Prentice Hall PTR, Upper Saddle River, NJ, USA, 2nd edition, 2001.
- [RBML08] Frédéric Rivard, Jonathan Bisson, François Michaud, and Dominic Létourneau. Ultrasonic relative positioning for multi-robot systems. In *Robotics and Automation, 2008. ICRA 2008. IEEE International Conference on*, pages 323–328. IEEE, 2008.
- [RBSJ79a] F.H. Raab, E.B. Blood, T.O. Steiner, and H.R. Jones. Magnetic position and orientation tracking system. *Aerospace and Electronic Systems, IEEE Transactions on*, AES-15(5):709–718, Sept 1979.
- [RBSJ79b] Frederick H Raab, Ernest B Blood, Terry O Steiner, and Herbert R Jones. Magnetic position and orientation tracking system. *Aerospace and Electronic Systems, IEEE Transactions on*, (5):709–718, 1979.
- [RC04] Duncan P Robertson and Roberto Cipolla. An image-based system for urban navigation. In *BMVC*, pages 1–10, 2004.
- [RS01] Padmanabha R Rao and Paolo L Siccardo. Location determination using rf fingerprinting, July 31 2001. US Patent 6,269,246.
- [RSF⁺06] N. Ravi, P. Shankar, A. Frankel, A. Elgammal, and L. Iftode. Indoor localization using camera phones. In *Mobile Computing Systems and Applications, 2006. WMCSA '06. Proceedings. 7th IEEE Workshop on*, pages 49–49, April 2006.
- [SBA14] U. Schatzberg, L. Banin, and Y. Amizur. Enhanced wifi tof indoor positioning system with mems-based ins and pedometric information. In *Position, Location and Navigation Symposium - PLANS 2014, 2014 IEEE/ION*, pages 185–192, May 2014.
- [SBG99] Albrecht Schmidt, Michael Beigl, and Hans-W Gellersen. There is more to context than location. *Computers & Graphics*, 23(6):893–901, 1999.
- [SBK05] Bharath Sundararaman, Ugo Buy, and Ajay D Kshemkalyani. Clock synchronization for wireless sensor networks: a survey. *Ad Hoc Networks*, 3(3):281–323, 2005.
- [SBT14] Stephan Sigg, Ulf Blanke, and Gerhard Troster. The telepathic phone: Frictionless activity recognition from wifi-rssi. In *Pervasive Computing and Communications (PerCom), 2014 IEEE International Conference on*, pages 148–155. IEEE, 2014.

- [SCGL05] Guolin Sun, Jie Chen, Wei Guo, and KJ Ray Liu. Signal processing techniques in network-aided positioning: a survey of state-of-the-art positioning designs. *Signal Processing Magazine, IEEE*, 22(4):12–23, 2005.
- [Sey05] John S Seybold. *Introduction to RF propagation*. John Wiley & Sons, 2005.
- [SGG08] Zafer Sahinoglu, Sinan Gezici, and Ismail Guvenc. Ultra-wideband positioning systems. *Cambridge, New York*, 2008.
- [SHSM10] Marcelo Segura, Hossein Hashemi, Cristian Sisterna, and Vicente Mut. Experimental demonstration of self-localized ultra wideband indoor mobile robot navigation system. In *Indoor Positioning and Indoor Navigation (IPIN), 2010 International Conference on*, pages 1–9. IEEE, 2010.
- [SJJ+00] Quentin H Spencer, Brian D Jeffs, Michael Jensen, et al. Modeling the statistical time and angle of arrival characteristics of an indoor multipath channel. *Selected Areas in Communications, IEEE Journal on*, 18(3):347–360, 2000.
- [SKCB02] Robert A Scholtz, P Vijay Kumar, and Carlos J Corrada-Bravo. Signal design for ultra-wideband radio. In *Sequences and their Applications*, pages 72–87. Springer, 2002.
- [SL07] D. Savio and T. Ludwig. Smart carpet: A footstep tracking interface. In *Advanced Information Networking and Applications Workshops, 2007, AINAW '07. 21st International Conference on*, volume 2, pages 754–760, May 2007.
- [SL08] Axel Steinhage and Christl Lauterbach. Sensfloor (r): Ein aal sensorsystem für sicherheit, homecare und komfort. *Ambient Assisted Living-AAL*, 2008.
- [SNE+08] Mitilineos A Stelios, Argyreas D Nick, Makri T Effie, Kyriazanos M Dimitris, and Stelios CA Thomopoulos. An indoor localization platform for ambient assisted living using uwb. In *Proceedings of the 6th international conference on advances in mobile computing and multimedia*, pages 178–182. ACM, 2008.
- [SNH03] Hartmut Surmann, Andreas Nüchter, and Joachim Hertzberg. An autonomous mobile robot with a 3d laser range finder for 3d exploration and digitalization of indoor environments. *Robotics and Autonomous Systems*, 45(3–4):181 – 198, 2003.
- [SOJ+06] Thomas Stiefmeier, Georg Ogris, Holger Junker, Paul Lukowicz, and Gerhard Troster. Combining motion sensors and ultrasonic hands tracking for continuous activity recognition in a maintenance scenario. In *Wearable Computers, 2006 10th IEEE International Symposium on*, pages 97–104. IEEE, 2006.
- [SPM+13] M. Scherhauf, M. Pichler, D. Muller, A. Ziroff, and A. Stelzer. Phase-of-arrival-based localization of passive uhf rfid tags. In *Microwave Symposium Digest (IMS), 2013 IEEE MTT-S International*, pages 1–3, June 2013.
- [SRF+92] Scott Y Seidel, Theodore S Rappaport, Martin J Feuerstein, Kenneth L Blackard, and L Grindstaff. The impact of surrounding buildings on propagation for wireless

Bibliography

- in-building personal communications system design. In *Vehicular Technology Conference, 1992, IEEE 42nd*, pages 814–818. IEEE, 1992.
- [SRJJ97] Q. Spencer, M. Rice, Brian Jeffs, and M. Jensen. A statistical model for angle of arrival in indoor multipath propagation. In *Vehicular Technology Conference, 1997, IEEE 47th*, volume 3, pages 1415–1419 vol.3, May 1997.
- [SSHH04] William M Spears, Diana F Spears, Jerry C Hamann, and Rodney Heil. Distributed, physics-based control of swarms of vehicles. *Autonomous Robots*, 17(2-3):137–162, 2004.
- [SV03] M.L. Sichitiu and C. Veerarittiphan. Simple, accurate time synchronization for wireless sensor networks. In *Wireless Communications and Networking, 2003. WCNC 2003. 2003 IEEE*, volume 2, pages 1266 –1273 vol.2, march 2003.
- [SWH⁺00] Robert A Scholtz, Robert Weaver, E Homier, JALJ Lee, PAHP Hilmes, A Taha, and RAWR Wilson. Uwb radio deployment challenges. In *Personal, Indoor and Mobile Radio Communications, 2000. PIMRC 2000. The 11th IEEE International Symposium on*, volume 1, pages 620–625. IEEE, 2000.
- [SY04] Fikret Sivrikaya and Bülent Yener. Time synchronization in sensor networks: a survey. *Network, IEEE*, 18(4):45–50, 2004.
- [SYS12] Ali Asghar Nazari Shirehjini, Abdulsalam Yassine, and Shervin Shirmohammadi. An rfid-based position and orientation measurement system for mobile objects in intelligent environments. *Instrumentation and Measurement, IEEE Transactions on*, 61(6):1664–1675, 2012.
- [Tan07] Andrew S. Tanenbaum. *Modern Operating Systems*. Prentice Hall Press, Upper Saddle River, NJ, USA, 3rd edition, 2007.
- [TDM11] Lorenzo Taponocco, AA D’Amico, and Umberto Mengali. Joint toa and aoa estimation for uwb localization applications. *Wireless Communications, IEEE Transactions on*, 10(7):2207–2217, 2011.
- [TFBD01] Sebastian Thrun, Dieter Fox, Wolfram Burgard, and Frank Dellaert. Robust monte carlo localization for mobile robots. *Artificial Intelligence*, 128(1–2):99 – 141, 2001.
- [TNNL02] Juan D Tardós, José Neira, Paul M Newman, and John J Leonard. Robust mapping and localization in indoor environments using sonar data. *The International Journal of Robotics Research*, 21(4):311–330, 2002.
- [TSFC] Jorge Torres-Solis, Tiago H Falk, and Tom Chau. *A review of indoor localization technologies: towards navigational assistance for topographical disorientation*.
- [TSH05] Michael Tuchler, Volker Schwarz, and Alexander Huber. Location accuracy of an uwb localization system in a multi-path environment. In *Ultra-Wideband, 2005. ICU 2005. 2005 IEEE International Conference on*, pages 414–419. IEEE, 2005.

- [UR04] Andreu Urruela and Jaume Riba. Novel closed-form ml position estimator for hyperbolic location. In *Acoustics, Speech, and Signal Processing, 2004. Proceedings.(ICASSP'04). IEEE International Conference on*, volume 2, pages ii–149. IEEE, 2004.
- [VB12] Anna Maria Vegni and Mauro Biagi. An indoor localization algorithm in a small-cell led-based lighting system. In *Indoor Positioning and Indoor Navigation (IPIN), 2012 International Conference on*, pages 1–7. IEEE, 2012.
- [VGR03] Jana Van Greunen and Jan Rabaey. Lightweight time synchronization for sensor networks. In *Proceedings of the 2nd ACM international conference on Wireless sensor networks and applications*, pages 11–19. ACM, 2003.
- [VMRL03] J.M. Valin, F. Michaud, J. Rouat, and D. Letourneau. Robust sound source localization using a microphone array on a mobile robot. In *Intelligent Robots and Systems, 2003. (IROS 2003). Proceedings. 2003 IEEE/RSJ International Conference on*, volume 2, pages 1228–1233 vol.2, Oct 2003.
- [VMV09] Miika Valtonen, Jaakko Mäentausta, and Jukka Vanhala. Tiletrack: Capacitive human tracking using floor tiles. In *Pervasive Computing and Communications, 2009. PerCom 2009. IEEE International Conference on*, pages 1–10. IEEE, 2009.
- [WE14] Ryan W Wolcott and Ryan M Eustice. Visual localization within lidar maps for automated urban driving. In *Intelligent Robots and Systems (IROS 2014), 2014 IEEE/RSJ International Conference on*, pages 176–183. IEEE, 2014.
- [WHFaG92] Roy Want, Andy Hopper, Veronica Falcão, and Jonathan Gibbons. The active badge location system. *ACM Trans. Inf. Syst.*, 10(1):91–102, January 1992.
- [WIB11] Andreas Wendel, Arnold Irschara, and Horst Bischof. Natural landmark-based monocular localization for mavs. In *Robotics and Automation (ICRA), 2011 IEEE International Conference on*, pages 5792–5799. IEEE, 2011.
- [WJH97] Andy Ward, A. Jones, and A. Hopper. A new location technique for the active office. *Personal Communications, IEEE*, 4(5):42–47, Oct 1997.
- [WMP+12] Mark J. Weal, Danus T. Michaelides, Kevin R. Page, David C. De Roure, Eloise Monger, and Mary Gobbi. Semantic annotation of ubiquitous learning environments. *IEEE Transactions on Learning Technologies*, 5(2):143–156, April 2012.
- [WSE+12] He Wang, Souvik Sen, Ahmed Elgohary, Moustafa Farid, Moustafa Youssef, and Romit Roy Choudhury. No need to war-drive: unsupervised indoor localization. In *Proceedings of the 10th international conference on Mobile systems, applications, and services*, pages 197–210. ACM, 2012.
- [Xio98] Li Xiong. A selective model to suppress nlos signals in angle-of-arrival (aoa) location estimation. In *Personal, Indoor and Mobile Radio Communications, 1998. The Ninth IEEE International Symposium on*, volume 1, pages 461–465. IEEE, 1998.

Bibliography

- [XLL⁺10] Jiuqiang Xu, Wei Liu, Fenggao Lang, Yuanyuan Zhang, and Chenglong Wang. Distance measurement model based on rssi in wsn. *Wireless Sensor Network*, 2(08):606, 2010.
- [XTL⁺14] Bo Xie, Guang Tan, Yunhuai Liu, Mingming Lu, Kongyang Chen, and Tian He. Lips: A light intensity based positioning system for indoor environments. *arXiv preprint arXiv:1403.2331*, 2014.
- [YGA⁺14] Y. Yelkovan, H. Guneren, A. Akgoz, F. Eybek, A. Turk, I. Gol, and O. Cetin. Infrared beacon based sub-meter indoor localization. In *Signal Processing and Communications Applications Conference (SIU), 2014 22nd*, pages 1427–1430, April 2014.
- [YRL10] Ruiqing Ye, Stephen Redfield, and Huaping Liu. High-precision indoor uwb localization: Technical challenges and method. In *Ultra-Wideband (ICUWB), 2010 IEEE International Conference on*, volume 2, pages 1–4, 2010.
- [ZCC⁺12] Ben Zhang, Kaifei Chen, Yun Cheng, Chieh-Jan Mike Liang, Xiaofan Jiang, and Feng Zhao. Location-log: bringing online shopping benefits to the physical world with magnetic-based proximity detection. 2012.
- [Zha12] Zhengyou Zhang. Microsoft kinect sensor and its effect. *MultiMedia, IEEE*, 19(2):4–10, 2012.
- [ZK06] Wei Zhang and Jana Kosecka. Image based localization in urban environments. In *3D Data Processing, Visualization, and Transmission, Third International Symposium on*, pages 33–40. IEEE, 2006.
- [ZSHZ12] Lukasz Zwirello, Tom Schipper, Marlene Harter, and Thomas Zwick. UWB Localization System for Indoor Applications: Concept, Realization and Analysis. *Journal of Electrical and Computer Engineering*, 2012:11, 2012.
- [ZXM⁺14] Xiaojie Zhao, Zhuoling Xiao, Andrew Markham, Niki Trigoni, and Yong Ren. Does btle measure up against wifi? a comparison of indoor location performance. In *European Wireless 2014; 20th European Wireless Conference; Proceedings of*, pages 1–6. VDE, 2014.
- [ZZXL14] Julie Yixuan Zhu, Anny Xijia Zheng, Jialing Xu, and Victor OK Li. Spatio-temporal (st) similarity model for constructing wifi-based rssi fingerprinting map for indoor localization. In *International Conference on Indoor Positioning and Indoor Navigation*, volume 27, page 30th, 2014.

Lebenslauf Dipl. Inf. Gerald Stephan Pirkl

Email: Gerald.pirkl@gmail.com

Geburtstag / Geburtsort: 1.4.1981, Deggendorf, Deutschland

Beruflicher Werdegang

10/2012 - jetzt **Wissenschaftlicher Mitarbeiter**

am Fachbereich Eingebettete Intelligenz, DFKI GmbH
Kaiserslautern, unter der Leitung von Prof. Dr. Paul Lukowicz
Erforschung verschiedener Lokalisierungssysteme,
Gestenerkennungssystem für Industrie und Handwerk
Projektmanagement und Berichtswesen

04/2007 – 09/2012 **Wissenschaftlicher Mitarbeiter** am Lehrstuhl für

Informatik, Eingebettete Systeme,
Universität Passau unter der Leitung von Prof. Dr. Paul Lukowicz
Betreuung verschiedener Übungen und studentischer Projekte,
Koordination und Projektbegleitung verschiedener Industrieprojekte mit
regionalen Firmen
Projektarbeit an diversen EU geförderten Projekten

Ausbildung

10/2000 – 04/2007 **Studium Diplom Informatik** mit Schwerpunkt

Medien und Design, Fakultät für Informatik und
Mathematik Universität Passau

Diplomarbeit: Proximity Estimation in Sensor Networks

09/1991 – 06/2000 **Abitur am Gymnasium Vilshofen**, Niederbayern